CYRIC

ANNUAL REPORT

1999

(January 1999 - December 1999)

CYCLOTRON AND RADIOISOTOPE CENTER
TOHOKU UNIVERSITY

PREFACE

In this twentieth issue of the CYRIC Annual Report, we summarize the activities for research and development and results of training for radioisotope safe-treatment at Cyclotron and Radioisotope Center, Tohoku University during the calendar year 1999.

It is my great pleasure to report here that the first acceleration of charged particles has successfully been performed on May 6, 2000, and the Opening-Ceremony for the new K=110 AVF-cyclotron was held with 100 distinguished guests on March 10, 2000 at CYRIC.

The year 1999 has been the second year when renewal of the AVF cyclotron and construction of experimental facilities, together with related infrastructures such as electricity and cooling water supplying system, etc., have been carried out. Construction of hard- and soft-ware for control systems of the cyclotron and the beam-transport equipment have been the most crucial task in this year. These jobs were performed by staffs of CYRIC. The present sophisticated control-system with PLC (Programmable Logic Controller) are expected to give us versatile utilities for the control of many devises.

Design, construction and installation of related experimental facilities such as neutron time of flight analyzing system including the beam swinger, automated synthesis system for short-lived positron emitter labeled compounds, on-line electromagnetic mass separator with three pairs of clover-type Ge detector system, and high-energy γ-ray detector have been carried out in this year.

Studies with PIXE (Particle Induced X-ray Emission) technique have been continuously performed by using electrostatic accelerator, installed at FNL (Fast Neutron Laboratory) in Graduate School of Technology, Tohoku University, under the scientific tie-up between CYRIC and FNL. Indeed, more than six groups are running under this project using a total of its 250 hours beam-time.

Synthesis of radiopharmaceuticals for clinical research with PET (Positron Emission Tomography) and other applications have been continuously carried out. The small size AVF cyclotron HM-12, installed under scientific and technical tie-up among IDAC, CYRIC and Sumitomo Heavy Industry Co. Ltd, has steadily been operated. Positron emitting radio-nuclides was provided with 281 hours exposure by 12-MeV proton beams, while those by 6-MeV deuteron beams were done with 255 hrs exposure. The amounts of radiopharmaceuticals, thus produced in this year, are 137, 48, 15, 0.6, 6, 7, 4, and 4GBq, for ^{18}F-FDG, ^{11}C-MET, ^{11}C-DOX, ^{11}C-YM, ^{15}O-H$_2$O, ^{15}O-O$_2$, ^{15}O-CO$_2$ and ^{15}O-CO, respectively. Biomedical applications of CYRIC cyclotron have been extended to cover many basic and clinical fields such as oncology, neuroscience, neurology, neurosurgery, cardiology,

gastroenterology, orthopedics, opththalmology, pediatrics, dentistry, pharmacology, sport science, rehabillitation, nuclear medicine and so on.

During 1999 school year, 495 of staff members and students of Tohoku University were trained at this Center in the beginner's course of safe handling of radiation and radioisotopes, while 235 staff members and students in the "x-ray course". In addition, 48 of staff members and students were trained in the course of safe handling of radiation from a SOR (Synchrotron Orbital Radiation).

Prof. M. Fujioka is going to reach his retirement age by the end of this March. He is the first scientific staff of CYRIC. Since 1977, he has been responsible enough for operation, maintain and development of the accelerator as the head of division of accelerator. His activity involves, as well, scientific research and education. His researches cover the following fields: by using an isotope separator on-line equipped with a tape-transport and an ion-guide systems: (1) Discovery of the heaviest two "mirror-decay" nuclei, ^{57}Cu and ^{59}Zn, (2) Implantation of radioactive isotopes to make good-quality samples for precision measurement of conversion-electrons up to the atomic valence shells to derive the Mössbauer isomer-shift scales DR/R. Researches, using a perturbation magnet specifically equipped with a pair of "active" magnetic channels to compensate for beam position and bending, have performed for measurement of magnetic moments for fifteen nuclear isomeric states in order to clarify their nuclear structure.

We are very grateful to Tohoku University and to the Ministry of Education, Science, Sports and Culture for their continuous support.

March, 2000

Hikonojo ORIHARA
Director
Cyclotron and Radioisotope Center, Tohoku University

Photograph pictures the new AVF cyclotron and beam extraction ports in the cyclotron vault.

CONTENTS

I. PHYSICS AND TECHNOLOGY

II. CHEMISTRY

III. MEDICINE AND BIOLOGY (Basic)

IV. MEDICINE AND BIOLOGY (Clinical)

V. RADIATION PROTECTION AND TRAINING OF SAFE HANDLING

VI. PUBLICATIONS

VII. MEMBERS OF COMMITTEE

VIII. PERSONNEL

I. PHYSICS AND TECHNOLOGY

I. 1. Isovector Part of Optical Potentials Studied through Analog Transitions in the (p, n) Reaction at 20 MeV

Jon G. C., Orihara H.*, Terakawa A.*, Suzuki H.*, Ishii K.,** and Ohnuma H.***

Institute of Physics, Academia Sinica, Nankang Taipei, Taiwan 11529
Cyclotron and Radioisotope Center, Tohoku University*
Department of Quantum Science and Energy Engineering, Tohoku University**
Department of Physics, Chiba Institute of Technology, Narashino-shi, Chiba 275-0023, Japan***

The isospin impurity in nuclei has been a long standing problem in nuclear physics. Studies of isospin symmetry have recently become again a popular subject of nuclear structure physics[1-3], especially due to the development of experimental facilities for charge-exchange reactions and those for radioactive beams. Spreading widths of the isobaric analog states (IAS) give us an important clue to the understanding of the charge-independence-breaking (CIB) and charge-symmetry-breaking (CSB) interactions in nuclei[4-6]. Our recent measurement of the spreading widths of the IAS via the $(p, n_{IAS}\vec{p})$ reaction and their analysis[7] have revealed that the coupling between the giant isovector monopole state and the IAS induced through the isovector part of the nucleon-nucleus potential is crucial to understand the mass number dependence of the spreading widths of the IAS.

The isovector nucleon-nucleus potential can be derived from optical-model analyses of IAS transitions in the (p, n) reaction, in which transferred total angular momentum and parity ΔJ^{π} are 0^{+} Such a transition is often called a Fermi-type transition or quasi-elastic scattering. However, since optical-model analyses suffer from well-known ambiguities in the parameters[8], it is necessary to accumulate data over a wide-range of target nuclei as well as over a wide-range of incident energies and carry out systematic analyses. Carlson and his collaborators reported a systematic optical model analysis of quasi-elastic (p, n) reactions at 22.8 MeV on 29 nuclei ranging from ^{9}Be to ^{208}Pb[9]. They derived the isovector potential for each target nucleus, and gave a smooth parametrization of the best-fit parameters for all the nuclei investigated. However, their data and analysis were limited by experimental conditions and theoretical treatment of mixed analog transitions.

We have reported[10,11] the data and the analysis of isobaric analog transitions at E_{p} = 35 MeV in (p, n) reactions on thirteen target nuclei over a wide range of nuclear masses $7 \le A \le 208$. The best-fit parameters for the Lane-type isovector potential were obtained for each transition, and then the mass-number dependence of each parameter was expressed as a linear function of $A^{1/3}$. The strengths of the real part of the Lane potential were determined within

±3 ~ ±5% accuracy in the mass region studied.   It was found that imaginary strengths of the Lane potential were almost independent of the mass number.

In this report we discuss further study of (p, n) reactions at E_p = 20 MeV leading to IAS on seven target nuclei in the regions $54 \le A \le 71$; namely, ^{54,56}Fe, ^{58,60,62,64}Ni, ^{70}Zn, and ^{71}Ga.   Analysis similar to our previous works has been made, and the best-fit parameters for the Lane potential were obtained for these nuclei.   Combining the present results with previous results at E_p = 22.8 and 35 MeV, this set was used to discuss energy dependence of A-dependent global parameters of the Lane potential.

The experiment was performed at the Cyclotron and Radioisotope Center, Tohoku University, with a 20-MeV proton beam from an AVF-cyclotron and a beam swinger system. The details of the experimental setup have been described previously[12,13].   Neutron energies were measured by the time-of-flight technique (TOF).   The neutron detectors, 23.2 liter in a total sensitive volume, were filled with organic liquid scintillator NE213, and located at 44.3 m from the target.   The absolute efficiencies of the detectors were obtained from the ^{7}Li$(p, n)^{7}$Be activation analyses with an error less than ±6%. Errors in the absolute magnitude of (p, n) cross sections were estimated to be less than 12%.   All the targets were enriched isotopes with enrichments better than 95%, and were self-supporting foil.   Figures 1, illustrates the angular distributions of the (p, n) reactions on ^{70}Zn leading to the ground state of ^{70}Ga as a representative cases.

The Lane-model optical potential[14] was used in the macroscopic distorted-wave Born approximation (DWBA) analyses of the quasi-scattering data.   It is expressed as ;

$$U(r)= - U_0(r)+(4/A)U_1(r)\, \vec{t} \cdot \vec{T}+U_{so}(r)+(1/2-t_z)V_c(r) \, ,$$

(1)

where $\vec{t}\,(\vec{T})$ is the projectile (target) isospin, U_{so} is the spin-orbit potential, and V_C is the Coulomb potential.   The isospin dependent $\vec{t} \cdot \vec{T}$ term yields $t_+\, T_-$, $t_-\, T_+$ and $t_z\, T_z$, corresponding to (p, n), (n, p) and (p, p) or (n, n) reactions, respectively.   The (p, n) quasi-scattering takes place through the term

$$U_{pn}(r)=(2/A)\sqrt{N-Z}\, \cdot U_1(r) \, .$$

(2)

The isovector potential U_1 was parametrized in terms of standard Woods-Saxon forms as

$$U_1(r)=V_1 f(x_R) - 4ia_I W_1 \frac{d}{dx_I} f(x_I) \, ,$$

(3)

where

$$f(x) = (1 + e^x)^{-1} ,$$

$$x = (r - R_i)/a_i \, ,$$

2

and

$$R_i = r_i A^{1/3}.$$

Here i = R or I. The parameters to be determined are the potential depths V_1 and W_1, geometrical parameters for the real part r_R and a_R, and those for the imaginary part r_I and a_I. To reduce the number of parameters to be fitted, the real geometrical parameters r_R and a_R were fixed to those by Becchetti and Greenlees[15]. Then we carried out a parameter search with the program IASEARCH[16] to find the best-fit parameter set to reproduce differential cross sections for each IAS transition.

Table 1 lists the best-fit parameters for each. These best-fit parameters are plotted as a function of $A^{1/3}$ in Figs. 2 and 3. Curves in the figures are those obtained for best-fit parameters at 35 MeV. They displayed for the comparison purpose. The radius of the imaginary potential decreases gradually, while the diffuseness parameter increases, as the mass number increases just on the curves at 35 MeV. The real potential depth V_1 also increases with the mass number. All of them seem to have linear dependence on $A^{1/3}$. The imaginary potential depth W_1, on the other hand, is almost constant in the mass region studied. However,

As discussed in Refs. [10-11], only minor effects were observed for the feedback of the finally obtained potential to the microscopic DWBA calculations and to the distorted waves in the entrance and exit channels in the macroscopic DWBA analysis. These correction terms are $\pm U_1 (N - Z)/A$ for the neutron and proton channels, respectively, and only a few % of the distorting potential strengths at most. Some of the data were reanalyzed by using the finally obtained optical potential parameters. Negligibly small contributions from the correction terms were found, and the results in the previous section are hardly changed.

The present results are in general agreement with those in Ref. [9] at $E_p = 22.8$ MeV. There are some differences, however, probably due partly to the incident-energy dependence of the potential and partly to a different analysis method. The imaginary depth of the isovector potential W_1 was fixed at $W_1/V_1 = 1/2$ in Ref. [9], while it was taken as a free parameter in the present analysis. As seen in Fig. 3, W_1 shows a different mass-number dependence from V_1. It is almost constant and about 6 MeV over the whole mass region studied. Furthermore, the present values for the geometrical parameters r_I and a_I show weaker $A^{1/3}$ dependence. The magnitudes of V_1 obtained here are about 20% smaller than those obtained by Carlson et al.

To summarize, we have extended our previous studies of the[10,11] isovector part of the optical potential at E_p=20 MeV. The best-fit parameters for the Lane-type isovector potential (V_1, W_1, r_I, a_I) were obtained for each transition. The values of V_1 were determined by present parametrization within $\pm 2 \sim \pm 4\%$ accuracy in the mass region studied. Our previous conclusion [10] that W_1 is almost independent of $A^{1/3}$ was confirmed.

References

1) Hamamoto I. and Sagawa H., Phys. Rev. C48, R960(1993).
2) Sagawa H., Van Giai N., and Suzuki T., Phys. Lett. B353, 7(1995).
3) Suzuki T., Sagawa H., and Colò G., Phys. Rev. C54, 2954(1996)
4) Suzuki T., Sagawa H., and Van Giai N., Phys. Rev. C 47, R1360(1993).
5) Colò G. and Van Giai N., Phys. Rev. C53, 2201(1996)
6) Van Kolck U., Friar J. L., and Goldman T., Phys. Lett. B271, 169(1996).
7) Orihara H. et al., Phys. Rev. Lett. 81, 3607(1998)
8) For example, Hodgson P. E., GROWTH POINTS IN NUCLEAR PHYSICS Vol. 3, Pergamon Press, Oxford, 1981.
9) Carlson J. D., Zafiratos C. D. and Lind D. A., Nucl. Phys. A249, 29 (1975).
10) Jon G. C., Orihara H., et al., Phys. Rev. C 56 , 900(1997).
11) Jon G. C., Orihara H., et al., Phys. Rev. C 62 , 044609(2000).
12) Orihara H. and Murakami T., Nucl. Instrum. Methods 181, 15 (1981).
13) Orihara H., et al., Nucl. Instrum. Methods A257, 189 (1987).
14) Lane A. M., Phys. Rev. 8, 171 (1962).
15) Becchetti F. D. and Greenlees G. W., Phys. Rev. 182, 1190 (1969).
16) A parameter search code for elastic and quasi-elastic scattering. Quasielastic calculations are made using the Lane model and adopted from the code DWUCK4 originally written by Kunz P. D.

Table 1. Best-fit parameters of isovector potential for each nucleus.

Reaction	E_{exc} of IAS (MeV)	V_1 (MeV)	W_1 (MeV)	r_1 (fm)	a_1 (fm)
$^{54}Fe(p, n)^{54}Co$	0.0	18.2±1.6	6.4±0.8	1.40±0.08	0.81±0.09
$^{56}Fe(p, n)^{56}Co$	3.5	19.5±0.9	8.2±0.4	1.39±0.05	0.86±0.09
$^{58}Ni(p, n)^{58}Cu$	0.203	17.4±2.1	7.3±0.9	1.34±0.05	0.90±0.09
$^{62}Ni(p, n)^{62}Cu$	2.54	18.9±1.7	6.9±0.8	1.42±0.06	0.80±0.07
$^{64}Ni(p, n)^{64}Cu$	4.63	19.0±1.2	8.6±1.2	1.41±0.05	0.81±0.08
$^{68}Zn(p, n)^{68}Ga$	6.71	17.3±2.4	7.1±1.3	1.36±0.07	0.85±0.08
$^{70}Zn(p, n)^{70}Ga$	8.26	19.7±0.3	6.6±1.1	1.36±0.05	0.85±0.13
$^{71}Ga(p, n)^{71}Ge$	8.96	19.0±0.6	7.7±1.2	1.36±0.10	0.81±0.14
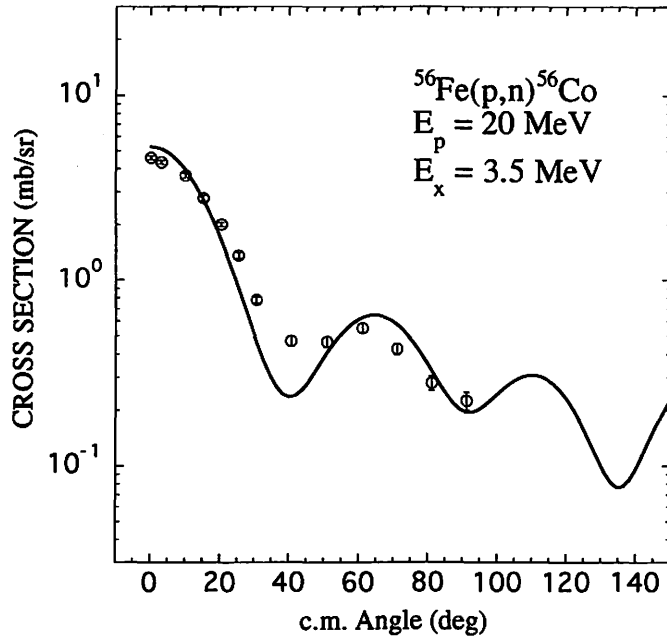
Fig. 1. Differential cross sections for neutrons leading to the 3.5-MeV IAS in ^{56}Co. This is an example of a pure IAS transition. The solid line shows the macroscopic DWBA calculation obtained with the best-fit parameters obtained for the isovector potential.
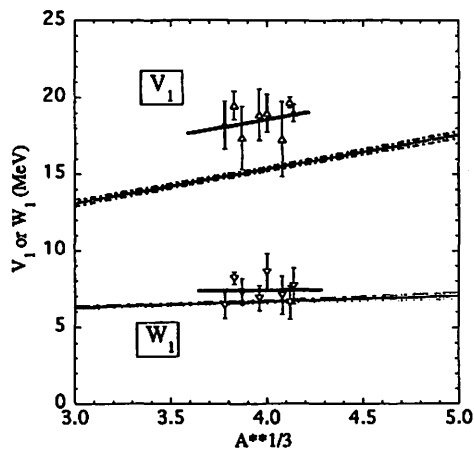
Fig. 2. Best-fit values of V_1 and W_1 plotted as a function of $A^{1/3}$. The solid lines indicate resultsof least-squares.
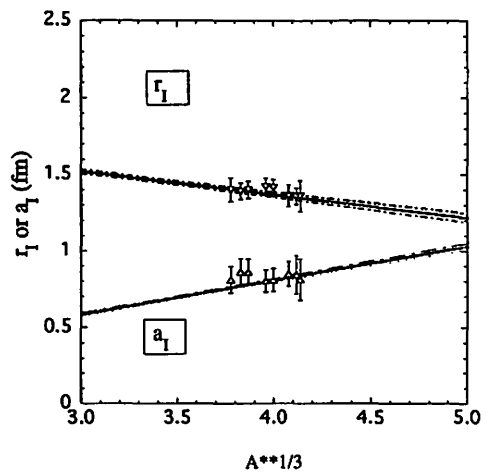
Fig.3. Same as Fig. 2 but for r_1 and a_1.

I. 2. Single-particle States in ^{69,71}Ga Studied through (*d,n*) Reactions on ^{68,70}Zn (II)

Kikuchi Y., Orihara H., Terakawa A., Suzuki H., Kumagai K., Fujisawa H., Hosaka M., Jon G. C.*, Ishii K.,** and Ohnuma H.***

Cyclotron and Radioisotope Center, Tohoku University
Institute of Physics, Academia Sinica, Nankang Taipei, Taiwan 11529*
Department of Quantum Science and Energy Engineering, Tohoku University**
Department of Physics, Chiba Institute of Technology, Narashino-shi, Chiba 275-0023, Japan***

The (d, n) reaction at sufficiently higher incident energy than ~15 MeV may provide a powerful spectroscopic tool for probing single-particle properties of nuclei since, being free from considering effects of compound nucleus formation, theoretical treatment for this reaction is more straightforward than other proton transfer reaction at lower energies[1].

Several interesting problems are associated with the structure of A ~ 70 nuclei. An example is evidence of a shape transition around N = 40. Moreover, electron capture rates in these fp shell nuclei, most of which are so far parametlized based on shell model, play an important role in stellar collapse leading to the formation of a super nova[2-3]. Such problems further include the topics in particle physics; double β-decay in A = 76 nuclei and *p-p* solar neutrino observation by ^{71}Ga (GALELEX at the Gran Dasso). Thus, test for such shell-model calculation by proper probe is essential. Single-particle properties studied by (d, n) reaction, for example, may provide a good place for a crucial test for these model calculations.

The single particle properties of states in ^{69,71}Ga have so far been examined through the (d, n) reaction at E_d = 10 MeV[4], and by (^{3}He, d) reactions at $E3_{He}$ = 15, 17 MeV[5]. The previous (d, n) and (^{3}He, d) works might be suffer from the ambiguities for the choice of optical-model parameters for complex particles, and from contributions of the compound nucleus formation process, since their projectile energies were rather low. The preliminary results have been given in a previous issue of CYRIC Annual Report[6]. In this second report, we present the results of further analysis for proton strength distributions over the higher excitation energy region in residual nuclei. Also given is comparison for summed spectroscopic factors $(2j+1)C^2S$ with those by shell-model.

The experiments were performed using a 25-MeV deuteron beam from the K=50 MeV AVF cyclotron at Cyclotron and Radioisotope Center (CYRIC), Tohoku University. Neutron energies were measured by the time of flight technique. Twelve neutron detectors

containing totally 23 litter of liquid-scintillator NE213 were set at a flight path of 44 m from the target, where the effective neutron detection solid angle was 0.23 msr. Angular distributions of neutrons were measured using a beam-swinger system. Detector efficiency for the most energetic neutrons was 3 %, which was determined by the ^{7}Li(p, n)^{7}Be reaction through activation analysis. Details of the CYRIC TOF facility have been described elsewhere[7-8]. Metallic foils of zinc enriched to 99 % in ^{68}Zn and 98% in ^{70}Zn with their thicknesses of 4.83 and 4.04 mg/cm^2, respectively, were used as targets. Overall energy resolution was 200 keV (FWHM) for the most energetic neutrons leading to the low lying states in the residual nuclei. Gamma-ray events have been rejected by pulse-shape-discrimination technique. Errors in the absolute magnitudes of cross section are estimated to be less than 12 %, the dominant part of which is due to the uncertainty of the detector efficiency. Typical excitation neutron spectra are shown in Figs. 1 and 2 for the (d, n) reactions on ^{68}Zn and ^{70}Zn, respectively. Numbers on peaks correspond to those listed in Tables 1 and 2.

Measured angular distributions of emitted neutrons are shown in Figs. 1 and 2 along with theoretical predictions. The zero-range distorted-wave Born-approximation (DWBA) calculation for angular distributions has been accomplished with the code DWUCK4[9]. Observed cross sections have been interpreted successfully by adiabatic deuteron breakup approximation (ADBA)[10] where s-wave deuteron breakup-effects are taken into accounts. Adiabatic deuteron potentials were derived from the sets of nucleon parameters at $E_p = E_n = 1/2 E_d$; those for protons have been given by Becchetti and Greenlees[11], while those for neutrons by Carlson et al[12]. Experimental spectroscopic factors (S) is extracted from the following equation:

$$\left(\frac{d\sigma}{d\Omega}\right)_{exp} = 1.55 \frac{(2J_f+1)}{(2J_i+1)} \frac{C^2S}{(2j+1)} \left(\frac{d\sigma}{d\Omega}\right)_{DWUCK} \quad (mb/sr), \quad (1)$$

where J_i and J_f are spins of initial and final states, respectively, and j is the spin of a transferred particle, while C is the Clebsh-Gordan coefficient for isospin coupling. The values of C^2 are 2/3 and 1/3 for the $T = T_0 - 1/2$ and $T_0 + 1/2$ states, respectively, T_0 being the target isospin.

Typical angular distributions of emitted neutrons leading to the isolated states in ^{71}Ga are illustrated in Fig. 3 together with DWBA comparison, while those for neutrons leading to the unresolved states are shown in Fig. 4 as the representative sample. Due to limited resolution to separate near lying peaks, their angular distribution are fitted with incoherent sum of the theoretical calculation. As shown in Fig. 4, good agreements between the experiment and theory have been obtained for the angular distribution shape. It is noticeable that higher ℓ transfer with f and g waves are readily enhanced comparing with the results at lower energy (d, n) and (^{3}He, d) reactions.

Transferred ℓ and spectroscopic factors for levels of ^{69}Ga and ^{71}Ga from the (d, n)

reactions on ^{68}Zn and ^{70}Zn are listed in Tables 1 and 2, respectively. Those obtained for (^{3}He, d) reactions are listed as well for comparison. The present $(2J_f + 1)C^2S$ values for l = 3 and 4 seem to be more reliable as seen in the transitions leading to the 1.35, 1.69 and 1.99 MeV peaks in ^{69}Ga, to the 1.49 and 2.20 MeV peaks in ^{71}Ga including those corresponding to highly excited states at E_x = 3.00, 3.25, 3.73 and 4.02 MeV. In Fig. Summed spectroscopic factors for each orbit obtained for ^{69}Ga and ^{71}Ga are illustrated. Dashed histogram in the figures are simple shell model comparison. As for the $1g_{9/2}$ and $2d_{5/2}$ orbits, there should be experimental difficulties to find peaks in highly excited rigion.

In a summary, we have observed proton single-particle states in ^{69}Ga and ^{71}Ga by the (d, n) reaction with a sufficiently high deuteron beam. Adiabatic deuteron break up approximation has been successfully applied to explain angular distributions of emitted neutrons, and to reduce hole-strength distribution for relevant orbital. The (d, n) cross sections leading to the unresolved peaks have been analyzed with the summed prediction yielding comprehensive spectroscopic factors up to E_x = 4MeV including the transition with higher transfer ℓ.

References

1) Miura K. et al., Nucl. Phys. A467(1987)79.
2) Fuller G. M., Astrophys. J 252(1982)741.
3) Cooperstein J. and Wambach J., Nucl. Phys. A420(1984)591.
4) Couch R. G. et al., Phys. Rev. C 2(1970)149.
5) Riccato A. and David P., Nucl. Phys. A228(1974)461.
6) Hosaka M. et al., CYRIC Annual Report 1991.
7) Johnson R. C. and Soper P. J. R., Phys. Rev. C1(1970)782.
8) Orihara H. et al., Nucl Instrum. and Methods 188(1981)15.
9) Orihara H. et al., Nucl Instrum. and Methods A257(1987)189.
10) Kunz P. D. unpublished.
11) Becchetti and Greenlees G. W., Phys. Rev. 182(1969)1190.
12) Carlson C. D., Zafiratos C. D. and Lind D. A., Nucl. Phys. A249(1979)15.

Table 1. Spectroscopic factor for levels of ^{69}Ga from the (d, n) reactions on ^{68}Zn. Those for (^{3}He, d) reactions at E_{3He} = 15 MeV are listed for comparison.

	^{68}Zn(d,n)^{69}Ga reaction. Present work E_d = 25 MeV				^{68}Zn(^{3}He, d)^{69}Ga Reaction by Riccato et al. E_{3He} = 15 MeV			
	E_x	ℓ	J^π	$(2j+1)C^2S$	E_x	ℓ	J^π	$(2j+1)C^2S$
1	0.00	1	$3/2^-$	1.51	0.000	1	$3/2^-$	1.55
2	0.31	1	$1/2^-$	1.03	0.319	1	$1/2^-$	1.27
3	0.58	3	$5/2^-$	3.94	0.574	3	$5/2^-$	4.47
4	0.89	1	$3/2^-$	0.46	0.872	1	$3/2^-$	0.34
5	1.12	1	$1/2^-$	0.14	1.027	1	$(1/2^-)$, $(3/2^-)$	0.14,(0.12)
6	1.35	1+3	$1/2^-+7/2^-$	0.08+0.74	1.336	(3)	$7/2^-$	≦0.65
			$3/2^-+7/2^-$	0.08+0.74	1.525		$(3/2^-)$, $(5/2^-)$	
7	1.69	3	$5/2^-$	0.64	1.723	3	$5/2^-$	0.7
					1.891			
8	1.99	1+3 +4	$1/2^-+5/2^-$ $9/2^+$	0.30+1.72 +2.19	1.971	4	$(9/2^+)$	3.58
			$1/2^-+5/2^-$ $9/2^+$	0.32+1.76 +2.11		1	$(1/2^-)$, $(3/2^-)$	(0.18).(0.16)
					2.002	(1)		≦0.05
					2.021	3	$(5/2^-)$, $(7/2^-)$	(1.36),(0.89)
					2.220	0	$1/2^+$	0.029
					2.476	2	$(5/2^+)$	0.14
					2.521	1	$(1/2^-)$, $(3/2^-)$	(0.04),(0.035)
9		1+4	$1/2^-+9/2^+$	0.13+1.65	2.564	4	$(9/2^+)$	1.32
					2.651	1	$(1/2^-)$, $(3/2^-)$	(0.13),(0.11)
					2.740	1	$(1/2^-)$, $(3/2^-)$	(0.035),(0.03)
					2.789	1	$(1/2^-)$, $(3/2^-)$	(0.042),(0.036)
10		1+2	$1/2^-+5/2^+$	0.05+0.15	2.916	2	$(5/2^+)$	0.15
11		1+2	$1/2^-+5/2^+$	0.09+0.09	3.089	2	$(5/2^+)$	0.21
					3.218			
12		(2)	$5/2^+$	0.15	3.314	2	$(5/2^+)$	0.068
					3.358	2	$(5/2^+)$	0.11
13		(0+1)	$1/2^++1/2^-$	0.02+0.09	3.760	1	$(1/2^-)$, $(3/2^-)$	(0.037),(0.033)
					3.803	0	$1/2^+$	0.009-0.015
14		1+3	$1/2^-+5/2^-$	0.18+0.95	4.021	1	$(1/2^-)$, $(3/2^-)$	(0.072),(0.063)
					4.115	0	$1/2^+$	0.023
					4.152	0	$1/2^+$	0.027
					4.190	0	$1/2^+$	0.016
					4.253	(0)	$1/2^+$	0.016
					4.321	(0)	$1/2^+$	0.042
					4.430			
					4.533	(0)	$1/2^+$	0.016
					4.830	0		0.028

Table 2. Spectroscopic factor for levels of ^{71}Ga from the (d, n) reactions on ^{70}Zn. Those for (^{3}He, d) reactions at E_{3He} = 17 MeV are listed for comparison.

No	^{70}Zn(d,n) ^{71}Ga reaction. Present work E_d = 25 MeV				^{70}Zn(^{3}He, d) ^{71}Ga Reaction by Riccato et al. E_{3He} = 17 MeV			
	E_x	ℓ	J^π	$(2j+1)C^2S$	E_x	ℓ	J^π	$(2j+1)C^2S$
1	0.00	1	$3/2^-$	1,86	0.000	1	$3/2^-$	1.88
					0.390	1	$1/2^-$	
2	0.48	1+3	$3/2^-+5/2^-$	0.56+3.30	0.487	3	$5/2^-$	3.18±0.5
					0.512	1	$3/2^-$	0.40±0.04
					0.912		$3/2^-$	
					0.965		$5/2^-$	
3	1.10	1	$1/2^-$	1.51	1.109	1	$1/2^-,(3/2^-)$	1.41,(1.23)
					1.397		$(5/2^-),(7/2^-)$	
4	1.49	2+4	$5/2^++9/2^+$	0.31+1.96	1.485	(2)	$(5/2^+)$	0.29
						4	$9/2^+$	2.90-3.60
					1.643	1	$3/2^-,(1/2^-)$	0.052,(0.061)
5	1.78	0+1+3	$1/2^++3/2^-$	0.04+0.12+	1.713	0	$1/2^+$	0.10
					2.075		$(1/2^-),(3/2^-)$	
					2.147	(1)		≦0.055
					2.206	3	$(5/2^-),(7/2^-)$	(1.82),(1.14)
6	2.20	1+3	$1/2^-+5/2^-$	0.42+1.45	2.260		$7/2^+$	
			$1/2^-+7/2^-$	0.40+1.09	2.310	1	$(1/2^-),(3/2^-)$	(0.22),(0.19)
					2.346	1	$(1/2^-),(3/2^-)$	(0.086),(0.073)
7	2.50	1+4	$1/2^-+9/2^+$	0.32+1.61	2.447	1	$(1/2^-),(3/2^-)$	(0.086),(0.077)
			$3/2^-+9/2^+$	0.36+1.56	2.516	1	$(1/2^-),(3/2^-)$	(0.14),(0.12)
					2.769			
					2.813			
					2.852			
					2.924			
8	3.00	1+3	$1/2^-+5/2^-$	0.25+1.23	2.967	(2)	$(5/2^+)$	0.18
			$3/2^-+52^-$	0.23+1.17	3.016			
					3.153	2	$(5/2^+)$	0.11
9	3.25	1+4	$1/2^-+9/2^+$	0.16+0.80	3.227	1	$(1/2^-),(3/2^-)$	(0.093),(0.084)
			$3/2^-+9/2^+$	0.15+0.80	3.438			
					3.506			
					3.607	2	$(5/2^+)$	0.16
					3.683			
10	3.73	(0+2)	$1/2^++5/2^+$	0.02+0.25	3.749	2	$(5/2^+)$	0.18
					3.813	0	$1/2^+$	0.052
					3.863			
11	4.02	(1+3)	$1/2^-+5/2^-$	0.31+1.00	4.060			
			$1/2^-+7/2^-$	0.31+0.70	4.130	0	$1/2^+$	0.032
					4.211	0	$1/2^+$	0.030
					4.278			
					4.382			
					4.487			
					4.644	0	$1/2^+$	0.026
					4.692			
					4.813	(2)	$(1/2^+)$	0.091
					5.221	0	$1/2^+$	0.050

Fig.1. Excitation-energy neutron spectra for the ^{68}Zn(d, n)^{69}Ga reactions taken at a laboratory angle of 10 deg.
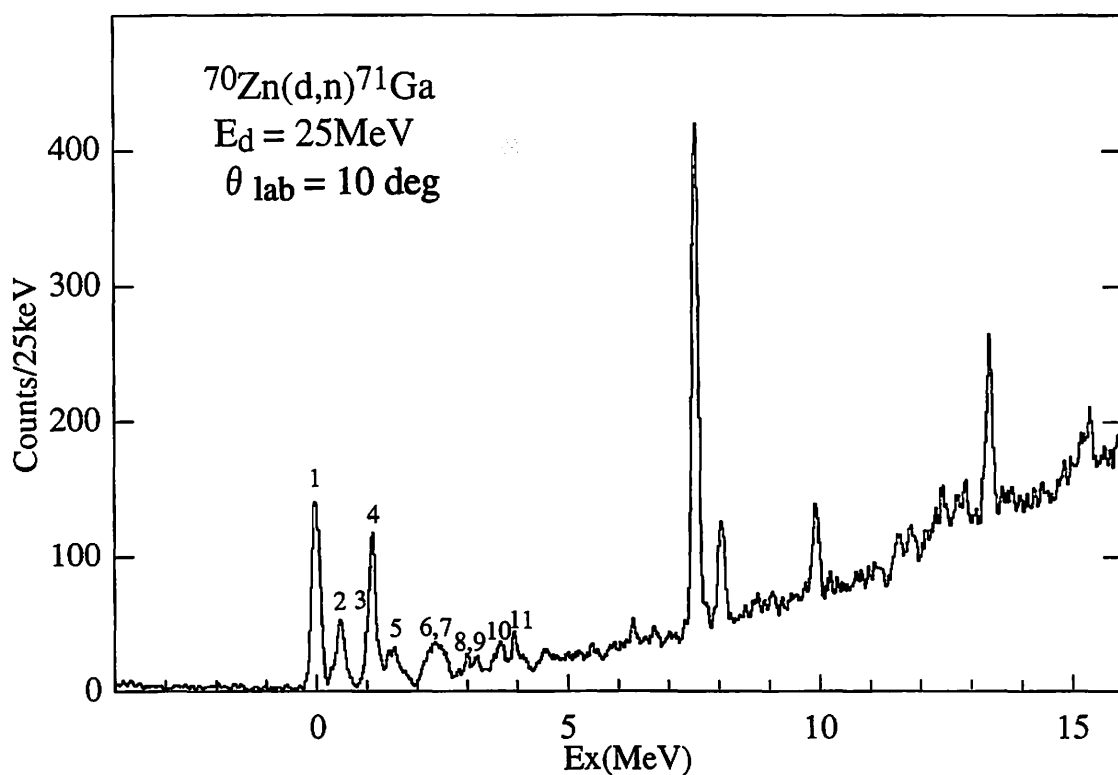
Fig.2. Excitation-energy neutron spectra for the ^{70}Zn(d, n)^{71}Ga reactions taken at a laboratory angle of 10 deg.
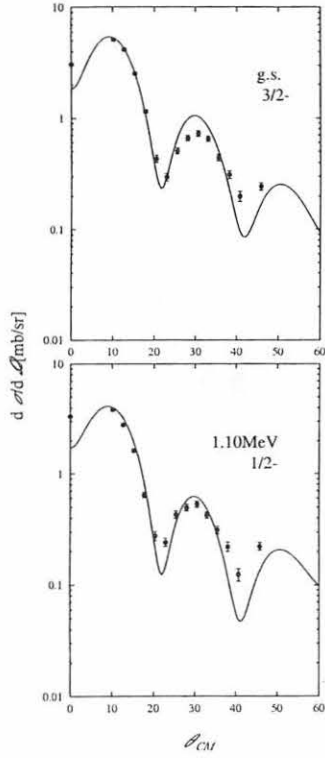
Fig. 3. Angular distribution of emitted neutrons leading to the isolated states in ^{71}Ga. Curves denote DWBA comparison.
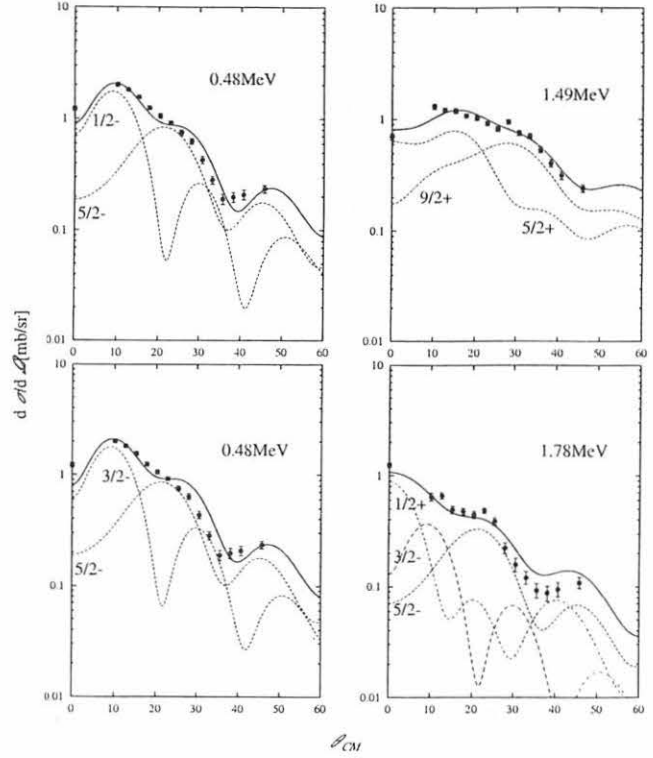
Fig. 4. Angular distribution of emitted neutrons leading to the unresolved states in ^{71}Ga. Curves denote DWBA comparison.
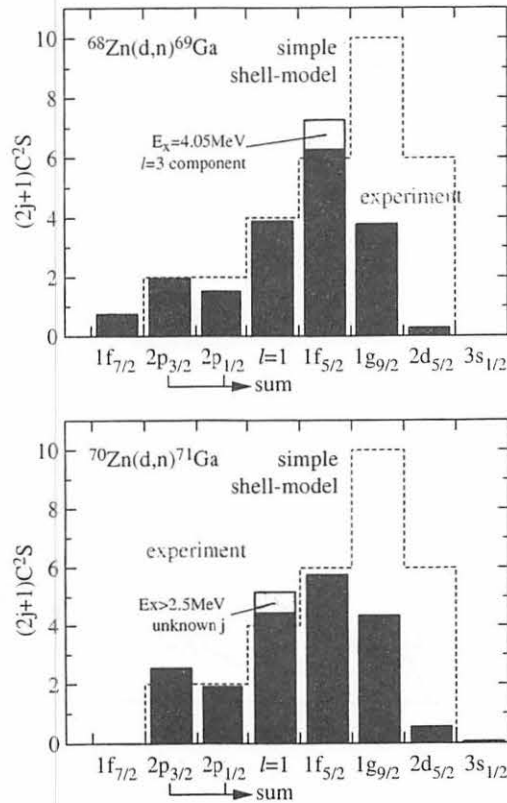
Fig. 5. Summed spectroscopic factors for each orbit obtained for ^{69}Ga and ^{71}Ga. Comparison with sum-rule by shell-model is also illustrated.

12

I. 3. An Empirical Rule for Preparation of ^{111}In PAC Source by Thermal Methods

Hanada R.

Institute for Materials Research, Tohoku University

Introduction

Preparation of the radioactive source is one of the most important steps for the application of PAC spectroscopy to various topics in various fields.   In the application of the spectroscopy for topics in materials science as well as in solid state physics, the present author has developed a melting method that originally has been devised by a Krakow-Göttingen group[1].   The technical detail has already been reported in the 1998 issue of the CYRIC report by the present author[2].

This paper reports an empirical rule for the ^{111}In source preparation for PAC spectroscopy in metallic elements by the melting method as well as diffusion methods, namely, by thermal methods.   These thermal methods are superior to the implantation method or the nuclear reaction method, since no accelerator is necessary and also the radioactivity yield has been found quite high.

An Empirical Rule for ^{111}In PAC Source Preparation

Fig.1 shows the maximum α solid solubility of In in elements as a function of the atomic number for the period 3 (Na-S) to the period 6 (Cs-Bi) as well as for the rare earth group (La-Yb)[3].

Fig.1 immediately reveals that there are two maximum in the solid solubility. Namely the first is centered at the IVB family (Ti,Zr,Hf) and the second is at the VIII family(Ni,Pd,Pt).   For those elements with a high solid solubility for In, several experimental trials have shown that ^{111}In -PAC specimens can be prepared easily by a diffusion method.   Namely, with applying ^{111}In chloride solution on the surface and annealing them at temperatures of 0.5-0.7 Tm (Tm: the melting point) in a vacuum or preferably in hydrogen atmosphere, a very high activity can be introduced in the specimen. As will be shown in several following papers, the diffusion method is also useful to rare earth metals (Gd,Dy,Tb,Er) which also have a high solid solubility for In.   So one can conclude that the In solid solubility in the element is a good measure whether ^{111}In-PAC specimen can be prepared by a diffusion method.   The only exception experienced by the present author is

V, where ^{111}In was found not to diffuse in despite of the relatively high solid solubility.

For those elements with the null or low solubility (Si,Fe,Co...), the diffusion method *does not* work with the negligible ^{111}In activity in specimens after the treatment.
The melting method, however, *does* work for those elements with a reasonably high activity after the treatment for PAC spectroscopy. Also the method has an advantage to prepare alloy specimens at the same time with the ^{111}In introduction. So PAC spectroscopy has been performed in several binary alloys (Fe,Ni,Si-alloys) and have already been reported[2].

This melting method has been extended to Ni-C alloys, many kind of Ni-substitutional alloys, a Si-Cu alloy with the Cu_3Si composition, rare earth elements (Nd, Sm,Gd,Tb,Dy,Ho,Er and Tm) and several of their binary alloys. Part of the results of PAC spectroscopy on these systems will be reported in several papers in this volume.

Though the diffusion method works for the elements with the high In solubility, the melting method has an advantage that the ^{111}In yield is much higher. This enables us to study many systems with a limited amount of ^{111}In solution (5mCi/ml specific activity) with the application of the melting method. Namely, only 0.01ml of it is required for Ni or rare earth elements with the high enough ^{111}In activity for the PAC spectroscopy.

During the alloy studies by the melting method, it was noticed that the ^{111}In activity yield depends on the combination of the elements. The combination of a high In solubility host (HH) and a high solubility solute (HS) has shown a quite high yield. The combinations of HH and a low solubility solute (LS) or LH-HS combinations have shown a reasonably high yield. The LH-LS combinations have shown a low yield though the activity was found high enough for the PAC spectroscopy.

Some Results on Low Melting Point Elements

The melting method also works for elements with the low melting point. Fig.2 shows the PAC spectrum for Sn, Mg and Zn after the melting method. For Sn, the diffusion method has also been applied for comparison. Since these elements have crystal structures different from the cubic (Mg,Zn: hexagonal, Sn: tetragonal), an EFG should be present at the substitutional site. Indeed, precession signals have been observed in these elements as in Fig.2 when the specimens are prepared by the melting method. The diffusion method seems not to work as shown by the Sn result where only a flat spectrum is observed suggesting ^{111}In atoms remain on the surface.

As will be shown in the following several reports, the melting method is quite useful to prepare the PAC source with a reasonable cost, labor and short preparation time. With the application of electron beam or high power laser, the method will be extended to elements with the high melting points as W or Ta.

References

1) Wodniecki P. et al., Hyp. Int., 120/121 (1999) 433.
2) Hanada R., CYRIC Annual report-1998 (1999) p49-p70.
3) *Binary Alloy Phase Diagrams*: ed. by Massalski T. B. et al., pub. by American Society for Metals (1986).
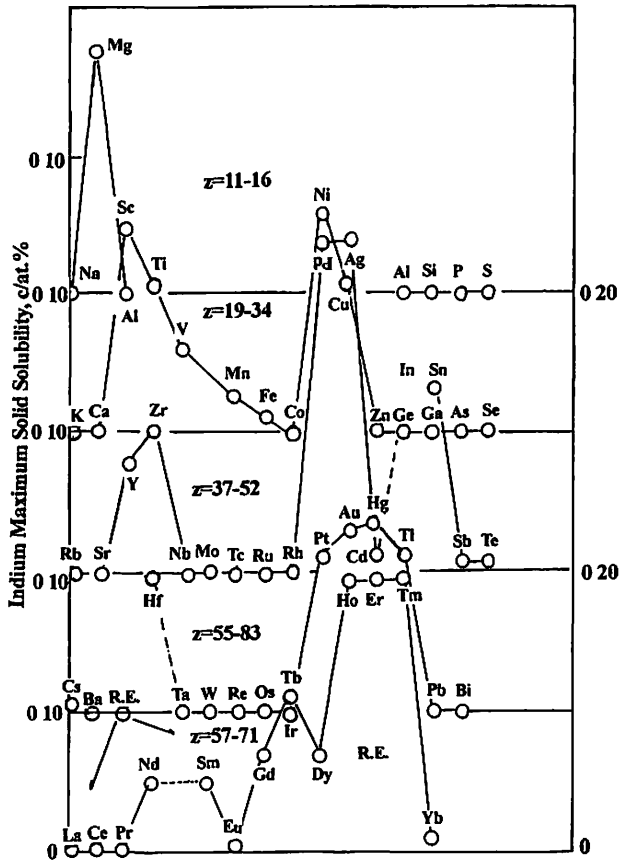
Fig. 1. α maximum solid solubility of In in elements. (Compiled from "Binary Alloys Phase Diagram" ed. by Massalski)
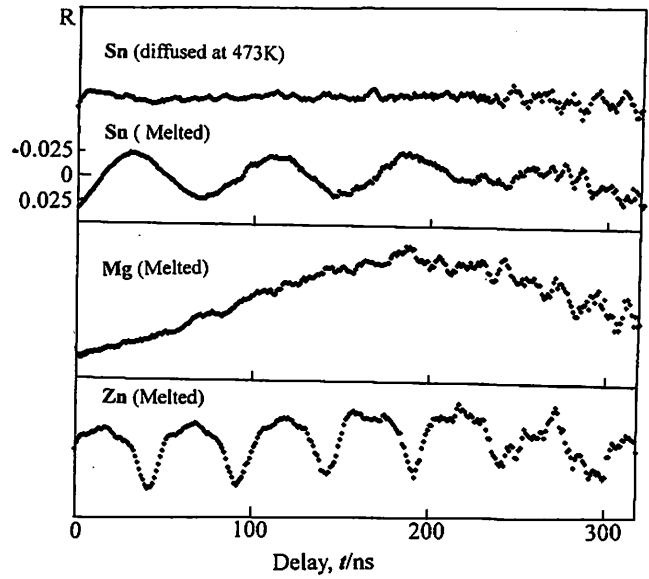
Fig. 2. ^{111}In-PAC spectrum for Sn,Mg and Zn prepared by the melting method. For comparison, the spectrum for Sn prepared by a diffusion method is also shown(top).

15

I. 4. PAC Spectroscopy on Nickel-Carbon Alloys

Hanada R.

Institute for Materials Research, Tohoku University

Introduction

Nickel has a face centered cubic crystal structure (fcc) and dissolves carbon as an interstitial impurity. The carbon atom occupies the octahedral site surrounded by the six nearest neighbor Ni atoms with an equal distance of a/2 where a is the lattice constant. Different from carbon atom in α-Fe (body centered cubic), carbon in Ni fcc octahedral site does not give rise to the elastic dipole. Namely, the magnitude of the outward displacement is the same for all the six nearest neighbor Ni atoms and hence the lattice strain by the interstitial carbon has no asymmetry. Because of this lack of the elastic dipole, the an elastic methods, as the internal friction or strain relaxation technique, can not be used to study the basic properties of interstitial atoms in fcc lattice. So the basic properties of carbon atom in Ni have been less known compared with those of carbon atoms in bcc Fe where many an elastic experimental results are available.

In the present work, PAC spectroscopy has been applied to study the properties of carbon in Ni. The study has become possible with the application of the melting method to prepare PAC source.

First, Ni-C alloys with ^{111}In probe were quenched from several high temperatures to RT and PAC spectroscopy was performed to examine how the hyperfine field is modified by the interstitial carbon atoms. Next, an annealing study has been performed to examine the precipitation process of carbon in Ni. This gives the diffusional property of carbon in Ni.

Experimental

A high purity Ni foil was melted with a known amount of graphite powder together with ^{111}In chloride solution in Ar atmosphere. The total carbon concentration was 3.6at.% slightly above the maximum solid solubility of carbon in Ni (2.7at.% at 1326C). Next, the specimen was quenched to an ice brine from the temperatures between 900C and 1300C for the PAC spectroscopy. With varying the quenching temperature, the concentration of the interstitially dissolved carbon should vary between 1.0 and 2.7 at.% according to the phase diagram[1]. The extra carbon precipitates as graphite and hence should not affect the PAC

spectrum. Indeed, specimens with two different total carbon concentrations (0.5 and 1.1 at.%) give essentially the same result as the present 3.6 at.% alloy.

PAC spectrum was measured at RT by three detectors set up with the 0.27T magnetic field vertical to the detector plane. As shown theoretically as well as by the spectroscopy on $Ni^{2)}$, the magnitude of the field is high enough to suppress the ω_L term to obtain only the $2\omega_L$ term where ω_L is Larmor frequency. This is to avoid the complexity in the spectrum due to the presence of the ω_L term.

For the annealing study, an isochronal (100C/1hr) annealing was given to the specimen in a vacuum after the quenching from 1300C and PAC spectrum was measured at RT after each annealing between 200C and 800C.

Result

Fig.1(a) shows the time spectra for the Ni-C alloy quenched from three different temperatures. The spectra show the amplitude decay and the rate of it becomes larger with the increasing quenching temperature or the increasing carbon concentration. Since no such decay is present for the spectrum for pure Ni, the decay must be caused by the presence of carbon atoms dissolved as an interstitial impurity. Indeed, with the increasing carbon concentration with the higher quenching temperature, the spectrum shows larger rate of the amplitude decay. Fig.1(b) shows the corresponding Fourier spectra for Fig.1(a) revealing the cause of the amplitude decay. Namely the spectrum mainly consists of two components, the main at 176Mrads^{-1} and a satellite at about 140 Mrads^{-1}. The main gives 6.1T as the magnitude of the hyperfine field slightly smaller than that for pure Ni (6.4T, S-component). The satellite yields 4.8 T. As seen in Fig.1(b), the relative population of the satellite to that of the main is found to increase with the increasing carbon concentration. So we can conclude that the satellite is due to the interstitial carbon, of which nature will be discussed in the next section. The main should be ascribed to the substitutional component without carbon atoms at the near neighbor sites. The slight lowering of the hyperfine field in the S component upon alloying has been often observed in ferromagnetic alloys.

Fig. 2 shows Fourier spectra for the Ni-C alloy during the annealing between 200C and 800C after the quenching from 1300C. The satellite at 140 Mrads^{-1} is present up to 500C and then annealed out above 600C with growing population of the S component with a slight increase in the hyperfine field. This shows that the quenched-in carbon becomes mobile and precipitates into graphite between 500C and 600C.

Discussion

Fig. 3 shows a fcc unit cell with octahedral sites (open circles). Around an octahedral site, six nearest neighbor Ni atoms form a regular octahedron. The probe ^{111}In in Ni has been known to occupy the substitutional site in Ni. So if the octahedral site is

occupied by a carbon atom, it is likely that the nearest neighbor Ni atoms (one of which is substituted by ^{111}In) are pushed toward outside. If one looks at the ^{111}In atom, the distance to 8 Ni atoms out of 12 nearest neighbors is increased by the presence of carbon atom. The magnitude of the hyperfine field is mainly determined by the overlap of d-band with the nearest neighbor atoms. This overlap is reduced with the increasing distance and hence the magnitude of the hyperfine field should be reduced when adding up the contribution of 12 Ni atoms. Although theoretical justification needed, this may explain the decrease of the hyperfine field at ^{111}In nucleus upon carbon alloying. This is in analogy with the case of Fe-C martensite where two nearest neighbor atoms are pushed toward outside thus giving rise to the hyperfine field reduction[2]. So it is concluded in the present that the satellite component at 4.8T is due to ^{111}In at the nearest neighbor site to the octahedral site occupied by C atom.

Next let us discuss the populations of the satellite and the S component with the presence of carbon. If ^{111}In atoms are distributed randomly without any interaction with carbon atoms, the percentage of Ni atoms affected by the carbon at the octahedral site should be 2.7×6=16.2%. Here we assume the maximum soluble carbon concentration of 2.7at.% and that only the six nearest neighbor sites are affected by it. On the other hand the experimental result in Fig.3 shows the ratio of the satellite to S component is 80% after the 1300C quenching, much higher than the expected. This suggests that ^{111}In distribution is not random in Ni-C alloy or ^{111}In atoms have an attractive interaction with carbon. Namely, ^{111}In atoms preferentially occupy the nearest neighbor sites to carbon atoms.

Next let us discuss the diffusion property of C in Ni. As has been discussed, no experimental result is available for the jump rate of a single carbon atom by anelastic methods. However, some results available for the carbon pair in Ni that gives rise to an elastic dipole and hence internal friction peak or strain relaxation[3]. From these results, the activation energy for a carbon jump in the pair has been determined as 1.63 ± 0.2 eV. With assuming the value for the pair is the same for a single carbon atom in Ni, the jump rate at 600C is obtained as 10^4/s with an attempt frequency of 10^{14}/s. So it is reasonable that a carbon atom becomes mobile at 600C to meet with other carbon atoms for precipitation as observed in Fig.3.

The present results show PAC spectroscopy is quite useful to study the properties of interstitial impurities in ferromagnetic fcc metals where anelastic methods or proper Mössbauer probes are not available.

References

1) *Binary Alloys Phase Diagram* ed. by Massalski T. B., pub. by A. S. M. (1986).
2) Fujita F. E., "Mössbauer Spectroscopy in Physical Metallurgy", in *Mössbauer Spectroscopy* ed. by Gonser U., pub. by Springer Verlag (1975).
3) Nowick A. S., and Berry B. S., *Anelstic Relaxation in Crystalline Solids* pub. by Academic Press (1972).
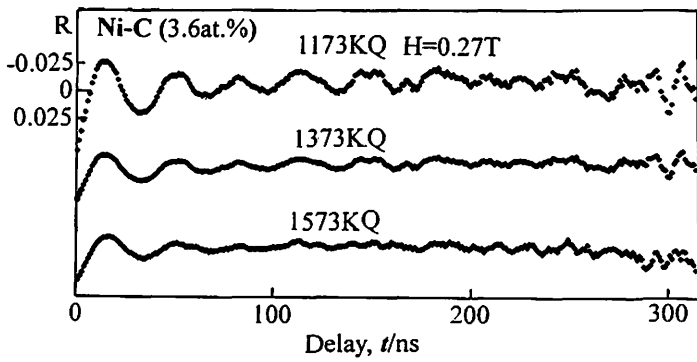
Fig. 1. (a) PAC spectrum for a Ni-carbon alloy quenched from temperatures between 900C and 1300C.
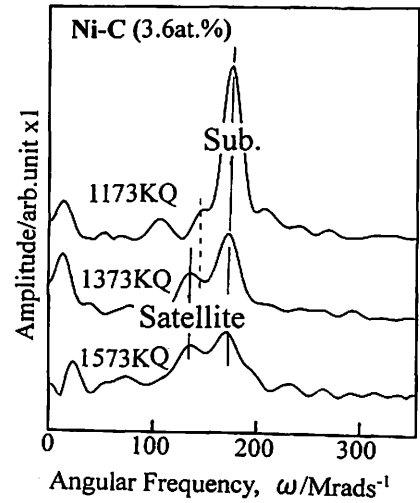
Fig. 1. (b) Fourier spectra for Fig.1 (a).
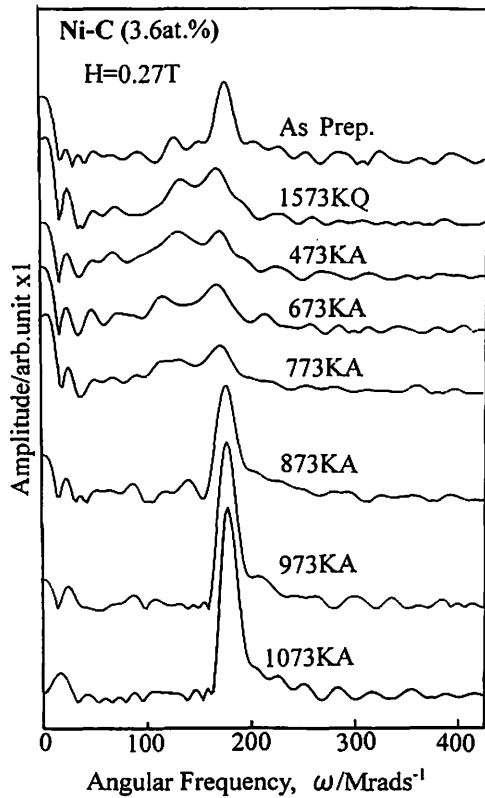
Fig. 2. Fourier spectra for a Ni carbon alloy during the annealing between 200C and 800C after the quench from 1300C.
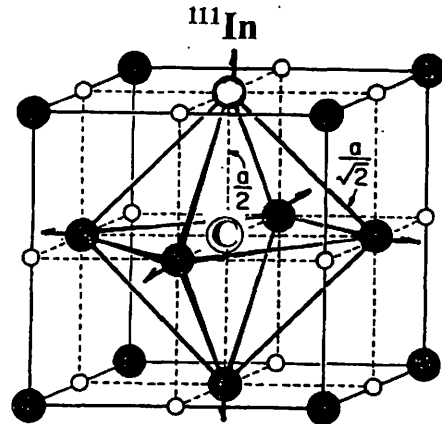
Fig. 3. A fcc lattice with a carbon atom at the octahedral site with one ^{111}In atom at the nearest neighbor site.

19

I. 5. PAC Spectroscopy of Ni-Substitutional Alloys

Hanada R.

Institute for Materials Research, Tohoku University

Introduction

In a previous report on Ni-Cu alloy, a reduction of the hyperfine field at ^{111}In at the Ni substitutional site has been reported[1]. This is interpreted as due to the substitution of one of the nearest neighbor 12 Ni atoms to ^{111}In by a non-magnetic Cu atom. Also the hyperfine field change upon alloying was calculated with the assumptions that the alloying element distributes randomly in Ni lattice and the hyperfine field reduction is proportional to the number of the non-magnetic atoms in the nearest neighbor sites.

In the present, a similar work has been extended to several Ni alloys.
The alloying elements were;
Si(2.6,5.4,8.3),Cu(1.2,3.5,7.0),Be(1.5,5.2),Al(1.0,3.5),Ti(3.1),Mn(0.53,1.9),Mo(1.5,3.2, Ir(0.8,1.8),Nb(2.3,5.3),Ge(3.5),B(4.2,6.4),Ru(3.5),Fe(7.7),Rh(5.9),Re(3.4),Gd(2.2),Dy 1.1),Er(2.3),Sm(0.9), where the number in the parenthesis is the concentrations in atomic percent. The elements and the concentrations were chosen so as that they are soluble as an α solid solution in Ni by consulting with phase diagrams[2]. The exceptions are B,Gd,Dy,Sm and Er which are not soluble in Ni and form metallic compounds.

Purposes of the experiment are; (1) to examine the random distribution model is valid or not in the Ni substitutional alloy. (2) how the phase diagram features are reflected in the PAC spectrum and (3) to demonstrate the usefulness of the melting method.

Experimental

A high purity Ni foil ($20 \times 20 \times 0.1mm^3$) was melted with an appropriate amount of the alloying element (mostly in a powder form) with ^{111}In-chrorde solution. The details of the melting method have already been reported in ref.(3). 10-15 specimens have been prepared using one vial (1ml, specific activity 5mCi/ml) of ^{111}In solution.

The PAC spectrum was measured by a three detectors system at RT with and without a magnetic field (0.27T) vertical to the detector plane. The magnitude of the field was high enough to suppress the ω_L term to obtain $2\omega_L$ term only.

Results

Fig. 1 shows PAC Fourier spectra for several Ni alloys, where the spectrum measurements were performed with the vertical magnetic field on. As expected, the ω_L term is suppressed and only the $2\omega_L$ term is present in the spectrum. The thin vertical lines show the positions of the ω_L and $2\omega_L$ term for pure Ni for comparison.

The effect of the alloying is particularly apparent for the cases of Si or Ti. Namely, the $2\omega_L$ terms are shifted to the lower side. Since the angular frequency is proportional to the magnitude of the hyperfine field as $2\omega_L = 2 \, g \, \mu_N \, H/\hbar$ in the case of the magnetic interactions, the results show that the alloying reduces the hyperfine field. Similar but smaller reductions are observed for Al and Cu and almost no reduction for Be and Mn. Also for Si, Ti, Al and Mn, the spectra are considerably broadened when compared with that of pure Ni. This shows that the alloying causes the distribution in the hyperfine field. On the other hand for Be or Cu, almost no broadening is observed.

To examine the effect of the heat treatment, the spectrum was measured in the as prepared state (right after the melting specimen preparation) or after the quenching from 970C or 1230C to show that it is almost independent on them. Namely the states of the solutes are almost the same α solid solution after these heat treatments.

Fig. 2 shows similar Fourier spectra for Mo, Ir, Ge, Mn, B and Ru alloys. Here, the effects of the vertical magnetic field and the annealing after the melting specimen preparation are examined. First, for Ge, Mn, B and Ru alloys, the spectrum was measured with and without the magnetic field in the as prepared state. Without the field, both ω_L and $2\omega_L$ terms are observed as expected. The shift to the lower field side upon the alloying is found in both ω_L and $2\omega_L$ terms, of which magnitudes are proportional to them. This is reasonable since $\Delta\omega_L$ and $\Delta2\omega_L$ terms are proportional to ΔH and $\Delta2H$, respectively. This confirms that the shift upon the alloying is real.

The spectra after the annealing between 800 and 1000C for several 10 hrs are the almost the same with that of the as prepared state. This shows that an equilibrium state has already be established during the cooling after the melting and only minor redistribution of the solutes take place in the annealing.

Fig. 3 summarizes the results in Fig. 1 and Fig. 2 as well as other alloys not shown here. Here, the magnitudes and the width (FWHF) of the hyperfine field are plotted against the concentrations of the alloying elements. For most of alloys, reduction and broadening in the hyperfine field are observed and yet for some alloys almost no reduction is present. In the next section, the concentration dependence will be discussed based on a random distribution model.

Discussion

In a previous paper on Ni-Cu alloy, the hyperfine field in Ni alloys has been calculated with two simplified assumptions.

Namely,

(1) The solute atoms distribution in Ni is completely random in α phase.

(2) The magnitude of the hyperfine field at ^{111}In nucleus is reduced by N/12 with the substitution of N sites by non-magnetic ions among 12 nearest neighbor Ni sites

With the assumption (1), the probability to occupy N sites is given by a binomial distribution. With the assumption (2) together with (1), the hyperfine distribution has been calculated as a function of the solute concentration. The calculated results are shown by dotted lines in Fig. 3, where the maximum of the distribution is shown to shift to the lower side and the width is broadened with the increasing solute concentration. This is reasonable since the probability to occupy N sites increases with the concentration to give the shift. Also the overlap of the fields due to different N's gives the broadening.

Both of these predictions qualitatively show a good agreement with the experimental results for most of alloys. However, quantitatively, the experimental results show deviations from the random solution model. With comparing the calculated results, the experimental hyperfine field shift for each solute may be summarized as follows.

(1) Mo and Nb:much larger shift than the random solution model.

(2) Al,Si,Be,Ru and Ti: Larger shift than the model.

(3) Cu,Ge and Re : Slightly larger or close to the model.

(4) Mn,B,Rh,Fe,Gd and Er: Almost no shift.

For the group (1) and (2), the hyperfine field shift and broadening are much larger than the ones expected from the random model. Namely, the solute concentration near the probe ^{111}In is about 3-5 times higher than the average. This suggests that these solutes have an attractive interaction with the probe ^{111}In. For the group (3), the experimental results are close to the random model though the shift is usually higher than the predicted. So the solutes have almost no interaction with the probe or the weak one if any. For the group (4), B, Gd and Er form metallic compounds and hence have no solubility in Ni. So the probe ^{111}In just sees the hyperfine field of pure Ni giving no shift. Also this shows that the probe has no interactions with the compound.

Rh and Fe in group (4) do not give rise to the hyperfine shift although they form a complete solid solution with Ni. This suggests either that they have a repulsive interaction with the probe or they do not give rise to the hyperfine field change even when they are at the nearest neighbor site.

The present results give a quick survey of the effects of solutes on the hyperfine field of Ni. Theoretical study will be necessary to examine the reduction of the hyperfine field upon alloying.

References

1) Hanada R., CYRIC Annual Report-1998 (1999) 66.
2) *Binary Alloys Phase Diagram* ed by Massalski.T.B., pub. by ASM (1986).
3) Hanada R.,CYRIC Annual Report-1998 (1999) 49.
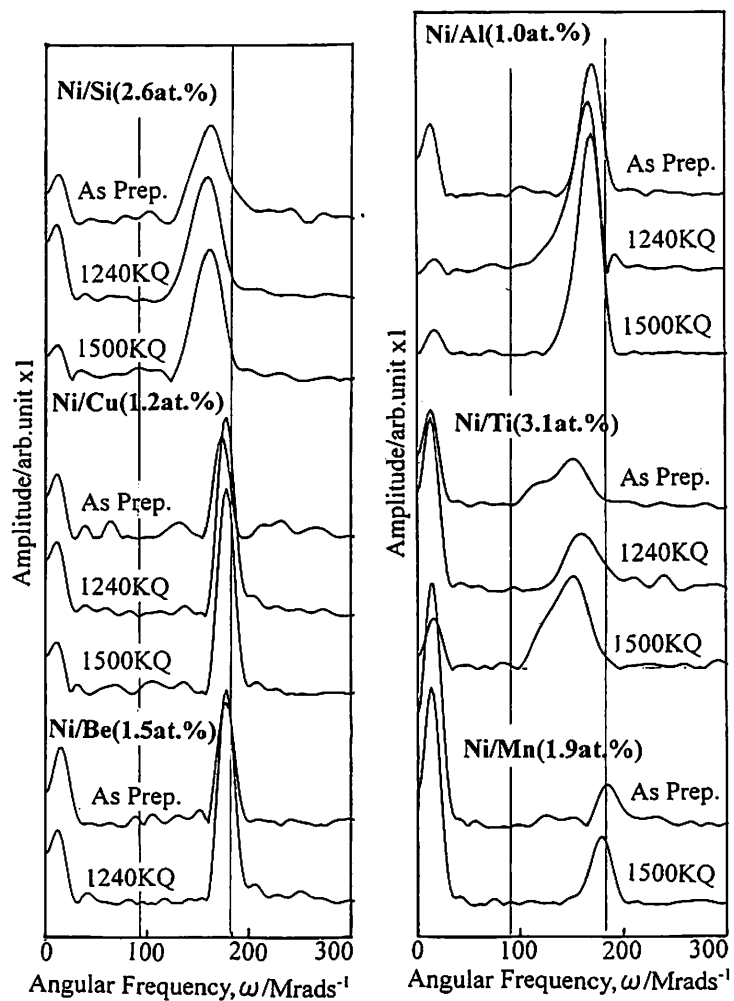
Fig. 1.   Fourier PAC spectra for Ni-substitutional Alloys.   Vertical magnetic field applied.   As Prep: as melt prepared: Q: quenched.
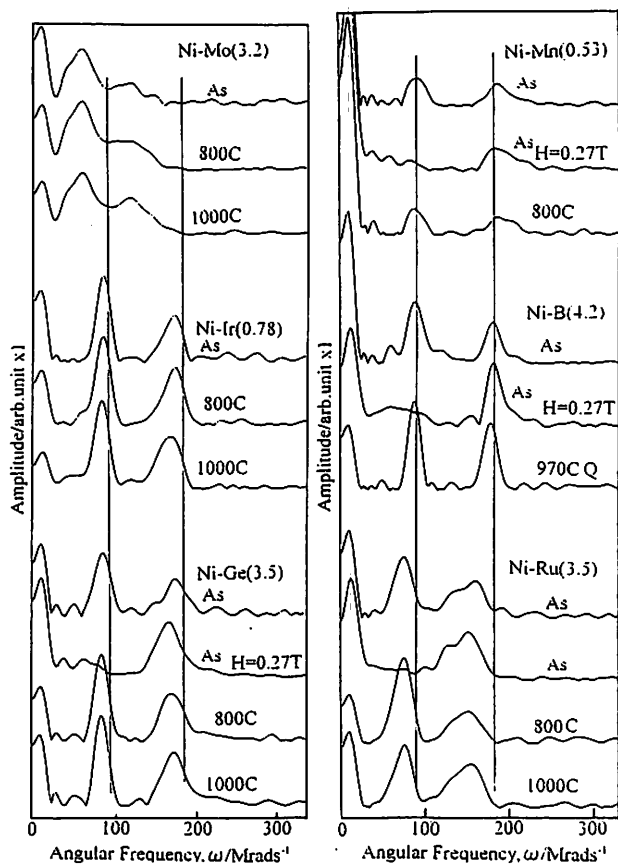
Fig. 2.   Fourier PAC spectra for Ni-substitutional alloys. No magnetic field
otherwise specified (H=0.27T) Annealed at the specified temperatures.
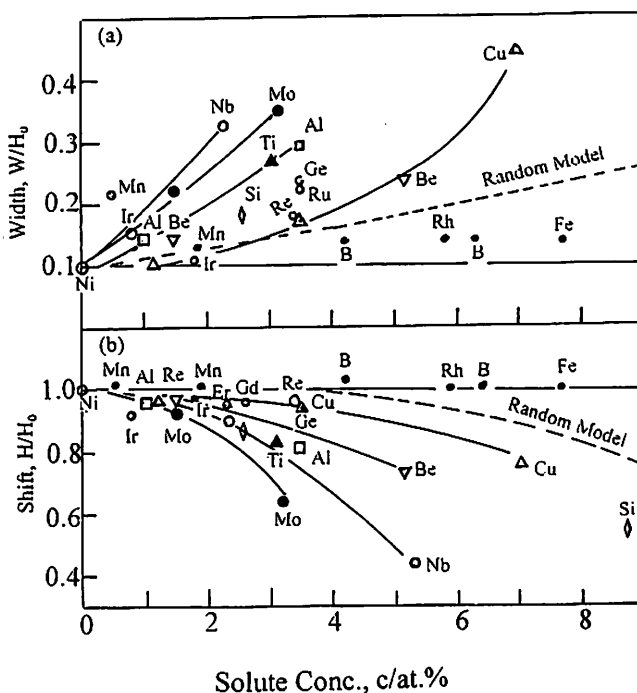
Fig. 3.   The line broadening (a) and shift (b) in the Fourier components upon
alloying.   Normalized to the hyperfine field of pure Ni.

24

I. 6. PAC Spectroscopy of Cu Silicide

Hanada R.

Institute for Materials Research, Tohoku University

Introduction

In a previous report by the present author on dilute Si-Cu alloys (Cu concentrations between 50at.ppm and 6.5at.%)[1], a simple PAC precession signal has been observed. The angular frequency was determined as 183Mrads^{-1} for 0.80at% alloy. With following the standard procedure of the aging study, namely, the quenching from high temperatures followed by successive annealing, the signal was concluded as due to ^{111}In-multiple Cu atoms complex.

As described in the previous report, the concentration of the probe ^{111}In is much lower than the Cu concentration. The maximum Cu solubility in Si is as low as 20at.ppm at 1300C and yet the probe ^{111}In concentration is much lower to give the ratio Cu/^{111}In as high as 10^6. Namely, 10^6 Cu atoms are available to precipitate around one ^{111}In atom. If such a clustering of Cu atoms takes place, ^{111}In should be considered as being in the precipitate rather than forming a complex with multiple Cu atoms as suggested in the previous paper.

Since PAC method is rather near sighted, it is difficult to distinguish between them on the basis of the spectrum analysis. In the present, therefore, a specimen with the composition Cu$_3$Si was prepared and the PAC spectrum was measured. The Cu-Si phase diagram shows that Cu precipitates into η phase with the composition Cu$_3$Si. So if the PAC signal for the Cu$_3$Si phase in the present is the same with those in the dilute alloys, we can conclude that Cu$_3$Si phase is formed around ^{111}In after the aging in these dilute alloys.

Experimental

Powder of high purity Si and Cu were weighted to give the composition Cu$_3$Si and they were mixed well. The mixed powder was pressed to form a disk, part of which was melted with ^{111}In chloride solution to form PAC radioactive source. Two spectrum measurements were performed, one after the specimen preparation (as melted) and after the annealing at 900C.

Result

Fig. 1 (a) shows the PAC spectrum for the present Cu-Si alloy with the composition

Cu_3Si. The corresponding Fourier spectrum, Fig. 1 (b), shows the spectrum consists of a single angular frequency of which magnitude is 180 Mrads^{-1} for the as prepared state and 189 Mrads^{-1} after the annealing at 900C. These values are very close to those observed in dilute Cu-Si alloys, for instance, 183 Mrads^{-1} for 0.80at.% Si-Cu alloy after the precipitation procedure. So in the present light of the experimental result, we can conclude that Cu_3Si phase is formed in a dilute Si-Cu alloys after the precipitation procedure. As already stated, the number of Cu atoms is much higher than that of ^{111}In probes even in the lowest concentration of Si-Cu dilute alloy investigated. So an island of Cu_3Si phase is formed around each ^{111}In probe even in a dilute Si-Cu alloy to give the Cu_3Si signal. Because of the short range of ^{111}In probe sight, it can not distinguish whether it is in an island in a previous report or in the continent of Cu_3Si phase as in the present, where the phase was intentionally prepared to cover all the bulk.

Next let us discuss the structure of the Cu_3Si phase in relation with the PAC spectrum.

Discussion

Most of transition metals form a metallic compound with Si, which are called as TM silicides[2]. For the case of Si-Cu case, three phases η(859C-558C(620C)), η'((620C(520)-558C(467)) and η''(below 570C(467)) have been reported for the Cu compositions between 75 and 76 at.%. Namely, the compound shows some width in the stoichiometry and the transition temperatures among them depend on it. The crystal structures of them are determined as rhombohedral(trigonal) for η, rhombohedral for η' and orthrhombic for η''[3]. Si crystal structure can be viewed as two penetrating fcc lattices and Cu atoms are known to occupy the interstitial octahedral sites. For this arrangement, the Si and Cu site forms a bcc structure. Upon the formation of the Cu silicides, the bcc structure is distorted along the 111 axis to give the rhombohedral (trigonal) symmetry[3]. So if ^{111}In substitutes the Si site in the silicides as usually assumed for Si lattice, an E.F.G. should be present to give the observed precession. Here in the silicide, the crystal structure is different from the cubic structures where no EFG is present. The slight variation in the frequency in Fig.1 (b) depending on the heat treatment or those from dilute alloys in Ref.(1) is probably due to the transformation among three η phases which give rise to a slightly different magnitude of EFG.

Detailed EFG calculation in Cu-slicides or the exact assignment of the angular frequency to each phase will be subjects of further studies.

So far the hyperfine interaction study on TM silicides is limited on Fe silicide by Mössbauer spectroscopy[4]. The present result shows that Cu silicides will be a good subject for further PAC study.

References

1) Hanada R., CYRIC Annual report-1998.
2) *Properties of Metal Silicides*: ed. by Maex K. and Van Rossum M., pub by IEEE (1995).
3) Solberg J. K., Acta.Cryst., **A34** (1978) 684.
4) see the article by Langouche G. in Ref.(2).
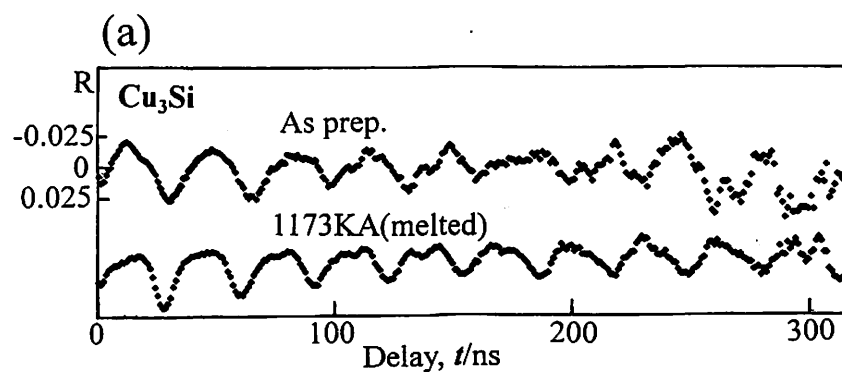
Fig. 1.　(a) [111]In PAC spectra in the Cu-Silicides with the composition Cu_3Si after two heat treatments.
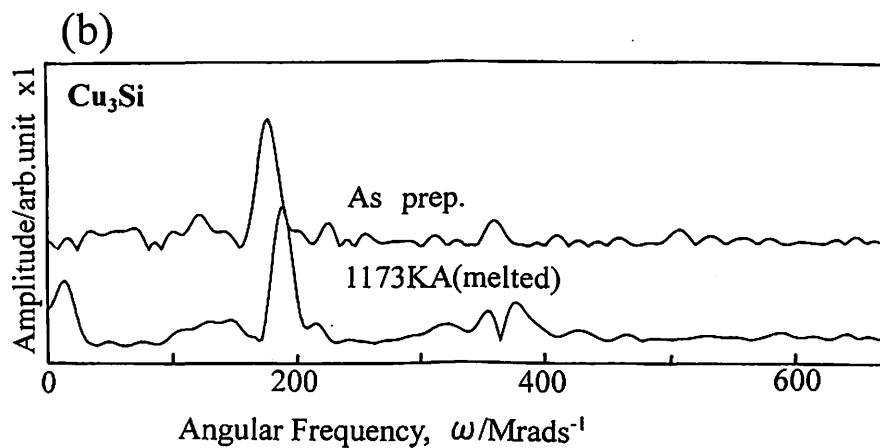
Fig. 1.　(b) Corresponding Fourier spectra for Fig.1 (a).

I. 7. Hyperfine Interactions with the Presence of Both Electric Field Gradient and Magnetic Field-An Application to ^{111}In PAC Spectroscopy

Hanada R.

Institute for Materials Research, Tohoku University

Introduction

Hyperfine interactions, the interactions between an atomic nucleus and the external crystal fields, have two origins. One is the magnetic interaction, namely the interactions between the nucleus magnetic moment and the external or internal magnetic field. The other is the electric interaction, the interaction of the nuclear quadrupole moment and the electric field gradient (EFG). When an element has a crystal structure different from the cubic, a finite EFG should take place at the atomic nuclei that is placed at the substitutional site. Such examples are Zn, Cd, Mg that have a closed packed hexagonal structure (hcp) or Sn that has a tetragonal structure. Indeed, PAC spectroscopy on them has shown precession signals of which origin is the electric.

Some elements with the hcp structure transform to ferromagnetic phase at a certain temperature. Such examples are Co and heavy rare earth elements as Gd, Tb, Dy, Ho, Er and Tm. So in their ferromagnetic phase, both the magnetic and the electric interactions are present at the probe nucleus. The purpose of the present work is to examine theoretically how this coexistence of the magnetic and electric hyperfine interactions is reflected on the PAC spectrum. Results of the calculation will be compared with the experimental results on rare earth elements and alloys in the following three papers.

In the present, we will give a general expression for the eigenvalues for I=5/2 nuclear level, for ^{111}In, with the coexistence of the magnetic and electric terms. The solution of the equation gives the energy levels as a function of the ratio $\omega_H/\omega_E(=y)$, η, the asymmetry parameter of EFG and the angles, α, β and γ which specify the relative orientation between the magnetic field and the EFG. Second, we also calculate the transition probability among these sublevels for a special case of $\eta=0$. The results of the former calculation should be compared with the angular frequencies of PAC signals and the latter with the relative population of them. The whole calculation is based on the formulation by Matthias[1].

Matthias has calculated the energy levels for selected combinations of I, y, η, α and β without the transition probability. Böstrom et al have also simulated PAC spectrum based

on the theory although without any explicit expressions on the energy levels or the transition probability[2].

Formulation

The matrix elements for the eigenvalue problem with both the electric and magnetic interactions read[1]:

$$H_{mm} = -\omega_H \hbar m + \omega_E \hbar \frac{1}{2}(3\cos^2\beta - 1 + \eta\sin^2\beta\cos 2\alpha)(3m^2 - I(I+1)),$$

$$H_{mm\pm 1} = \frac{3}{2}\omega_E \hbar \sin\beta\left(\cos\beta \mp \frac{\eta}{6}[(1\pm\cos\beta)e^{2i\alpha}\right.$$

$$\left. - (1\mp\cos\beta)e^{-2i\alpha}]\right)e^{\pm i\gamma}(2m\pm 1)[(I\mp m)(I\pm m+1)]^{1/2}, \quad (1)$$

$$H_{mm\pm 2} = \omega_E \hbar \frac{3}{4}\left(\sin^2\beta + \frac{\eta}{6}[(1\pm\cos\beta)^2 e^{2i\alpha}\right.$$

$$\left. + (1\mp\cos\beta)^2 e^{-2i\alpha}]\right)e^{\pm 2i\gamma}[(I\pm m+2)(I\pm m+1)(I\mp m)(I\mp m-1)]^{1/2}.$$

where ω_H and ω_E are magnetic and electric interaction frequency, respectively. Explicitly, $\omega_H = g\mu_N H/\hbar$ and $\omega_E = eqV_{zz}/\hbar\ 4I(2I-1)$. α, β and γ are defined as in Fig. 1(a). The diagonalization of the hermitian matrix gives the eigenvalues for I=5/2 state together with the eigenvectors u.

The attenuation factor (the PAC spectrum) reads[3];

$$G_{kk}(t) = \overline{G^{N_1 N_2}_{k_1 k_2}}^{\alpha,\beta,\gamma}(t) = \sum_{N, m_a, m_b} \sum_{n, n'} (-1)^{2I+m_a+m_b}$$

$$\times \begin{pmatrix} I & I & k \\ m'_a & -m_a & N \end{pmatrix}\begin{pmatrix} I & I & k \\ m'_b & -m_b & N \end{pmatrix} \quad (2)$$

$$\times u^*_{n, m_b} u_{n, m_a} u_{n', m_b} u^*_{n', m_a} \exp\left(-\frac{i}{\hbar}(E_n - E_{n'})t\right)$$

So one can calculate the transition probability among sublevels (E_n and $E_{n'}$) by calculating the coefficient of the exponential term in eq.(2).

Calculated results.

Eigenvalues

The diagonalization of the matrix elements results in a characteristic equation shown in Fig. 1(b) of which solution gives the eigenvalues in terms of y($=\omega_H/\omega_E$), η, α and β (independent on γ when polycrystal). Note that this is a general solution and with it one can calculate the eigenvalues for I=5/2 level with any combination of the parameters y, η, α and β when both the magnetic and electric interactions are present. Fig. 2(a) shows an example of such a calculation for the case of β=90 and η=0 (independent on α when η=0) with y varying

between 0 and 20. At y=0, namely, for pure quadrupole interaction only, we have three levels 10,-2 and -8, the transitions among them give the well known quadrupole frequencies of $\omega_1(=6\omega_E)$, $2\omega_1$ and $3\omega_1$. However, each sublevel is doubly degenerated and hence split into two with the application of the magnetic field thus giving 6 magnetic sublevels as expected for I=5/2 spin. Without the quadrupole interaction, namely for the pure magnetic interaction, the energy differences between the neighboring sublevels are the same. So the transitions between two neighboring levels (the total number of 5 for n'-n=1) give only one frequency, ω_H, Larmor frequency. The 1st harmonic of it, namely, $2\omega_H$ is also possible for n'-n=2. So we have the well known two frequencies of ω_H and $2\omega_H$ for the pure magnetic interactions

With the presence of the quadrupole interaction, however, the differences become dependent on the magnetic quantum number as shown in Fig. 2(a). So we should have 5 different frequencies in the PAC spectrum when both the magnetic and the electric interaction are present.

Transition Probability and PAC Fourier Spectrum

The transition probability can be obtained by calculating the coefficient of the exponential term of eq.(2). This gives the relative population of each transition. The eigenvectors u's are obtained during the process of the diagonalization of the hamiltonian matrix of eq.(1)

The relative populations of each transition are shown by Fig. 2(b) for (n-n'=0), Fig, 2(c) for (n-n'=1) and Fig. 2(d) for (n-n'=2) transition. So if these results are applied to the PAC spectrum, for instance, for the n-n'=1 transition, we should have 5 different frequencies derived from the results in Fig. 1(a), each of which has the different populations given by Fig. 1(c). If these are combined, one can simulate a PAC Fourier spectrum for the n-n'=1 case when both the magnetic and the electric interactions coexist. Such an example is shown in Fig. 3 for the n-n'=1 case. These should be compared with the component near the basic frequency $1\omega_H$ when both the magnetic and EFG with $\eta=0$ are present. Although not shown here, the same applies to the unperturbed term (n-n'=0) with those in Fig. 2(b) or the 1st harmonic $2\omega_H$ (n-n'=2) with Fig. 2(d)

A Limiting Case of y>>20

A limiting case of large y, namely, the case of much larger magnetic field than the EFG will be discussed in the next paper on Tb. There, the PAC spectrum was measured at RT (paramagnetic with only the EFG to give ω_E) and at 77K (ferromagnetic with both the magnetic hyperfine field to give ω_H and ω_E) where $\omega_H >> \omega_E$ was found. In the limiting case of large y, one can apply a simplified treatment of which relation to the present exact calculation will also be discussed.

Eigenvalues for Variable Parameters including the $\eta \neq 0$ *case*

Fig. 4(a) through Fig. 4(d) show the energy level of I=5/2 spin as a function of y for several set of α, β, η. The population of each transition can also be calculated by eq.(4), though the presentation of them is beyond the scope of the present paper. Also it is possible to simulate the PAC Fourier spectra as in Fig. 3 for the general case of $\eta \neq 0$.

Application to Experimental Results

The present results apply not only for the analysis of PAC spectrum but also for those of NMR/ON or β -NMR on specimens with the EFG. These methods require to apply the external magnetic field and hence the analysis as in the present is inevitable. In these external magnetic field experiments, though, single crystals must be used to define the angles relation as shown in Fig. 1(a). For the case of the internal field as the hyperfine field, the magnetization axis and the EFG axis have a definite angle relation in each grain of the polycrystal and hence the present analysis can apply even to the experimental results on polycrystals.

References

1) Matthias E. et al., Arkiv F . r Fysik, Bd24 (1963) 97.
2) Boström L. et al., Physica Scripta 2 (1970) 65.
3) Frauenfelder H. and Steffen R. M., in *α-β-γ-rays Spectroscopy II* ed by Siegbahn K., pub. by North-Holland pub. co (1968).

(a)

(b)

$$\lambda^6 + \left(-168 - 56\,\eta^2 - \frac{35}{4}\,y^2\right)\lambda^4$$

$$+ \Big(56\,\%1 - 56\,\%3 - 168\,\%2 - 320 + 56\,y^2 + 320\,\eta^2 \Big)\lambda^3 + \Big(\frac{259}{16}\,y^4 + 492\,y^2$$

$$+ 4704\,\eta^2 - 972\,\%2 - 52\,y^2\,\eta^2 - 648\,\%1 + 7056 + 648\,\%3 + 784\,\eta^4$$

$$+ 324\,y^2\,\eta^2\,\cos(\beta)^2\Big)\lambda^2 + \big(-1440\,\%2 + 26880 - 1360\,y^2 + 2000\,y^2\,\eta^2 - 480\,\%3$$

$$- 8960\,\eta^4 + 160\,\eta^3\,y^2\,\cos(2\,\alpha)\,\cos(\beta)^2 - 17920\,\eta^2 - 110\,y^4 + 110\,y^4\,\eta\,\cos(2\,\alpha)$$

$$+ 330\,y^4\,\cos(\beta)^2 - 480\,y^2\,\eta^2\,\cos(\beta)^2 - 110\,y^4\,\eta\,\cos(2\,\alpha)\,\cos(\beta)^2$$

$$- 160\,\eta^3\,y^2\,\cos(2\,\alpha) + 480\,\%1\big)\lambda + 25600\,\eta^4 - 4000\,\eta^3\,y^2\,\cos(2\,\alpha)\,\cos(\beta)^2$$

$$- 4000\,\%3 - 51200\,\eta^2 - 12000\,\%2 - 9400\,y^2\,\eta^2 + 12000\,y^2\,\eta^2\,\cos(\beta)^2$$

$$- 650\,y^4\,\eta\,\cos(2\,\alpha) - \frac{225}{64}\,y^6 - \frac{25}{2}\,y^4 + 1250\,y^4\,\eta\,\cos(2\,\alpha)\,\cos(\beta)^2$$

$$+ 100\,\eta^2\,\cos(2\,\alpha)^2\,y^4 + 4000\,\eta^3\,y^2\,\cos(2\,\alpha) + 75\,y^4\,\cos(\beta)^2 + 900\,y^4\,\cos(\beta)^4$$

$$- 4100\,y^2 - 200\,\eta^2\,\cos(2\,\alpha)^2\,y^4\,\cos(\beta)^2 + 100\,\eta^2\,\cos(\beta)^4\,\cos(2\,\alpha)^2\,y^4 + 25600$$

$$- 900\,\eta^4\,y^2 - 225\,\eta^2\,y^4\,\cos(\beta)^2 + \frac{225}{2}\,\eta^2\,y^4 + 4000\,\%1$$

$$- 600\,y^4\,\eta\,\cos(2\,\alpha)\,\cos(\beta)^4 = 0$$

$$\%1 := y^2\,\cos(\beta)^2\,\eta\,\cos(2\,\alpha)$$

$$\%2 := y^2\,\cos(\beta)^2$$

$$\%3 := y^2\,\eta\,\cos(2\,\alpha)$$
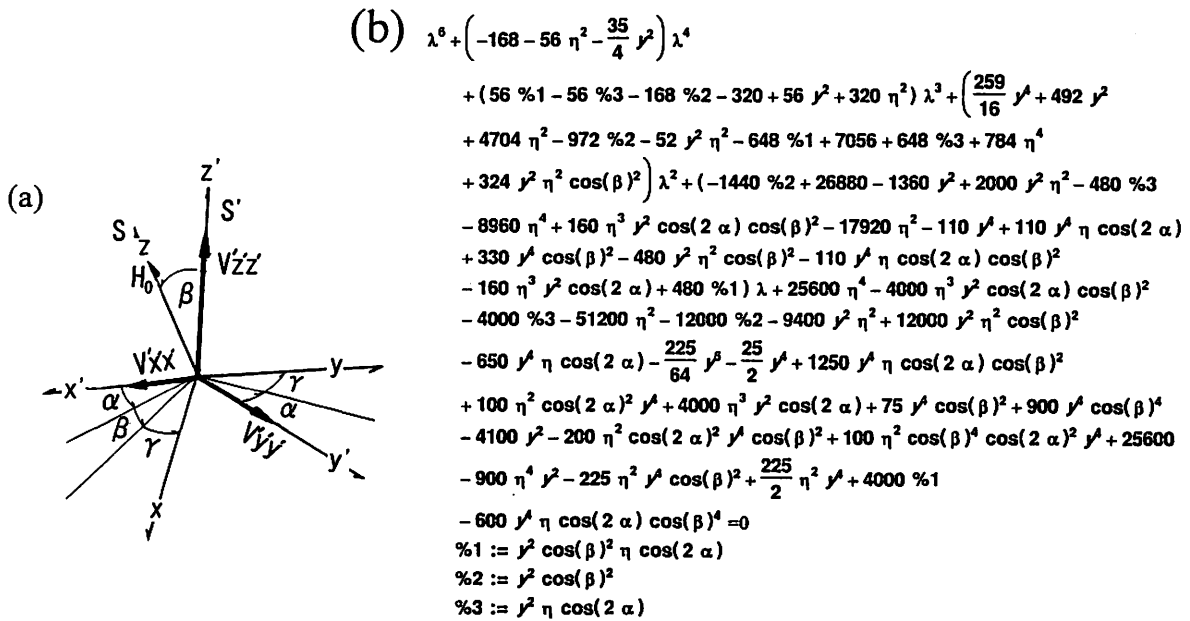
Fig. 1. (a) The angular relations used in the present calculation according to Ref. (1).

Fig. 1. (b) The characteristic equation to give the eigenvalues for I = 5/2 spin with y($= \omega_H/\omega_E$), α, β and η as the parameters.

31
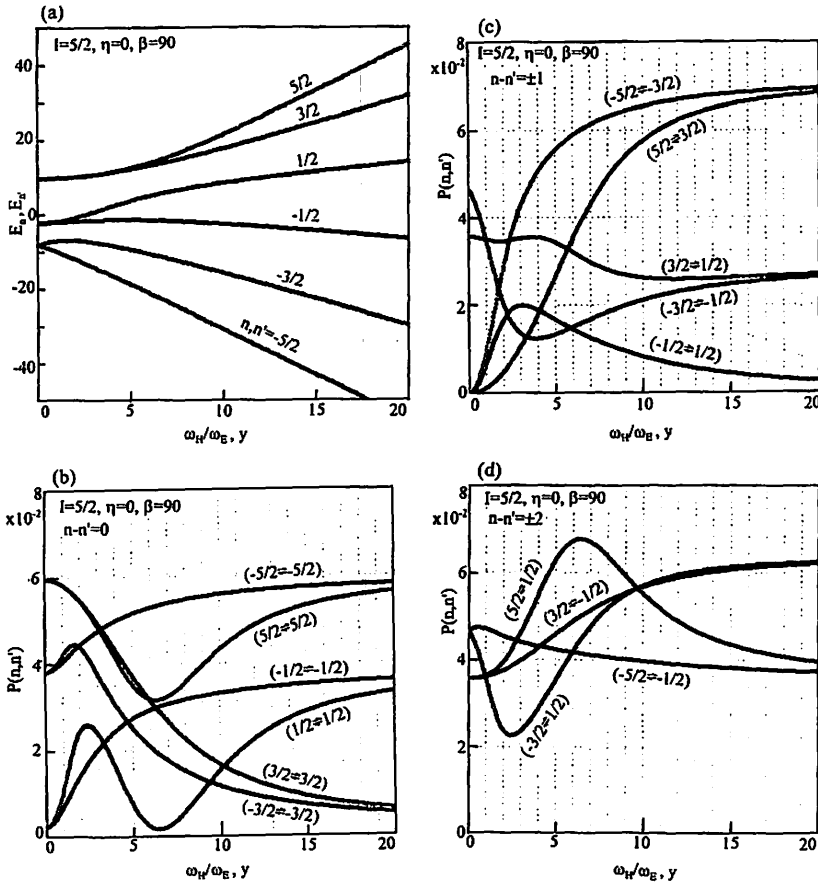
Fig. 2. (a) Eigenvalues for I=5/2 spin with β=90 and η=0 as a function of y(=ω_H/ω_E).

Fig. 2. (b)-(d) the transitionprobabilities as a function of y(=ω_H/ω_E) for I=5/2 spin with β=90 and η = 0.(b) n-n' =0 ,(c) n-n'=±1 and (d) n-n'=±2
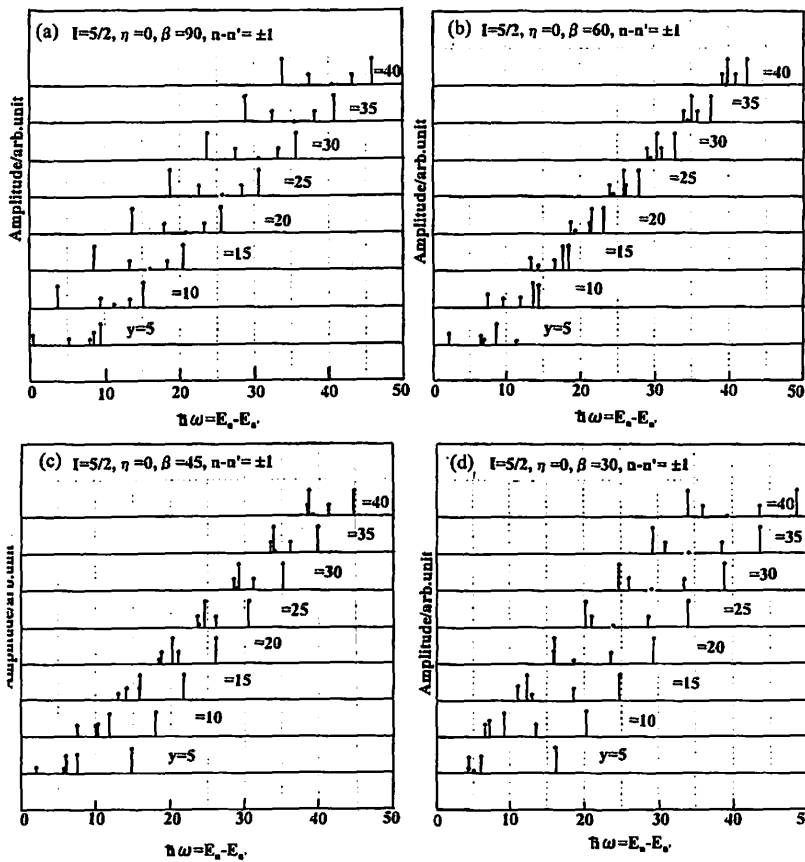
Fig. 3. A simulated Fourier spectra for I=5/2 spin with η=0 as y(=ω_H/ω_E) the parameter. Horizontal axis: the basic frequency (n-n'=±1). Vertical axis: the relative populations (a) β=90, (b) β=60, (c) β=45 and (d) β=30.

32
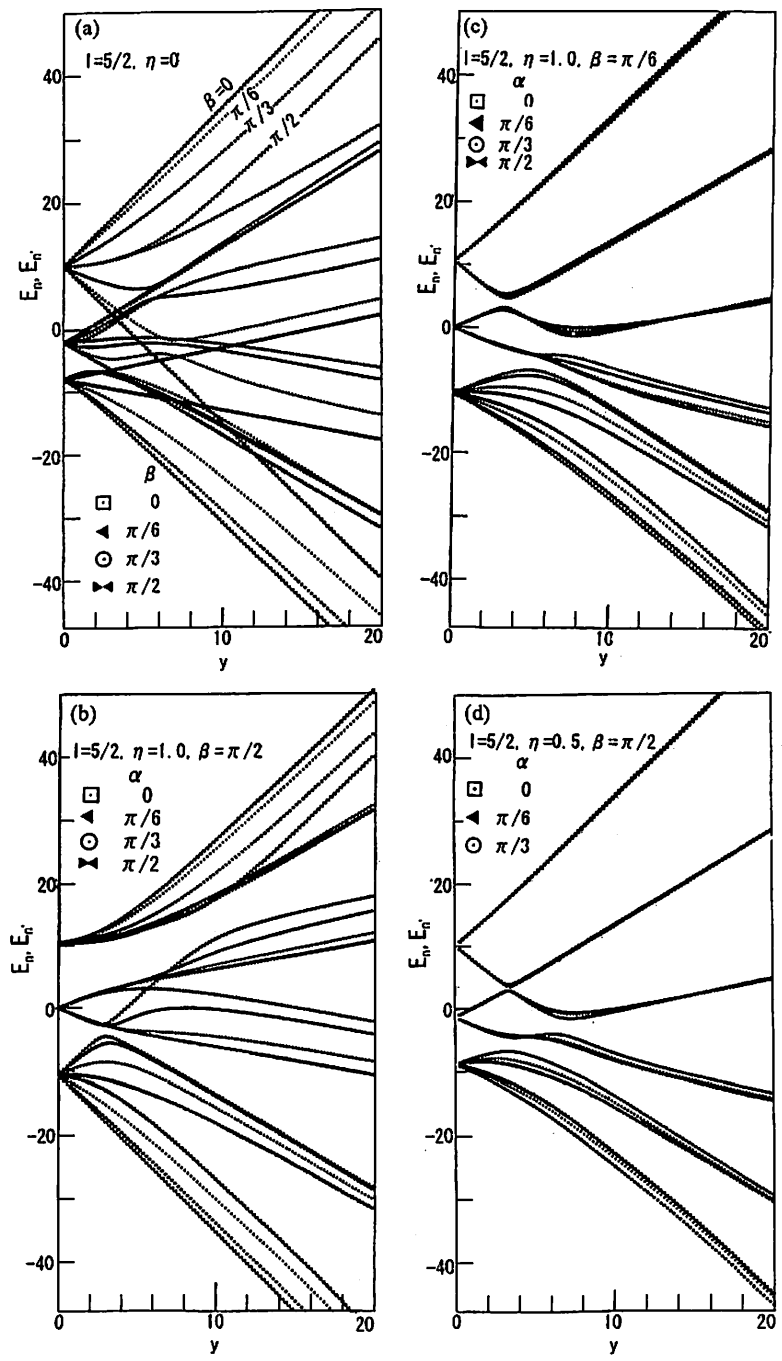
Fig. 4. The eigenvalues for I = 5/2 spin. (a) η = 0, β dependence. (b)(c) η = 1, α dependence with a fixed β. (d) η = 0.5, α dependence with a fixed β.

I. 8. PAC Spectroscopy on Tb at 77K and RT

Hanada R.

Institute for Materials Research, Tohoku University

Introduction

In a previous report in this volume[1], we have shown calculated results of the nuclear energy levels and the transition probability among them when both the magnetic and electric terms are present. There, the cases where the magnetic and electronic interactions have a comparable magnitude were studied and hence an exact calculation was necessary.

Here in this paper, we will report a result of PAC spectroscopy on Tb at RT and 77K. Since Tb has a hcp structure, an EFG with $\eta=0$ should be present at the probe site at RT where it is paramagnetic. Also the V_z axis in a hcp structure has been known to be parallel to the crystal c-axis. On the other hand, it is ferromagnetic at 77K with keeping the hcp structure. So we should have both the magnetic and electric interactions at 77K in Tb. By measuring the PAC spectrum at both temperatures, therefore, we can study how these two interactions will be reflected at PAC spectrum. Our main concern is to determine the angle between the V_z axis and the magnetization direction, β(see Fig. 1(a) in Ref.(1)).

As will be shown later, the magnitude of the magnetic interaction at 77K was found much larger than the electric for Tb. So we are in the range where $y(=\omega_H/\omega_E)>>20$, which is a limiting case of the calculated ones in the previous paper where the cases $y<20$ were studied. As will be shown later, the exact calculation results are found to converge to the present limiting case quite nicely, of which details will be described in the present.

Experimental

PAC source of ^{111}In -Tb was prepared either by the melting or a diffusion method. Since almost the same results were obtained for the specimens prepared by the two methods, we will show that by the melting method.

PAC spectrum of Tb at RT and 77K

Fig. 1(a) shows the PAC spectrum for Tb measured at RT in the paramagnetic region and Fig. 1(b) at 77K in ferromagnetic region. The RT spectrum is characterized by the low frequency component of which period is about 240ns. On the other hand the 77K spectrum is characterized by a high frequency component of which period is 16.5ns, though

the amplitude of the spectrum shows a trend of a beating. The beating indicates that the spectrum consists of the several signals of which frequencies are different by a small amount from each other.

Fig. 2(a) and (b) shows the corresponding Fourier spectra to show that the RT spectrum consists of 3 different frequencies of $27(\omega_1)$, $54(2\omega_1)$ and 81Mrad/s$(3\omega_1)$. This is an expected result for the electric interaction for I=5/2 spin in the EFG with $\eta=0$. On the other hand, the 77K Fourier spectrum shows two components at 356 and 408Mrad/s. The average of them, 382Mrad/s, gives the absolute magnitude of the hyperfine field for Tb at 77K as 27T.

Most importantly in the present, the separation between the two components at 77K, 52Mrad/s, is found very close to the value of $2\omega_1$ =54Mrad/s of the spectrum at RT. This observation will be discussed in terms of a simplified model of the magnetic sublevels splitting due to the quadrupole interactions and the transition probabilities among them in the next section.

No difference was observed in the spectrum with the application of an external magnetic field (0.27 T), Fig. 1(c) and Fig. 2(c), or after the removal of a thin oxide layer from the specimen surface, Fig. 1(d) and Fig. 2(d). The former indicates that the field strength is too weak to align the magnetization direction. The latter indicates that the spectrum is due to the ^{111}In in the bulk metallic phase.

Discussion

Range of y

The ratio of the observed ω_H to ω_1 is about 15. Since $\omega_1=6\omega_{E'}$,

the ratio $(\omega_H/\omega_E)=y$ is as high as 90 far above the range calculated in the previous paper, namely y<20. So we may use an approximation where it is valid when $\omega_H>>\omega_E$.

Analysis of the results on a simplified model

In the limit $\omega_H>>\omega_E$, the eigenvalues for spin I in both a magnetic field and an EFG with $\eta=0$ is given by eq.(1) ;

$$E_m= -\omega_H\hbar\ m + \omega_E\hbar\ (1/2)(3\ \cos^2\beta-1)\ (3m^2-I(I+1)) \tag{1}$$

ω_H and ω_E are magnetic and electric interaction frequency, respectively. Explicitly, $\omega_H=g\mu_N H/\hbar$ and $\omega_E=eqV_{zz}/\hbar\ 4I(2I-1)$. β is the angle between EFG principal axis and the magnetization direction and all other symbols have conventional meanings. This approximation is equivalent to neglect the off diagonal terms in the hamiltonian matrix elements. (Eq.(1) in Ref.(1)). Then the transition frequencies $(E_m-E_m/\hbar)$ for m-m'=1 transitions are given by Eq.(2)

$(m=5/2 \leftrightarrow 3/2)$	$\omega_H + 6\omega_E(3\cos^2\beta - 1)$
$(m=3/2 \leftrightarrow 1/2)$	$\omega_H + 3\omega_E(3\cos^2\beta - 1)$
$(m=1/2 \leftrightarrow -1/2)$	ω_H
$(m=-1/2 \leftrightarrow -3/2)$	$\omega_H - 3\omega_E(3\cos^2\beta - 1)$
$(m=-3/2 \leftrightarrow -5/2)$	$\omega_H - 6\omega_E(3\cos^2\beta - 1)$

(2)

Next, in the limit y>>20, we assume that the transition probabilities among these sublevels are given by those for the pure magnetic transitions despite of the presence of the quadrupole term.   Then, the transition probabilities among the magnetic sub-levels are given by 3j symbol for the pure magnetic interaction as eq.(3)[2].

$$P(m \leftrightarrow m') = \begin{pmatrix} I & I & k \\ m' & -m & N \end{pmatrix}^2$$

(3)

Substituting $I=5/2$, $k=2$, $m-m'=N=1$ for $1\omega_H$ term, $P(m \rightarrow m')$ is obtained as;

$$P(5/2 \leftrightarrow 3/2) = P(-3/2 \leftrightarrow -5/2) = 0.0714279$$

$$P(3/2 \leftrightarrow 1/2) = P(-1/2 \leftrightarrow -3/2) = 0.0285715$$

(4)

$$P(1/2 \leftrightarrow -1/2) = 0$$

Summarizing these and using $\omega_1 = 6\omega_E$, we should have 4 different frequencies $\omega_H \pm \omega_1(3\cos^2\beta - 1)$ with the relative population of approximately 0.7 and $\omega_H \pm 1/2\omega_1(3\cos^2\beta - 1)$ with 0.3.   Note that the ω_H term corresponding $(1/2 \leftrightarrow -1/2)$ transition vanishes because of the selection rule in eqs.(4) .

Now we can apply the theoretical results to the experimental result .   According to the theory, we should have major components separated by $2\omega_1(3\cos^2\beta - 1)$ which should be compared with the observed separation of 52Mrad/s.   Since this value is almost the same with the observed quadrupole frequency at RT, $2\omega_1 = 54$Mrad/s, it is required that the angular term $(3\cos^2\beta - 1)$ must be unity or β must be 90 deg.   Since the V_{zz} direction is directed along the c axis in the case of a hcp structure, the magnetization direction in Tb at 77K should be 90 deg to the c-axis or should lie in the basal plane.   Indeed, this has been confirmed by several other measurements in Tb at low temperatures[3].

Unfortunately, the minor terms $\omega_H \pm 1/2\omega_1$ are not resolved in the Fourier spectrum in the present though their presence is suggested by the broadening of the main component in some of the spectrum in Fig. 2.   The population of them is about 1/3 of the main component and hence easily be merged to the major ones.

Comparison with the exact calculation

Finally we will compare the present results of a high magnetic field limit with those of the exact calculation. The six magnetic sublevels was found to increase almost linearly for y>20 with the same quadrupole splitting as given by Eq.(2). (see Fig. 1(a) in Ref.(1)) in the exact calculation). So the Eq.(2) in the present should be a good approximation for the magnetic sublevels when y>20.

Also the transition probability for m-m'=1 (see Fig. 2(c) in ref.(1)) converges to the same values as in eq.(4) in the present for (5/2↔ 3/2), (-5/2↔ -3/2) as well as (3/2 ↔1/2), (-3/2↔ -1/2) transitions with increasing y. Also the probability for (1/2↔ -1/2) transition tends to be null with the increasing y, which also shows a good agreement with the present approximation. So one can safely use the high magnetic field approximation if y> 20.

For y<20, however, one can not use the approximations and must use the results of the exact calculation, since the magnetic sublevels as well as the transition probabilities are considerably different from those in the high field limit. (see Fig. 2-4 in Ref.1)).

References

1) Hanada R., see an article in this volume.
2) Frauenfelder H. and Steffen R.M., in α-β-γ-rays Spectroscopy II ed. by Siegbahn K., pub.by North-Holland pub.co.(1968).p230.
3) Legvold S., "Rare Earth Metals and Alloys" in Ferromagnetic Materials vol.1 ed. by Wohlfarth EP., pub. by North-Holland pub.co.(1980).
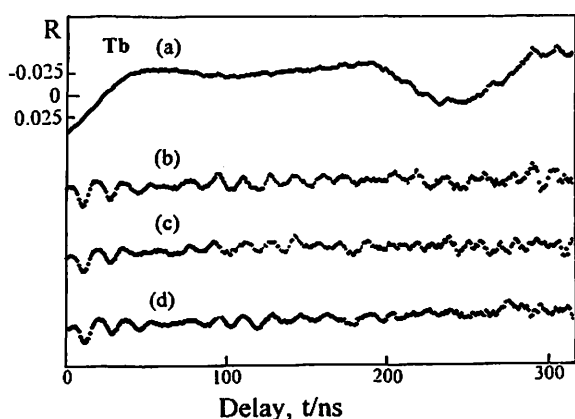
Fig. 1. PAC spectrum for Tb.
(a) measured at RT. (b) measured at 77K. (c) 77K with avertical magnetic field with no change in the spectrum. (d) surface oxide removed with no change in the spectrum.
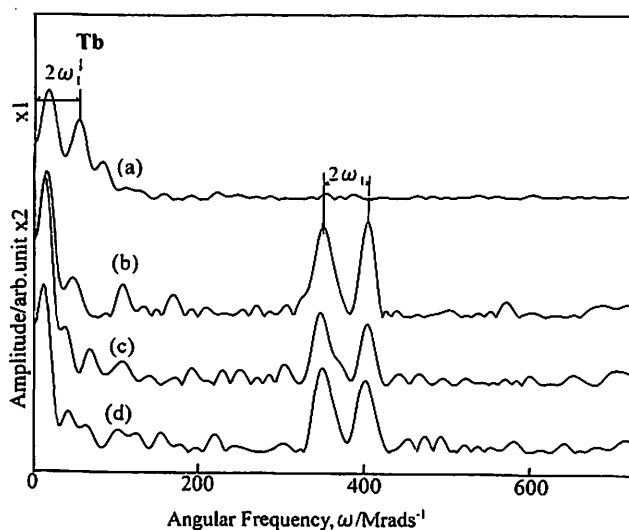
Fig. 2. Fourier spectrum for Fig.1 Note that the $2\omega_1$ at RT is almost equal to the separation at 77K. For details, see text.

I. 9. PAC Spectroscopy of Gd between 18K and RT

Hanada R.

Institute for Materials Research, Tohoku University

Introduction

Magnetism of heavy rare earth elements (Gd,Tb,Dy,Ho,Er,Tm) is one of the most interesting subjects in solid state physics. They have mostly close packed hexagonal structure and paramagnetic at RT. However, they transform to a ferromagnetic phase at a certain temperature below RT. In the ferromagnetic phases, they have shown a variety of magnetic phases as ferro-, helix- , ferrocone-,APD- cone ,CAM- and ferri-magnetism[1]. We have performed PAC spectroscopy on these elements between 18K and RT using ^{111}In as the probe. Here, in the present, a result on Gd will be reported. A result and an analysis on Tb measured at 77K and RT have already been reported in one of the preceding paper[2].

Gd is ferromagnetic below 293K and the magnetization direction is along c-axis of the hcp structure between 243 and 293K. Below 243K, the direction varies with temperature[1]. The purpose of the present work is to examine how this variation will be reflected in the PAC spectrum.

Experimental

[111]In -Gd specimens were prepared either by a melting method or diffusion method. Since the results are almost the same for each other, the result on the specimen prepared by a diffusion method (1000C× 6hrs in a vacuum) will be reported.

The specimen was set in a cryostat of which temperature was regulated by 0.01K and PAC spectroscopy was performed at temperatures between 18K and 300K.

Results

Fig. 1 shows PAC spectrum for Gd between 18K and 300K. Below 70K the spectrum is almost the same with that of Tb. Namely, very high frequency with a trend of the beating showing the spectrum consists of several components of which frequency is very close to each other. At 130K, the beating disappears and it seems to consist of almost one frequency. At 200 and 260K, the spectra are not so well defined but several components are visible as will be shown later. At 300K, the spectrum changes in to the one with the very long period of 265 ns revealing that it transforms to a paramagnetic phase and the precession

is only due to the EFG of the hcp structure of Gd. The corresponding Fourier spectrum, Fig. 2, reveals quantitatively the features described above. Namely at 18K, the spectrum consists of two components, 468 and 531Mrad/s, the separation between them 63Mrad/s. The frequencies of them gradually decrease with temperature and 458 and 507Mrad/s at 70K. At 130K, we see almost one component of 435Mrad/s and the frequency keep decreasing down to 350Mrad/s at 200K and possibly to 230Mrad/s at 260K. At 300K we have a quadrupole frequency of 49Mrad/s which should be ascribed to the 1st harmonic $(2\omega_1)$ among the three quadrupole frequencies in the electric interaction. This is because that the spectrum at 300K in Fig. 1 shows a large bulge at 130ns, half of the period of 260ns, which is the characteristic of the spectrum with the 1st harmonic as the main component. This indicates that the present specimen is not a perfect poly-crystal but have such a preferred orientation to give the 1st harmonic as the main component.

Summarizing these results;

(1) The separation between the two components at 18K, 63Mrad/s, is close to but definitely higher than that at 300K, 49Mrad/s. This is a different result from Tb, where these two values almost coincide. This result will be used to determine β for Gd at 18K, the angle between the crystal c-axis and the magnetization direction.

(2) In some temperature range, 130-200K, the spectrum shows a trend that it consists of a single component. This will be discussed also in terms of β which have a temperature dependence in the case of Gd.

(3) The average of the two components at 18K, 500Mrad/s, yields 34.8T as the magnitude of the hyperfine field. The sign of the field has been determined as minus[3]. The gradual shift of the components to the lower field with the increasing temperature is just a manifestation of Curie-Weiss law in the hyperfine field and hence will not be discussed here.

Discussion

First let us compare the magnitude of the quadrupole to that of the magnetic frequency. This is to examine in which range of $y(=\omega_H/\omega_E)$ we are dealing with, since the calculated results in Ref.(4) were given as a function of y. The ratio ω_H/ω_1 is determined from the results at 18K and 300K as about 20. For the $\eta=0$ case, $\omega_1=6\omega_E$ holds. So we are in the range y>100, far above the range where an approximation neglecting the off-diagonal terms in the hamiltonian is completely valid. Following the procedure applied for Tb (see ref.(2)), we have a relation as eq.(1),

$$2\omega_1(3\cos^2\beta-1)= \Delta H \qquad (1)$$

where ΔH is the separation between the two components observed below 70K. Substituting the observed values, $2\omega_1=49$ at 300K and $\Delta H=63$Mrad/s at 18K, we obtain $\cos(\beta)=0.873$ or $\beta=29$ deg. Namely different from Tb where $\beta=90$deg was found, for Gd the

magnetization direction is found inclined by 30 degree from the crystal c axis at 18K. This value of β found in the present shows a good agreement with that obtained by a macroscopic magnetization measurement, namely, 28deg. below 50K[1]. The eq.(1) also shows that at the angle, $\cos(\beta)=1/\sqrt{3}$, namely at $\beta=54.4$, ΔH becomes null. Namely, at this angle the quadrupole effect completely vanishes in the PAC spectrum even when both the quadrupole and magnetic interactions are present. This explains the observed single line at 130K. Because of the peculiar magnetic behavior of rare earth, the magnetization direction has been known to vary with the temperature. For the case of Gd, β stays at 28deg below 50K but gradually increases to 55 deg at 130K and reaches to the maximum 65deg at 170K[1]. So at 130K where a single line spectrum observed, we are observing a spectrum with only the magnetic effect in Gd without the EFG effect.

This situation can be seen clearly in Fig. 3 in Ref.(4) where the components in PAC spectrum were calculated as a function of y with β as a parameter. At $\beta=45$ or 60 deg, the splitting, ΔH, is found to become much smaller than that at 0 or 90 deg.

The calculated results in Fig. (3) in Ref.(4) suggest several interesting experiment for low value of y. Namely, if we apply an external magnetic field to a single crystal of, say, Cd or Zn with the EFG, we should have the PAC spectrum of which components are given as in Fig. 3(a)-(d) in Ref.(4) depending on β. The magnitude of the magnetic field is estimated as about 8T for y=6 in the case of Cd with knowing the quadrupole frequency.

Acknowledgement

References

1) Legvold S., Rare Earth Metals and Alloys in *Ferromagnetic Materials I* ed. by Wohlfarth E. P. pub. by North-Holland Pub.Co.(1980).
2) Hanada R., in this volume.
3) Boström L. et al., Physica Scripta, 2 (1970) 65.
4) Hanada R., in this volume.
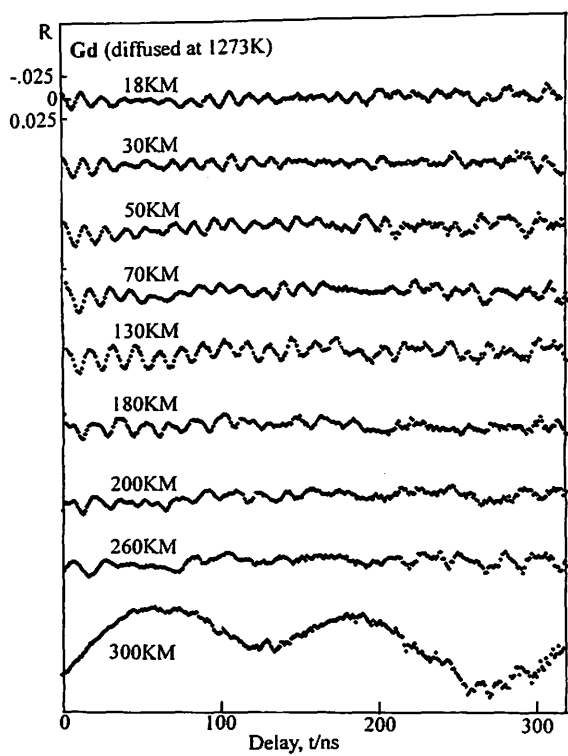
Fig. 1. PAC spectrum for Gd between 18K
and RT.
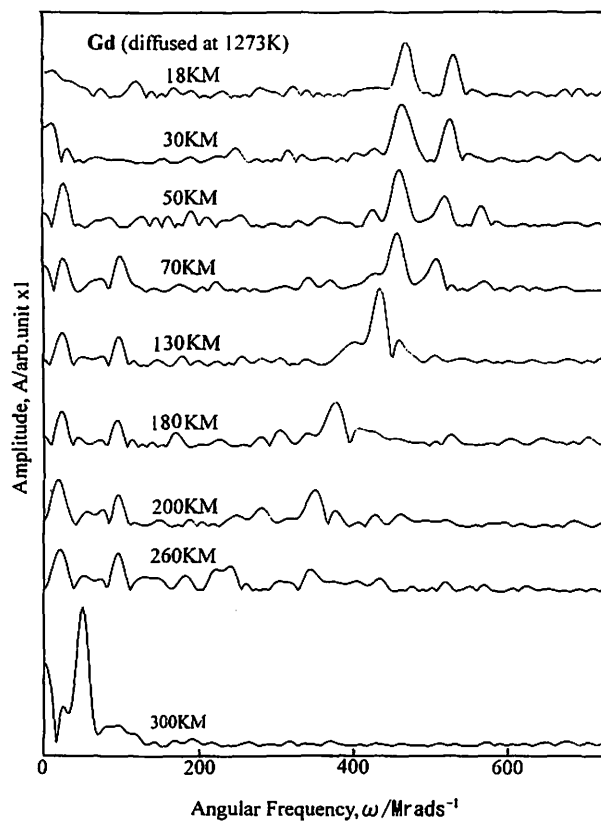
Fig. 2. Fourier spectrum for Fig. 1.

I. 10. PAC Spectroscopy of Gd-Tb Alloy between 18K and RT

Hanada R.

Institute for Materials Research, Tohoku University

Introduction

As have been described in several reports in this volume, heavy rare earth elements have peculiar magnetic properties as helix- or ferrocone-magnetism. These are interpreted as a result of a RKKY type interaction of conduction electrons[1].

Adding to the basic research for the magnetism, alloy magnets for practical uses have been developed with a rare earth element as one of the constituent. Such examples are Sm-Co or Nd-Fe-B magnet.

The motive of the present work is rather simple and intuitive. Namely, if two rare earth elements with the different easy axis of the magnetization are mixed together, which direction the axis will be directed ? Although many alloys were studied, a result on a Gd-Tb alloy will be described in the following. As has been described in previous reports, Tb has the easy axis in the basal plane. On the other hand that of Gd is almost parallel to the c-axis below 50K

Experimental

Known amounts of Tb and Gd were melted in Ar atmosphere together with ^{111}In-chloride solution to prepare a PAC source. Tb and Gd form a complete solid solution and hence both atoms should be distributed randomly in the alloy.

The specimen was set in a cryostat of which temperature is regulated by 0.01K and the PAC spectroscopy was performed at temperatures between 18K and RT.

Result and Discussion

Fig. 1. shows the PAC spectrum for Gd-Tb alloy (Tb: 53.3 at.%) and the corresponding Fourier spectrum in Fig. 2. As in the cases of Gd or Tb, a precession signal with a trend of beating is observed between 18K and 50K although the amplitude is much more reduced. Although several components are resolved in the Fourier spectrum, the amplitudes are comparable with the noise level. Nevertheless, with assuming the hyperfine field in the alloy is comparable with those of the constituents, we can resolve four components near 400Mrad/s as in the cases of Gd or Tb marked by arrows in Fig. 2.

This gives 28T as the magnitude of the hyperfine field in the alloy at 18K, which is comparble with that for Tb at 77K, 27T.

At the temperature of 52.5K, a broad bulge develops at about 60ns as shown in Fig. 1, of which component is resolved as 100Mrad/s component in Fig. 2. This component develops with the increasing temperature and become the main component above 55K corresponding to the precession signal with the 60ns period in Fig. 1. Since the magnitude of the frequency is almost temperature independent up to 300K, the origin must be of an electric type. This shows that the alloy transforms to the paramagnetic phase as low as at 53K despite of that the Curie temperature of Gd or Tb is near RT. Namely, by alloying, Curie temperature of Gd or Tb is shifted to the lower temperature of 50K-55K from RT. This shifting of the Curie temperature upon alloying has been found in most of rare earth binary alloys or the alloys with 3d transition metals and seems to be a quite common phenomenon. Intuitively, the long range interaction to give rise to the magnetic ordering in pure rare earth metals seems to be destroyed upon alloying to give such a shift. The cause of the shifting should be examined based on the solid state theory of the rare earth magnetism.

Next let us discuss the EFG in the alloy. Comparing with those in pure Gd or Tb, the period of the precession in the alloy is considerably reduced by a factor of four. Namely, the magnitude of the EFG is about 4 times larger in the alloy than those in Tb or Gd. Different from pure Gd or Tb to give a symmetric EFG ($\eta=0$) because of the hcp structure, the alloy should, in principle, give an asymmetric EFG. This is because that the local hcp symmetry is destroyed by the alloying element even when the alloy has kept the hcp structure. These as well as the cause of the increased EFG also should be treated theoretically.

The site of ^{111}In in the alloy is somewhat uncertain in the present. However, it is speculated that it will occupy equally both Gd and Tb site in the alloy, since the chemical properties are almost the same for these two elements. Nevertheless, we observe only one EFG frequency. This indicates that the magnitude of the EFG for ^{111}In at Gd site is almost the same with that at Tb site. This is reasonable for the present 50:50 alloy, since the local environment is almost the same for each site for such a high concentration alloy.

Finally we discussed the direction of the magnetization axis in the alloy in the ferromagnetic state at 18K. With assuming the faint four lines marked by arrows in Fig. 2 are due to the quadrupole splitting, the same analysis as in pure Tb or Gd was done to give $\beta=90$. Although tentatively at present because of the faint signal, the magnetization direction of the alloy is concluded to lie in the basal plane just as the case of pure Tb.

Summarizing these results on the Tb-Gd alloy;

(1) The magnitude of the hyperfine field is almost the same with those in pure Tb.

(2) The Curie temperature is considerably reduced upon alloying.

(3) The magnitude of the EFG is increased about 4 times upon alloying.

43

The application of the melting method for the source preparation and the subsequent PAC spectroscopy will provide a useful mean for the development of new magnetic materials. Namely, once one finds a very high hyperfine field in the PAC spectrum, the material is likely to have a high macroscopic magnetization for the practical use. This is so for the case of 3d transition metals as Fe or Ni although the sign of the field is reversed. The relation between the microscopic hyperfine field and that of the macroscopic should be established both empirically and theoretically

Acknowledgement

References

1) Fukunaga H., "Magnetism in Rare Earth Elements" in *Science of Rare Earth Elements*, ed. by Adachi G., pub. by Kagaku-Donin (1999) (in Japanese).
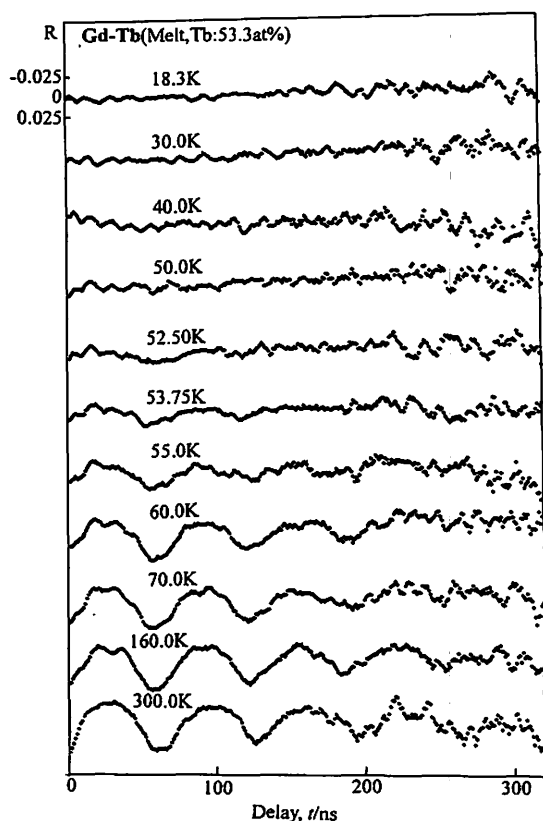
Fig. 1. PAC spectrum for Gd-Tb alloy between 18K and RT.
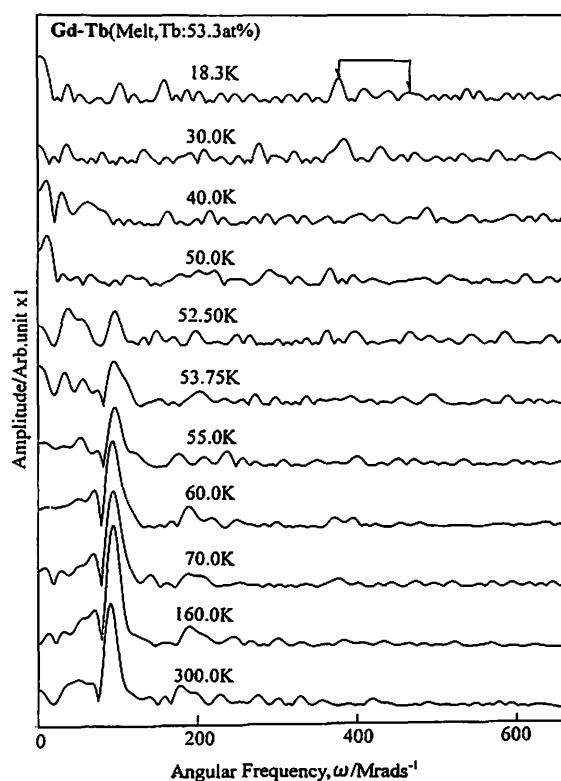
Fig. 2. Fourier spectrum for Fig. 1.

I. 11. Attempt at Elemental Analysis of Soluble and Insoluble Fractions of River-waters by PIXE

Yamazaki H., Ishii K., Matsuyama S., Takahashi Y., Sasaki T., Orihara H.*,
and Izumi Y.**

Department of Quantum Science and Energy Engineering, Graduate School of Engineering, Tohoku University
Cyclotron and Radioisotope Center, Tohoku University*
Japan Environment Research Co. Ltd., 7-8-13 Shinjuku-ku, Tokyo 160, Japan**

INTRODUCTION

Owing to a greater awareness of the problem of pollution, the composition of rain and surface water has been studied for many years with the analysis of such samples often being carried out by absorptiometry and atomic absorption spectrophotometry. In these analyses, water samples are filtered to remove insoluble components which are then not analyzed. Particle-induced X-ray emission (PIXE) is a rapid and multielemental technique. This technique has been used extensively for analyzing aerosol samples[1,2], but it has not often been applied to water samples because of problems in target preparation[3,4]. However, the use of PIXE analysis permits convenient determination of both soluble and insoluble materials in natural waters due to versatility in the form of specimens to be analyzed, providing for some useful information about chemical forms of elements in a water samples.

The PIXE technique is conveniently applied to the analysis of thin samples and offers the possibility of a high absolute sensitivity (nanogram levels). In our previous studies[5], a combination of chelation by dibenzyldithiocarbamate (DBDTC) ions with subsequent condensation into dibenzylidene-D-sorbitol (DBS) gels has been developed for preconcentration of trace amounts of heavy metals in water samples, in conjunction with rapid preparation of thin uniform targets containing zirconium as an internal standard. We also have developed a simple preparation method for thin polycarbonate film and used it as a target backing in the PIXE analysis of anions such as sulfate, chromate and arsenate in a wide concentration range (10-2000 ppb).

It is the purpose of the present study to combine these techniques for sample preparation with Nuclepore filtration of insoluble constituents, which results in rapid determination of elemental concentrations in both soluble and insoluble fractions of river waters.

EXPERIMENTAL

Target Preparation

We collected 12 water samples at 2-hour intervals on July 16, 1998 at two locations of the Hirose river, which is a class A river flowing through Sendai city. One sampling point located at the beginning of our town and the other was a 8-km downstream point on the outskirts of the town. The samples were stored in Nalgene linear polyethylene containers and processed into PIXE-targets within 24 hours. After pH measurement, insoluble components in 30 ml of each sample were filtered under suction with a Nuclepore filter of 0.4-μm pores. The filter was mounted on a Mylar target frame and kept in desiccator for several days. The filtration efficiency was over 98 % for colloids of ferric hydroxide and silver chloride in the range of 20-2000 ppb. The targets for these colloids in a known amount (40 and 400 ppb) were prepared in the same manner and used as an external standard for normalization of PIXE spectra for the insoluble components.

In the preparation of PIXE targets for heavy metals in the soluble fraction of river waters, 2.5 ml of 0.1 % (w/v) DBDTC solution and 25 μl of 1000 ppm Zr in 1M HNO_3, respectively, were added to 25 ml of each filtrate as a chelating agent and as an internal standard, and then the pH of solution was kept around 5 for 4 minutes. The solution gelled immediately after addition of 10 μl of 4 %(w/v) of DBS solution, and the DBS gels containing metal-DBDTC complexes were filtered on a Nuclepore filter of 0.4-μm pores. In our previous study[4], quantitative recoveries of 7 metals (Fe, Co, Ni, Cu, Cd, Hg, Pb) were confirmed up to the concentration of 1 ppm, and the coexistence of Mg, Ca and humic acid in 40 ppm did not interfere with the recovery of the heavy metals.

On the other hand, alkali metals, alkaline earth metals and anionic species in the soluble fraction are not picked up in the preconcentration step described above. The targets for these elements were prepared by depositing 30 μl of filtrate on an user-made polycarbonate film; 10 μl of 1000 ppm Ga in 1M HNO_3 was added to 4 ml of filtrate beforehand. After drying at 60°C, the procedure was repeated four more times to give a total of 150 μl dried on the foil. As we have revealed in our previous study[5], a polycarbonate film of thin and uniform thickness is prepared by dropping a polycarbonate solution in chloroform-benzene mixture slowly on a water surface within a 20-mm aperture of Mylar target frame floating on 50 wt% sucrose aqueous solution. The film offers a good combination of mechanical strength, chemical stability and low X-ray continuum background.

PIXE Analysis

The samples were analyzed by in-air PIXE system at Tohoku University and by a vacuum PIXE system at Nishina Memorial Cyclotron Center (NMCC) of Japan Radioisotope Association (apparent current of 3-MeV protons: 10 nA; 5-min irradiation). The in-air PIXE system at Tohoku University has a vertical beam line and a beam exit assembly composed of a

Si(Li) detector and a Si-PIN photodiode detector. The solid angle of Si-PIN photodiode detector is much larger than that of Si(Li) detector, but the maximum energy of X-ray detection of Si-PIN photodiode detector is limited to 15 keV[6,7]. In the PIXE system of NMCC, X-rays from targets were measured with two Si(Li) detectors; one having 300-μm Mylar absorber and high geometric efficiency allows the detection of X-rays > 4 keV, and the other one with a low geometric efficiency is well suited for the detection of elements of the atomic number $Z \leq 20$[8].

For PIXE spectra analysis, we used a least-squares fitting computer program, which has been developed in our laboratory based on a theoretical approach for the background continuum in PIXE spectra[9]. In this program, a background function for elements with atomic number $Z=6-30$ was obtained as a function of Z and X-ray energy from bremsstrahlung emission cross-sections derived by the theoretical formula based on PWBA and BEA. Then, the spectra of continuous and characteristic X-rays of elements were determined with the background functions and were used to least-squares fit to a measured PIXE spectrum. The detector's intrinsic efficiency and the transmission through absorbers were determined experimentally in the X-ray range of 1-60 keV. The values for the total production cross-sections of X-rays of interest and the correction factors for the relative intensities of multiplets for each characteristic X-ray were obtained from the text book by Johansson and Campbell[10].

RESULTS AND DISCUSSION

The measurements for 12 river-water samples collected at two locations over 10 hours were done by PIXE, each sample being separated into soluble and insoluble fractions by means of the procedure described before. The detection limits of the PIXE analysis were on the order of several tenths of ppb for elements producing X-rays >5 keV, while the large continuum background of the backings in PIXE spectra incurs an inferior limit, that is, several tens of ppb for elements with atomic number $Z < 20$.

The K and L X-ray lines were observed for 24 elements in the spectra of three kinds of targets. This indicates that the PIXE technique has the advantages of a truly multielemental character and high speed of analysis with a small amount of samples. The X-ray lines of many heavy metals were clearly detected in the spectrum of the target prepared with the DBDTC-DBS preconcentration. From this result, we can understand why the preconcentration step is indispensable to the PIXE analysis for heavy metals in a low concentration of ng/ml level. In contrast to this, the spectra obtained from the deposit of filtered river-water allows us to determine the concentrations of soluble elements such as alkali and alkaline earth metals, which cannot be picked up in the preconcentration step. An important result is that the PIXE analysis for the three kinds of targets reveals elemental distribution between the soluble and insoluble fractions of river waters.

We now review time-variation in concentrations of major components in the soluble and insoluble fractions (Fig. 1). The error bars on the individual data points of Figure 1 are error estimates from the spectral fitting program. It is found from this figure that the elemenand insoluble fractions (Fig. 1). The error bars on the individual data points of Figure 1 are tal concentrations appreciably change with time in a different fashion between the soluble and insoluble fractions. The concentrations of soluble components increased largely on the fourth sample collected at the downstream of the river. On the contrary, the increase of concentrations in the insoluble fraction was observed on the last sample collected at the upstream point. The details for these different observations cannot be discussed because of a short period of collecting the samples. Here it should be noted that PIXE analysis with high sensitivity clearly distinguishes the change of elemental concentrations in the widespread range from 0.1 ppb to 20 ppm (in five orders of magnitude).

The averaged concentrations of the soluble and insoluble components for each six samples collected at two locations are tabulated in Table 1, together with the deviations. Most of alkali metals, alkaline earth metals and anionic species for P, S and Cl are present as soluble components in the range of concentration from 0.5 to 20 ppm. The insoluble fractions include a large amount of Al, Si and Fe, which suggests that the compounds of these elements are insoluble minerals derived from soil. The concentrations of Al and Si, however, are much higher in the soluble fractions than in the insoluble ones, indicating very fine particles of clay and colloidal hydroxides of the elements in the river waters. Most of Ti, Mn, Hg, and Pb are included in the insoluble fraction, and the significant portions of other heavy metals are found in both soluble and insoluble fractions.

The elemental concentrations in the soluble fractions are found to be rather independent of the location of collecting samples due to the large deviation with time. On the other hand, concentrations of most elements detected in the insoluble fractions are almost two times higher at the downstream point than at the upstream one, while the composition of the insoluble materials does not differ between the two points. This experimental result naturally implies that clay-colloids condense in the flow of river to form particles large enough to be filtered out with a filter of 0.4-μm pores.

CONCLUSION

In this study, a procedure has been developed and tested for the PIXE analysis of soluble and insoluble constituents in river waters. The target preparation and the PIXE measurement are not time-consuming; the preconcentration step requires less than 10 minutes, and the samples are analyzed by PIXE in which targets are irradiated by a 3 MeV proton beam for 5 minutes. Many kinds of elements can be detected simultaneously in the widespread range of concentrations from several tenths of ppb to a few tens of ppm. The elemental concentrations largely vary with time, and the change in the soluble fraction is not correlated to that of the insoluble fraction. Moreover, some heavy metals of importance as an

indication to water-pollution problem are predominant in the insoluble fraction of river waters. Hence, the methodology for preparing targets of both soluble and insoluble components promotes the PIXE analysis to a truly effective means for monitoring a pollution problem of rivers.

References

1) Akselsson, K.R., *Nucl. Instr. and Meth.*, **B3**, 425 (1984).
2) Kasahara, M., et al., *Nucl. Instr. and Meth.*, **B109**, 471 (1996).
3) Tanaka, S., et al., *Environ. Sci. Technol.*, **15**, 354 (1981).
4) Johansson, E. M. and Johansson, S. A. E., *Nucl. Instr. and Meth.*, **B3**, 154 (1984).
5) Yamazaki, H., et al., *Int. J. PIXE*, **6** (3&4), 483 (1996); *ibid*, **7** (1&2), 31, 101 (1997).
6) Iwasaki, S., et al., *Int. J. PIXE*, **5** (2&3), 163 (1995).
7) Matsuyama, S., et al., *Int. J. PIXE*, **9** (1&2), 51 (1999).
8) Futatsukawa, S., et al., *Int. J. PIXE*, **7** (3&4), 171 (1997).
9) Murozono, K., et al., , *Int. J. PIXE*, **6** (1&2), 135 (1996).
10) Johansson, S.A.E. and Campbell, J.L., *"PIXE. A Novel Technique for Elemental Analysis,"* John Wiley & Sons, New York, 1988, pp.313-329.

Table 1. Concentration of the Soluble and Insoluble Components of River Waters.

Element	Concentration of soluble components (ng / ml)		Concentration of insoluble components (ng / ml)	
	Upstream	Downstream	Upstream	Downstream
Na	6900 ± 1200	8900 ± 3800	42 ± 15	88 ± 11
Mg	2600 ± 410	3800 ± 1200	54 ± 16	108 ± 12
Al	990 ± 220	1410 ± 600	140 ± 45	270 ± 23
Si	12600 ± 2000	17700 ± 6000	610 ± 160	1250 ± 140
P	780 ± 180	1100 ± 390	35 ± 5	69 ± 9
S	8400 ± 1500	11400 ± 2800	34 ± 5	63 ± 9
Cl	490 ± 140	690 ± 330	25 ± 4	41 ± 5
K	1580 ± 250	2420 ± 560	26 ± 6	57 ± 8
Ca	14700 ± 2400	18200 ± 3700	38 ± 14	85 ± 12
Ti	0 ± 0.1	0.2 ± 0.3	4.2 ± 2.6	6.5 ± 0.6
Cr	1.8 ± 0.4	2.0 ± 0.8	0.4 ± 0.1	0.9 ± 0.4
Mn	0.7 ± 0.1	1.1 ± 0.2	12 ± 0.3	32 ± 4
Fe	21 ± 3	56 ± 12	97 ± 41	240 ± 15
Ni	1.3 ± 0.1	1.5 ± 0.3	0.3 ± 0.2	0.6 ± 0.1
Cu	2.8 ± 0.4	3.0 ± 0.2	0.3 ± 0.2	0.5 ± 0.1
Zn	5.4 ± 0.9	6.0 ± 0.2	1.5 ± 0.5	2.9 ± 0.4
As	0.9 ± 0.4	1.1 ± 0.6	0.2 ± 0.2	0.1 ± 0.1
Br	29 ± 2	31 ± 18	0.1 ± 0.1	0.6 ± 0.5
Rb	1.5 ± 0.6	1.8 ± 0.4	0.4 ± 0.3	0.6 ± 0.2
Sr	38 ± 9	55 ± 17	0.2 ± 0.1	0.3 ± 0.1
Cd	1.3 ± 0.6	2.4 ± 0.8	0.3 ± 0.3	0.4 ± 0.3
Ag	2.9 ± 1.1	3.5 ± 1.3	0.2 ± 0.1	0.3 ± 0.3
Hg	0.1 ± 0.1	0.1 ± 0.1	0.4 ± 0.3	1.0 ± 0.5
Pb	0.4 ± 0.4	1.2 ± 0.6	1.6 ± 1.2	3.5 ± 0.7

The mean values and the deviations in the concentrations were calculated for the six samples at each sampling point.
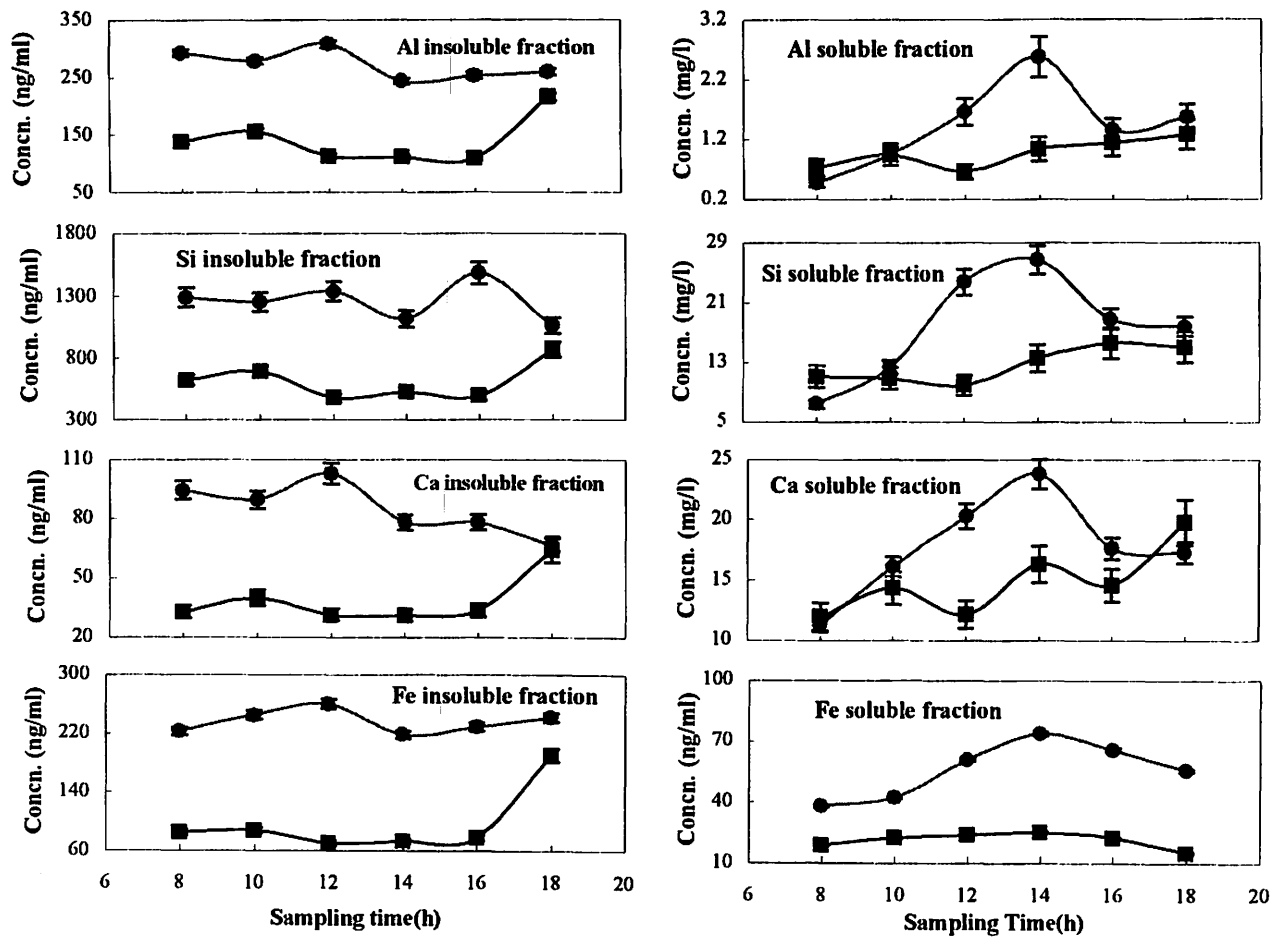
Fig. 1. Time variation of elemental concentrations in both soluble and insoluble fractions of river waters.
■: the upstream sampling point, ●: the downstream sampling point.

50

I. 12. An Open Experiment of a Submilli-PIXE Camera

Matsuyama S., Ishii K., Yamazaki H., Iwasaki S., Tokai Y., Sugimoto A.,
*Endo H., Ozawa T. and Orihara H.**

Department of Quantum Science and Energy Engineering, Tohoku University
*Cyclotron Radioisotope Center, Tohoku University**

Introduction

Recent young Japanese generations tend to be not interested in science.   One of the reasons is that young people like to take easier subjects.   To help understanding nuclear technology or radiation science, we have held an open experiment of PIXE once a year since 1996.   Among many scientific experiments, PIXE analysis is one of the most appropriate experiment, because to know what elements are contained in our belongings is the most interesting thing for us and PIXE can easily and quickly analyze them without their deterioration by beam irradiation.

The open experiments of PIXE analysis using a vertical in-air PIXE (ViaPIXE) system[1] were held at a Dynamitron laboratory of Tohoku University[2].   Lecture and inspection for the Dynamitron accelerator and the in-air PIXE system were performed in the open experiments.   The participants themselves went to the place of the ViaPIXE system and, on a target stage, set their sample which they brought from their houses or elsewhere and then, the sample was irradiated with 3 MeV proton beams.   Observing PIXE spectra, we made them to understand the X-ray peaks of the elements which were contained in the sample. The first and second open experiments were held as an event of an open school which has been held during the period of annual meetings of Atomic Energy Society of Japan.   After these events, the open experiments were held during the period of an open campus aimed to introduce activities of Tohoku University to high school students.   Up to the present, more than 270 people joined the open experiments of PIXE.   Most of the participants were impressed into quick and easy elemental analysis by PIXE.   This seems to result that the participants felt interest in nuclear technology and radiation science.

A submilli-PIXE camera was recently developed in our laboratory[1] and was introduced in the open experiment.   The submilli-PIXE camera can measure spatial distribution of elements.   This system consists of a submilli-beam line with a high-speed beam scanning system and a spatial distribution imaging system of elements in the region of 3 cm×3 cm.   The submilli-beams are formed by using two slits and are always scanned on an interesting region of the sample. When an X-ray is detected, the X-ray energy and the beam

position are simultaneously measured for each event. This system can display the spatial distribution image of element even while the data are being collected. By comparing the measured elemental images with the shape of the sample, the participants may easily consider meanings of the distribution of elements in the sample. In the submilli-PIXE camera, samples can be analyzed in atmosphere. This in-air analysis is an important performance for the open experiments, since we can analyze any sample which participants will bring.

Open experiment

The 4th open experiment of PIXE was held on 29 and 30 July 1999 when the open campus of Tohoku University was held. We visited junior high schools in Sendai City to explain the aim of the open experiment of PIXE to science teachers. More than one thousand people participated in the open campus of Tohoku University. About 400 participants of them visited our department and were advised to participate in the open experiment of PIXE. We had nine groups (sixty-nine persons). It took about one hour to perform the open experiment. The participants were led to the Dynamitron laboratory in every one hour from the main hall of our department, at which our research activities are exhibited. We gave lectures to the participants for the Dynamitron accelerator, principle of PIXE and the submilli-PIXE camera using graphic panels. Easy sentences and figures in the graphic panels were very useful to help understanding of junior high school students. After an inspection of the submilli-PIXE camera, we received a sample from them and set it together with them. There were a few participants who offered a sample, since we did not request them to bring something want to analyze. We considered the belongings of participants as samples, because the results of analysis might be left in their impression strongly. In the case that they did not have an appropriate sample, we made them choose one of the samples which were prepared by ourselves. Before irradiation of the sample, we showed the beams spots on the beam viewer at the upstream side of the sample position. Then we pulled out the viewer and irradiated the sample. It is very important to visualize the beam spot to get their better understanding.

We showed the elements contained in the sample by observing the PIXE spectrum. At the previous experiments, the participants had been surprised at the PIXE spectrum being formed in a moment. However, this time, the participants were not so impressed. Since we too much emphasized spatial distribution of elements, they were not interested in the PIXE spectrum itself. This point should be reconsidered. We showed the elemental distribution images for major elements. Samples were school badges, a can of Cola drinks, a magnetic card, a watch, a necklace, earrings, a sandstone and a ball-point pen. It took only a few minutes to get elemental images. The participants were strongly impressed in that an elemental distribution was displayed as an image. The participant who analyzed her school badge was surprised at the elemental image which corresponded to the shape of character on the badge. Figure 1 shows the photograph and the elemental images of Ni and Pb in the

school badge. The elemental image of Ni shows very clearly the shape of character in the badge. Since the spatial distribution of elements showed the shape of the sample or the character on the sample, the participants seemed to easily understand nuclear technology and its application.

The participants who joined the open campus tended to visit as many places as possible and their visiting time was restricted to several hours. Nevertheless, twenty percents of the persons who visited our department joined the open experiment of PIXE which lasted one hour. It results that the open experiment of PIXE attracts their interest. Since the open experiment was held during a period of the open campus of Tohoku University, half of the participants were high school students. About ten percents of the participants were junior high school students. At the first open experiments of PIXE held in 1996, junior high school students occupied more than a half of the participants, however, the number of junior high school students decreased. The first open experiment of PIXE was held in the holiday on September 1996, therefore, the rate of junior high school students was high because their teacher accompanied them. In spite of our effort for advertisement of the open experiments of PIXE, junior high school students did not participate so much at the present. Recently, the open experiments were held at the end of July when a summer vacation began. When a summer vacation begins, it may be difficult for junior high school students to participate in the event. To continue to hold the open experiments, we are now considering and seeking an appropriate period when junior high school students can participate easily.

References

1) Iwasaki S., Ishii K., Matsuyama S., Murozono K., Inoue J., Tanaka M. Ymazaki H., and Orihara H., International Journal of PIXE 6, 1&2, 117 (1996).
2) Matsuyama S., Isl1ii K., Yamazaki H., Iwasaki S., Murozono K, Inoue J., Tanaka M., and Orihara H., International Journal of PIXE 6, 3&4, 453 (1996).
3) Matsuyama S., Gotoh K., Ishii K., Yamazaki H., Satoh T., Ymamoto K., Sugimoto A., Tokai Y., Endoh H., and Orihara H., International Journal of PIXE 8, 2&3, 209 (1998).
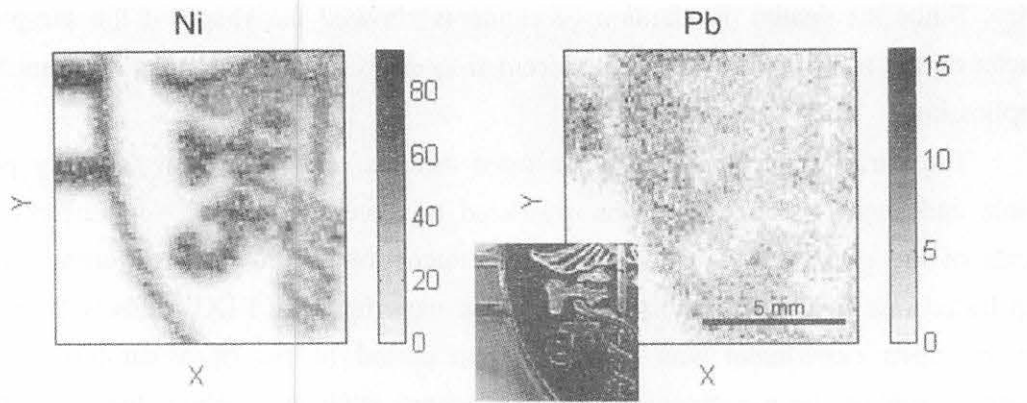
Fig. 1.   Photograph and elemental distribution images of Ni and Pb in the school badge.

I. 13. No Deterioration Elemental Analysis with In-air Subumilli PIXE Camera

Matsuyama S., Ishii K., Yamazaki H., Endoh H., Gotoh K., Satoh T., Yamamoto K., Sugimoto A., Tokai Y., Orihara H.[*], Yokota.[**] S, Fujisawa A.[***], Sekine T.[***], Nara Y.[***], Chiba N.[**], and Sutoh T.[***]

Department of Quantum Science and Energy Engineering, Tohoku University
Cyclotron and Radioisotope Center, Tohoku University[*]
Laboratory of Plant and Environmental Research, Faculty of Agriculture, Tohoku University[**]
The Archaeological Research Center on the Campus of Tohoku University[***]

Introduction

In the usual PIXE analysis, the most of biological and archaeological samples are destroyed and analyzed, since the samples are in place in the vacuum chamber. But this situation can be improved in in-air PIXE analysis[1-5]. Recently, we developed a submilli-PIXE probe at a Dynamitron laboratory in Tohoku University, which can measure spatial distribution of elements in the region of several cm^2 with a resolution of submilli-meters[1]. We call this system a submilli-PIXE camera, because this probe provides us images of elements on a surface of sample. The name of camera may be easily understandable for people. An in-air submilli-PIXE camera where samples are analyzed in air enables to analyze even wet samples[5,6]. Therefore, the in-air submilli-PIXE camera will be a powerful tool in the analysis of biological samples *in vivo*. The most of biological and archaeological samples are easily damaged with beam irradiation[2,3]. In their analyses, it is very useful to study non-deteriorated samples. Here, we present the examples of non deteriorated samples with the in-air submilli-PIXE camera.

In-Air Submilli-PIXE Camera

The submilli-beams are scanned vertically and horizontally on the surface of a sample[6]. To scan the beams in a wide area with a high-speed, an air-core coil and a laminate core magnet are used in the vertical and horizontal scanning axes, respectively. The maximum scanning area could be obtained to be 3×3 cm^2. A beam exit assembly which has five windows for beam exit and X-ray detection is settled at the end of the submilli-beam line. Samples were put at the downstream side of the exit window (Kapton foil, 12.5 μm thick). X-rays were measured by a Si(Li) detector at the direction of 135 degrees with respect to the beam axis and were absorbed with Kapton foils of detection window (7.5 μm thick) and exit window, air path of 5 cm and a Maylar filter of 1 μm thickness.

In order to obtain elemental distribution images, the X-ray energy and the beam position are simultaneously measured, because the beams are always scanning in our present system[1]. High-speed scanning reduces irradiation damage for sample. Moreover, the sample can be cooled with gas jet.

Samples

Since elemental distribution images will reflect the physiological activity of plant cells, the in-air submilli-PIXE camera might offer useful informations in determining pathological mechanism of plant. The in-air submilli-PIXE camera was used to examine leaves of Notohikari which is a variety of rice plants. This rice plant was cultivated in a laboratory, and had leaves lesioned by an unknown illness. The leaf sample was fixed on a Maylar plate of 500 m thick and was settled at the beam exit assembly. An end of the leaf sample was soaked in water during the beam irradiation.

The bowls painted with lacquer resin (Japan bowls) were excavated from the Edo-period stratum at Kawauchi campus of Tohoku University. The japan bowls were kept in water to preserve the lacquer resin. These articles should be analyzed under wet condition. Elemental images of decoration on japan bowls are useful for elucidation of classical techniques of decorative lacquer-working.

The Japanese vessels (Shigaraki ware) were excavated from the stratum mentioned above. Shigaraki ware is a famous Japanese glazed ceramics. Decoration on the surface of glazed ceramics is called overglaze enamels. Original color of the overglaze enamels might fade during the burial. By analyzing the elemental distribution of overglaze enamels, original picture may be reproduced. Determination of elemental composition of the pigments enables us to investigate classical decoration technique[2,3].

The wooden tablets on which some characters were written in a vermilion and black inks were excavated at Katahira Campus of Tohoku University. The wooden tablets were used by soldiers in the Meiji period. Interpretation of faded characters written in a black ink is possible by means of an infrared camera[2]. However, characters written by a vermilion ink are invisible even if an infrared camera is used. The submilli-PIXE camera can reveal elemental distributions of faded characters written in a vermilion ink.

Results and Discussion

Deterioration of rice leaves

Elemental distribution images of the intact and lesion parts of rice leaves were taken with the size of 12 mm×12 mm. The scanning speed was 18 sec/scan. The beam currents and the irradiation dose were about 500 pA and 6.5 nC/mm^2, respectively. The traces of beam irradiation were not observed by a microscope. Intactness of leaf cells was checked by that of chlorophyll. Intensity of chlorophyll fluorescence excited by light with 450 nm wavelength corresponds to the degree of intactness. Figure 1 shows the image of

chlorophyll fluorescence. A decrease in the intensity of fluorescence was not seriously observed in the irradiation area.

The elemental distribution images of K, Ca and Mn are shown in Fig. 2. This figure shows that Ca and Mn elements were accumulated in the lesion part where K elements decreased. In the plant, the mobility of Ca and Mn elements is generally lower than that of K elements[11]. Calcium elements tend to remain in the cell wall of old leaves, in contrast, K elements are intensively transported to newer tissues.

Deterioration of Archaeological samples

Analysis of the japan bowls were performed with the beam currents of 200-300 pA and the irradiation dose of 1.8 nC/mm^2. The surfaces of the bowls were not visually damaged. Figure 3 shows the elemental image of As on the japan bowl. A family crest painted on the surface of the bowl appeared in the image. It was estimated by the tone of color that the family crest was painted by pigment containing silver. However, the result in Fig.3 reveals that the family crest was drawn by using the pigment of Orpiment (As_2S_3) instead of gold.

The Shigaraki vessels were irradiated under the conditions of 0.8-8 nC/mm^2 with beam currents of 200 pA. The traces of beam irradiation were clearly observed even in the dose of 0.8 nC/mm^2. Then, the traces gradually faded and finally disappeared after 10 days from irradiation. Similar results were reported by Swan[5]. The unglazed part of the vessels were also irradiated, but was not discolored. This indicates that the glassy part of glaze is sensitive to discoloration. The radiation damage of glazed part could be faded by heating at a temperature higher than 100°C. It pointed out from these results that the color centers were formed in the glassy part by beam irradiation but faded away by thermal energy. Typical elemental distribution images are shown in Fig.4. Lead elements are distributed mainly in the blue part of the vessel, but Ca elements are inversely distributed. The blue part is overglaze enamel. Lead elements are considered to be mixed in pigment since this metal easily melts at a low temperature. Calcium elements are a component of glaze. X-rays from Ca elements were absorbed by overglaze enamel. Irradiation conditions are as follows; the beam currents were about 500pA, the scanning area was 11mm×11mm and the dose was 5 nC/mm^2.

The surfaces of wooden tablets were not visually damaged. The elemental image of Hg elements on the wooden tablet is shown in Fig.5. A character can be recognized in the elemental image of the tablet. The beam current was 200 pA and the irradiation area was 11mm×11mm. The accumulated dose was 3 nC/mm^2.

In conclusion, the rice leaves could be analyzed in vivo. The japan bowls and the wooden tablets were analyzed without discoloration. The Shigaraki vessels were discolored first, but their colors faded after 10 days from irradiation. In the in-air submilli-PIXE camera, these samples can be analyzed without serious deterioration.

References

1) Iwasaki S. Et al., International Journal of PIXE, **6**, 1&2, 117 (1996).
2) Iwasaki S. Et al., International Journal of PIXE, **5**, 2&3, 163 (1995).
3) Cahill T.A., Kusko B. and Schwab R.N., Nucl. Instr. and Meth., **181**, 205(1981).
4) Yokota S.et al., International Journal of PIXE, **7**, 1&2, 93 (1997).
5) Swann CP. and Fleming S.J., Nucl. Instr. and Meth., **B22**, 407(1987).
6) Matsuyama S. et al., International Journal of PIXE, **8**, 2&3, 209 (1998).
7) Matsuyama S. et al., International Journal of PIXE, **8**, 2&3, 203 (1998).
8) Lin E.K. et al., Nucl. Instr. and Meth., **B150**, 581(1999).
9) Uda M., Akiyoshi K. and Nakamura M., Nucl. Instr. and Meth., **B150**, 601(1999).
10) Lucarelli F. and Mando P.A., Nucl. Instr. and Meth., **B109/110**, 644 (1996).
11) Marschner H., Mineral, Nutrition of Higher Plants, Second Edition, (Academic Press, San Diego, (1995).
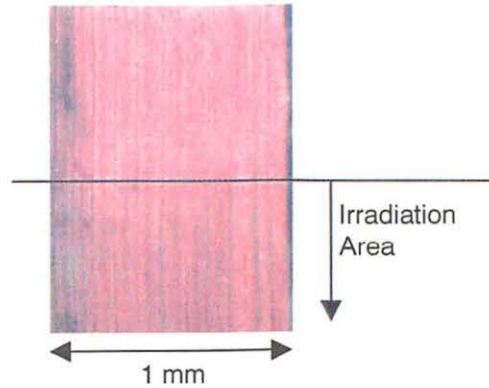
Fig. 1. Image of chlorophyll fruorescence of a rice leaf.
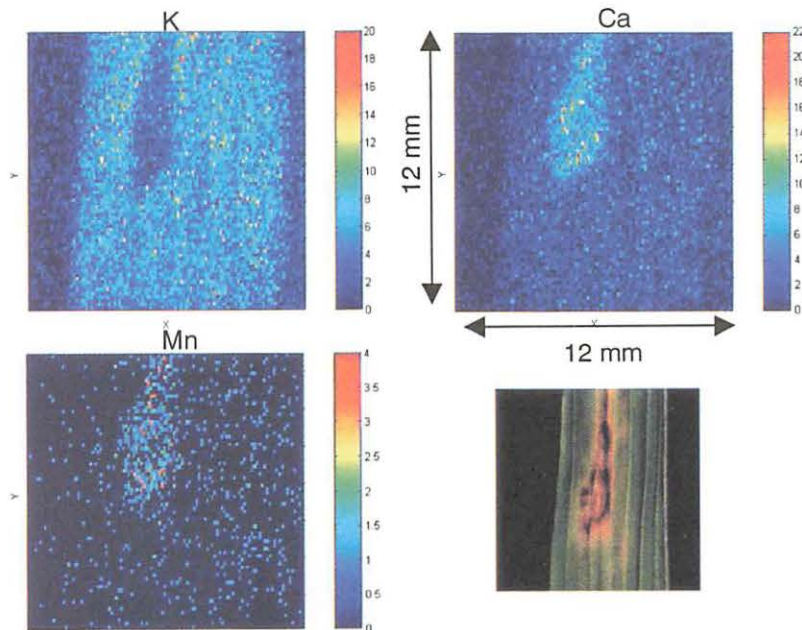
Fig. 2. Photograph and elemental distribution images of K, Ca and Mn in a rice leaf.

Fig. 3. Photograph and elemental distribution images of As on the surface of the japan bowl.
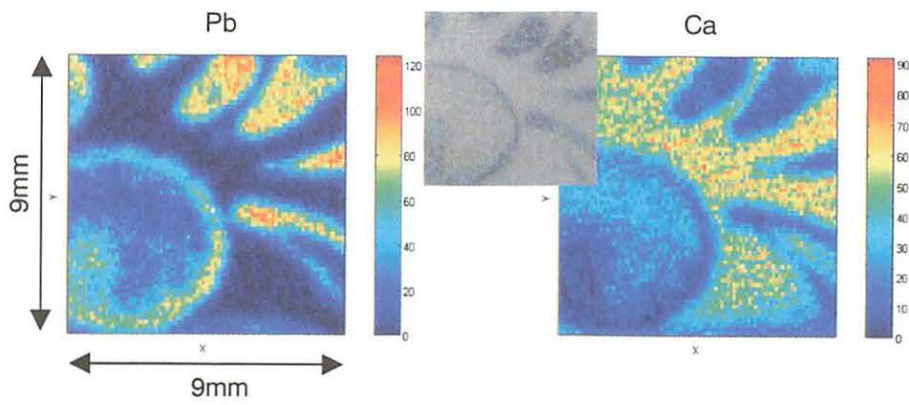
Fig. 4. Photograph and elemental distribution images of Pb and Ca on the surface of the Shigaraki vessel.
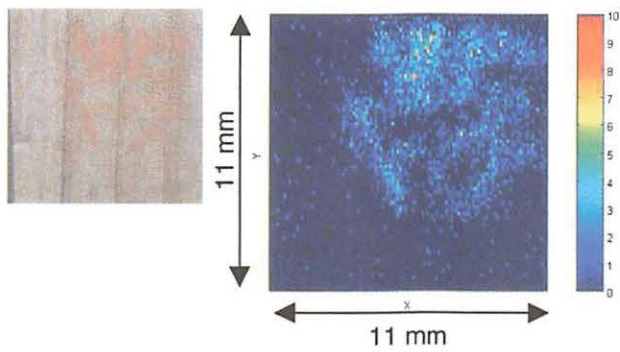
Fig. 5. Photograph and elemental distribution image of Hg in the wooden tablet.
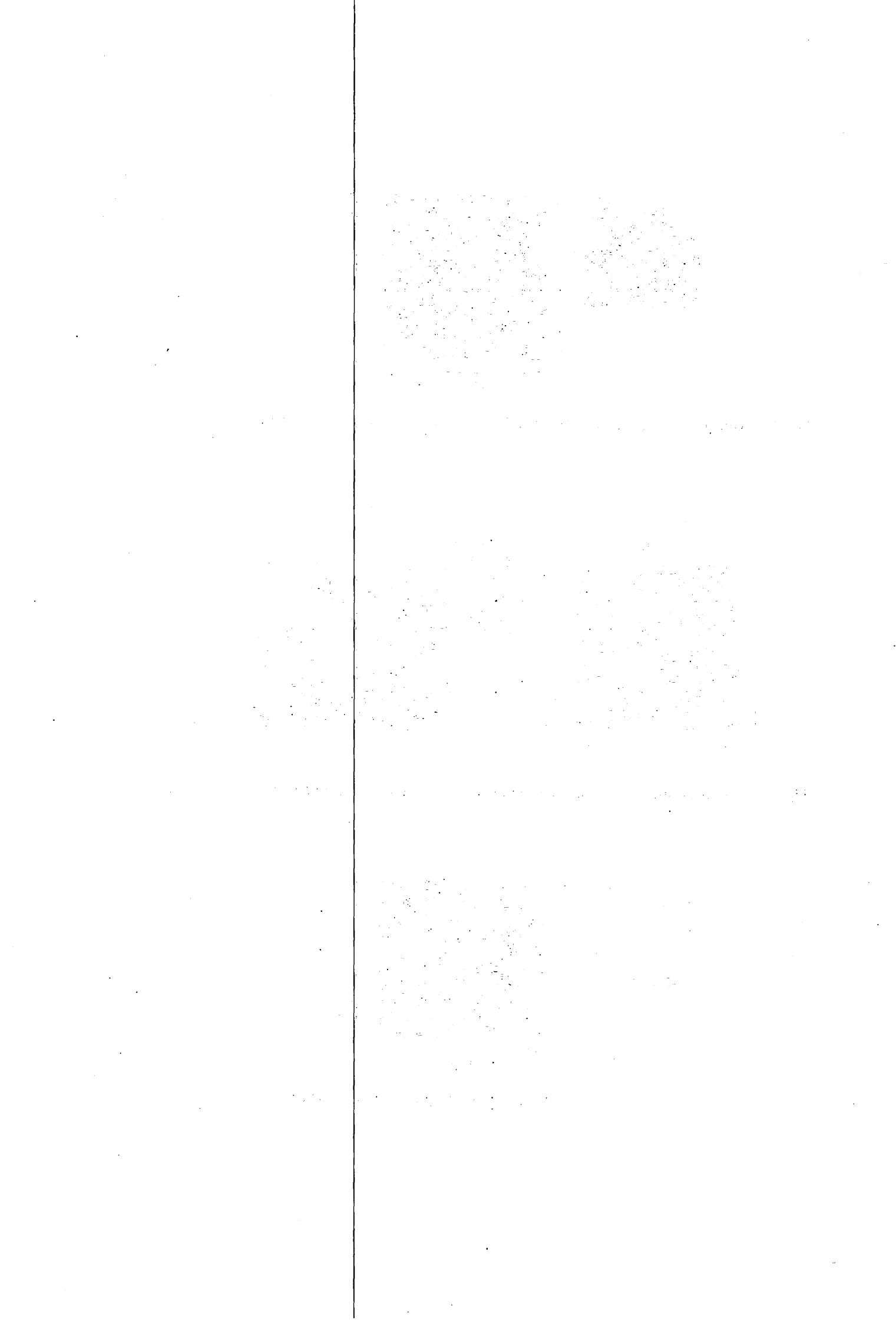
I. 14. Via-PIXE Analysis of Elemental Composition of Plant Root Exposed to Environmental Stress

Yokota S., Matsuyama S.*, Endoh H.*, Sugimoto A.*, Tokai Y.*, Yamazaki H.*, Ishii K.*, and Mae T.**

Laboratory of Plant and Environmental Research, Graduate School of Agricultural Science, Tohoku University
Dept. of Quantum Science and Energy Engineering, Graduate School of Engineering, Tohoku University*
Division of Life Science, Graduate School of Agricultural Science, Tohoku University**

Introduction

Via-PIXE (Vertical-beam in-air particle-induced X-ray emission) is one of non-destructive analytical techniques that can observe *in situ* elemental distribution of biological samples[1]. The elemental compositions of living organs, tissues and cells relate to those physiological statuses. We applied Via-PIXE method to analysis of short-term changes in elemental composition of plant root surface by aluminum stress, which is the major environmental stress factor that decreases crop productivity in acid soils[2]. In our preliminary study, the ratio of potassium to phosphorous (K/P ratio) of alfalfa (*Medicago sativa* L) root-tip was found to be fallen by short-term exposure of root to Al in a solution culture system[3,4]. We investigated here the relation between K/P ratio and Al stress using two plant species alfalfa and wheat (*Triticum aestivum* L.) which have different susceptibility to Al.

Materials and Methods

Plant material and Al-stressed solution culture system

Young seedlings with 5-mm root(s) of alfalfa (*Medicago sativa* L. natsuwakaba) and wheat (*Triticum aestivum* L. Aoba) were transferred to the Al-stressed (1 mM $CaCl_2$, 20 μM $AlCl_3$, pH 4.8) or control (1 mM $CaCl_2$, pH 4.8) rooting solution. Plants were allowed to grow for 6 h in those solutions at room temperature, followed by Via-PIXE analysis.

Via-PIXE analysis

The details of Via-PIXE system in FNL (Fast Neutron Laboratory, Tohoku University) was described in Iwasaki et al.[1]. Energy of accelerated protons was 3 MeV and beam flux was in the range of 200-600 pA. Special attentions for living plant materials were

paid as described in Yokota et al.[4]. Briefly, samples were placed on a ashless-type filter paper (Advantec No. 6, Advantec Toyo, Tokyo) which was moistened with distilled water in order to avoid living samples from drying. According to this method, roots of alfalfa and wheat were kept alive within a measurement. The net X-ray counts corresponding to P and K were estimated using SAPIX program developed by Sera et al.[5].

Results and discussion

Inhibition of root elongation by Al commonly appears within minutes or hours after exposure of root to $Al^{6,7)}$. Despite there have been many studies on Al phytotoxicity, its mechanism is still unclear. As one of indexes of physiological status of living cells change in elemental composition is supposed to give information of effects of Al on cells. Then we tried to analyze *in situ* elemental composition of root surface cells treated with Al by Via-PIXE method.

Figure 1 shows Via-PIXE spectra of tip and basal region of alfalfa and wheat root treated with or without Al. Most apparent change by Al was found in relative count of P and K. In alfalfa and wheat, K/P ratios of root-tip or basal region without Al were almost equivalent (Fig. 2). The K/P ratios in Al-treated alfalfa root-tip and basal region were less than the others. Adversely, increase of K/P ratio was observed in the case of Al-treated wheat root (Fig. 2).

Potassium is one of macronutrients for plants and has important roles in growth and development of cells as a regulator of turgor pressure and enzymic activities. Phosphorus concerns almost all of biological processes in cells. The change in K/P ratio suggests the relation between Al and cellular homeostasis, however, we have to know absolute amount of those elements that is expected to show dynamic movement of elements within a root.

In this study, the advantages of Via-PIXE method were reevaluated. Based on data and techniques obtained here, the next approach will be trial of *in situ* mapping of root surface by in-air scanning PIXE method.

References

1) Iwasaki S. et al., International J. PIXE 5 (1995) 163.
2) Kochian L. V., Annu. Rev. Plant Physol. Plant Mol. Biol. 46 (1995) 237.
3) Yokota S. et al., International J. PIXE 4 (1994) 263.
4) Yokota S. et al., International J. PIXE 7 (1997) 93.
5) Sera K. et al., International J. PIXE 2 (1992) 325.
6) Llugany M. et al., Physiol. Plant. 93 (1995) 265.
7) Yokota S. and Ojima K., Plant Soil 171 (1994) 163.
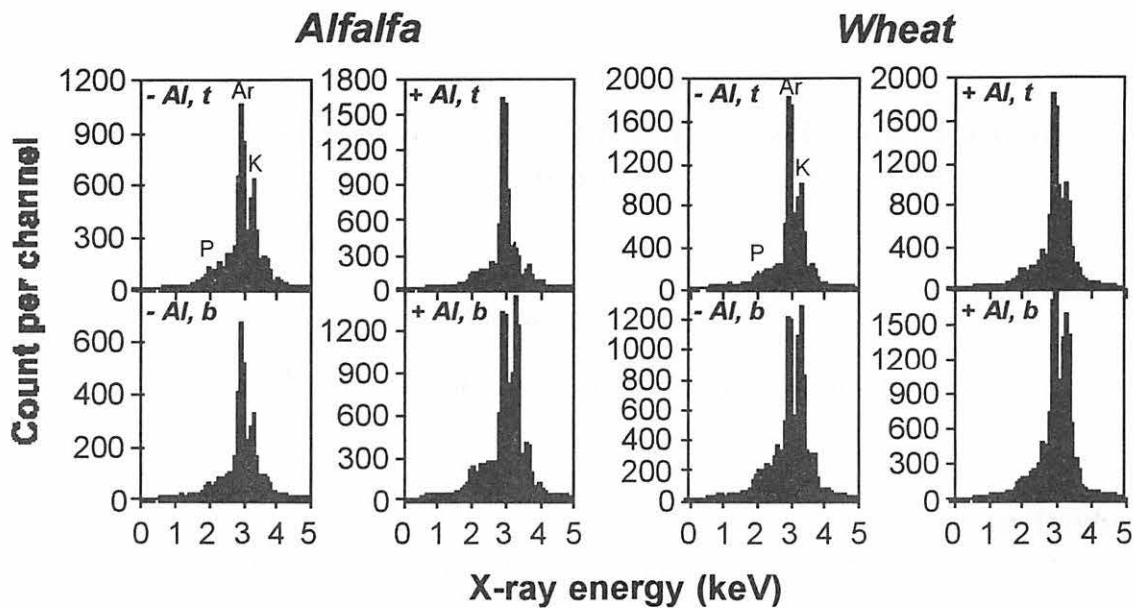
Fig. 1. Via-PIXE spectra of alfalfa root (left panel) and wheat root (right panel) grown with Al (+Al) or without Al (- Al). Both tip region (t) and basal region (b) were analyzed. Peaks corresponding to phosporus, argon and potassium were indicated as P, Ar and K, respectively. Each spectrum was obtained within 6 min after exposure of root to the 3-MeV proton beam.
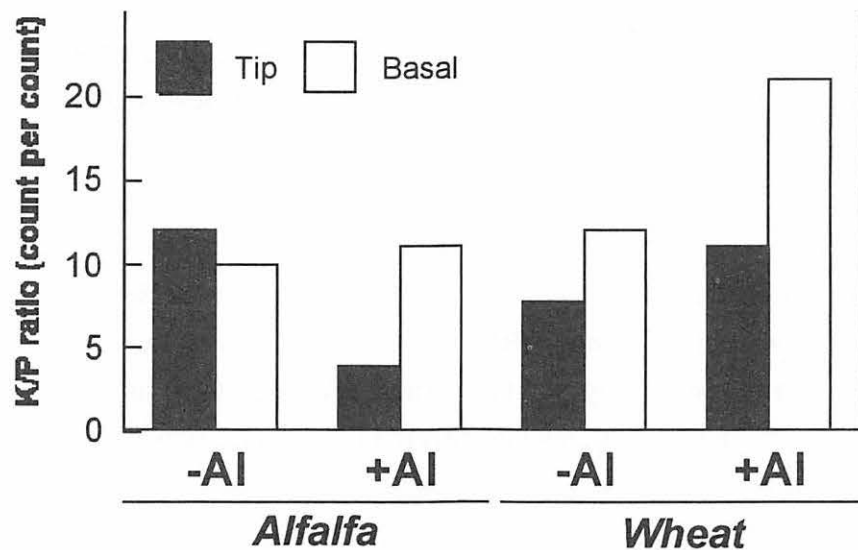
Fig. 2. Effect of Al on the K/P ratio of tip (closed column) or basal (open column) region of alfalfa and wheat root. The K/P ratios (count per count) were calculated using the Via-PIXE data in Fig. 1. For details, see "Materials and methods".

62

I. 15. Beam Properties of the CYRIC AVF Cyclotron in the Central Region

Misu T. and Shinozuka T.

Cyclotron and Radioisotope Center, Tohoku University

Introduction

Cyclotron and Radioisotope Center (CYRIC) at Tohoku University has recently completed the construction for a four-sector variable energy AVF machine with an extraction radius of 923mm. In order to prepare for upcoming operations aimed for fundamental nuclear physics and medical use, the development of the simulation codes tracking ions in the cyclotron is highly desired.

The optical simulations for the central region of the newly designed AVF cyclotron at CYRIC require a large number of physical theories and calculation codes in order to achieve reliable demonstrations of the beam properties. At CYRIC the simulation code, which was originally developed at the Institute of Physical and Chemical Research (IPCR)[1] as part of the separated-sector-cyclotron project and later modified for the AVF cyclotron at Japan Atomic Energy Research Institute (JAERI)[2], has been adapted to serve as a numerical integration program for tracking particles with an inclusion of space charge effects.

In this report, the brief description and present status regarding the development of the simulation codes adapted for the CYRIC 930 cyclotron are presented. Since space-charge forces are strongest at low energy and the vertical focusing at the machine center is rather weak, numerical estimates of space-charge effects in the central region of the cyclotron is of great importance. However, the three-dimensional space-charge calculation code has not been fully incorporated, and thus the space-charge related subjects will be discussed elsewhere.

Magnetic and Electric Field Maps

Due to a limited amount of the measured magnetic fields, the search for the suitable parameter sets which reproduce the actual magnetic fields for a wide range of excitations remains as a hard task. As a momentary treatment, we have compared the magnetic field maps measured at both JAERI and CYRIC as shown in Fig. 1, and deduced a rough statistical relation for two excitation points only. At both excitations the magnetic fields at the same radial positions measured at both facilities can be well fitted with a straight line as

illustrated in Fig. 2. From the linear-regression analysis, one obtains two sets of parameters (a, b) in a straight-line model, i. e., $y(x)=ax+b$, where x and y represent the average fields produced by a main coil at JAERI and CYRIC, respectively. By imposing $a \to 1$ for large current values and $b \to 0$ for diminishing currents, we have temporarily estimated the excitation dependence of two parameters (a, b) as $a(I) \cong \coth(0.257I^{4/9})$ and $b(I) \cong 76.4\tanh(0.0062I)$. Since we are allowed to use only two sets of the measured fields, the above approximations are not free from large uncertainties and further modifications are necessary in the future.

With the above field-conversion procedures appropriate for the CYRIC machine, the field in the cylindrical coordinate system (r, θ, z) must be expanded in z to obtain the values off the median plane as

$$B_z(r,\theta,z) = B_z(r,\theta) + z\frac{\partial B_z}{\partial z} - \frac{z^2}{2}B' \ , \tag{1-a}$$

$$B_r(r,\theta,z) = B_r(r,\theta) + z\frac{\partial B_z}{\partial r} + \frac{z^2}{2}\frac{\partial^2 B_z}{\partial r \partial z} \ , \tag{1-b}$$

$$B_\theta(r,\theta,z) = B_\theta(r,\theta) + \frac{z}{r}\frac{\partial B_z}{\partial \theta} + \frac{z^2}{2r}\frac{\partial^2 B_z}{\partial \theta \partial z} \ , \tag{1-c}$$

$$B' = \frac{1}{r}\frac{\partial B_z}{\partial \theta} + \frac{\partial^2 B_z}{\partial r^2} + \frac{1}{r^2}\frac{\partial^2 B_z}{\partial \theta^2} \ , \tag{1-d}$$

where $B_i(r,\theta)$ for $i=r$, θ, z are the field components measured in the median plane of $z=0$. Only fist terms in Eqs. 1a-c are taken into account in the present simulation code.

On the other hand, the electric field produced by the acceleration electrodes consisting of 86-degree dees in the central region of the machine cannot be analytically obtained due to their complex geometry together with the presence of the inflector and the puller. For numerical estimates of the three-dimensional electric field, one often uses the code known as RELAX3D[3] developed at the TRIUMF, which solves the three-dimensional second-order elliptic partial differential equation with the relaxation method. An example of electric equipotential map in the central-region geometry evaluated with RELAX3D is displayed in Fig. 3. Here, the mesh points were taken as $101 \times 101 \times 45$ with a step size of 1.0 mm for all direction. The present code adopts the form of the electric field as the Gaussian function with standard deviations of $\sigma = 0.4W + 0.2H^{4}$, where W and H are the gap width and the aperture of the dee, respectively. We are in the process of simplifying the electric field map calculated with RELAX3D to optimize the computational performance.

Orbit Simulations

The Lorentz equation of motion for a particle of charge q and mass m,

$$\vec{F} = q\left(\vec{E} + \vec{v} \times \vec{B}\right), \tag{2}$$

can be decomposed into

$$\dot{r} = \frac{p_r}{m}, \quad \dot{\theta} = \frac{p_\theta}{mr}, \quad \dot{z} = \frac{p_z}{m}, \tag{3-a}$$

$$\dot{p}_r = \frac{1}{m}\left(\frac{p_\theta^2}{r} - qp_\theta B_z + qp_z B_\theta\right) + qE_r, \tag{3-b}$$

$$\dot{p}_\theta = \frac{1}{m}\left(-\frac{p_r p_\theta}{r} - qp_z B_r + qp_r B_z\right) + qE_\theta, \tag{3-c}$$

$$\dot{p}_z = \frac{1}{m}\left(-qp_r B_\theta + qp_\theta B_r\right) + qE_z, \tag{3-d}$$

$$\dot{m} = \frac{q}{mc^2}\left(p_r E_r + p_\theta E_\theta + p_z E_z\right). \tag{3-e}$$

Here, p_i, B_i and E_i for $i=r$, θ, z are three cylindrical components of the momentum, the magnetic and electric fields, respectively. With time as the independent variable, a Runge-Kutta integration is employed to calculate the particle trajectory in a magnetic field map obtained from the procedures described above. The present simulation code is also modified to produce the postscript-formatted files which display the central-region geometry and the first few orbits plot, as illustrated in Fig. 4. Note that a most of this section is a brief repeat of information described in the programming manual of orbit calculations by A. Goto[1], and more details can be found therein.

Concluding Remark

A code development is currently underway to incorporate the three-dimensional space-charge estimates into the main orbit-simulation codes. Due to limited computer resources, the three-dimensional multiparticle approach together with an interpolation technique of the magnetic and electric fields makes us rely upon some simplifying assumptions. Further optimization of the program is also possible if the spatial and excitation dependence of the measured magnetic field can be well fitted to simple analytic forms instead of an interpolation procedure.

The need for platform-independent interactive programs to be developed and delivered across networks, may also be inevitable for a practical reason, and one possible choice is to convert a Fortran 77 source file into an equivalent Java source file.

References

1) Goto A., Sci. Papers I. P. C. R. **74** (1980) 124.
2) Fukuda M., Notes on Program for Calculating Beam Orbits in Cyclotron (1999).
3) Kost C. J. and Jones F. W., RELAX3D-TRIUMF internal report TRI-CD-88-01 (1992).
4) Hazewindus N. et al., Nucl. Instr. and Meth. **118** (1974) 125.
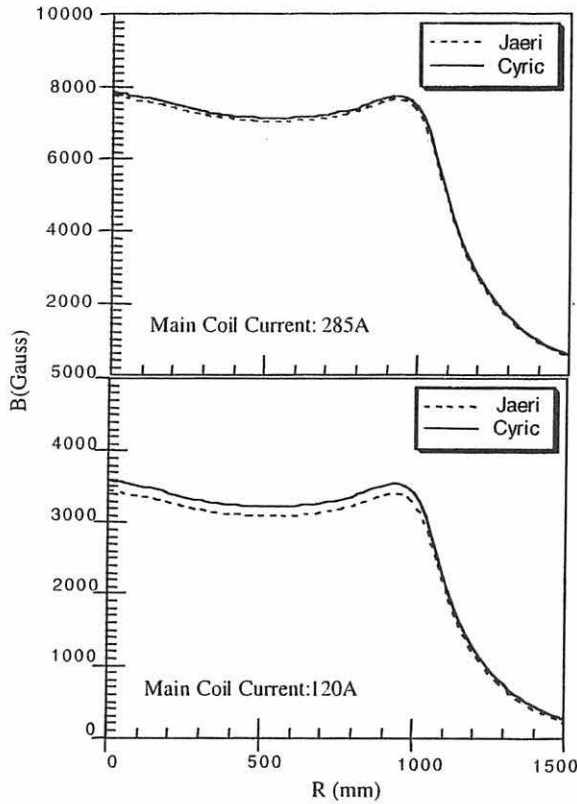
Fig. 1. Average magnetic field produced by a main coil measured at JAERI and CYRIC are compared as a function of radial distance from the machine center.
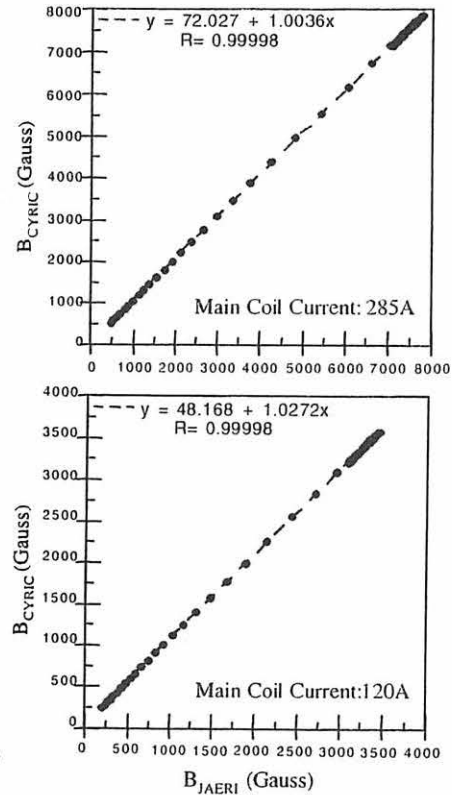
Fig. 2. Average main-coil magnetic field strengths measured at CYRIC are plotted as a function of those measured at JAERI for the same radial points.
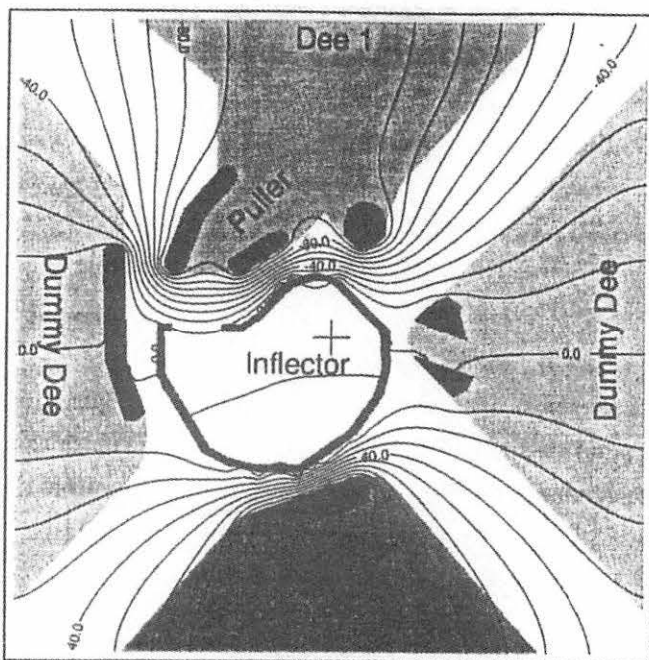
Fig. 3. Example of equipotential contours in the median plane of the central region calculated with RELAX3D codes.
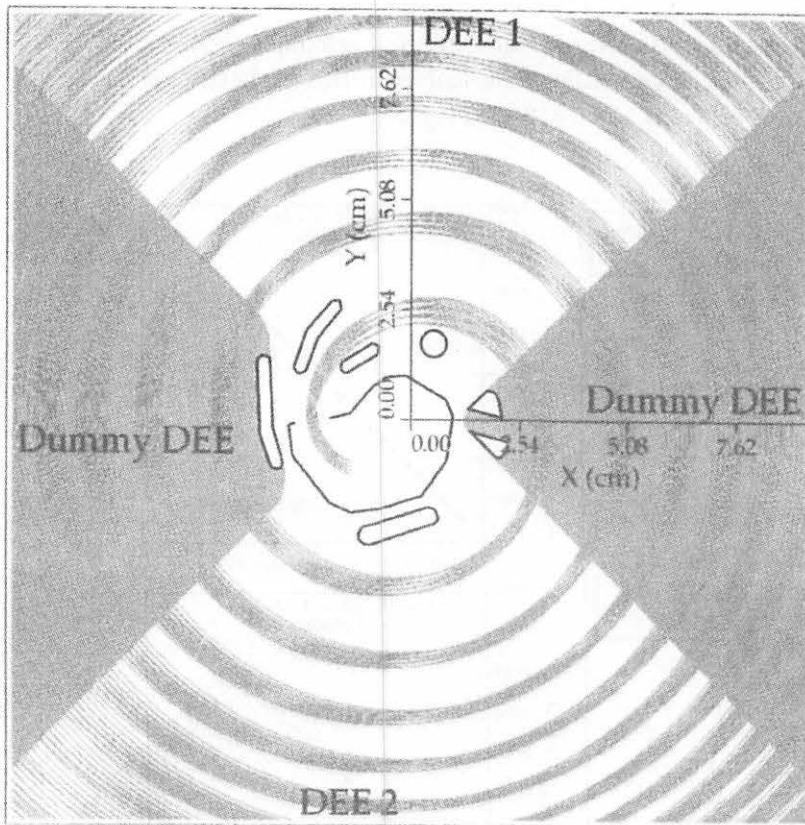
Beam Status
taken from parmtest.dat

Cyclotron Facility:		CYRIC
Charge State	:	1
Mass Number	:	1
Atomic Number	:	1
Ion Energy (MeV)	:	70.00
Dee 1 Max. Vol.(V):		49.05
Dee 2 Max. Vol.(V):		47.50
RF Frequency (MHz):		18.92
Ion Source Vol.(V):		12.47
Harmonic Number	:	1
Initial Phase	:	102.50

Coil Current (A)
taken from   /opt2/users/misu/orbit. source/coiltest.dat

Main Coil	:	548.67
Trim Coil #1	:	325.55
Trim Coil #2	:	-431.00
Trim Coil #3	:	-201.00
Trim Coil #4	:	-139.00
Trim Coil #5	:	-134.00
Trim Coil #6	:	-61.00
Trim Coil #7	:	-93.00
Trim Coil #8	:	-24.00
Trim Coil #9	:	-70.00
Trim Coil #10	:	391.88
Trim Coil #11	:	-517.00
Trim Coil #12	:	32.79
IH13 Coil	:	-30.98
IH24 Coil	:	19.06
EH13 Coil	:	16.58
EH24 Coil	:	43.91

Fig. 4. Actual postscript-formatted output of simulated beam trajectories in the central region of the CYRIC AVF cyclotron for H+ 70MeV in the first harmonic mode. All beam parameters used for the simulation are indicated on the right side.

I. 16.   Optical Properties of the Spiral Inflector with Space Charge Effect

Misu T.

Cyclotron and Radioisotope Center, Tohoku University

Introduction

In our newly constructed AVF cyclotron, the beam of ions entering vertically along the center axis of the magnet from the bottom of the machine is deflected through an angle of 90 degrees by a novel device known as a spiral inflector.   A spiral inflector operates to turn the movement of particles from the axial into the radial-azimuthal direction.   Although numerous calculations related to the inflector beam optics have been reported to date, the recent improvement in the production of high intensity beams calls for more detailed analysis of a beam trajectory through this device. With increasing beam intensity, one would expect that the space-charge force is no longer negligible and starts to play a crucial role.

In this report, the possible effects of space charge on the optical properties of the inflector are investigated, and it was found that the initial emittance conditions have considerable effects on the transmission in the spiral inflector, while the space-charge effects remain rather weak for the beam intensity exceeding a few mA.

Computational Approach

Particle Trajectory in the Optical Coordinates

Since a spiral inflector essentially consists of a twisted cylindrical capacitor, one usually assumes that the electrical field vector $\vec{E}$ along the central trajectory is always perpendicular to the velocity vector $\vec{V}$ of a particle. This assumption allows us to define the optical coordinate system (h,v,u) in terms of the fixed cartesian coordinates (x,y,z), see also Fig. 1, as

$$h = \frac{V_y i - V_x j}{\sqrt{V_x^2 + V_y^2}}, \quad v = \frac{V_x i + V_y j + V_z k}{\sqrt{V_x^2 + V_y^2 + V_z^2}}, \quad u = h \times v, \tag{1}$$

where V_x, V_y, V_z are the velocity components of the central trajectory ion.

Let the position vectors of the paraxial and central trajectory particles of charge q and mass m at time t be denoted by $\vec{r}(t)$ and $\vec{r}_c(t)$, respectively. Both position vectors must follow the Lorentz equation of motion,

$$m\Delta\ddot{r} = q\{\vec{E}(\vec{r}) - \vec{E}(\vec{r}_c) + \Delta\dot{\vec{r}} \times \vec{B}(\vec{r})\}, \quad \Delta\vec{r} = \vec{r} - \vec{r}_c, \qquad (2)$$

where $\vec{B}(\vec{r})$ is the magnetic field, and $\vec{E}(\vec{r})$ corresponds to the electric field with/without space-charge field. The above Lorentz equation of motion can be expressed in terms of the optical coordinates[1] and solved by means of a standard fourth and/or fifth order Runge-Kutta method[2].

In the following analysis, I shall also define the beam divergences P_u, P_h and P_v at time t as

$$P_u(t) = \dot{\vec{r}}(t) \cdot u / V_0 \,, P_h(t) = \dot{\vec{r}}(t) \cdot h / V_0 \,, \quad P_v(t) = \{\dot{\vec{r}}(t) - V_0 v\} u / V_0, \qquad (3)$$

where V_0 is the speed of the central trajectory ion.

Treatment of Space Charge Effect

For the analysis of the space-charge field, several computational approaches[3-5] are available and one can classify them in three categories; Particle-to-Particle Interaction (PPI) procedure often takes the linear space-charge potential inside spherical clouds and the interaction among spherical clouds within a bunch obeys Coulomb's law; Particle-In-Cell (PIC) method computes the space-charge field at mesh points superimposed on a bunch; a bunched beam can be represented by a spherical or ellipsoidal charge distribution. In the present analysis, I have employed the following two models for a mere comparison.

1) Segmented Long-Rod Approximation

To develop some feeling for the effect of space charge, let us first suppose that the ion beam can be viewed as an infinitely-long uniformly-charged rod for simplicity. The self-induced transverse electric and magnetic fields at distance r due to the beam with radius r_b and current I are given by

$$E_r = \left(\frac{1}{4\pi\varepsilon_0}\right) 2\lambda \frac{r}{r_b^2}, \quad B_\varphi = \left(\frac{c\mu_0}{\sqrt{4\pi}}\right) 2\lambda\beta \frac{r}{r_b^2} \quad \text{for } r < r_b, \qquad (3\text{-a})$$

$$E_r = \left(\frac{1}{4\pi\varepsilon_0}\right) 2\lambda \frac{1}{r}, \quad B_\varphi = \left(\frac{c\mu_0}{\sqrt{4\pi}}\right) 2\lambda\beta \frac{1}{r} \quad \text{for } r \geq r_b, \qquad (3\text{-b})$$

where ε_0 is the electric permittivity; μ_0 is the magnetic permeability; $\lambda = I/\beta c$ with $\beta = v/c$, v and c being the speed of ions and light, respectively. Consequently, the resultant transverse space-charge force can be expressed as

$$F_r = q(1 - \beta^2)E_r; \qquad (4)$$

The above equations imply the optical properties of the inflector would be affected for a low energy and/or high current beam.

Although the above simplification is often used in many other calculations, the results become rather unphysical at higher beam currents, and one would modify it by dividing a whole beam rod into a large number of segmented rods. Space-charge force $\vec{F}_i^{(sc)}$ acting on the ith segmented rod at position $\vec{r}_i$ due to surrounding beam rods can be expressed as

$$\vec{F}_i^{(sc)} = \sum_{\substack{k=1 \\ k \neq i}}^{N} \vec{f}_{ik}(\vec{r}_{ik}) = \left(\frac{1}{4\pi\varepsilon_0}\right) 2q \frac{\lambda}{N}(1-\beta^2) \sum_{\substack{k=1 \\ k \neq i}}^{N} \chi(\vec{r}_i - \vec{r}_k)$$ (5)

with

$$\chi(\vec{r}_i - \vec{r}_k) = \begin{cases} (\vec{r}_i - \vec{r}_k)/|\vec{r}_i - \vec{r}_k|^2, & \text{for } r \geq \delta r_b \\ (\vec{r}_i - \vec{r}_k)/|\vec{r}_i - \vec{r}_k|\delta r_b^2, & \text{for } r < \delta r_b \end{cases}$$

where δr_b is the radius of each segmented rod.

2) Three-dimensional PPI Method

A space-charge calculation for a bunched beam can be carried out by extending the above segmented long-rod approximation, and a beam bunch is modeled to be a collection of macroparticles as done in a standard PPI procedure. In addition, the effects due to fringing electric fields which extend beyond the geometric limits of the inflector electrodes were estimated. According to Ref. 6, the fringe field is assumed to lie solely in the u direction and its magnitude E at distance s from the inflector entrance (or exit) is given by

$$E=(E_0/2)[1-\tanh((s+\delta)\alpha)], \quad \delta=d(0.37-e^{-2.5}), \quad \alpha=1.35,$$ (6)

where d is the spacing of the electrodes. In the present analysis, the fringe field was taken into account only for the three-dimensional PPI method.

Results and Discussion

Beam Divergence due to Space-Charge Force

To investigate the general characteristics of the beam dynamics due to space charge in the inflector, three physical quantities were defined and compared under the segmented long-rod approximation: the beam divergence ratio η defined by the ratio of the beam radii at the inflector exit to the one at the entrance, the maximum and average space-charge fields divided by the inflector electric field, denoted by e_{max} and e_{avg}, respectively. The present results are obtained only for the case of the first harmonic mode and the half sizes of the initial beam cross section being 3.0mm vertically by 3.0mm horizontally.

As illustrated in Fig. 2, all three quantities η, e_{max} and e_{avg} quickly decrease for increasing initial spatial deviations denoted by σ_u and σ_h (see Fig. 2a). In particular, the effect is most significant for the spatial deviations $\sigma_{uh}<2.0$mm. For fixed spatial deviations $\sigma_{uh}=3.0$mm, the maximum space-charge effect drastically decreases for $\sigma_{Puhv} <0.1$, while it remains roughly constant for larger values of the beam divergence deviations (see Fig. 2b), implying that the space-charge force appears to affect a total beam radius for the estimated initial emittance $\varepsilon_i = \sigma_i \tan^{-1}(\sigma_{Pi}) <300$mm·mrad (i=u,h,v).

In Figs. 3 and 4, a proton beam u-h cross-section at the input and output of the inflector are illustrated for different initial beam conditions. It is interesting to note that the beam distributions at the inflector exit for a normally distributed initial beam are more spatially extended than those for an uniformly distributed one, while the values of η, e_{max} and e_{avg} are less enhanced for a normally distributed initial beam, as demonstrated in Fig. 3. When the initial u-h cross-sections are highly elongated along h direction, more preferable beam conditions can be achieved at the exit, see Fig. 4.

Beam Transmission of A Bunched Beam

For a beam bunch initially located at the inflector entrance, several test runs have been performed to evaluate the differences arising from the change in the initial beam conditions. It must be noted that the numerical results due to the presence of the fringing field are omitted in the present report.

Figure 5 shows the beam transmission rate for a 1 mA proton beam bunch at 10keV as a function of instantaneous angle b defined by $b=v_0t/A$, where v_0, t, and A are ion velocity, time, and the electrical radius of curvature, respectively. When the initial divergence deviations are introduced, only half of the injected beam can pass through the inflector. The effects due to the self-induced space-charge field only result in negligible beam losses, whereas an inclusion of emittance strongly affects the beam transmission rate, indicating the importance of the initial emittance conditions rather than the space-charge force in the actual machine operations. Furthermore, when a 10mA proton beam with $\sigma_{Pu}=\sigma_{Ph}=\sigma_{Pv}=0.0$ is injected instead, the beam transmission rate amounts to 89%, which is 10% less than the transmission of a 1mA beam. Similar conclusion can be made from Fig. 6, where the instantaneous-angle dependence of the emittance growth is shown to indicate the negligible contributions from the space-charge field.

Figures 7a and 7b display the time evolutions of the clouds of particles with and without the emittance spread, respectively. Figures demonstrate the considerable beam losses arising from the worsening of initial emittance conditions. A further analysis with an inclusion of the fringing field, which also predicts serious beam losses, will be presented elsewhere.

References

1) Root L. W., Diploma Thesis, University of British Columbia (unpublished, 1972)
2) Press W. H., et. al.,"Numerical Recipes in FORTRAN", Cambridge University Press (1986), Chap.16.
3) Koltenbah B. E. C. and Parazzoli, Nucl. Instr. and Meth. in Phys. Res. A429 (1999)281.
4) Adam S., Proc. 14th Int. Conf. on Cyclotrons and their Application, Cape Town, (1995)446.
5) Lapostolle P., et al., Nucl. Instr. and Meth. in Phys. Res. A379 (1996)21.
6) Milton B. F. and Pearson J. B., CASINO-TRIUMF internal report TRI-DN-89-19 (1989).
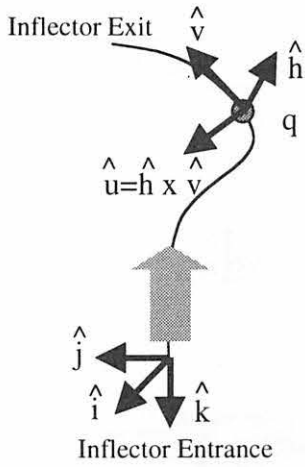
Fig. 1. Optical coordinate systems of the spiral inflector.
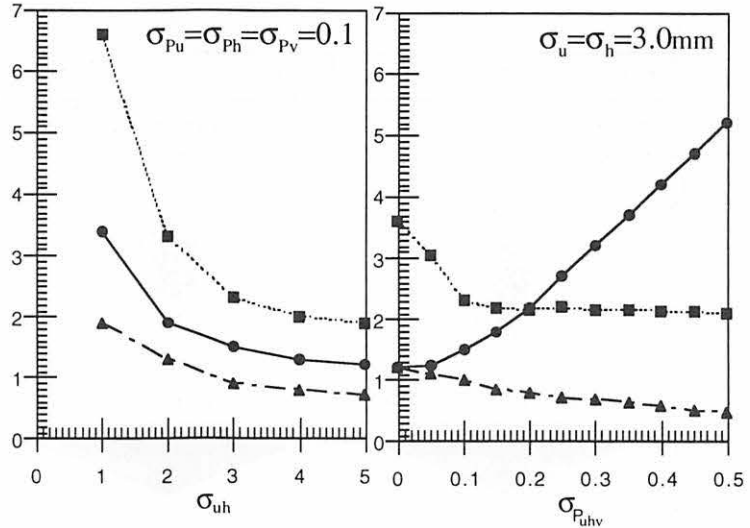
Fig. 2. Radial beam divergence (circles), maximum (squares) and average (triangles) space-charge effects for a 10mA proton beam at 10keV are shown as function of spatial (left) and divergence (right) deviates. Left: initial isotropic divergence deviates are set for 0.1. Right: initial spatial deviates in the u-h plane are taken as 3.0 mm.
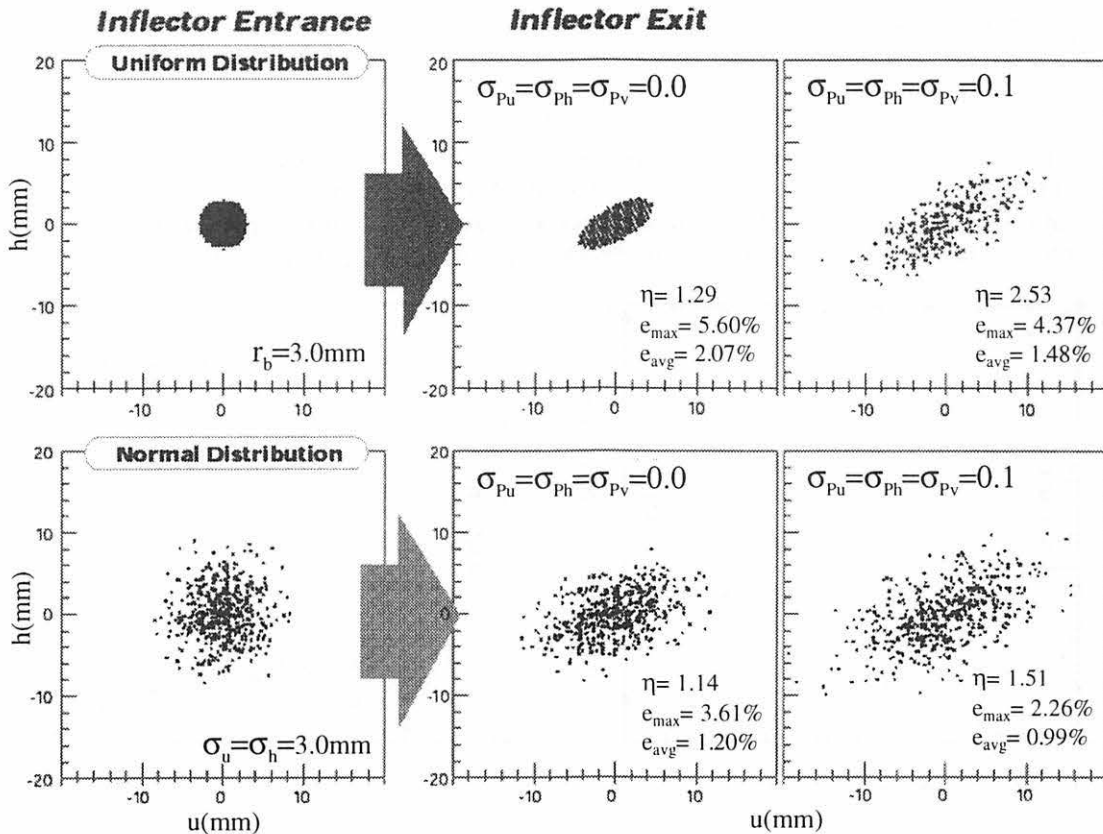
Fig. 3. Proton beam u-h cross-section plots at the entrance(left panels) and exit(center and right panels) of the inflector. Here, a 10mA proton beam at 10 keV is assumed for two types of initial charge distribution: uniform (top) and normal (bottom) distributions with uniform/normal spatial deviates of 3.0 mm, isotropic beam divergence of 0.0 (center) and 0.1 (right) at the entrance. As described in the text, the values denoted by η, e_{max} and e_{avg} correspond to the radial beam divergence, maximum and average space-charge effects, respectively.

(a)   (b)   (c)

$\eta= 1.28$, $e_{max}= 2.59\%$, $e_{avg}= 0.99\%$ $\eta= 1.51$, $e_{max}= 2.26\%$, $e_{avg}= 0.99\%$ $\eta= 1.59$, $e_{max}= 2.26\%$, $e_{avg}= 0.91\%$

$\sigma_r=3.0mm$, $\sigma_h/\sigma_u=2.0$ $\sigma_r=3.0mm$, $\sigma_h/\sigma_u=1.0$ $\sigma_r=3.0mm$, $\sigma_h/\sigma_u=0.5$

$\sigma_{Pu}=\sigma_{Ph}=\sigma_{Pv}=0.1$ $\sigma_{Pu}=\sigma_{Ph}=\sigma_{Pv}=0.1$ $\sigma_{Pu}=\sigma_{Ph}=\sigma_{Pv}=0.1$

r.m.s. emittance (u): 0.871   r.m.s. emittance (u): 1.232   r.m.s. emittance (u): 1.742

r.m.s. emittance (h): 1.961   r.m.s. emittance (h): 1.386   r.m.s. emittance (h): 0.980

r.m.s. emittance (u): 2.982   r.m.s. emittance (u): 3.330   r.m.s. emittance (u): 4.087

r.m.s. emittance (h): 2.785   r.m.s. emittance (h): 2.935   r.m.s. emittance (h): 3.351

h(mm)

u(mm)   note: r.m.s. emittance in mm · rad

Fig. 4. Proton u-h cross-section plots at the inflector entrance (upper panels) and exit (lower panels) for three different initial distributions: (a)σ_h/σ_u=2.0, (b)σ_h/σ_u=1.0, and (c)σ_h/σ_u=0.5. Here, a proton beam at 10keV with 10mA in the first harmonic mode is assumed, and its initial spatial and divergence deviates are taken as 3.0mm and 0.1, respectively. Descriptions of η, e_{max} and e_{avg} are given in the text.
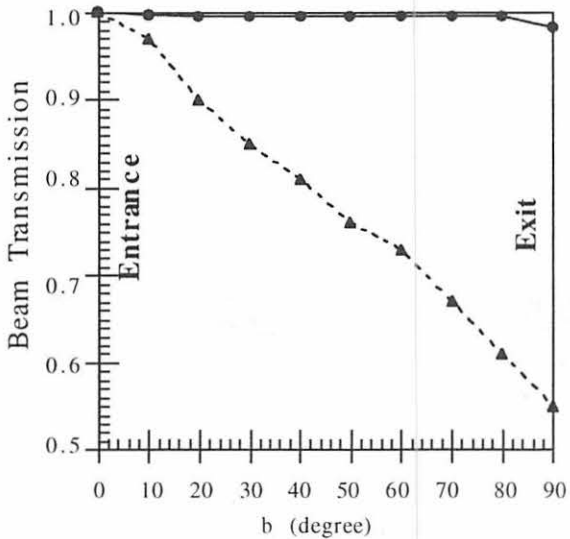
Fig. 5. Beam transmission rate as a function of instantaneous angle b. Filled circles and triangles correspond to a 1mA proton beam with $\sigma_{Pu}=\sigma_{Ph}=\sigma_{Pv}=0.0$ and $\sigma_{Pu}=\sigma_{Ph}=\sigma_{Pv}=01$, respectively.
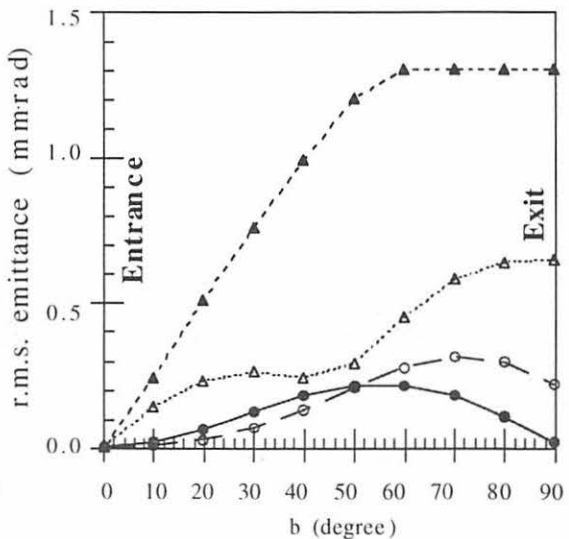
Fig. 6. Two sets of r.m.s. emittance for a 1mA proton beam with $\sigma_{Pu}=\sigma_{Ph}=\sigma_{Pv}=0.0$ (circles) and $\sigma_{Pu}=\sigma_{Ph}=\sigma_{Pv}=0.1$ (triangles) are plotted as a function of instantaneous angle b. Filled and open marks indicate the projected values in the u-u' and h-h' planes, respectively.

73

b= 0°

b= 0°

b=20°

b=20°

b=40°

b=40°

b=60°

b=60°

b=80°

b=80°

(a)

(b)
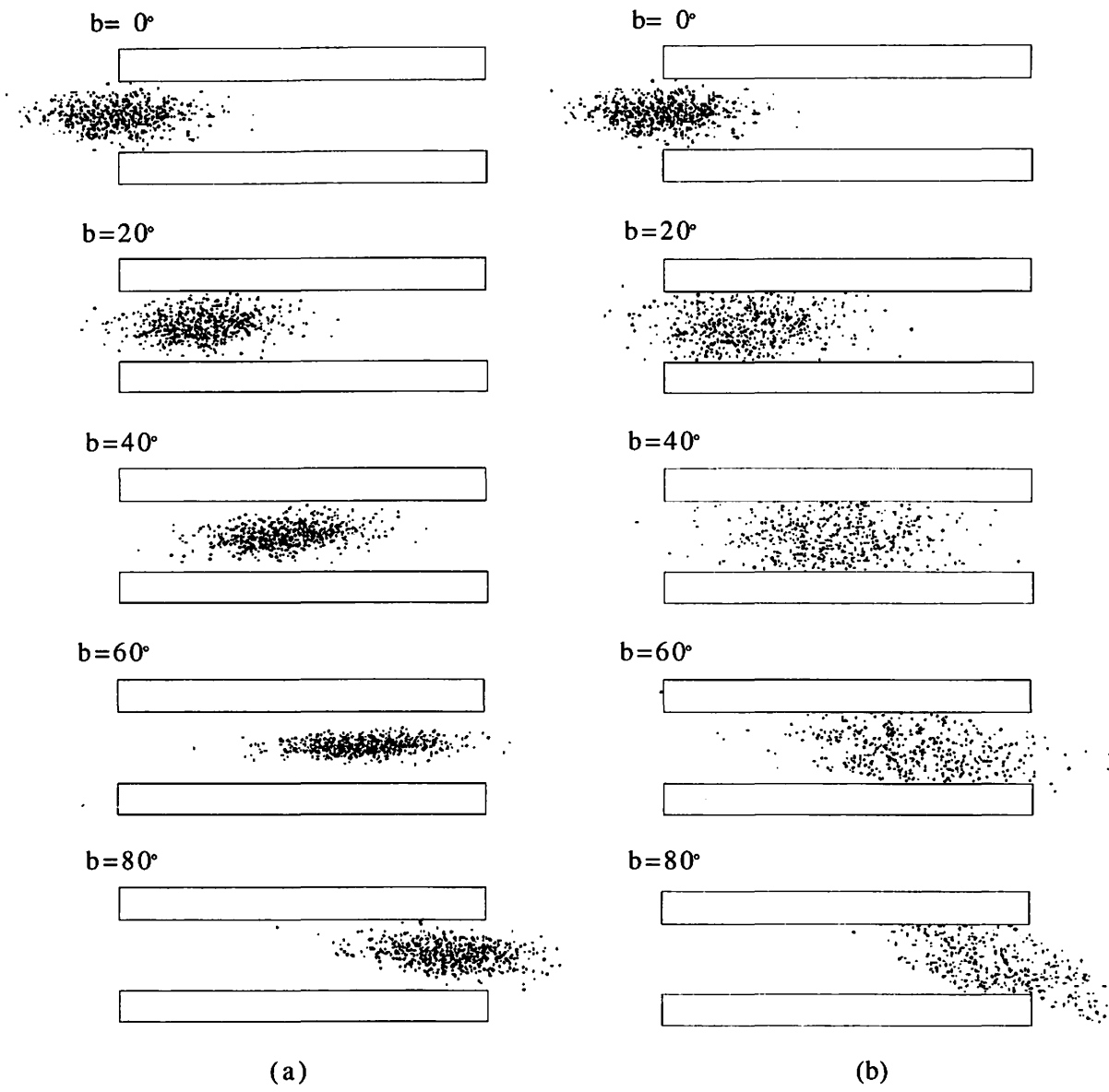
Fig. 7. Evolution of the cloud of particles in the inflector. A 1mA proton beam bunch with $\sigma_u = \sigma_h = 1.0$mm is injected. Initial divergence deviations are taken as (a) $\sigma_{Pu} = \sigma_{Ph} = \sigma_{Pv} = 0.0$ and (b) $\sigma_{Pu} = \sigma_{Ph} = \sigma_{Pv} = 0.1$.

I. 17. Classical Periodic Orbits in Reflection-Asymmetric Deformed Cavity –Fission Model-

Misu T.

Cyclotron and Radioisotope Center, Tohoku University

Introduction

The semiclassical origins of shell structures widely observed in finite fermion systems are not yet fully understood and needs to be explored further in the language of semiclassical periodic orbit theory[1-3]. Recently, the significant correlation between the bifurcation of periodic orbits and the appearance of quantum shell at stationary nuclear deformations was suggested by several authors[4-6]. In our last report[5,6], the investigation of the superdeformed shell structures in the elliptic billiard was carried out and led to both quantitative and qualitative evidence for the importance of the orbital bifurcation in the emergence of shell structure. Since all previous works were, however, based on the use of highly-symmetric cavity models, I have investigated the effects due to the removal of such higher degeneracy and determined the role of the orbital bifurcation in general axially-symmetric, but non-integrable cavity: fission model.

Methods and Results

Nuclear Shape

In the present report, I employed the axially-symmetric fission model based on Ref. 7, and the shape of the nuclear surface is defined in the dimensionless coordinates (u, v) by an equation

$$\pi(\beta,u,v)=v^2-(1-u^2)(A+Bu^2+\alpha u), \tag{1}$$

where β is a set of deformation parameters, and u and v are related to the ordinary polar coordinates (ρ, z) by

$$z= cR_0 u, \quad \rho=cR_0 v. \tag{2}$$

Here, c is a dimensionless elongation parameter, and R_0 is the radius of the sphere.

The parameter α in Eq. 1 represents the asymmetry of the nuclear surface along z direction, and a family of symmetric shapes can be produced for $\alpha=0$. In addition, the coefficients A and B in Eq. 1 are expressed in terms of a deformation parameter c and a necking parameter h as

$$B=2h+(c-1)/2, \quad A=(1/c^3)-B/5. \tag{3}$$

Figure 1 demonstrates a set of shapes in the c-h plane for some fixed values of α.

Single-particle energies of a particle moving freely inside of the considered cavity can be obtained by solving Schrödinger equation under Dirichlet boundary condition with the spherical-wave decomposition method[4,5].

Bifurcation of Periodic Orbits

As is well known for the case of the spheroidal cavity, i. e., removal of spherical symmetry, the linear orbits along diameter in the spherical cavity bifurcate into those along the major axis and along the minor axis, while the planar orbits at the spherical limit bifurcate into those in the meridian and equatorial planes. Further shape deformation also leads to the bifurcations of linear and planar orbits in the equatorial plane into hyperbolic orbits in the meridian plane and three-dimensional orbits (see Fig. 2a). According to Ref. 8, such three-dimensional orbits for axially symmetric cavity can be created when the equatorial orbit labeled by (p, t) with p and t being the numbers of vibration and rotation meets the bifurcation condition, see also Fig. 2b,

$$\frac{R_2}{R_1} = \frac{\sin^2(\pi t/p)}{\sin^2(\pi q/p)},$$ (4)

where R_1 and R_2 represent the curvatures of the cavity at the edge of equatorial plane, and q is an integer. Figure 4 shows a set of bifurcation lines, i. e., constant curvature ratio given by Eq. (4), as functions of both c and h at $\alpha=0$.

Based on our recent findings that the orbital bifurcation satisfying Eq. (4) is responsible for the emergence of shell structure, one must clarify whether the important role of the orbital bifurcation in shell structure is even present in non-integrable cavities. In the following sections, the shell structures are compared along the constant curvature ratio where all equatorial orbits complete their bifurcation process for the creation of the three-dimensional orbits, and six points labeled by a through f are chosen for a comparison, as shown in Fig. 4, where a point f corresponds to a superdeformed spheroidal shape.

Shell Structure and Fourier Spectra

The shell-structure energy δE can be defined as the difference between the sum of single-particle energies filling N states from the bottom of the well and the Strutinsky averaged energies, i.e.,

$$\delta E = 2\sum_{i=1}^{N} \varepsilon_i - \tilde{E}, \quad \tilde{E} = 2\int_{-\infty}^{\tilde{\varepsilon}_F} d\varepsilon' \varepsilon' \tilde{g}(\varepsilon'),$$ (5)

with the Fermi energy $\tilde{\varepsilon}_F$ satisfying

$$N = 2\int_{-\infty}^{\tilde{\varepsilon}_F} d\varepsilon' \tilde{g}(\varepsilon').$$ (6)

In Fig. 4, the shell-structure energy for the case of the spheroidal cavity is shown for mere reference only. The emergence of the prominent magic gaps seen at the superdeformed shape can be regarded as the result of the orbital bifurcations as demonstrated by previous studies.

Figure 5 illustrates the oscillating pattern of the shell-structure energy δE as

functions of both c and h for a fixed particle number N, and it is compared with the constant orbital bifurcation lines R_1/R_2 and the elongation of the surface, χ, defined by

$$\chi = \int_v \rho |z| dV \Big/ \int_v \rho \, dV \tag{7}$$

It is clear from the figure that for small elongation the shell valley follows the constant elongation points, see Fig. 5a, whereas the role of the bifurcated equatorial orbits increases for larger values of χ, see Fig. 5b.

In terms of semiclassical trace formula, the level density $g_{scl}(\varepsilon)$ can be written as

$$g_{scl}(\varepsilon) = \tilde{g}(\varepsilon) + \sum_\beta A_\beta(k) \cos\left(kL_\beta - \frac{\pi}{2}\mu_\beta \right), \tag{8}$$

where $\tilde{g}(\varepsilon)$ denotes the smooth part corresponding to the contribution of zero-length orbit, A_β the amplitude, and μ_β the Maslov phase.

Since the oscillating part of the semiclassical level density in Eq. 7 represents the Fourier sum, the classical-quantum correspondence on shell structure can be obtained from the Fourier transform $F(L)$ of the quantum level density $g(\varepsilon)$ with respect to the wave number, which may be regarded as 'length spectrum' exhibiting peaks at lengths of individual periodic orbits.

Figure 6 illustrates the deformation dependence of the Fourier peaks for six previously chosen shapes. The nuclear shape corresponding to a point a results in strong shell fluctuation, and its Fourier spectrum indicates that the main contribution comes from the meridian planar orbits of lengths roughly ranging from 5 to 7, while the peaks related to the three-dimensional orbits bifurcated from the equatorial orbits, labeled by α, β, γ in the figure, are less pronounced in the moderately-elongated region. When the system starts to elongate further, the shell oscillations due the meridian and three-dimensional orbits contribute destructively, leading to flattening of the shell structure, see Figs. 6b-e. As the nuclear shape approaches to the highly-symmetric superdeformed spheroidal one as in Fig. 6f, the origin of the prominent shell structure can be understood in terms of the constructive interference among the three-dimensional orbits originated from the equatorial planar orbits.

Conclusions

The role of classical periodic orbits in the emergence of shell structure for single-particle motions in axially-symmetric fission cavity was identified. In particular, the importance of orbital bifurcation as indicated by previous investigations for highly symmetric (elliptic and spheroidal) cavities was carefully analyzed.

It was shown that the contributions from the bifurcated orbits originated from the equatorial planar orbits play a significant role in the regions around superdeformed spheroidal shape, while its enhancement becomes less pronounced for less-elongated shapes, indicating the importance of the orbital bifurcation in the emergence of prominent quantum shells in highly-deformed fermion systems.

It remains as a future challenge to investigate the semiclassical origin of shell formation in finite fermion systems for finite-depth potentials, and the Green's function approach[8] may be applied to calculate the continuum level density in such systems.

References

1) Gutzwiller M. C., J. Math. Phys. **12** (1971)343.

2) Balian R. B. and Bloch C., Ann. Phys. (N.Y.) **69** (1972)76.

3) Berry M. V. and Tabor M., J. Phys. **A10** (1977)371.

4) Arita K. and Matsuyanagi K., Nucl. Phys. **A592** (1995)9.

5) Sugita A., Arita K. and Matsuyanagi K., Prog. Theor. Phys. **100** (1998)597.

6) Magner A. G., et al., Prog. Theor. Phys. **102** (1999)551.

7) Misu T., Arita K., Matsuyanagi K., CYRIC Annual Report (1998)38.

8) Kruppa A. T., Phys. Lett. **B431** (1998)237.
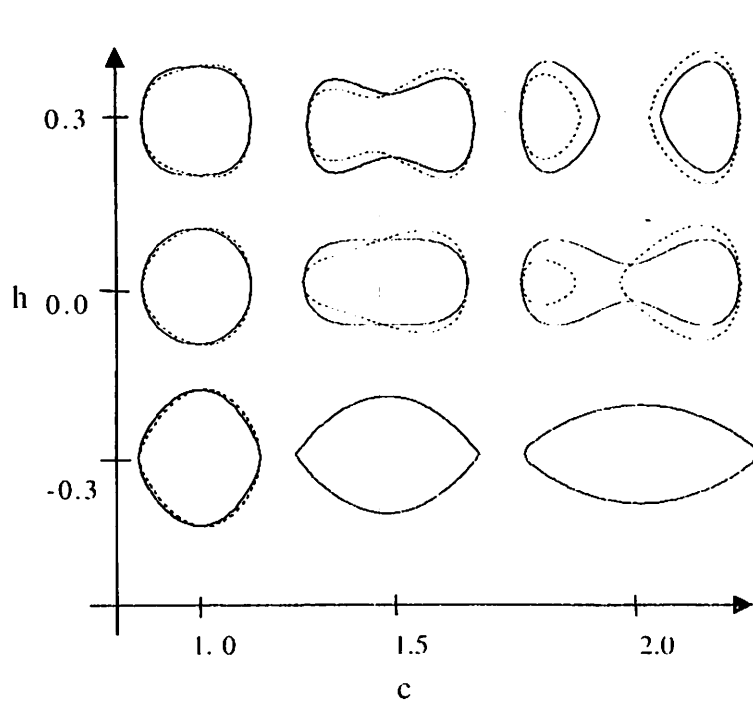
Fig. 1 . Shapes in the c-h parameterization at α=0 (solid lines) and α=0.3 (dotted lines).
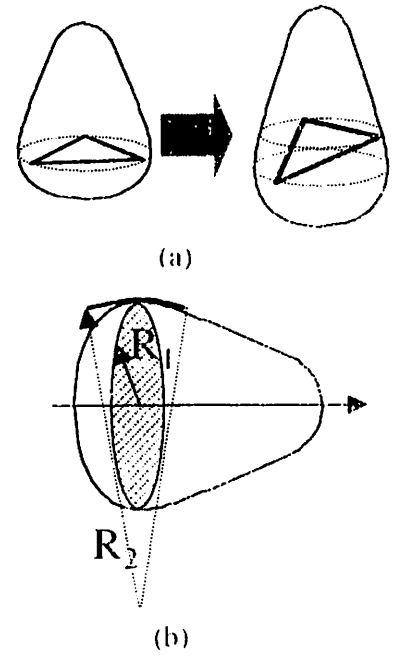
Fig. 2. (a) Schematic drawings of the orbital bifurcation of the equatorial triangular orbit (6,2) as an example.
(b) Description of curvatures R_1 and R_2 given in Eq.4.
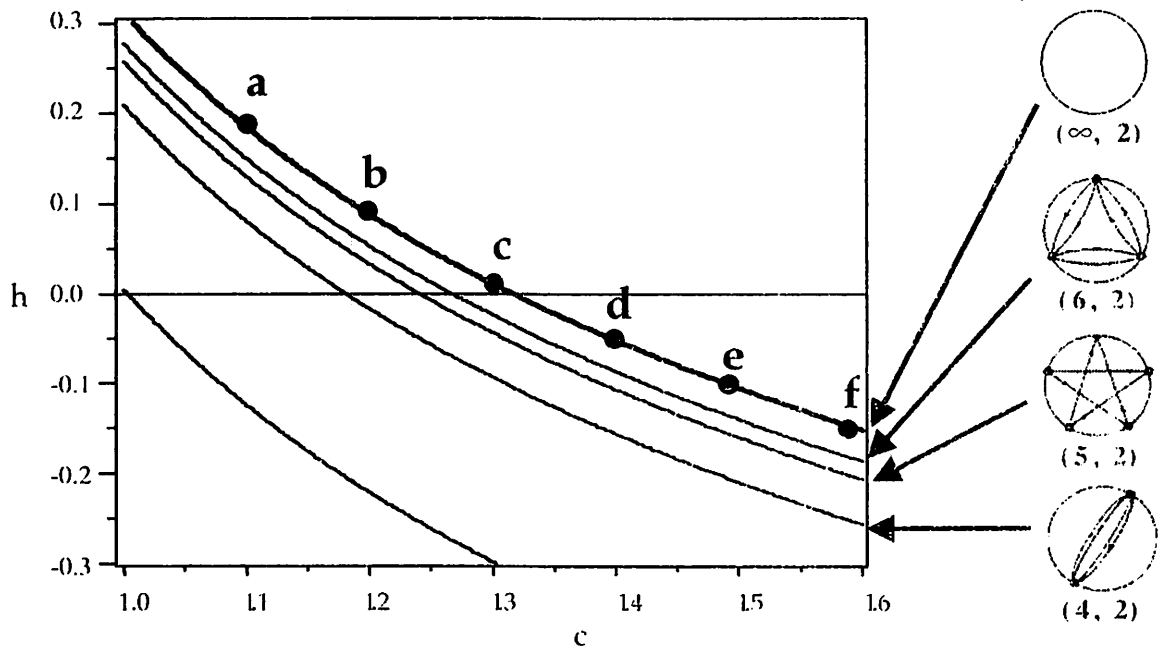
Fig. 3. Constant bifurcation lines defined by R_1/R_2 in Eq. 4 are plotted as functions of two deformation parameters c and h at α=0 for four types of equatorial planar orbits and the corresponding orbits are also shown schematically (right figures).

79
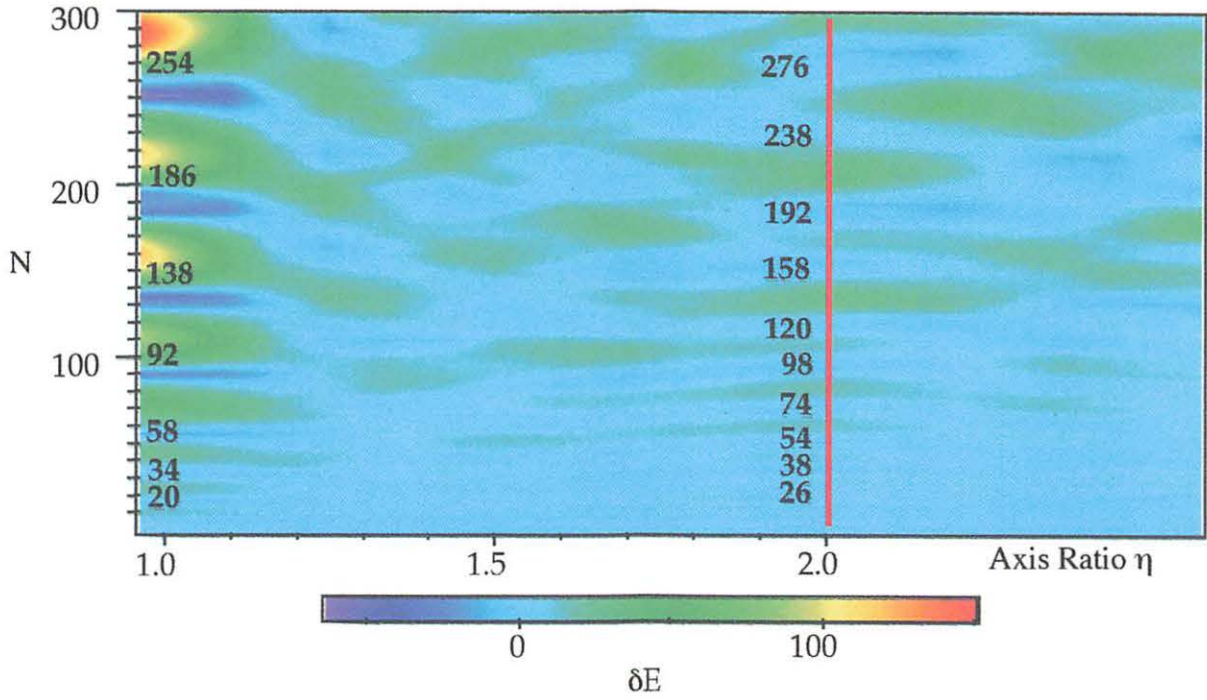
Fig. 4. Shell-structure energy δE for the spheroidal cavity as functions of axis ratio η and occupation particle number N. A superdeformed spheroidal shape at η=2 corresponds to a point *f* in Fig. 3, and its magic numbers are indicated.
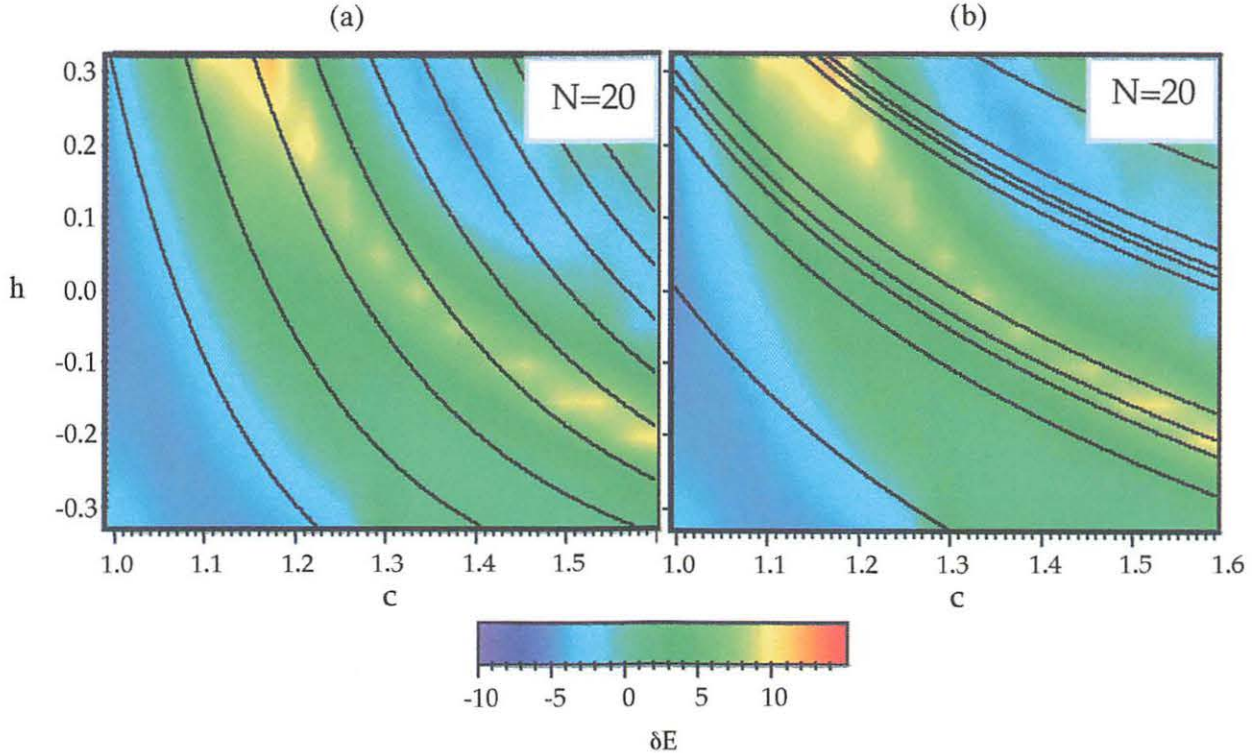
Fig. 5. Shell-structure energy δE for the axially symmetric cavities parameterized by c and h at α=0 for the occupation particle number N=20. Solid lines in (a) and (b) represent the constant elongation and bifurcation points, respectively.

Fig. 6. (a) Shell-structure energy δE calculated for six deformed shapes specified in Fig. 3 as a function of N$^{1/3}$, N being the occupation particle number, and (b) their Fourier spectra are shown. The peaks labeled by α, β, γ correspond to the three-dimensional orbits bifurcated from the equatorial (4,2), (5,2), (6,2) orbits, respectively.

I. 18. A Boundary Formation Method Using a Median Filter Processing for Attenuation Correction in 3-D PET

Mizuta T., Ishii K., Yamazaki H., Matsuyama S., Oishi Y.,
Itoh M.*, Yamaguchi K.*, Watanuki S.*, and Orihara H.*

Department of Quantum Science and Energy Engineering, Tohoku University
*Cyclotron and Radioisotope Center, Tohoku University

Introduction

Recently, 3-D PET has been used in whole body imaging because of high sensitivity performance and wide axial field of view (FOV). The PET system with 20-cm axial FOV allows us to acquire the whole body data with 8 or 9 frames. Since data acquisition in 3-D mode cannot exclude scatter components, however, blank and transmission scans on 3-D PET are performed in 2-D mode with the septa in and the attenuation correction factors (ACF) are calculated by forward-projecting attenuation images in each slice to all possible directions of the coincidence lines. In theory, this technique provides a perfect correction for photon attenuation, but in practice it is limited by noise in the transmission measurement[1,2]. Hence, a long acquisition time for transmission scans is required to achieve adequate statistical quality, but it is impractical to acquire a statistically adequate transmission data-set in the whole body PET imaging[3]. Without suitable technique for processing count-limited transmission data, the whole body imaging technique for PET is subjected to attenuation artifacts.

Sinogram smoothing is most commonly employed for reducing noise in data of short transmission scans. While this is effective in minimizing noise propagation, it can also degrade the quantitative accuracy in PET images[4]. On the other hand, a boundary method for attenuation correction has been suggested for the application to cardiac PET studies[5]. This method has the potential to greatly reduce the acquisition time for transmission scans without increasing noise in attenuation images, but it is time-consuming for operators to manually draw ROIs corresponding to lung and body outline. A method of local threshold segmentation has been developed for the use in PET studies on thorax and chest regions, and this technique permits to automatically determine boundaries between anatomical tissues[6-8]. However, this technique cannot give proper assessment of the attenuation value in lung region, which tends to fluctuate in a wide range. In addition, mismatch between emission and trasmission resolutions causes attenuation artifacts on the soft tissue side of a soft tissue/lung interface. Therefore,

improved strategies for processing count-limited transmission data should be developed.

In this study, two kinds of methods were applied for accurate attenuation correction based on count-limited transmission data. The first method used a median-filter processing of measured attenuation images. This process not only reduced noise in an image of poor statistical quality but also formed a smooth boundary partitioning the image into different regions; this method for attenuation correction (AC) was called a median AC. In the other method, we combined the median filter processing with segmentation of measured attenuation images in order to produce an attenuation image without noise; we call this process as a segmented AC. These methods have been tested with a phantom study and with clinical whole-body PET study.

Technical Description

Original attenuation images were reconstructed into 128×128 matrix in each slice by taking the logarithm of the ratio of counts in blank scans (B) to ones in transmission scans (T). Prior to this step, two-dimensional linear smoothing was applied to the sinogram of T/B by 5×5 matrix. The bound 2-D images of 63 slices in one frame were treated as a 3-D continuous matrix. The voxel size was 4.6 mm×4.6 mm×3.12 mm based on the maximum FOV of PET machine used in this experiment.

The original attenuation images were processed with two different methods for noise suppression and extraction of a smooth boundary partitioning the images into different regions: a three-dimensional median filter processing (the median AC), and a local threshold segmentation combined with the median filter processing (the segmented AC). In the former method, the three dimensional filter of the smallest size, 3×3×3 matrix of pixels, was used in order to utilize information of adjoining slices with the minimum distarbance of smoothing. In the latter method, the median filter was applied to original images, and then the processed images were segmented by the use of the local threshold segmentation algorithm proposed by M. Xu et. al.[7]. This localizing operation, which is based on an optimal threshold selection algorithm proposed by N. Otsu[9], is effective means to separate mixed populations of pixels of different attenuation coefficients. In Otsu's algorithm, the total variance, σ_T^2, and the between class variance, $\sigma_B(k)^2$, are calculated as a function of a threshold, k, dividing pixel-histogram of a image into two classes. The optimal threshold can be obtained when the ratio of $\sigma_B(k)^2/\sigma_T^2$ is maximized. The obtained k-value is very stable, since this threshold selection criterion is derived from a calculation of a series of integrations. The chest image can be a typical example of the local threshold segmentation. In this case, the following procedure is used to discriminate lung, soft tissue and background. Firstly, threshold k_1 is determined from the global histogram in order to distinguish pixels inside and outside the body, and a closed loop is formed describing the body contour by searching an attenuation image from outside for

eliminating backgrounds less than k_1 value. In this stage, a local histogram is calculated including only pixels within the body contour. Then, a second threshold k_2 is calculated from the local histogram to separate the body into soft tissue and lung, and there by defines a closed contour describing the lungs. In this stage, a second local histogram is calculated using the original image excluding lungs, and using this local histogram an updated value of k_1 is determined and the body contour is redefined. After these steps, average values of attenuation coefficients in segmented pixels are assigned to corresponding regions. In our experiment, segmented bed image in phantom studies was obtained from different transmission scan in order to be combined to the segmented body image, and that in clinical studies was reproduced by subtracting segmented body image from the original image. Thus, we can obtain a noise-less attenuation image.

In the final step of image reconstruction, new ACFs in 2-D and 3-D mode were computed by forward projection of the processed attenuation images into emission sinograms in each mode for correction of emission data. Then, the attenuation corrected emission data were reconstructed in terms of 2-D and 3-D filtered-back projection. The image reconstruction and the forward projection processes were performed by the use of Shimadzu-software, and the processing of attenuation images were coded in C-programming language and implemented on a personal computer.

Experimental

Both phantom and clinical data, which were acquired by Shimadzu HEADTOME-V SET-2400W at Cyclotron and Radioisotope Center of Tohoku University, were used to validate the two techniques for attenuation correction of PET images. This scanner was equipped with 32 detector rings of 89-cm diameter, of which each ring was composed of 672 crystals of $Bi_4Ge_3O_{12}$ in size of 3.8×6.3×30.0 mm. The FOVs in transaxial and axial directions were 59.5 cm and 20.0 cm, respectively. This PET machine had also a rotated rod source of $^{68}Ge/^{68}Ga$ of approximately 10 mCi at the time of our experiment.

Figure 1 shows the heterogeneous phantom used in this study. This acrylic phantom consisted of the main space of water, Teflon in 30-mm diameter and two mixed spaces of polystyrene beads and water in 30-mm and 58-mm diameters. These regions, respectively, were assumed to be a soft tissue (water region), a bone (Teflon region) and a lung (polystyrene beads + water). The main space assumed to be soft tissue was filled with 0.93 mCi/ml of ^{18}F-solution. The emission data were acquired for 120 minutes in each of 2-D and 3-D modes. After the activity in the phantom had decayed away, the 2-D transmission scan was performed for 1, 3, 5, 10 and 60 minutes. Total transmission counts are shown in Table 1.

To confirm the applicability of these techniques for attenuation correction in clinical PET studies, we used a whole-body PET image which was performed in 2-D mode for 70-year-

old man with cancer disease. The patient was administered by [18]FDG and the emission scan consisted of 6×5 min frames. The pre-injection transmission scan was carried out in the same frame size. In this experiment, the image for abdomen section was investigated and the total counts in the examined frame were 13.2×10^8 for the transmission scan and 3.1×10^8 for the emission scan, respectively.

Results and Discussion

It is well known that the median filter processing of a image achieves some degree of noise suppression and also maintains a resolution across the edge of pixels of a different value. Furthermore, this filter processing has a promising property to extract a smooth object boundary contour from a image complicatedly disturbed in regions smaller than the filter size. Figure 2 shows the average and the standard deviation (1σ) of pixel values in the 30-mm diameter Teflon region for attenuation images of the phantom, which were reconstructed from 3-min transmission data with or without three-dimensional median-filter processing of different times. In this figure, the values of 60-min scan without the filter processing were also plotted as the most reliable ones. The non-processed attenuation image of 3-min scan had very poor statistical quality. On the other hand, the signal-to-noise ratio (standard deviation) was largely improved at the first processing time, but additional filter processing was not already effective for noise suppression. By returning attention, the average of pixel values in the small Teflon region decreased by 15 % of the initial value at five-times processing; this value was smaller than the average value in the image of 60-min transmission data. This indicates the smoothing of median filter processing in a smaller region than the filter size; the average value of pixels in a small region may be influenced by the value of neighboring pixels in a large region. Hence, the filter processing should not be repeated many times. The one-time operation was found to be effective in noise suppression without degradation of pixel values in a small region of a image.

The segmentation operation for the attenuation image of 1-min transmission data of the phantom gave incomplete contours of Teflon and of the small mixed space of polystyrene beads plus water even when the median filter processing was repeated eight times. In contrast to this, the contours of these regions were perfectly reproduced by segmentation operation for the attenuation image of 3-min transmission data. These findings indicate that the total transmission counts of 12×10^8 per frame permit a rather complete segmentation of an absorber in 200 mm diameter with the attenuation coefficient eqal to that of water (see Table 1).

Figure 3 shows the 2-D and 3-D emission images of the phantom, which were corrected with different attenuation images; these images, respectively, were obtained with the standard attenuation correction (AC) based on 3-min transmission scan (the 3-min original in the first column of the figure), the median AC (the 3-min median in the second column) and the

segmented AC (the 3-min segmentation in the third column). For the most reliable image, the fourth column shows the emission images corrected by ACFs calculated from 60-min transmission data, which is called the 60-min original. Although the 2-D emission image of the 3-min original was quite noisy, 2-D image with the segmented AC using the same transmission data had higher quality than that of the 60-min original. The quality of 2-D image with the median AC was inferior to that of the image with the segmented AC, but it was largely improved as compared with the 3-min original. Hence, the segmentation is the most appropriate method for application in the count-limited situation, when a constant attenuation coefficient can be assumed in each region of measured objects. As well as this, the 3-D emission images clearly represented the favorable effect of the median filter processing and the segmentation procedure for attenuation correction using count-limited transmission data. The difference in the image quality between the 3-min median and the 60-min original became much smaller in 3-D images than in 2-D ones. This will be resulted from additionally increased accuracy for the correction from oblique directions in 3-D images.

Figure 4 shows the attenuation images (the top row) and the 2-D emission images (the bottom row) of the abdomen section of whole-body ^{18}FDG PET study performed on a male cancer patient. The emission images, respectively, were obtained by the use of standard attenuation correction (the first column in the figure), the median AC (the second column) and the segmented AC (the third column). The attenuation coefficient can be considered constant in the abdomen section of human body. It is naturally implicated from the results of phantom studies that we can put our trust in the emission image corrected by the segmented attenuation image reconstructed from data for 5-min transmission scan. The emission image corrected by standard method was considerably poor in quality and produced an artifact diagonally behind the left hot spot. In contrast, there was no large difference in quality between the image with the median AC and that with the segmented AC. As well, Fig. 5 reveals good agreement of pixel values in these clinical images; for the plot of pixel values in the emission image with the median AC versus those in the image with the segmentation AC, linear fit found the slope of 1.099 and correlation coefficient, R^2, was 0.975. In contrast to this, the standard measured method for attenuation correction was less linearly correlated (slope=1.169 and R^2 =0.914) with the segmented AC. These results of Figs. 4 and 5 naturally imply that the median filter processing of measured attenuation images is effective to improve the accuracy of attenuation correction for emission images of total-count level common in clinical PET studies.

Moreover, we applied the segmentation AC to the image of head region of the clinical PET study, but the contour of skeleton bone was not extracted. This may be ascribed to a very small difference in absorption coefficients (μ) for 511 keV gamma photons between soft tissues ($\mu = 0.089$ cm^{-1}) and bones ($\mu = 0.104$ cm^{-1}). It is a serious problem to ignore the existence of bones, since the skeleton bone occupies a large portion of the head and the quantitative emission

image is especially required in clinical PET studies.

Conclusion

Results of the phantom study indicated that emission images with median AC using transmission data of 3-min scan was comparable in quality to the images corrected for the attenuation using transmission data with less statistical noise (60-min transmission scan). It was also revealed that the segmented AC produced a rather good quality of emission images as compared with the standard AC using 60-min transmission data. For the abdomen section of a clinical PET image, however, there was little difference in improvement of image quality between the median filter AC and the segmented AC. Implementation of the segmented attenuation correction will be restricted for the emission images of other sections of human body due to the lack of the performance of extracting bone contour and of reproducing a delicate variation of attenuation coefficients in an anatomical section such as the lung. It cannot be avoided that the segmented AC causes attenuation artifacts in emission images for tissues of which the absorption coefficients are unsuitably allocated. Especially in the case of 3-D reconstructed images, this damage expands throughout oblique LORs in the axial direction. Keeping this in mind, we can conclude that the median filter processing is feasible in clinical PET studies to correct the attenuation for emission images using count-limited transmission data.

References

1) Huang S.C., Hoffman E.J., Phelps M.E. and Kuhl D.E., J. Comput. Assist. Tomogr., 3, 804-814 (1979).
2) Dahlbom M. and Hoffman E.J., IEEE Trans. Nucl. Sci., 34, 288-293 (1987).
3) Guerrero T.M., Hoffman E.J., Dahlbom M., Cutler P.D., Hawkins R.A. and Phelps M.E., IEEE Trans. Nucl. Sci., 37, 676-680 (1990).
4) Polmer M.R., Rogers J.G., Bergstrom M., Beddoes M.P. and Pate B.D., IEEE Trans. Nucl. Sci., 33, 478-481 (1986).
5) Huang S.C., Carson R.E., Phelps M.E., Hoffman E.J., Schelbert H.R. and Kuhl D.E., J. Nucl. Med., 22, 627-637 (1981).
6) Xu E.Z., Mullani N.A., Gould L. and Anderson W.L., J. Nucl. Med., 32, 161-165 (1991).
7) Xu M., Luk W.K., Culter P.D. and Digby W.M., IEEE Trans. Nucl. Sci., 41, 1532-1537 (1994).
8) Meikle S.R., Dahlbom M. and Cherry S.R., J. Nucl. Med., 34, 143-150 (1993).
9) Otsu N., IEEE Trans. Syst. Man. Cyber., SMC-9(1), 62-66 (1979).

Table 1. Total transmission counts in the phantom study.

Scan time [min]	Total count($\times 10^8$) [counts/frame]
1	4
3	12
5	20
10	40
60	240

polystyrene beads and water(μ=0.0355cm^{-1})
water(μ=0.0956cm^{-1})
acrylic(μ=0.0956cm^{-1})
teflon(μ=0.1638cm^{-1})
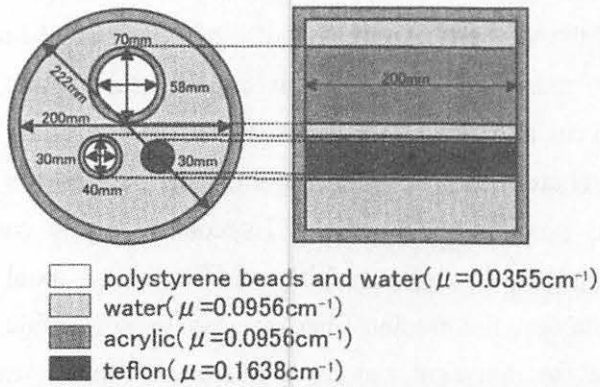
Fig. 1. Geometry of heterogeneous phantom used in this study.
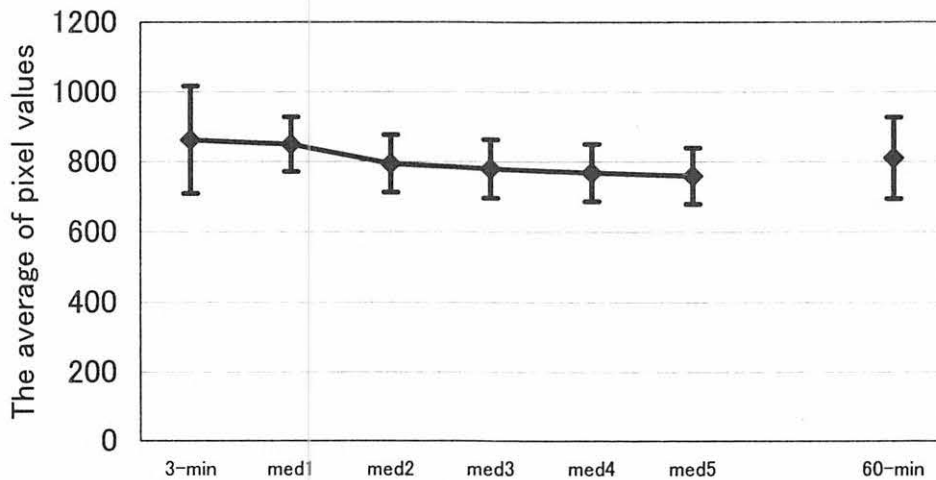
Fig. 2. Effect of the number of median filter processing on the average and the standard deviation of pixel values of attenuation image for Teflon region of phantom at the 32-slice. 3-min: the measured image reconstructed with 3-min transmission data; 60-min: the most reliable image based on 60-min transmission data; med 1 to med 5: the attenuation image processed once to five times with median filter.

3-min Original   3-min Median   3-min Segmentation   60-min Original

Attenuation Images

2-D Emission Images
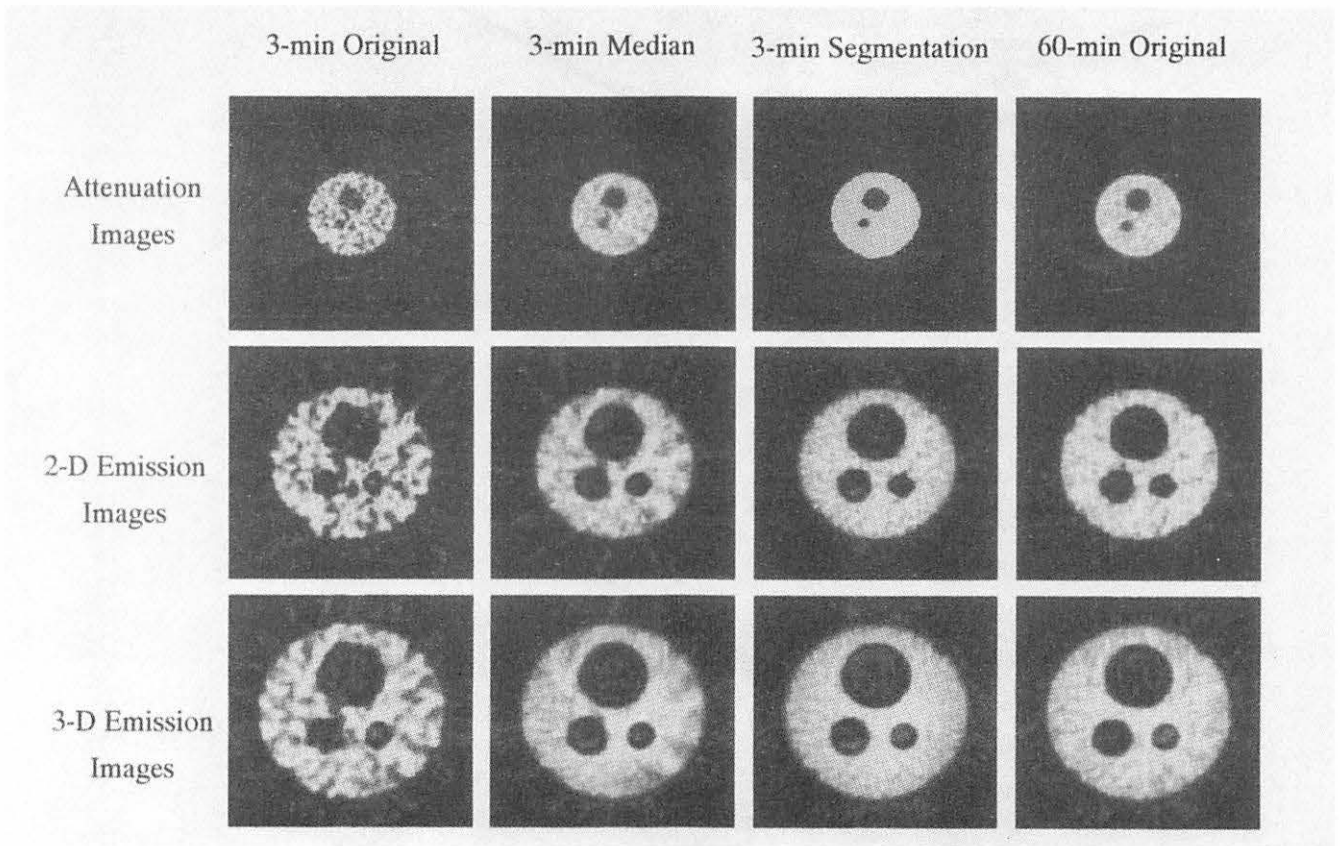
3-D Emission Images

Fig. 3. Accuracy of different methods for attenuation correction of 2-D and 3-D emission images of phantom (32-slice, the middle of axial FOV). 3-min original: the measured image based on 3-min transmission data; 3-min median: the image with median AC using 3-min transmission data; 3-min segmentation: the image with segmented AC using 3-min transmission data; 60-min original: the measured image based on 60-min transmission data.

Original   Median AC   Segmented AC
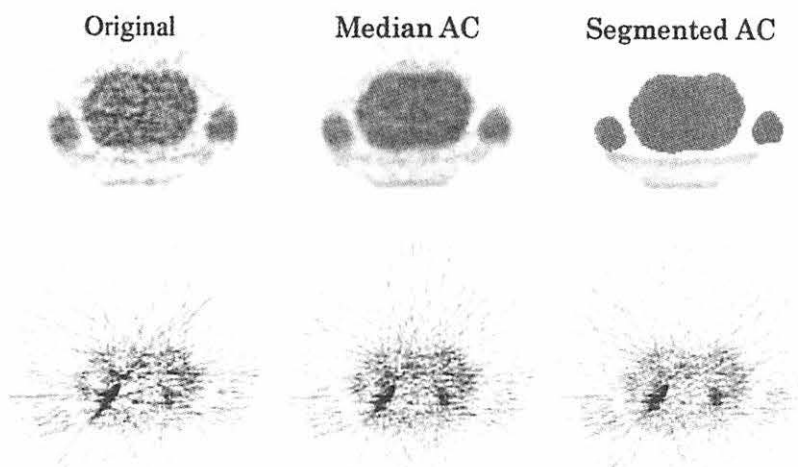
Fig. 4. Attenuation images (top row) and 2-D emission images (bottom row) of the abdomen section for whole-body ^{18}FDG PET study performed on a cancer patient (5-min transmission scan of 1.32×10^9 counts / frame and 5-min emission scan of 3.1×10^8 counts / frame).

89
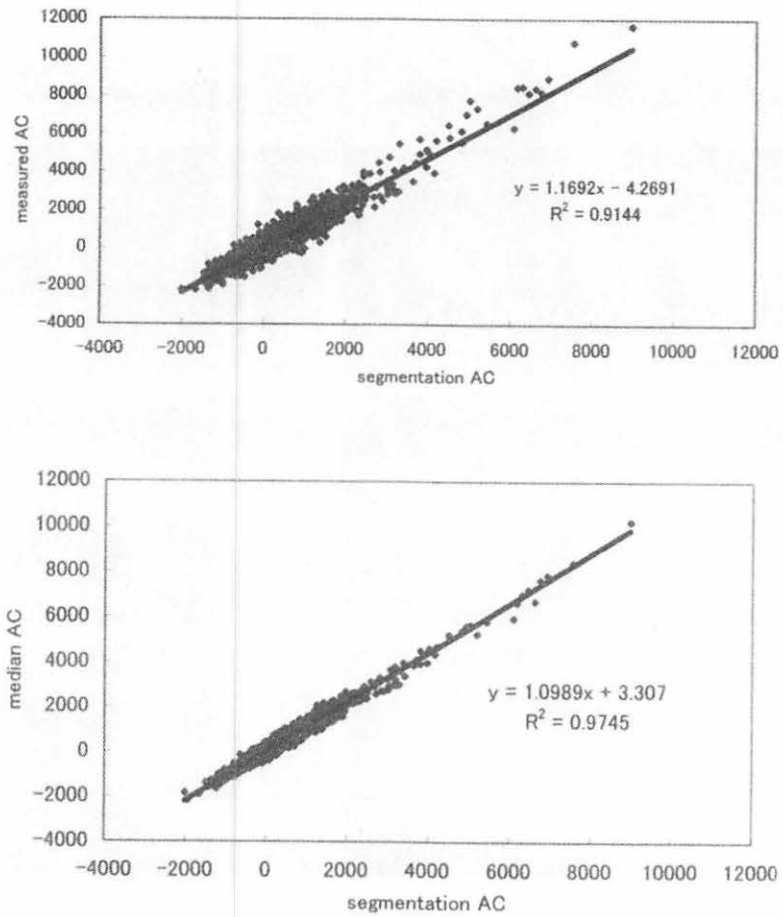
Fig. 5. Correlation between the emission image with or without median AC and that with segmentation AC. The emission images are the same in Fig. 4. The abscissa indicates pixel-values of emission image corrected with segmented attenuation image. The ordinate indicates pixel-values of emission image with measured AC (A) or with median AC (B). S: slope of linear correlation; R^2: correlation factor.

I. 19. Phase Correction Analysis between EEG and MEG Simultaneously Measured by a Simple System Composed of One-channel SQUID Fluxmeter and Two-channel EEG Dvice

Nagasawa M., Suzuki A., Ishii K., Yamazaki H., Matsuyama N., Watanuki S. ,
Itoh M.*, and Orihara H* .*

Department of Quantum Science and Energy Engineering, Tohoku University
Cyclotron and Radioisotope Center,Tohoku University*

Introduction

The brain-generated currents that produce electric potentials measured as the electroencephalogram (EEG) also produce magnetic fields measured as the magnetoencephalogram (MEG)[1]. The brain is considered as a complex and open system that exhibits spatiotemporal behavior at various time and length scales[2]. Hence modern biomagnetic measurements require simultaneous detection of brain-magnetic signals over large areas of the cortex. To satisfy this requirement, various multichannel instruments covering variable areas of the cortex have been constructed in recent years[3-6]. This equipment is mainly used for identification of area of activity of the brain by photic or auditory stimulation. However, the induced magnetoencephalo wave can not be detected without the enormous arithmetic mean of the data, since the standard rhythm of brains such as the α wave becomes a large noise. Furthermore, this data-processing method does not become an effective means for detecting an induced magnetoencephalo wave because of the habituation for repeated stimulation. On the other hand, the EEGs are not only derived from a generator near the electrode but also signals away from it, since an electric potential is conducted to the whole head and appears on the scalp. It naturally is supposed that the strength of EEG signals for the induction stimulation is not too small to be buried in large signals of the standard rhythm.

Keeping the facts described above, we will next consider to provide a fundamental information in the neural network controlling highly intellectual functions of brain by using a simple equipment simultaneously recording one channel of MEG and two channels of EEG data; the MEGs were measured at the occiput with a second-order SQUID gradiometer and the two EEG data were measured on head corresponding to highly intellectual functions of the brain. We analyzed a two-dimensional phase difference between MEG and EEG signals when the MEG showed only α rhythm pattern. If the highly intellectual function of the brain works simultaneously, the EEG shows the wave derived from the high-order brain activities

as well as the strong generator of α rhythm far from the electrode position. Then, the phase correlation between the MEG and the EEG data can show the brain activities induced by some kind of task without overlapping of large α rhythm background, even if we do not use the multichannel equipment. In this paper, we report the development of simple measurement system for a high-order brain activity, including speculation on quantitative analysis of phase correlation between the MEG and EEG signals from examinee imposed by different kinds of task.

System Description

We measured magnetoencephalo-waves from human brain under a small environmental magnetic noise. Our laboratory is located in the place which adjoins Kawatabi farm of Tohoku university; there is no source of enormous magnetic field such as the elevator. In the laboratory, there is a simple shielding room which surrounded by aluminum plate of the about 0.04mm thickness and copper wire gauze(0.45mmø) with about 1.7mm texture width. This shielded room removes the electromagnetic field with exceeding the modulation frequency (500Hz) of dc-SQUID feedback loop used in this experiment: this high-frequency electro-magnetic field causes a magnetic flux trap in the SQUID element. The room also fills the role of the electrostatic shield for measuring the EEG.

We used a second order dc-SQUID gradiometer (Quantum Design Inc.) having a good S/N ratio and the controller, Quantum Design Inc., Model 5000, for measuring MEG. The detection coil was the 24mm diameter, and the base line is 30mm. The SQUID Dewar was put on a wooden pedestal of adjustable height. For EEG measurement, we used 2-channel EEG system, Nihon Kohden Co., Model MEG-2000, and silver-silver chloride electrodes in dish type; these electrodes did not cause interference to the magnetic signals from brain activity. We tried to decrease electromagnetic noise from the measurement system. For example, because the SQUID sensor detected the horizontal synchronizing signal from CRT display, we used a book-sized personal computer with a liquid crystal display. One channel output from the SQUID controller and two channels of EEG's outputs were taken into the book-size personal computer through the ADC card (National Instruments Co., DAQCard-1200). The software controlling measurement, LabVIEW, (National Instruments Co.), was installed in the computer, and the three-channel data were displayed on TFT display for the sequential comparison. In measuring mode, the each data were stored into RAM in order to keep the processing speed of personal computer.

Though the second order SQUID gradiometer showed a rather stable base line of the background magnetic field throughout a day, the SQUID sensor detected a large electromagnetic noise (50Hz) from the commercial power line in or out of the laboratory. The data recorded by the SQUID sensor were processed to remove high frequency components over 30Hz by means of a wavelet-based multiscale decomposition using

Daubechies' wavelet of N=6. Then, we analyzed the phase correlation between the processed SQUID data and the original EEG data.

Experimental

The MEG was measured at the position of the largest α-rhythm response on the head: 8cm rear and 10cm upper part from the left ear hole in the position. The detection coil of SQUID was set above the about 1cm upper part from the measuring position. The EEG was measured by the monopolar recording, and two reference electrodes were put on each of earlobes in diagonal side of active electrodes, and the body earth was taken in the center of forehead. Based on the international 10-20 system of electrode layout, two active electrodes were placed in the region of the cerebral cortex which controlled respectively the memory (F8) and the imaging (T3) activities. The analog bandwidths were, respectively, 0-100 Hz for the MEG and 0.5-30 Hz for the EEG. The data of each channel were digitized at 300 Hz.

The examinee was a 24-year-old male (normal). He lay on his stomach on a wooden bed with closing his eyes in the dark shielded room. Two kinds of tasks were imposed on the examinee. Task A was that he tried to think or image nothing during the measurement. We tend to think or image something, so in an our awakening this task corresponds to producing the brain activity for retaining the unreal condition. Task B was that the examinee tried to keep remembering somewhat about his family. So he mainly used the highly intellectual function of brain such as memory or imaging. Eye-closed data under these two kinds of tasks were measured for two minutes, and the portions with strong α-rhythm were mainly investigated

Results and Discussion

In the two-dimensional analysis of phase difference, each of the amplitude of MEG and EEG signals measured at the same time was plotted on the X coordinate and on the Y coordinate. When both of MEG and EEG data show α rhythm pattern, the trajectory keeps a definite form because of the similarity of waveform and stable phase difference. For example, when these two waves have an equal frequency and the phase difference of ±π (rad), this locus of phase correlation will move on the straight line due to proportionality of X and Y coordinates. On the other hand, the locus of phase correlation draws a round shape when and the phase difference is ±π/2 (rad). However, if the EEG includes a different wave overlapped on α wave, the trajectory shows a random figure due to the unstable phase difference.

We selected the start point of analyzed data where a peak (mountain or rill) of α rhythm appeared in the MEG recordings, and divided the MEG and the EEG data measured at the same time into every 0.3-second intervals. These data of 0.3-second interval were used as one sample where the two-dimensional analysis of phase difference was conducted. The

frequency of the α rhythm of the measured examinee was about 10 Hz so that the duration of 0.3 second included 3 wavelength of the α rhythm. But the duration length of the signal in the brain induced by the task is unknown. Hence, the period of examining correlation between MEG and EEG data was set to be 0.3 second in order to reveal the change in the phase correlation. The total periods of the MEG and EEG recordings respectively were 1840 seconds in the case of the task A and 700 seconds in the case of the task B.The portion of MEG data with α rhythm pattern was about 56 seconds in the case of task A, and that was about 40 seconds in the case of task B. These corresponded respectively to 186 samples in the case of the task A and to 133 samples in the case of the task B, where the 2-D analysis of phase difference was conducted between the EEG and the MEG data.

Figure 1 shows a typical example of MEG at the occiput, EEGs at F8 and T3 of the international 10-20 electrode layout system and the results of 2-D analysis of phase difference in the condition that two different tasks. The trajectory in the condition of task A seems to be the π-correlation in the phase difference between MEG and two EEGs, and that in the condition of task B appears to be the π/2-correlation. The difference was not clearly detected at two different functional area of the brain in the same condition of imposed task, since trajectory was somewhat random even for the waves of equal frequency. This implies that the trajectories cannot be visually distinguished. Hence, we adopted an analysis of trajectory pattern by the Topology that is used to investigate a common property of different figures. The number of Euler characteristic was calculated for every sample, and the distribution was compared in the condition of task A and B (see Figs. 2 and 3). In the condition of task A, the Eulerian index number is distributed widely and has the tailing to the smaller side. On the other hand, the distribution in the condition of task B shows the sharp peak at -3 and its width is narrower than that in the condition of task A. It follows from these findings that many trajectories in the condition of task A are not topologically an in-phase in comparison with those in task B. In the condition of task A, the examinee is subjected to great stress to keep selflessness. Because various functional regions of the brain may be activated in order to stay in the condition of task A, trajectories of 2-D analysis of phase difference between EEG and MEG data appear in rather random patterns. On the other hand, the examinee uses the neural network controlling a specific brain activity when he keeps thinking or imaging his family (task B), resulting in the trajectory's patterns with a topologically common property.

In conclusion, it was effective practice for the visual inspection of change in brain activity that we conducted two-dimensional analysis of phase difference between MEG and EEG data measured at the same time and then investigated the distribution of the Eulerian indexes of those trajectories. The measuring system composed of one SQUID fluxmeter and two-channel EEG device can sensitively detect the data necessary for the phase difference analysis.

References

1) Cohen D., Science, **175**, 664-666 (1972).

2) Jirsa V. K. and Haken H., Physical Review Letters, **77** (No.5), 960-963 (1996).

3) Ahonen A. I., Hamalainen M. S., Kajola M. J., et al., IEEE Trans. Magn., **MAG 27**, 2793-2796 (1991).

4) Foglietti V., del Gratta C., Pasquarelli A., et al., IEEE Trans. Magn., **MAG 27**, 2959-2962 (1991).

5) Honig H. E., Daalmans G. M., Bar L., et al., IEEE Trans. Magn., **MAG 27**, 2777-2785 (1991).

6) Vrba J., Betts K., Burbank M., et al., IEEE Trans. on Applied Superconductivity, 3(No.1), 1878-1882 (1993).
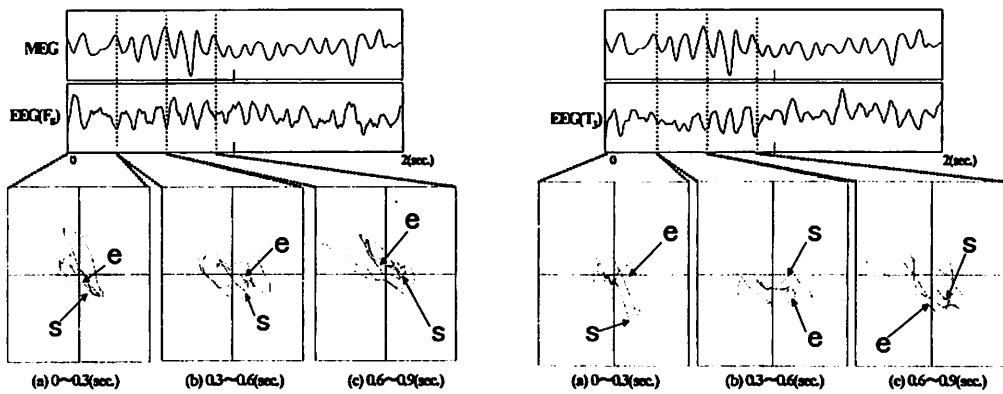
(a)The phase correlation (task A, at F8)   (b)The phase correlation (task A, at T3)
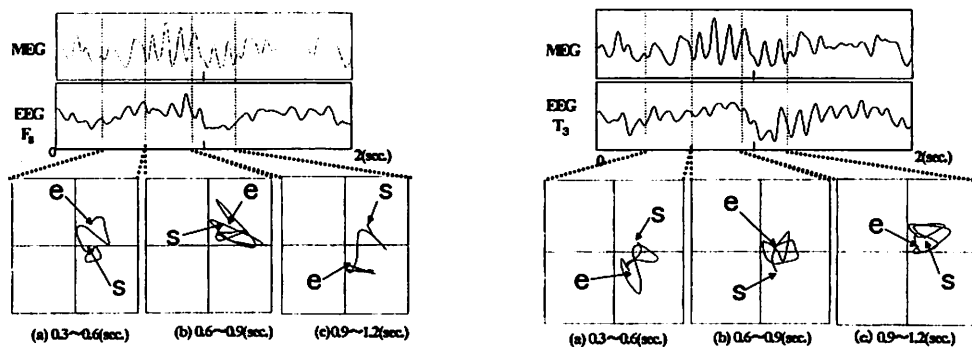
(c)The phase correlation (task B, at F8)   (d)The phase correlation (task B, at T3)

Fig. 1. The MEG data measured at the same time in the condition of two different tasks and their trajectory plots. (a):task A, EEG at F8, (b):task A, EEG at T3, (c):task B,EEG at F8, (d):task B,EEG at T3. The symbols of s and e respective denote the starting and the end points of the phase correlation.

95
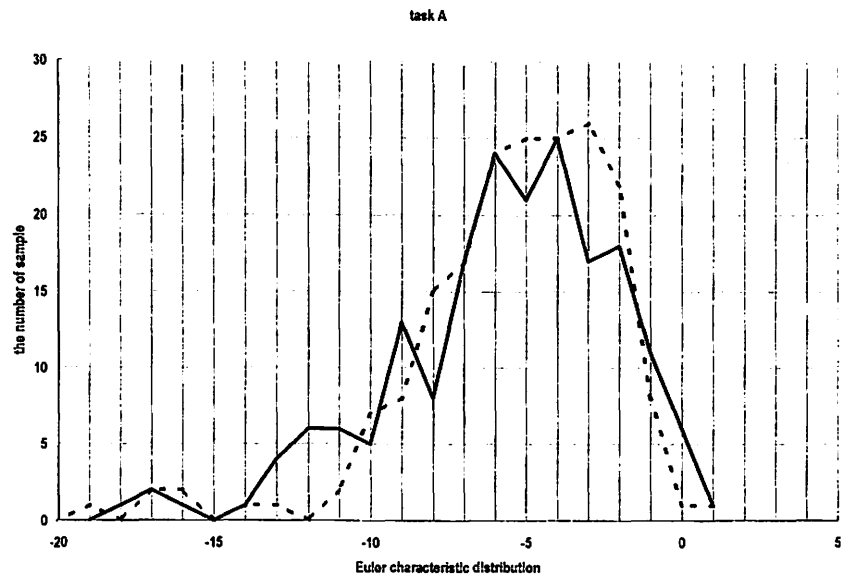
Fig. 2. The Euler characteristic distribution of 2-D analysis of phase difference between MEG and EEG in the condition of task A.   Solid line : EEG at F8 (right brain), Dashed line : EEG at T3 (left brain).
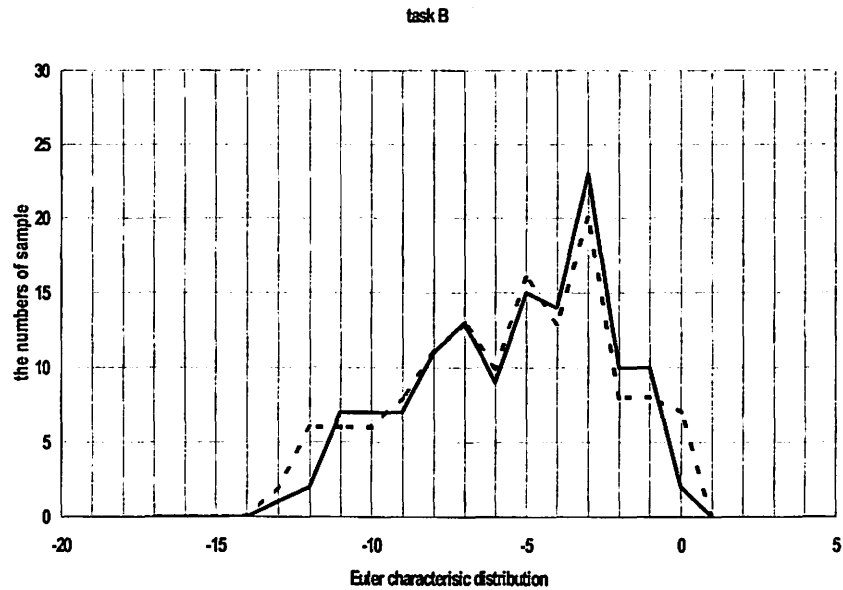
task B

Fig. 3.   The Euler characteristic distribution of 2-D analysis of phase difference between MEG and EEG in the condition of task B. Solid line : EEG at F8 (right brain), Dashed line : EEG at T3 (left brain).

II. CHEMISTRY

II. 1. Radiosynthesis of 1-[2-[^{18}F]Fluoro-1-(hydroxymethyl)-Ethoxy]methyl-2-Nitroimidazole ([^{18}F]FENI)

Wada H., Iwata R., Ido T., and Takai Y**.*

*CYRIC Tohoku University, Quantum Science and Energy Engineering, Tohoku University**
*School of Medicine, Tohoku University***.*

The 2-nitroimidazole nucleoside analog, RP-170[1-3], was developed as a potential radiosensitizer for hypoxic tumor cells and is reported to have similar reduction potential and radiosensitizing activity to those of misonidazole and etanidazole, which are metabolically trapped by hypoxic cells. Based on their selective binding and retention in hypoxic regions, it was expected that the radiolabeled derivative of RP-170 would serve as a useful probe for hypoxic tissues as does [^{18}F]fluoromisonidazole (FMISO)[4-8].

In this report, we describe a radiosynthesis of a fluorinated analog of RP-170, 1-[2-fluoro-1-(hydroxymethyl)-ethoxy]methyl-2-nitroimidazole (FENI) from no-carrier-added [^{18}F]fluoride.

The precursor 4 for the preparation of [^{18}F]FENI ([^{18}F]2) was synthesized from RP-170 (1), which was supplied by POLA Chemical Industries, Inc., according to the synthetic scheme shown in Figure 1. It was prepared in the overall yield of 44% based on 1.

Nca [^{18}F]fluoride was produced via the ^{18}O(p,n)^{18}F reaction with a Cypris HM12 cyclotron (Sumitomo Heavy Ind.) and added to a glass vial containing K.2.2.2. (30 mg) in MeCN (1 mL). The solution was heated at 110℃ and evaporated to dryness with the aid of a He flow. To the residue was added a solution of 4 (5-6 mg) in dry DMF (1 mL), and the reaction mixture was heated at 110℃ for 5 min (see Fig. 2a). The reaction was quenched by adding H$_2$O (10 mL), and the resulting mixture was passed through a Sep-Pak Plus C18 cartridge, which was then washed with 0.05 N HCl (10 mL) and H$_2$O (10 mL). The ^{18}F-fluorinated product, [^{18}F]5, retained by the C18 was eluted with MeCN (4 mL). The eluate was evaporated to dryness. To the residue was added a 0.05 N NaOH solution of 50% ethanol-in-water and the mixture was heated for 1 min at 40℃ (see Fig. 2b). The reaction mixture was passed through an IC-H Plus cartridge for neutralization, and the eluate was evaporated to dryness. The residue was dissolved in an HPLC solvent (MeCN-H$_2$O: 15/85) and injected onto a semi-preparative HPLC C18 column (A-324, 10 mm×300 mm, YMC). The effluent at a flow rate of 6.0 mL/min was monitored with both radioactivity and UV detectors, and the fraction containing the desired product was collected (see Fig. 3).

Chemical and radiochemical purity was assayed by analytical HPLC on a reverse phase C18 column (Inertsil ODS 80A, 4.6 mm×250 mm, GL Sciences) with a solvent system of MeCN-H_2O (30/70). No other radioactive peak than [^{18}F]FENI or no UV peak corresponding to FENI was found.

The radiosynthesis consists of commonly used procedures, two reaction steps of ^{18}F-substitution and deprotection and two purification steps of solid phase extraction and final HPLC separation. Among them the first step mainly determined the radiochemical yield of the present preparation. As shown in Fig. 2a, it was observed that the radiochemical yield of [^{18}F]5 gradually increased up to only 14% during the first 4 min and then decreased and more hydrophilic degradation products were found to increase in the reaction solution. It is suggested that the ether bond of 3 is likely to be cleaved by prolonged heating under the basic conditions.

The radioactive peak eluting at 6.5-7.0 min, corresponding to [^{18}F]FENI ([^{18}F]2), was collected and evaporated to dryness under reduced pressure. The residue was dissolved in saline. The overall synthesis time including HPLC purification and formulation was less than 90 min. The specific activity was estimated to be higher than 26 GBq/mmol (0.7 Ci/mmol) at the end of the synthesis. The average decay-corrected overall radiochemical yield was 6.2% (3-11%, 12 runs).

REFERENCES

1) Murayama C., Suzuki A., Suzuki T., Miyata Y., Sakaguchi M., Tanabe Y., Tanaka N., Mori T., *J. Radiation Oncology Biol. Phys.* 17 (1989) 575.

2) Sasai K., Shibamoto Y., Takahashi M., Abe M., Wang J., Zhou L., Nishimoto S., Kagiya T., *Jpn. J. Cancer Res.* 80 (1989) 1113.

3) Murayama C., Suzuki A., Sato C., Tanabe Y., Miyata Y., Shoji T., Suzuki T., Sakaguchi M., Mori T., *Int. J. Radiation Oncology Biol. Phys.* 22 (1991) 557.

4) Jerabek P.A, Patrick T.B., Kilbourn M.R., Dischino D.D., Welch M.J., *Appl. Radiat. Isot.* 37 (1986) 599.

5) Grierson J.R., Link J.M., Mathis C.A., Rasey J.S., Krohn K.A., *J. Nucl. Med.* 30 (1989) 343.

6) Lim J.-L., Berridge M.S., *Appl. Radiat. Isot.* 44 (1993) 1085.

7) McCarthy T.J., Dence C.S., Welch M.J. *Appl. Radiat. Isot.* 44 (1993) 1129.

8) Tada M., Iwata R., Sugiyama H. *et al.*, *J. Labelled Cpd. Radiopharm.* 38 (1996) 771.

Figure 1.   Synthetic method for [^{18}F]FENI.
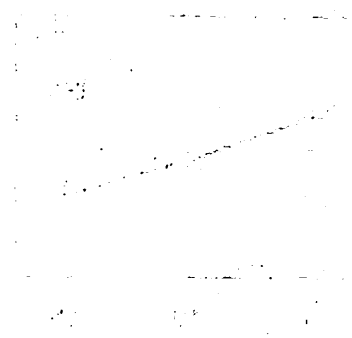
Figure 2.   Optimization of ^{18}F-substitution (a) and deprotection (b).

Figure 3.   Semi-preparative HPLC separation.

99
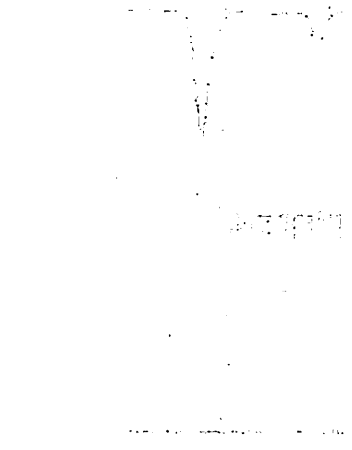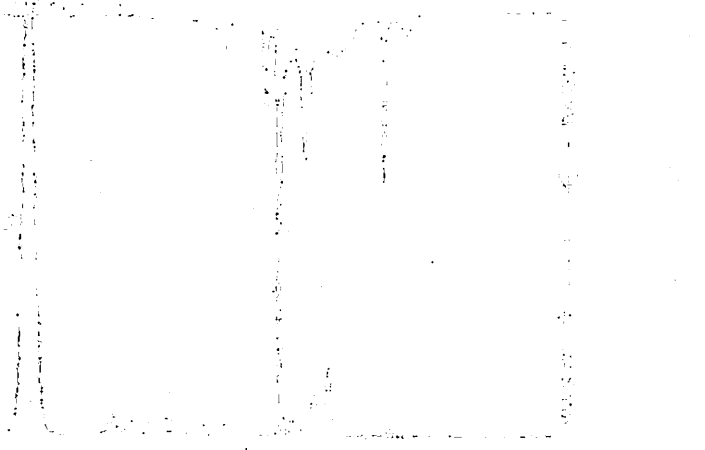
III.   MEDICINE AND BIOLOGY (Basic)

III. 1.   Mastoparan Causes Ca²⁺ Release from Skeletal Muscle Sarcoplasmic Reticulum through its Binding to a 97 kDa Protein

*Hirata Y. ⃰, Nakahata N.·** and Ohizumi Y.⃰*

Department of Pharmaceutical Molecular Biology, Graduate School of Pharmaceutical Sciences,
Tohoku University⃰
Department of Pharmaceutical Cellular Signaling Graduate School of Pharmaceutical Sciences,
*Tohoku University**

The $^{45}Ca^{2+}$ release from the heavy fraction of sarcoplasmic reticulum (HSR) was accelerated by mastoparan (MP), radiolabelable $[Tyr^3]MP$ or caffeine in a concentration-dependent manner.   The EC_{50} values for MP, $[Tyr^3]MP$ and caffeine were approximately 2.0 μM, 7.7 μM and 1.8 mM, respectively.   We succeeded in the synthesis of $[^{125}I\text{-}Tyr^3]MP$ with a high specific activity. $[^{125}I\text{-}Tyr^3]MP$ bound specifically to HSR with the K_D 4.0 μM and the B_{max} of 3.0 nmol/mg.   Furthermore, $[^{125}I\text{-}Tyr^3]MP$ specifically cross-linked to the 97 kDa protein without direct binding to ryanodine receptor.   The protein was not triadin or Ca^{2+}-pump, because anti-triadin antibody or anti-Ca^{2+}-pump antibody did not immunoprecipitate the protein.   These results suggest that the 97 kDa MP binding protein may have an important role in the excitation-contraction coupling of skeletal muscle.

Introduction

Ryanodine receptor (RyR) is highly enriched in endings of the skeletal muscle sarcoplasmic reticulum (SR) called terminal cisternae, which permit allosteric coupling between plasmalemmal dihydropyridine receptor and RyR[1].   The N-terminal domain of the RyR is a major site of interaction with regulatory proteins of the channel function[2]. However, the detailed mechanism of the modulation of RyR by the regulatory proteins containing SR intrinsic proteins remains to be solved.

MP, a tetradecapeptide from wasp venom, is originally found as a histamine releaser from mast cells[3].   Recently, MP-induced Ca^{2+} release from SR has been reported by two groups[4,5].   However, its detailed mechanism of action is unknown.

To clarify the molecular basis of action of MP, we synthesized $[^{125}I\text{-}Tyr^3]MP$ with a high specific activity.   Using the pharmacological probe, we showed for the first time that MP bound specifically to a 97 kDa protein in HSR of rabbit skeletal muscles.

Experimental Procedures

Materials.

MP (Ile-Asn-Leu-Lys-Ala-Leu-Ala-Ala-Leu-Ala-Lys-Lys-Ile-Leu-NH$_2$) and [Tyr^3]MP (Ile-Asn-Tyr-Lys-Ala-Leu-Ala-Ala-Leu-Ala-Lys-Lys-Ile-Leu-NH$_2$) were synthesized by a peptide synthesizer. HSR was prepared from rabbit skeletal muscle[6]. Synthesis of [^{125}I-Tyr^3]MP was performed by the chloramine-T method[7].

$^{45}Ca^{2+}$ release experiments.

The $^{45}Ca^{2+}$ release from HSR passively preloaded with $^{45}Ca^{2+}$ was measured at 0°C as described previously[8].

[^{125}I-Tyr^3]MP binding assay.

[^{125}I-Tyr^3]MP binding was examined as follows. HSR (200 µg/ml) was incubated with 0.1-100 µM [^{125}I-Tyr^3]MP for 15 min at 0°C 90 mM KCl, 50 mM MOPS-Tris (pH 7.0) and pCa 7. The amount of [^{125}I-Tyr^3]MP bound was determined by filtration using Whatman GF/B filters under reduced pressure. Nonspecific binding was determined in the presence of 0.5-1 mM unlabeled [Tyr^3]MP .

Cross-linking experiments.

The heterobifunctional photoreactive cross-linking agent Sulfo-SANPAH (10 mM) was reacted first with primary amines of [^{125}I-Tyr^3]MP (25 µM) to form a succinimindyl linkage at 0 °C in the dark in buffer containing 50 mM HEPES-Na (pH 7.4), 90 mM KCl, and pCa 7. The modified [^{125}I-Tyr^3]MP was coupled with free amino groups of HSR proteins (1 mg/ml) by photoactivation. The photoactivation was performed by exposing with long wave (254 nm) and short wave (360 nm) for 4 min at 0 °C. After ultrafiltration, the sample was incubated in the SDS sample buffer overnight at room temperature. After the samples were subjected to SDS-PAGE, analysis of [^{125}I-Tyr^3]MP binding to HSR proteins was performed by using with an image analyzer (Molecular Imager GS-363, Bio-Rad laboratories).

Immunoprecipitation experiments.

HSR proteins or HSR proteins cross-linked with [^{125}I-Tyr^3]MP were solubilized for 1h on ice at a protein concentration of 1 mg/ml in buffer containing 3% (w/v) CHAPS, 1.0 M NaCl, 1 mM dithiothreitol, 20 mM Tris-HCl (pH 7.4), and protease inhibitors. CHAPS-solubilized HSR proteins were diluted 10-fold in 20 mM Tris-HCl (pH 7.4) to reduce the high salt and detergent concentrations. Monoclonal (mouse) anti-triadin antibody (1: 50), monoclonal (mouse) anti- SR Ca^{2+}-pump antibody (1: 50) or monoclonal (mouse) anti-RyR antibody (1: 50) was added to the supernatants, and the samples were incubated for 2 h at 4°C, followed by further incubation with protein A-Sepharose 4B beads (0.27 mg/ml) for 2 h at

4°C.   Immunoprecipitates were washed two or three times with buffer containing 20 mM Tris-HCl (pH 7.4), 0.15 M NaCl, 0.3% CHAPS and pCa 7.   The samples were subjected to SDS-PAGE after the SDS sample buffer was added.

Results

Ca^{2+} release from HSR induced by MP or [Tyr^3]MP.

The effects of MP, [Tyr^3]MP and caffeine on $^{45}Ca^{2+}$ release from HSR vesicles were measured under the conditions in which the Ca^{2+}-pump did not work.   The $^{45}Ca^{2+}$ release was accelerated by MP, [Tyr^3]MP or caffeine in a concentration-dependent manner, but the maximum response to MP or [Tyr^3]MP was larger than that to caffeine (Fig. 1).   The EC_{50} values for MP, [Tyr^3]MP and caffeine were approximately 2.0 µM, 7.7 µM and 1.8 mM, respectively.

[^{125}I-Tyr^3]MP Binding to HSR.

We succeeded in the synthesis of a radio-labeled MP analogue [^{125}I-Tyr^3]MP with a high specific activity (1.3 kBq /pmol).   Fig. 2 shows a saturation curve and a corresponding Scatchard plot of [^{125}I-Tyr^3]MP binding to HSR.   Specific binding of [^{125}I-Tyr^3]MP to HSR was saturable (Fig. 2A).   Scatchard analysis revealed that [^{125}I-Tyr^3]MP bound to a single biding site with a K_D of 4.0 µM and B_{max} of 3.0 nmol/mg (Fig. 2B).   The K_D value was close to the EC_{50} value for [Tyr^3]MP in Ca^{2+} release.

Identification of 97 kDa protein bound to [^{125}I-Tyr^3]MP.

In order to identify the binding protein(s) for [^{125}I-Tyr^3]MP in HSR vesicles, we performed cross-linking experiments with using Sulfo-SANPAH.   We found that [^{125}I-Tyr^3]MP did not bind to RyR but to another protein of 97 kDa (Fig. 3B).   [^{125}I-Tyr^3]MP binding to the 97 kDa protein was inhibited by MP or unlabeled [Tyr^3]MP (500 µM) (Fig. 3 C).   To examine whether the 97 kDa protein is triadin or Ca^{2+}-pump, CHAPS-solubilized HSR proteins cross-linked with [^{125}I-Tyr^3]MP were immunoprecipitated with anti-triadin monoclonal antibody or anti-SR Ca^{2+}-pump monoclonal antibody.   These immunoprecipitated proteins were identified as triadin and Ca^{2+}-pump by immunoblotting using corresponding antibodies. (Fig. 4A and B).   However, the 97 kDa [^{125}I-Tyr^3]MP binding protein was not immunoprecipitated with anti-triadin monoclonal antibody or anti-SR Ca^{2+}-pump monoclonal antibody (Fig. 4C).   The 97 kDa protein was still detected in the supernatant after the immunoprecipitation (Fig. 4C).

Discussion

Under the conditions lacking the activity of the Ca^{2+}-pump at 0°C, MP or [Tyr^3]MP, like caffeine, induced $^{45}Ca^{2+}$ release from the $^{45}Ca^{2+}$-preloaded HSR in a concentration-dependent manner.   MP is 4-times more potent than [Tyr^3]MP in Ca^{2+} releasing activity.

The low sensitivity of [Tyr^3]MP would be the results from the replacement of Leu^3 by Tyr in the structure. However, it is likely that [Tyr^3]MP causes Ca^{2+} release with the same mechanism as MP, because both drugs showed the same maximum response.

We succeeded in the synthesis of [^{125}I-Tyr^3] MP to characterize the MP binding site. We found that [^{125}I-Tyr^3]MP bound to HSR in a replaceable and saturable manner, indicating the existence of a specific binding site. This site was of a single class with the K$_D$ value of 4.0 μM, which was similar to the EC$_{50}$ value for [Tyr^3]MP in ^{45}Ca^{2+} release. Therefore, the binding site of [^{125}I-Tyr^3]MP might be functionally important for the ^{45}Ca^{2+} release.

We found that [^{125}I-Tyr^3]MP specifically cross-linked with a 97 kDa protein, and the cross-linking was inhibited by MP or unlabeled [Tyr^3]MP. An immunoprecipitation by anti-RyR antibody did not recognize [^{125}I-Tyr^3]MP-bound RyR, then we can rule out a possibility that MP binds directly to RyRs (data not shown). These observations suggest that the 97 kDa protein interacts directly or indirectly with RyRs .

There are some proteins that have molecular mass of around 97 kDa in HSR, such as triadin[9], Ca^{2+}-pump[10] and the 90 kDa[11]. We examined whether the 97 kDa [^{125}I-Tyr^3]MP binding protein is triadin or not. However, the immunoprecipitated protein with anti-triadin monoclonal antibody was not [^{125}I-Tyr^3]MP binding protein, showing that the 97 kDa protein was not triadin. Furthermore, the immunoprecipitated protein with anti-SR Ca^{2+}-pump monoclonal antibody was not the 97 kDa [^{125}I-Tyr^3]MP binding protein.

In conclusion, MP induces Ca^{2+} release through RyR from HSR vesicle without directly binding to RyR. We identified a 97 kDa protein as the target protein for MP in HSR vesicle. The 97 kDa protein may have an important role in the excitation-contraction coupling of skeletal muscle. MP is a useful pharmacology probe for elucidating the functional role of the 97 kDa protein.

Acknowledgements

References

1) Rios E., Karhanek M., Ma J., and Gonzalez A., *J. Gen. Physiol.* **102** (1993) 449-481.
2) MacKrill J.J., *Biochem. J.* **337** (1999) 345-361.
3) Hirai Y., Kuwada M., Yasuhara T., Yoshida H., and Nakajima T., *Chem. Pharm. Bull.* **27**(1979)1945-1946.
4) Ikemoto T., Iino M. and Endo M., *Br. J. Pharmacol.***118** (1996) 690-694.
5) Longland C.L., Mezna M., Langel U., Hallbrink M., Soomets U., Wheatley M., Michelangeli F., and Howl J., (1998) *Cell. Calcium.* **24** (1998) 27-34.
6) Seino A., Kobayashi M., Kobayashi J., Fang Y.I., Ishibashi M., Nakamura H., Momose K.,

Ohizumi Y., *J. Pharmacol. Exp. Ther.* **256** (1991) 861-867.

7)   Hirata Y., Nakahata N., Ohkura M. and Ohizumi Y., *Biochim Biophys Acta* **1451** (1999)132-140.
8)   Furukawa K-I., Funayama K., Ohkura M., Oshima Y., Tu A.T. and Ohizumi Y., *Br. J Pharmacol.* **113** (1994) 233-239.
9)   Caswell A.H., Brandt N.R., Brunschwig J.P. and Purkerson S., *Biochemistry* **30** (1991) 7507-7513.
10) MacLennan D.H., Rice W.J. and Green N.M., *J. Biol. Chem.* **272** (1997) 28815-28818.
11) Guo W., Jorgensen A.O. and Campbell K.P., *J. Biol. Chem.* **269** (1994) 28359-28365.
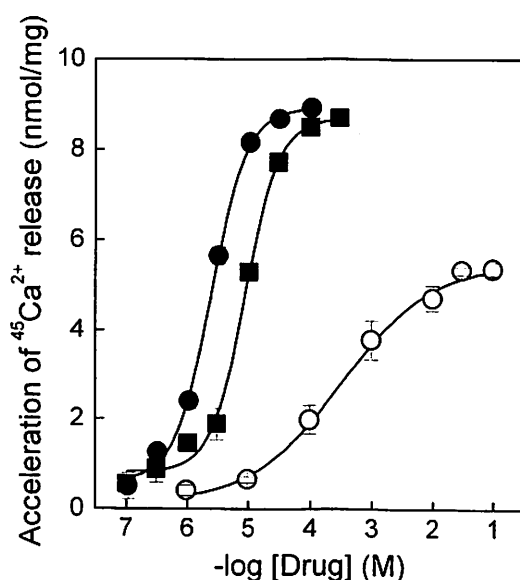
Fig. 1.   Concentration-dependent acceleration of $^{45}Ca^{2+}$ release from HSR by MP, [Tyr^3]MP and caffeine at pCa 7.   The content of $^{45}Ca^{2+}$ in HSR was measured at 0°C by the filtration method.   Each value was calculated as difference in the amount of released $^{45}Ca^{2+}$ measured in the presence and absence of the test substance.   caffeine (O); MP (●); [Tyr^3] MP (■).   Values are means ± S.E.M. (n=3).
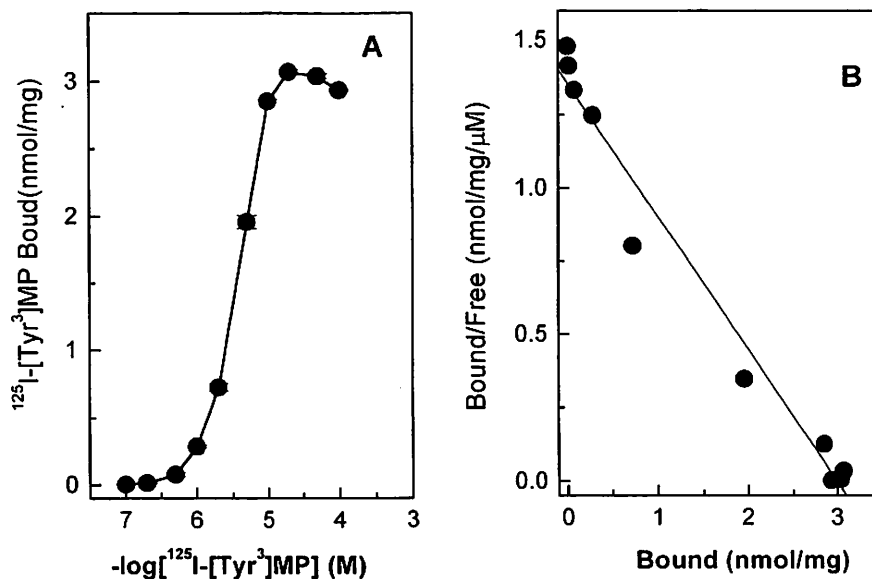
Fig. 2.   Saturation (A) and Scatchard (B) plots of [^{125}I-Tyr^3] MP binding to HSR.   HSR (200 μg/ml) was incubated with ^{125}I-Tyr^3]MP (0.1-100 μM) at 0°C for 15 min.   The amount of [^{125}I-Tyr^3]MP bound was measured, as described in *Experimental Procedures*.   Values are means ± S.E.M. (n=3).
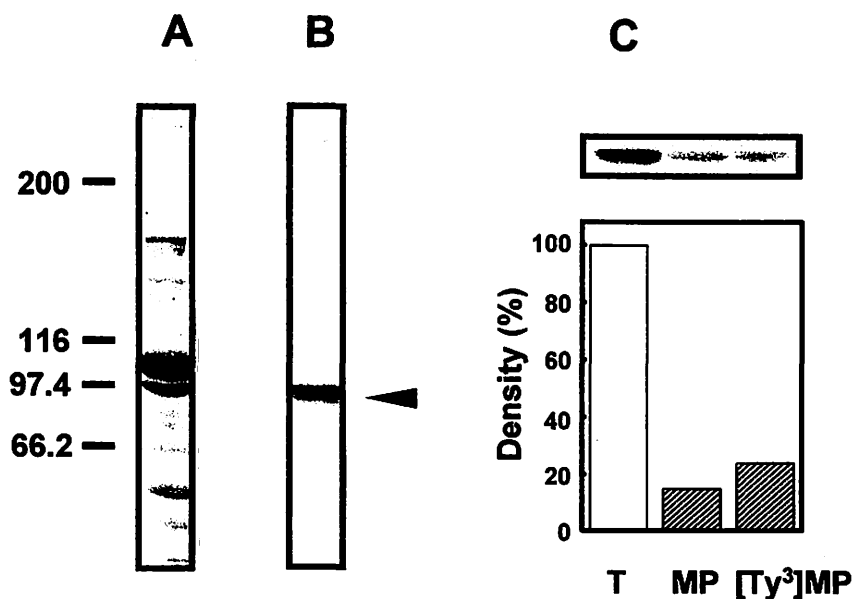
Fig. 3. Identification of the 97 kDa [^{125}I-Tyr^3] MP binding protein. A, a coomassie blue-stained HSR proteins. B, 97 kDa protein cross-linked with [^{125}I-Tyr^3]MP using Sulfo-SANPAH. C, Inhibition of [^{125}I-Tyr^3]MP binding to the 97 kDa protein by MP (500 μM) or unlabeled [Tyr^3]MP (500 μM). The relative density of 97 kDa protein cross-linked with [^{125}I]MP (T) was analyzed in the presence of MP or [Tyr^3]MP.
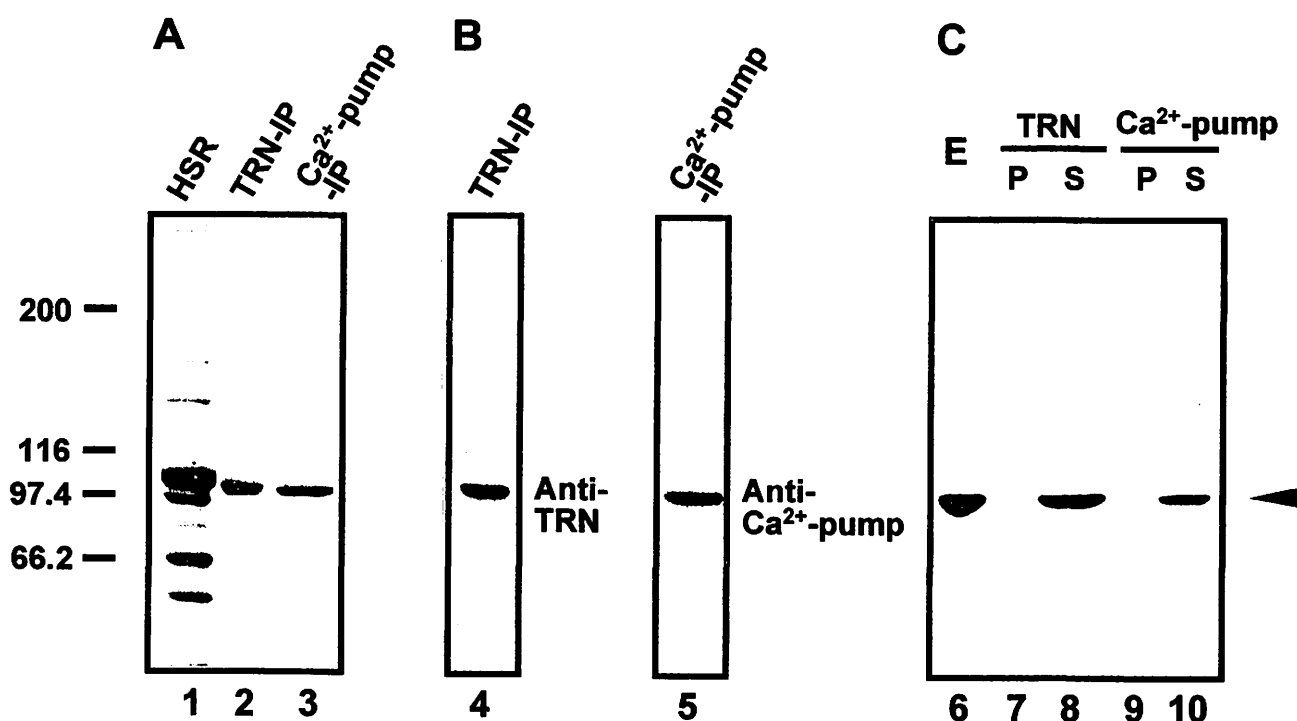
Fig. 4. Immunoprecipitation with anti-triadin or anti-Ca^{2+}-pump antibody of solubilized HSR proteins cross-linked with [^{125}I-Tyr^3]MP. A, a Coomassie blue-staining. Native HSR proteins (HSR, lane 1), immunoprecipitate with anti-triadin monoclonal antibody (TRN-IP, lane 2) and immunoprecipitate of anti-SR Ca^{2+}-pump monoclonal antibody (Ca^{2+}-pump-IP, lane 3). B, immunoblotting of immunoprecipitated material with anti-triadin monoclonal antibody (Anti-TRN, lane 4) or anti-SR Ca^{2+}-pump monoclonal antibody (Anti-Ca^{2+}-pump, lane 5). C, the CHAPS extract prepared from HSR proteins cross-linked with [^{125}I-Tyr^3]MP was incubated with anti-triadin monoclonal antibody (TRN) or with anti-SR Ca^{2+}-pump monoclonal antibody (Ca^{2+}-pump). [^{125}I-Tyr^3]MP binding protein was analyzed with an image analyzer. The CHAPS extract (E, lane 6), immunoprecipitate with anti-triadin monoclonal antibody (P, lane 7) or anti-SR Ca^{2+}-pump monoclonal antibody (P, lane 9), and the corresponding supernatants (S, lane 8, 10).

III. 2. Neuroprotective Effects of Monoamine Oxidase Inhibitor and Glutamate Receptor Inhibitor on MPTP-induced Dopamine and DOPAC Depletion in Mice

Kumagai T., Kosaka R., Ido T., Araki T.*, Imai Y.*, Mizugaki M.**
and Itoyama Y.***

Cyclotron and Radioisotope Center, Tohoku University
Department of Clinical Pharmacology and Therapeutics,
Tohoku University Graduate School of Science and Medicine*
Department of Pharmaceutical Sciences, Tohoku University Hospital**
Department of Neurology, Tohoku University School of Medicine***

Introduction

1-Methyl-4-phenyl-1,2,3,6-tetrahydropyridine (MPTP) is well known to produce clinical, biochemical and neuropathological changes analogous to those observed in idiopathic Parkinson's disease. This neurotoxin also leads to a decrease of dopamine content in the striatum and loss in the number of the nigrostriatal dopaminergic neurons in several species including monkeys[1,2], dogs[3,4], cats[5] and mice[6,7]. The neurotoxic effects of MPTP are thought to be initiated by MPP$^+$, which is a major metabolite formed by the monoamine oxidase (MAO) B-mediated oxidation of MPTP[8]. MPP$^+$ is relatively taken up by high affinity dopamine and noradrenaline uptake systems and is subsequently accumulated within mitochondria of nigrostriatal dopaminergic cells. There it disrupts oxidative phosphorylation by inhibiting complex I of the electron transport chain[9]. This can lead to a number of deleterious effects on cellular functions, resulting in neuronal cell death. Therefore, MPTP is widely used as a rodent model of Parkinson's disease.

To examine whether N-methyl-D-aspartate (NMDA) receptors or MAO are related to the neurotoxicity induced by MPTP, we investigated possible effects of NMDA receptor antagonist MK-801 and MAO inhibitor pargyline in the striatum of MPTP-treated mice.

Materials and Methods

Male C57BL/6 mice (22-28 g) were used in this study. The mice received intraperioneal four injections of MPTP (10 mg/kg) at 1 h intervals, the total dose per mice being 40 mg/kg. In the present study, there were no died animals after MPTP treatments. The mice were sacrificed by cervical dislocation at 1, 3 and 7 days after the last MPTP injection for biochemical study as described below.

Measurement of dopamine and its metabolite

The mice were killed by cervical dislocation at 1, 3 and 7 days after MPTP treatments. After decapitation, brains were quickly removed and the two striata were rapidly dissected out freehand on an ice-cold glass Petri dish. Samples were immediately weighted, then frozen and stored at -80°C until assay. The dissection procedure was performed in less than 2 min. Striata were sonicated ice-cold 0.2 M perchloric acid containing 100 ng/ml isoproterenol as internal standard. Homogenates were centrifuged at 2500 rpm for 15 min at 4°C. The supernatant was filtered (pore size 0.45 μm, Millipore filter) and a 30 μl aliquot of the supernatant was used for determination of the content of the dopamine, 3,4-dihydroxyphenyl acetic acid (DOPAC) and isoproterenol by high-performance liquid chromatography (HPLC) with an electrochemical detector (ECD) (Eicom, Japan). The mobile phase consisted of 0.1 M sodium citrate-0.1 M sodium acetate solution (pH 3.5) including 1.064 M octane sulfonic acid and 0.013 mM EDTA 2Na and 15% (v/v) methanol. The recoveries of dopamine, DOPAC and isoproterenol through the present procedures were > 93%. Levels of dopamine and its metabolite were calculated from the comparison of simple peak area with internal standard peak region and are expressed as μg/g tissue weight. Each group contained 5-9 mice.

Experimental design

The animals were divided into 7 groups; (1) Vehicle (saline)-treated group; (2)Pargyline (10 mg/kg)-treated group; (3) MK-801 (3 mg/kg)-treated group; (4) MPTP- and saline-treated group; (5) MPTP- and pargyline (10 mg/kg)-treated group; (6) MPTP- and MK-801 (1 mg/kg)-treated group; (7) MPTP- and MK-801 (3 mg/kg)-treated group. The mice were injected intraperitoneally (i.p.) with pargyline, MK-801 or saline 30 min before and 90 min after the first administration of MPTP (Groups 4, 5, 6 and 7). For groups 1, 2 and 3, pargyline (10 mg/kg)-, MK-801 (3 mg/kg)- or saline-treated mice were injected i.p. in the same manner with saline treatments instead of MPTP. In addition, pargyline hydrochloride (Sigma) and MK-801 maleate (Research Biochemicals Int.) were dissolved in saline. The mice were killed by cervical dislocation at 3 days after the last MPTP treatment to measure dopamine and its metabolite in the striatum.

All values were expressed as means ±S.E. and statistical significance was evaluated using an analysis of variance (ANOVA) followed by Williams multiple range test.

Results

The depletion in dopamine and DOPAC content of the striatum induced by MPTP is shown in Fig. 1. Effects of pargyline and MK-801 on the striatal dopamine and DOPAC depletion in MPTP-treated mice are presented in Tables 1 and 2.

The striatal dopamine and DOPAC levels were significantly decreased from 1 day after MPTP treatments. Thereafter, the striatal dopamine and DOPAC levels were markedly

reduced at 3 and 7 days after MPTP treatments as shown in Fig. 1. In addition, the depletion in striatal dopamine and DOPAC concentrations reached maximal levels at 3 days after MPTP treatments. Although four injections of MPTP caused a marked decrease in dopamine and DOPAC content of the mouse striatum after 3 days, pargyline was completely protective against MPTP-induced dopamine depletion in the striatum of mice (Table 1). However, this compound did not show a significant effect on the striatal DOPAC levels in mice 3 days after MPTP treatments (Table 1). In contrast, MK-801 failed to protect against MPTP-induced dopamine depletion in the mouse striatum. However, this drug prevented a significant reduction in the striatal DOPAC content of mice 3 days after MPTP treatments (Table 2).

Discussion

In the present study, we investigated the neuroprotective effects of pargyline and MK-801 on MPTP-induced decrease in dopamine and its metabolite in the mouse striatum. MPTP caused a significant reduction in dopamine and DOPAC levels from 1 day. Thereafter, the depletion in the striatal dopamine and DOPAC concentrations reached maximal levels at 3 days after MPTP treatments. Therefore, we evaluated the effects of two drugs on the striatal dopamine and DOPAC levels at 3 days after MPTP treatments.

MPTP is known to convert by the action of MAO-B to MPP[+], which is the neurotoxic metabolite[10]. It has been shown that MAO inhibitors, especially MAO-B inhibitors, can protect against MPTP-induced dopamine depletion and nigrostriatal dopaminergic cell death by preventing the conversion of MPTP to MPP[+] [6,11]. In the presented study, pargyline (a relatively selective inhibitor of MAO-B) was completely protective against MPTP-induced striatal dopamine depletion in mice. Furthermore, mice given pargyline and saline had the striatal dopamine levels higher than saline values. The findings suggest that pargyline can inhibit the conversion of dopamine to DOPAC.

MK-801 is one of the most potent and selective NMDA receptor antagonist available and has been used as a neuroprotectant to decrease ischemic injury in experimental animals. The role of NMDA receptors had also been extensively discussed in epilepsy, stroke and neurodegenerative disorders such as Huntington's disease, Alzheimer's disease, and amyotrophic lateral sclerosis[12]. Interestingly, some previous evidences demonstrate that MPP[+] toxicity is mediated by NMDA receptors[13,14]. In contrast, other reports suggest that MK-801 failed to protect against the nigral neurotoxicity caused by systemic administration of MPTP in mice or after local MPP[+] injections in rats[15,16]. Thus, much evidence for the efficacy of MK-801 against MPTP-induced parkinsonian animals is contradictory. In the present study, MK-801 showed no significant change on MPTP-induced dopamine depletion of the mouse striatum. Therefore, our findings seem to suggest that NMDA receptors are not mainly involved in mediating MPTP- or MPP[+]-induced neurodegeneration.

In the present study, of interest is that MK-801 dose-dependently protected against MPTP-induced DOPAC depletion in the striatum of mice. The reason for this phenomenon is presently unclear. However, for both dopamine and DOPAC concentrations in MPTP-treated mice, MK-801 showed a tendency to increase these concentrations. Therefore, the findings seem to suggest that NMDA receptor antagonist can partially protect against MPTP-induced neurodegeneration.

In conclusion, our results show that NMDA receptors are not mainly involved in mediating MPTP-induced neurodegeneration, whereas MAO-B plays a crucial role in MPTP-induced degeneration of the nigrostriatal dopaminergic neuronal pathway.

References

1) Burns R. S., Chiuen C. C., Markey S. P., Ebert M. H., Jacobowitz D. M. and Kopin I. J., Proc. Natl. Acad. Sci. USA **80** (1983) 4546.

2) Ferrante R. J., Hantraye P., Brouilet E. and Beal M. F., Brain Res. **823** (1999) 177.

3) Rapisardi S. C., Warrington V. O. and Willson J. S., Brain Res. **512** (1990) 147.

4) Johannessen J. N., Sobotka T. J., Weise V. K. and Markey S. P., J. Neurochem. **57** (1991) 981.

5) Schneider J. S. and Markhan C. H., Brain Res. **373** (1986) 258.

6) Heikkila R. E., Manzino L., Cabbat F. S. and Duvoisin R. C., Nature **311** (1984) 467.

7) Arai N., Misugi K., Goshima Y. and Misu Y., Brain Res. **515** (1990) 57.

8) Tipton K. F. and Singer T. P., J. Neurochem. **61** (1993) 1191.

9) Gluck M. R., Krueger M. J., Ramsey R. R., Sabin S. O., Singer T. P. and Nicklas W. J., J. Biol. Chem. **269** (1994) 3167.

10) Markey S. P., Johannessen J. N., Chiuen C. C., Burns R. S. and Herkenham M. A., Nature **311** (1984) 464.

11) Heikkila R. E., Hess A., Duvoisin R. C., Science **224** (1984) 1451.

12) Olney J. W., Biol. Psychiatr. **26** (1989) 505.

13) Turski L., Bressler K., Rettig K. J., Löshmann P. A. and Wachel H., Nature **349** (1991) 414.

14) Storey E., Hyman B. T., Jenkins B., Brouillet E., Miller J. M., Rosen B. R. and Beal M. F., J. Neurochem. **58** (1992) 1975.

15) Kupsh A., Löshmann P. A., Sauer H., Arnold G., Renner P., Pufer D., Burg M., Wachtel H., ten Bruggencate G. and Oertel W. H., Brain Res. **592** (1992) 74.

16) Sonsalla P. K., Zeevalk G. D., Manzino L., Giovanni A. and Nicklas W. J., J. Neurochem. **58** (1992) 1979.

Table 1. Effects of pargyline on the striatal dopamine and DOPAC content in MPTP-treated mice

Treatments	Dopamine (μg/g tissue)	DOPAC (μg/g tissue)
Vehicle(saline)	9.69 ± 0.70**	4.60 ± 0.58**
Pargyline (10 mg/kg)	14.83 ± 1.32**	2.40 ± 0.32
MPTP+saline	1.97 ± 0.30	2.01 ± 0.21
MPTP+pargyline (10 mg/kg)	12.82 ± 0.42**	2.35 ± 0.13

Values are expressed as mean±S.E. **p<0.01, compared with MPTP+saline group (Williams multiple range test). n=5-6. Drug treatments schedules were expressed in experimental design section.

Table 2. Effects of MK-801 on the striatal dopamine and DOPAC content in MPTP-treated mice

Treatments	Dopamine (μg/g tissue)	DOPAC (μg/g tissue)
Vehicle(saline)	9.69 ± 0.70**	4.60 ± 0.58*
MK-801 (10 mg/kg)	11.11 ± 0.46**	4.91 ± 0.35*
MPTP+saline	1.97 ± 0.30	2.01 ± 0.21
MPTP+MK-801 (3 mg/kg)	3.22 ± 0.69	5.32 ± 1.37**
MPTP+MK-801 (10 mg/kg)	1.83 ± 0.19	6.31 ± 0.75**

Values are expressed as mean±S.E. *p<0.05, **p<0.01, compared with MPTP+saline group (Williams multiple range test). n=5. Drug treatments schedules were expressed in experimental design section.
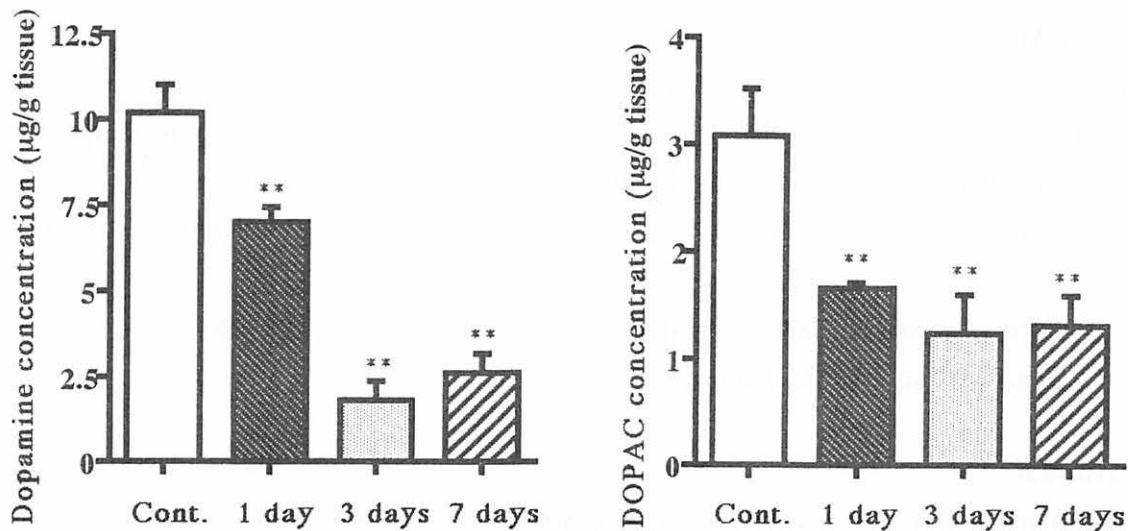
Figure 1. Levels of dopamine and DOPAC in the striatum after MPTP treatments.
Cont. ; saline-treated mice, 1 day; mice 1 day after MPTP treatments, 3 days; mice 3 days after MPTP treatments, 7 days; mice 7 days after MPTP treatments.   Left half: dopamine levels.   Right half; DOPAC levels.   Values are expressed as mean ±S.E. **p<0.01, compared with (Cont.) saline-treated group (Williams multiple tange test). n=6-9.

III. 3. Metabolism of [18F]fluorodiacylglycerol in Rat Hippocampal Neurons *in Vitro*

Wakayama K. and Ido T.

Cyclotron and Radioisotope Center, Tohoku University

Introduction

Positron emission tomography (PET) has been contributed for the clinical diagnosis of various diseases, especially brain disorders by measuring cerebral blood flow, oxygen consumption and metabolism. Recent developments in positron-emitting radio labeled ligands have made it to measure the binding capacity of many kinds of neurotransmitter receptors in humans. However, it is difficult to measure exactly the neuronal activities in the central nervous system (CNS) at present. In order to solve this problem, Imahori *et al.* have focused on the diacylglycerol as a second messenger in intracellular signal transduction system and designed carbon-11 labeled 1,2-*O*-diacylglycerol ([11C]DAG) as an excellent tracer to enter the receptor-mediated Phosphoinositide (PI) turnover[1]. These attempts are of interest in relation to the viewpoint for imaging second messenger systems in human brains.

We recently succeeded to synthesize the DAG analogues with fluorine-18 (*rac*-1,2-[18F]FDAG). We also observed that these compounds can produce unique patterns in PI turnover, as compared with [11C]DAG. The administrated *rac*-1,2-[18F]FDAG in rats was mainly metabolized into phosphatidyl-ethanolamine (PE) and phosphatidylcholine (PC), which are potent substrates for phospholipase D (PLD)[2]. These results indicate that *rac*-1,2-[18F]FDAG can be a novel tracer to evaluate receptor-mediated neuronal activities linked with PLD.

In order to examine exactly possible role of novel tracer with fluorine-18, we carried out in vitro study using hippocampal neurons.

Methods

Isolation and culture of rat hippocampal neurons

Rat embryonic hippocampal neurons were obtained from pregnant Sprague-Dawley rats with 18 days gestation. Brains were removed quickly from the embryos. Typically, hippocampi were dissected from the brains, and placed in 5.0 ml of Ca^{2+}- and Mg^{2+}-free phosphate-buffered saline (PBS) containing 0.125% trypsin/ 0.01% DNase for 10 min at 37°C. After adding 1 ml of fetal calf serum (FCS) to inhibit the activity of trypsin, cells

were dissociated by trituration with 1 ml and 200 µl polypropylene pipet tips. The preparation was centrifuged at 800 g for 5 min and then the pellet was gently re-suspended in Neurobasal/B27 (25µM 2-mercaptoethanol) medium. The cells were seeded on a 25 cm^2 flask coated with poly-D-lysine at concentration of 3.2×10^5 cells /cm^2.

Radio synthesis of rac-1,2-[^{18}F]FDAG

rac-1,2-[^{18}F]FDAG was synthesized from no-carrier-added [^{18}F]fluoride[3] and solubilized to Ca^{2+}- and Mg^{2+}-free PBS with negative charged liposome[4].

Metabolism of rac-1,2-[^{18}F]FDAG on rat hippocampal neurons

Rat hippocampal neurons cultured for 7-10 days were used. After washing twice cell surface with 2 ml of PBS, rac-1,2-[^{18}F]FDAG preparation in this study (0.5 mCi /2 ml /flask) was applied to the neurons with or without indicated drugs, and the cells were incubated up to 60 min. The reaction was terminated by removing the solution and adding 2 ml of ice-cold PBS to each flask.

Lipid extraction

After stopping the reaction, cell surface was washed twice by adding 2 ml of ice-cold PBS. The cells were detached by adding 0.125% trypsin, replaced to 15 ml tube, centrifuged at 800 g for 5 min. After removing supernatant, the cells were further washed by adding 1 ml of PBS and repeated passings through a 1 ml blue pipet tip. After centrifugation of the cell suspension at 1200 g for 5 min, 400 µl of chloroform/methanol (2/1 v/v) and 20µl of water were added into the pellet; the mixture was sonicated at 30°C for 5 min and centrifuged at 1200 g after adding 200 µl of methanol. The supernatant was transferred to other tube, and 100 µl of chloroform/methanol (1/2 v/v) and 5 µl of 5% KCl solution were added into the pellet by the same procedure as described above. Then the supernatants were collected.

Metabolites analysis

Radioactivities in the extract was measured with a well-type gamma counter and the radioactive metabolites in the extract were separated by thin layer chromatography (TLC) using a silica gel plate and a solvent system (chloroform:acetone: methanol:acetic acid:water, 45:15:13:12:8 v/v). The radioactivity in each metabolite was measured using image analyzer BAS5000.

Results and Discussion

Lipidic fractions were extracted from neurons exposed to rac-1,2-[^{18}F]FDAG up to 60min. rac-1,2-[^{18}F]FDAG metabolites produced by phospholipid turnover such as [^{18}F]PE,

[^{18}F]PC and [^{18}F]phosphoinositides ([^{18}F]PIs) were detected by TLC analysis (Fig. 1(A)). By measuring these activities, the present study was showed that [^{18}F]PE and [^{18}F]PC were the main metabolites (37% and 24% in whole phospholipid, respectively)(Fig. 1(B)). These findings suggest that rac-1,2-[^{18}F]FDAG was trapped on cell surfaces of neurons and incorporated into the phospholipid turnover associated with the intracellular signal transduction, particularly PLD.

rac-1,2-[^{18}F]FDAG metabolism into phospholipids without a drug stimulus reached a steady state at 30 min. On the other hand, the stimulus with carbachol, agonist of muscarinic cholinergic receptor (mAChR) conjugated with PLC, caused a time-dependent increase of the rac-1,2-[^{18}F]FDAG incorporation at least up to 60 min (Fig. 2(A)). As shown in Fig. 2(B), the increase of whole phospholipid was mainly due to the incorporation of rac-1,2-[^{18}F]FDAG into [^{18}F]PE.

There was no correlation between metabolism of rac-1,2-[^{18}F]FDAG and carbachol concentration (>10μM). The metabolic ratio into phospholipids was significantly larger than the control (about 150% of control). Among them, [^{18}F]PIs and [^{18}F]PE was increased as compared with the control (150% and 170% of control respectively), whereas [^{18}F]PC did not show significant difference (Fig. 3). These responses were inhibited by pre-incubation of atropine, mAChR antagonist (Fig. 4). Since PIs and PE are substrates for PLC and PLD, respectively, it is conceivable that rac-1,2-[^{18}F]FDAG is incorporated into the phospholipid turnover associated with neuronal signal transduction. No difference was observed in metabolism into [^{18}F]PC between carbachol-treated and the control neurons. The results suggest that the conversion of rac-1,2-[^{18}F]FDAG into [^{18}F]PC is caused by re-construction of cellular membrane.

When neurons were treated with phorbol 12-myristate 13-acetate (PMA), PKC-dependent PLD activator, the rac-1,2-[^{18}F]FDAG metabolic ratio into [^{18}F]PIs had a low value as compared with carbachol-treated neurons (about 120% of control)(Fig. 5). It is well known that PMA doesn't activate PLC directly. Therefore, our findings suggest that PLD activation caused the increase of rac-1,2-[^{18}F]FDAG metabolic ratio into [^{18}F]PE because that rac-1,2-[^{18}F]FDAG could not be incorporated into the PI turnover. It also suggests that the increase of [^{18}F]PE in carbachol-treated neurons is not due to the PLC activation but due to the PLD activation.

Both stimulus studies with carbachol and PMA showed 5-fold higher metabolic ratio into [^{18}F]PE as compared with into [^{18}F]PIs. Taken together, these results suggest that rac-1,2-[^{18}F]FDAG is incorporated into the PE-PLD turnover mainly and metabolized into [^{18}F]PE finally.

In conclusion, these results demonstrate the activation of rac-1,2-[^{18}F]FDAG metabolism mediated by PLD in rat hippocampal neurons. Therefore, we suggest that rac-1,2-[^{18}F]FDAG may be useful as a novel tracer for imaging signal transductions in brain

neurons.

References

1) Imahori Y. and Ido T., *Med. Chem. Res.*, **5**, 97 (1995).
2) Takahashi Y., Ido T. et al., *J. Label. Compd. Radiopharm.*, **35**, 517 (1994).
3) Furumoto S., Iwata R., Ido T., *J. Labelled Compd. Radiopharm.* (in press).
4) Ido T., Imahori Y. et al., *J. Label. Compd. Radiopharm.*, **40**, 631 (1995).
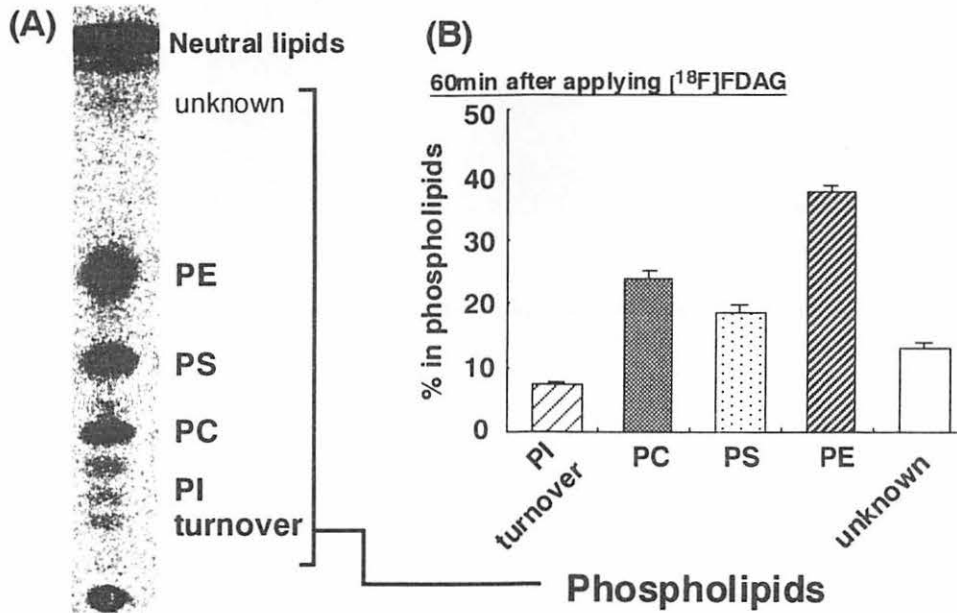
Fig. 1. Chromatographic analysis of phospholipids in rat hippocampal neurons using [18F]FDAG.
(A) radio-TLC profile of rat hippocampal neurons after 60min labeling. Chloroform/ Acetone/ MeOH/ AcOH/ Water = 45/ 15/ 13/ 12/ 8. (B) Phospholipids ratio in rat hippocampal neurons after 60min labeling. Each column represents the mean ± S.E.M. (n=15).
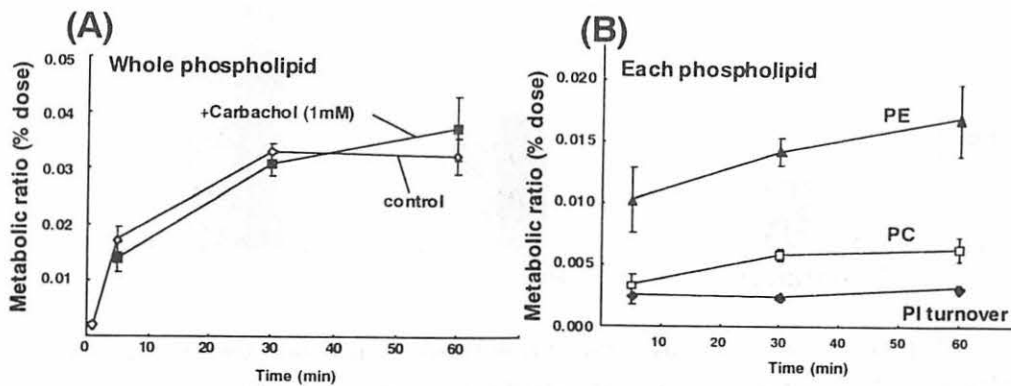
Fig. 2. Time course of [18F]FDAG metabolic ratio into phospholipids of neurons exposed to carbachol (1mM) and [18F]FDAG
Each point represents the mean ± S.E.M.(n=3-15).

114
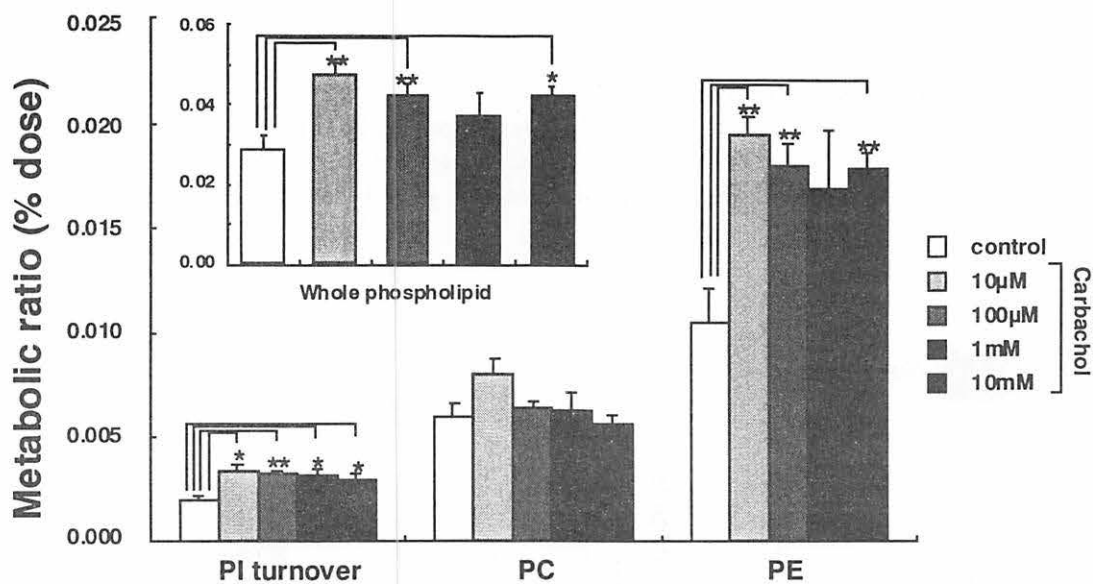
Fig. 3. [^{18}F]FDAG metabolic ratio into phospholipids of neurons exposed to carbachol and [^{18}F]FDAG for 60min

Each column represents the mean ± S.E.M.(n=3-14). **:P<0.01, *:P<0.05: significantly different from the control by Student's t -test.
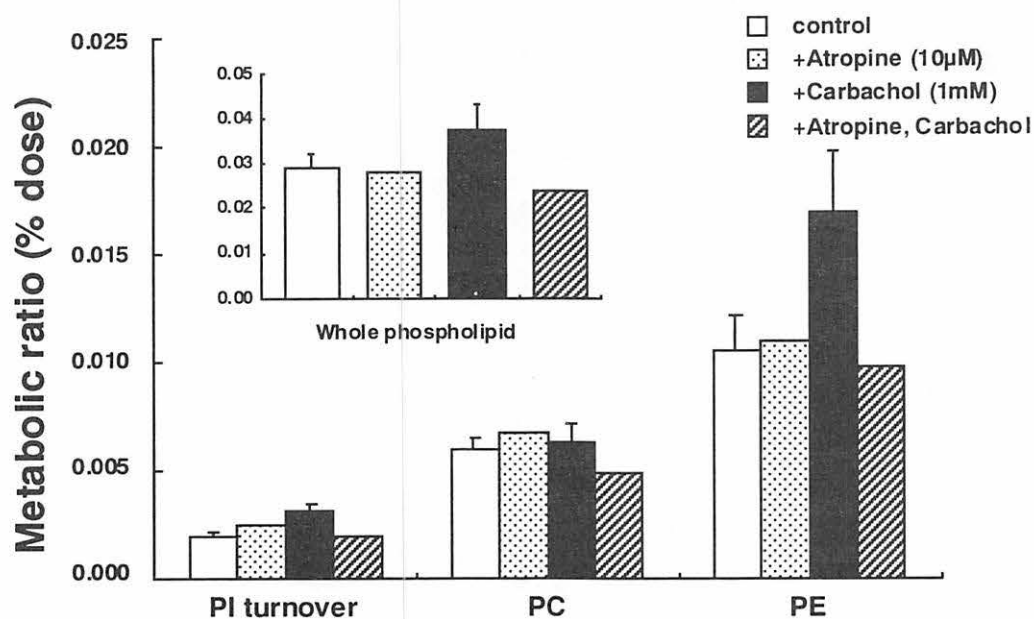
Fig. 4. [^{18}F]FDAG metabolic ratio into phospholipids of neurons exposed to carbachol and [^{18}F]FDAG for 60min after pre-incubated with atropine for 10min

Open- and closed-column represents the mean ± S.E.M. (n=3-15).
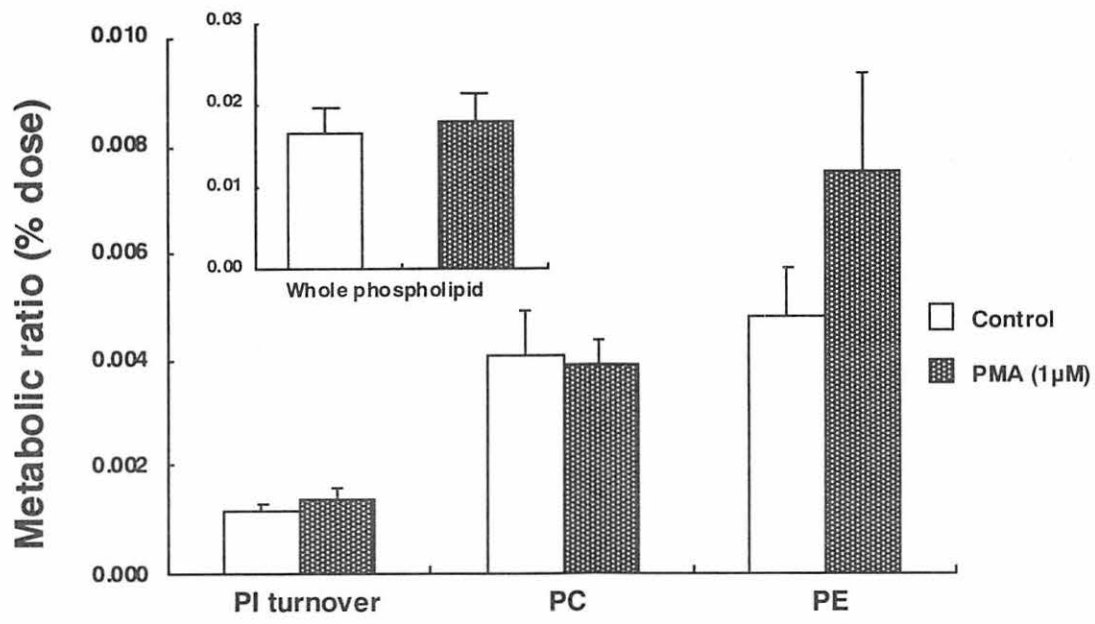
Fig. 5. [^{18}F]FDAG metabolic ratio into phospholipids of neurons exposed to PMA and [^{18}F]FDAG for 60min

Each column represents the mean ± S.E.M.(n=3-5).

III. 4. Nitric Oxide Synthase Inhibitors Induce Motor Abnormality in Mice

Mizutani H., Araki T.*, Matsubara M.**, Imai Y.*, Mizugaki M.
and Itoyama Y.***

Department of Pharmaceutical Sciences, Tohoku University Hospital
Department of Clinical Pharmacology and Therapeutics, Tohoku University Graduate
School of Science and Medicine *
Second Department of Internal Medicine, Tohoku University School of Medicine **
Department of Neurology, Tohoku University School of Medicine ***

Introduction

Nitric oxide (NO) is an intracellular and short-lasting messenger molecule that is synthesized from L-arginine in several tissues by a reaction catalyzed by NO synthase (NOS)[1,2]. In the central nervous system (CNS), NO has been proposed to be implicated in many physiological, pathological and biochemical conditions, such as learning and memory[3,4]. NOS has been also localized in the neuronal cells in specific regions, with highest expression in neurons of the cerebellum and olfactory bulb of rat brains, by immunohistochemical studies[5]. Therefore, these observations are of interest with regard to the role of NO in the regulation of neuronal function.

Several studies suggest that N^G-nitro-L-arginine, a non-selective NOS inhibitor, can cause catalepsy in experimental animals[6-8]. It is known that NOS-positive cells are found in the striatum[9] and antagonism of NO formation has been shown to decrease dopamine release in this structure[10]. However, a recent study indicates that NOS inhibitors can cause a marked increase of dopamine content in the rat striatum[11]. Thus conflicting results regarding the possible role of NO are apparent in dopaminergic transmission.

It is known that catalepsy has been defined as a failure to correct an extremely imposed posture. Therefore, it has been widely used to evaluate motor effects of various drugs, particularly those related to the extrapyramidal system[12]. Previous studies also reported that pole test may be of value in the screening of anti-parkinsonian agents[13]. In the present study, therefore, we investigated possible motor effects of N^G-nitro-L-arginine methyl ester (L-NAME), a non-selective NOS inhibitor, and 7-nitroindazole (7-NI), a neuronal NOS (nNOS) inhibitor, using both catalepsy and pole tests in mice. We also examined the dopamine and its metabolite contents in each drug-treated mouse.

Material and Methods

Male ddy mice, 5 weeks old (25-32g) were used in this study. The animals were housed in air-conditioned rooms at room temperature of $22 \pm 1°C$ and under a 12-hr light-dark cycle with standard food and tap water available at libitum.

7-NI (Research Biochemicals Int.), L-NAME hydrochloride (Research Biochemicals Int.) and L-arginine (Sigma) were used in this study. 7-NI (40, 80 and 160 mg/kg) was suspended in peanut oil and was given subcutaneously (sc) in mice. L-NAME was dissolved in saline and was given sc in mice. L-Arginine was dissolved in saline and was injected intraperitoneally (ip) in mice.

Catalepsy test

To measure cataleptic symptoms such as akinesia and rigidity, bar-test catalepsy was evaluated by placing both forepaws of the mouse over a horizontal bar (diameter: 0.2 cm), elevated 15 cm from floor. The time during which the animals maintained this position was recorded up. In preliminary study, the test was performed at immediately before (0 hr) and 1, 2, 4 and 24 hr after the treatment of each drug. For the evaluation of drugs, the test was performed at immediately before (0 hr) and 2 and 4 hr after drug treatment. Each group contained 7 mice. All values were expressed as means±S.E. and statistical significance was evaluated using an analysis of variance (ANOVA) followed by Williams multiple range test.

Pole test

To measure the degree of bradykinesia, a typical symptom of parkinsonism, pole test was performed according to the method of Ogawa et al.[13] with minor modifications[14]. The mouse was placed head upward on the top of a rough-surfaced pole (8 mm in diameter and 50 cm in height) which was wrapped doubly with gauze to prevent slipping: the time until it turned completely downward (Tturn) and the time until it climbed down to the floor (TLA) were examined. In preliminary study, the test was performed at immediately before (0 hr) and 1, 2, 4 and 24 hr after the treatment of each drug. For the evaluation of drugs, the test was performed at immediately before (0 hr) and 2 and 4 hr after drug treatment. Each group contained 7 mice. All values were expressed as means±S.E. and statistical significance was evaluated using an analysis of variance (ANOVA) followed by Williams multiple range test.

Measurement of dopamine and its metabolites

The mice were killed by cervical dislocation at 4 hr after the treatment of each drug. After decapitation, brains were quickly removed and the two striata were rapidly dissected out freehand on an ice-cold glass Petri dish. Samples were immediately weighted, then frozen and stored at $-80°C$ until assay. The dissection procedure was performed in less than 2 min. Striata were sonicated ice-cold 0.2M perchloric acid containing 100 ng/ml isoproterenol as internal standard. Homogenates were centrifuged at 3000 rpm for 20 min at 4°C. The

supernatant was filtered (pore size 0.45μm, Millipore filter) and a 30-μl aliquot of the supernatant was used for determination of the dopamine, 3,4-dihydroxyphenylacetic acid (DOPAC), homovanillic acid (HVA) and isoproterenol by high-performance liquid chromatography (HPLC) with an electrochemical detector (ECD) (Eicom, Japan). The mobile phase consisted of 0.1M sodium citrate-0.1M sodium acetate solution (pH 3.5) including 1.064 M octane sulfonic acid and 0.013 mM Na_2EDTA and 15% (v/v) methanol. The recoveries of dopamine, DOPAC, HVA and isoproterenol through the present procedures were >93%. Levels of dopamine, DOPAC and HVA were calculated from the comparison of simple peak area with internal standard peak region and are expressed as μg/g tissue weight. Each group contained 4 mice. All values were expressed as means±S.E. and statistical significance was evaluated using an analysis of variance (ANOVA) followed by Williams multiple range test.

Results

Effect of L-NAME treatment on motor activity

L-NAME caused a significant and dose-dependent cataleptic effect in the range of 40-160 mg/kg as shown in Fig. 1. The cataleptic effect developed gradually from 1 hr after L-NAME injection and lasted more than 4 hr. After 24 hr, L-NAME-induced cataleptic effect was not observed in mice. In pole test, L-NAME also produced a prolongation of Tturn and TLA in a dose-dependent manner as shown in Fig. 2. These motor deficits were especially noted in higher dose of 160 mg/kg and developed gradually from 1 hr after L-NAME treatment and lasting more than 4 hr. After 24 hr, however, this effect was not evident in mice.

Effect of 7-NI treatment on motor activity

7-NI caused a significant and dose-dependent cataleptic effect in the range of 40-160 mg/kg as shown in Fig. 3. The cataleptic effect developed gradually from 1 hr after 7-NI injection and lasted more than 4 hr. After 24 hr, 7-NI-induced cataleptic effect was not observed in mice. In pole test, 7-NI also produced a prolongation of Tturn and TLA in a dose-dependent manner as shown in Fig. 4. These motor deficits were especially noted in higher dose of 160 mg/kg and developed gradually from 1 hr after 7-NI treatment and lasting more than 4 hr. After 24 hr, however, this effect was not significance in mice.

Effect of each drug on the content of dopamine and its metabolites in the striatum

Four hours after L-NAME (160 mg/kg) treatment, no significant change in dopamine, DOPAC and HVA content were observed in the striatum. Therefore, the change for dopamine turnover was not found. On the other hand, 7-NI (160 mg/kg) caused a significant increase in the striatal dopamine content 4 hr after the treatment. In contrast, no

significant change in DOPAC and HVA content was observed. For dopamine turnover, 7-NI produced a significant reduction in the striatum (Fig. 5).

Effect of L-arginine on L-NAME- or 7-NI-induced catalepsy

L-NAME or 7-NI increased catalepsy compared with the effect of vehicle. The effects were especially noticed at 2 and 4 hr after each drug treatment. The cataleptic action of L-NAME or 7-NI was significantly antagonized by the treatment with L-arginine (Fig. 6).

Discussion

In this study, L-NAME and 7-NI also caused a significant and dose-dependent cataleptic effect in the range of 40-160 mg/kg. In pole test, both drugs produced a significant prolongation of Tturn and TLA in a dose-dependent manner. The motor deficit in 7-NI-treated mice was more pronounced than that in L-NAME-treated animals. These findings strongly indicate that NOS inhibitors can induce motor deficiency in mice.

It is possible that NOS inhibitors decrease locomotor activity by interfering with striatal dopamine. For example, it is known that antagonism of NO formation attenuates dopamine release in the striatum[10,15] and inhibits the increased locomotor activity found after dopamine agonist treatment[16,17]. In the present study, L-NAME showed no significant change in dopamine, DOPAC and HVA content in the striatum. On the other hand, 7-NI caused a significant increase in the striatal dopamine content, whereas this drug showed no significant change in DOPAC and HVA content in the striatum. That is why 7-NI produced a significant decrease in the dopamine turnover. Thus, these results suggest that the mechanism in the motor deficit caused by NOS inhibitors is different from that in the motor deficit induced by the decrease of dopaminergic neurotransmission in the striatum, such as haloperidol. Recent studies demonstrate that 7-NI has a MAO inhibitory-like property besides its action on NOS[11,18]. Therefore, it is suggested that NOS inhibitor can cause a significant increase in dopamine content in the striatum. These observations are, at least in part, consistent with our present findings.

To further precise the mechanism of NOS inhibitors, we studied the effect of L-arginine on motor deficit induced by NOS inhibitors. In the present study, the cataleptic action of L-NAME or 7-NI was significantly antagonized by the treatment with L-arginine, suggesting that inhibition of NO formation may be implicated. These findings suggest that NO also plays a key role in control of motor behavior. In the present study, however, it is difficult to infer at the moment whether antagonism of the peripheral or the central enzyme is involved. From our findings that the motor deficit induced by 7-NI was more pronounced than that caused by L-NAME, it is conceivable that the inhibition of nNOS may induce motor deficit in mice.

NO has complex interactions with NMDA-mediated neurotransmission. For example, NO can mediate the NMDA-induced increase in cyclic GMP, but inhibit NMDA-

induced increase in intracellular Ca^{2+} and NOS activity, and antagonize the NMDA receptors[19-22]. It has been also suggested that NO can regulate excitatory amino acid release[23]. In the present study, therefore, the action of NOS inhibitors against NMDA-mediated neurotransmission may explain the motor deficit induced by these inhibitors. However, further studies are necessary to clarify the precise mechanisms for our findings.

In conclusion, our results show that NOS inhibitors can induce motor deficit in mice. Furthermore, we speculate that nNOS may play some role in control of motor behavior.

References

1) Ignarro, I.L., Ann. Rev. Pharmacol. Toxicol. **30** (1990) 535.
2) Dawson, T.M.and Snyder, S.H., J. Neurosci. **14** (1994) 5147.
3) Daniel, H., Hermart, N., Jailard, D., et al., Eur. J. Neurosci. **5** (1993) 1079.
4) Indecola, C., Pelligrinno, D.A., Moskowitz, M.A., et al., J. Cereb. Blood Flow. Metab. **14** (1944) 175.
5) Bredt, D.S., Hwang, P.M.and Snyder, S.H., Nature **347** (1990) 768-.
6) Marras, R.A., Martins, A.P., Del Bel, E.A., et al., Neuoreport **7** (1995) 158.
7) Krzascik, P.and Kostowski, W., Pol. J. Pharmacol. **49** (1997) 263-266.
8) Del Bel, E.A., da Silva, C.A.and Guimarnnães, F.S., Gen. Pharmacol. **30** (1998) 245.
9) Vincent, S.R.and Kimura, H., Neuroscience **46** (1992) 755.
10) Sandor, N.T., Brassai, A., Puskas, A., et al., Brain Res. Bull. **36** (1995) 483.
11) Desvignes, C., Bert, L., Vinet, L., et al., Neurosci. Lett. **261** (1999) 175.
12) Sanberg, P.R., Bunsey, M.D., Giordano, M., et al., Behav. Neurosci. **102** (1988) 748.
13) Ogawa, N., Mizukawa, K., Hirose, et al., Eur. Neurol. **26** (1987) 16.
14) Kobayashi, T., Araki, T., Itoyama, Y., et al., Life Sci. **61** (1997) 2529.
15) Bowyer, J.F., Clausing, P., Gough, B., et al., Brain Res. **699** (1995) 62.
16) Abekawa, T., Ohinori, T. and Koyama, T., Brain Res. **666** (1994) 147.
17) Starr, M.S.and Starr, B.S., Eur. J. Pharmacol. **272** (1995) 211.
18) Di Monte, D.A., Royland, J.E., Anderson, A., et al., J. Neurochem. **69** (1997) 1771.
19) Hoyt, K.R., Tang, L.H., Aizenman, E., et al., Brain Res. **592** (1992) 310.
20) Choi, D.W., Proc. Natl. Acad. Sci. USA **90** (1993) 974.
21) Lipton, S.A., Choi, Y.B., Pan, Z.H., et al., Nature **364** (1993) 626.
22) Manzoni, O.and Bockaet, J., J. Neurochem. **61** (1993) 368.
23) Segieth, J., Getting, S.J., Biggs, C.S., et al., Neurosci. Lett. **200** (1995) 101.
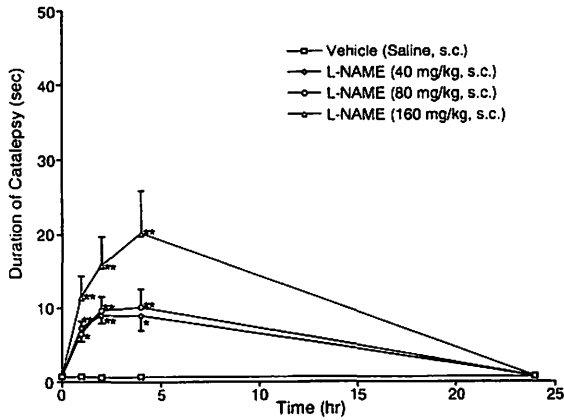
Fig. 1. Time course of the catalepsy induced by L-NAME in mice. Points show the means±S.E. of 7 mice. *p<0.05, **p<0.01 vs. the corresponding value in vehicle group (Williams multiple range test).
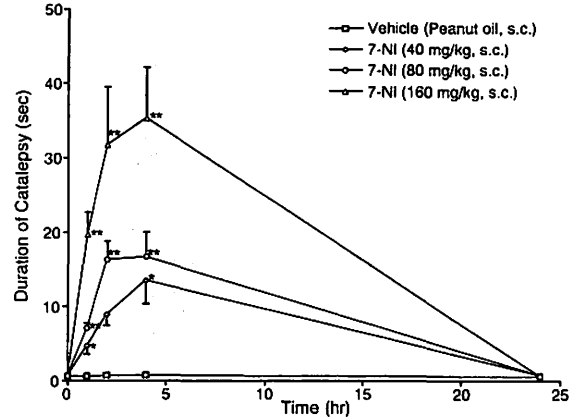
Fig. 3. Time course of the catalepsy induced by 7-nitroindazole (7-NI) in mice. Points show the means±S.E. of 7 mice. *p<0.05, **p<0.01 vs. the corresponding value in vehicle group (Williams multiple range test).
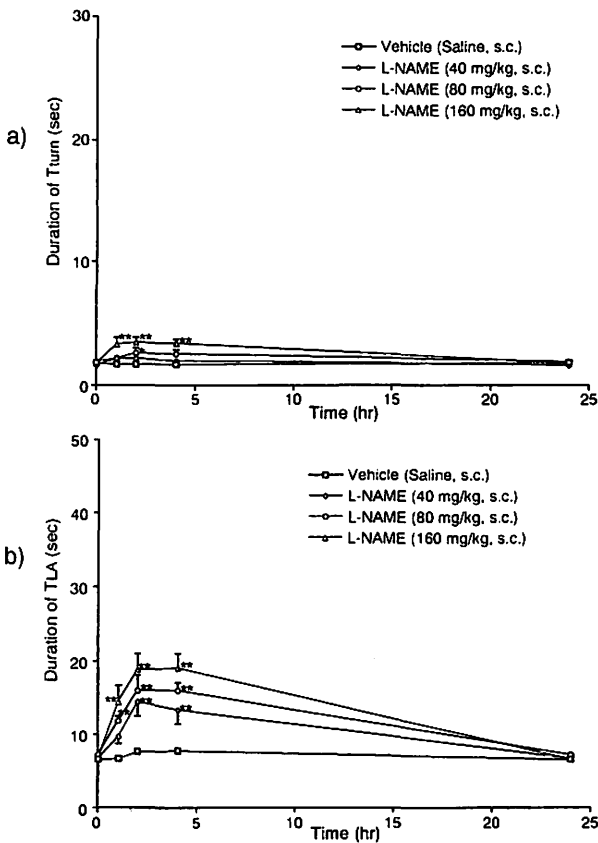
Fig. 2. Time course of the values of the Tturn and TLA in L-NAME-treated mice. Points show the means±S.E. of 7 mice. *p<0.05, **p<0.01 vs. the corresponding value in vehicle group (Williams multiple range test). a) Tturn; b) TLA.
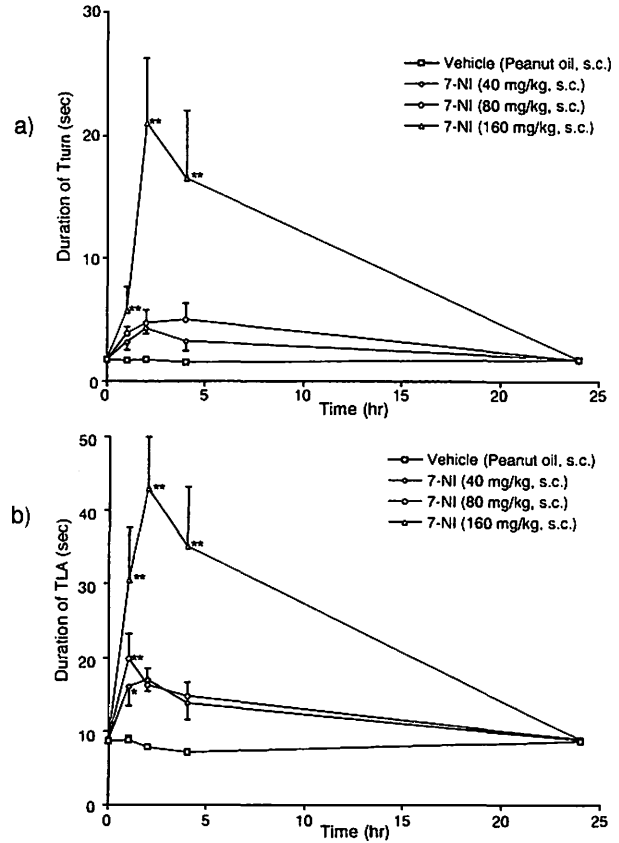
Fig. 4. Time course of the values of the Tturn and TLA in 7-NI-treated mice. Points show the means±S.E. of 7 mice. *p<0.05, **p<0.01 vs. the corresponding value in vehicle group (Williams multiple range test). a) Tturn; b)

122
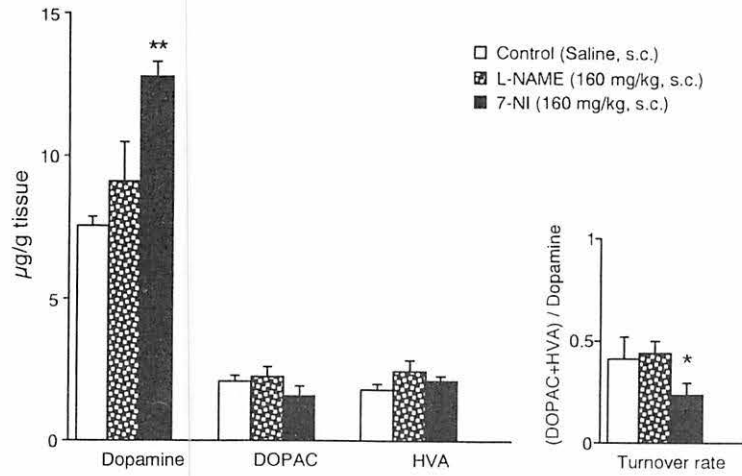
Fig. 5. Effects of L-NAME and 7-NI on the content of dopamine, DOPAC and HVA and turnover (DOPAC+HVA/Dopamine) in mice. Points show the means $\pm$ S.E. of 4 mice. *$p<0.05$, **$p<0.01$ vs. control group (Williams multiple range test). The measurement of dopamine, DOPAC and HVA was examined 4 hr after each drug treatment
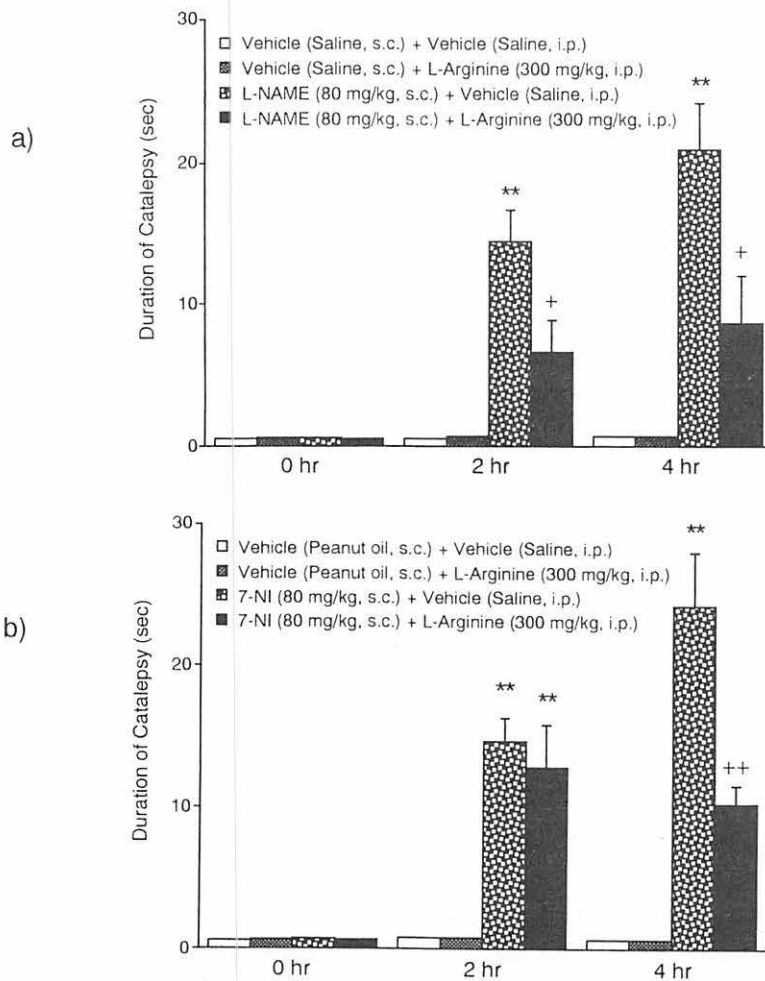
Fig. 6. Antagonitic effects of L-arginine on L-NAME or 7-NI-induced catalepsy in mice. *$p<0.05$, **$p<0.01$ vs. the corresponding value in vehicle group (Williams multiple range test). +$p<0.05$, ++$p<0.01$ vs. L-NAME + Vehicle group or 7-NI + Vehicle group (Student's t-test). a) L-NAME; b) 7-NI

III. 5. Characterization of Neuropeptide Interactions with Glycolipid Receptors by Surface Plasmon Resonance

Valdes-Gonzalez T., Inagawa J.*, and Ido T.

Cyclotron and Radioisotope Center, Tohoku University Biacore, Tokyo*

In this study we used the Surface Plasmon Resonance (SPR) to characterize the interaction of neuropeptides with liposomes containing gangliosides. Besides we investigated which moiety of gangliosides has the fundamental role in the interaction with the neuropeptides. We also analyzed the effect of Ca^{2+} in the ganglioside-neuropeptide bindings. We found that it is possible to characterize with reproducibility the peptide-ganglioside interactions with a HPA sensor chip, using SPR and that all the studied peptides showed affinity from 10^{-5} to 10^{-7} M with the gangliosides. The interactions were as follows:

for GM1, DYN=AMY42=GAL=SUB>SOM=BRD>OXY=ENK;
· for GD1a, DYN>AMY42=GAL=SUB=SOM=BRA=OXY=ENK and
for GT1b, DYN=AMY42=SUB >GAL=SOM=BRA=OXY>ENK.

The ganglioside sugar moiety has an important role in the interaction because peptides interacted fundamentally with the ganglioside sialic acid. Ca^{2+} promotes several changes in peptide-glycolipid bindings.

Introduction

Data about ganglioside-neuropeptide affinity, kinetics, and specificity, could greatly contribute to understand the molecular mechanisms underlying the interaction between neuropeptides and gangliosides. Unfortunately, there is only a few information about these parameters[1-3] and it is not always used a technique with sensibility enough to obtain them with confidence. Besides, in most of the techniques the gangliosides do not have cell surface-like presentation, which is important for understanding gangliosides real behaviour[4,5].

Surface plasmon resonance (SPR) is a sensitive method that has provided good results for protein binding to glycolipid receptor, using CM5 sensor chip[6,7]. A higher response has been reported recently for interaction of asialo-GM1 with the H2G10 protein using HPA sensor, where liposomes containing gangliosides were fused to the chip to form a hybrid bilayer surface and the HPA sensor showed ten times higher capacity for H2G10 binding as liposomal surface, than experiments with CM5 chips[8]. Due to the low molecular

weight of neuropeptides it is necessary to prepare chips that provides more molecule bound/sensor surface. In this study we have used the SPR technique to obtain kinetic and affinity constants to characterize the interaction of peptides (Table 1) with liposomes containing gangliosides. Besides, we investigated which ganglioside moiety has the main role in these interactions and also, the effect that Ca^{2+} has in peptide-ganglioside bindings.

Methods

Liposome preparation- Mixtures containing DMPC and a single ganglioside were dissolved in $CHCl_3$ and dried in glass vials under vacuum for 10 min. The mixtures were resuspended by vortexing in 0.5 ml HEPES buffer and placed in a sonic bath for 30s. Suspensions containing the liposomes were extruded (30 passes) through 2 polycarbonate filters of 50 nm in a Liposofast apparatus and injected immediately to the sensor chip.

HPA chips preparation- HPA sensor was docked in a BIACORE 2000 biosensor system, washed with 20 ul of 20mM CHAPS or n-octylglucoside at 5ul/min and after 30 uL of liposome preparation was fused to the surface of sensor flow cell to form flat hybrid bilayer at 1uL/min. Then, 5uL of 10mM NaOH were injected to remove the incompletely fused liposomes. The preparation of each flow cell was made individually, to obtain DMPC, GM1, GT1b and GD1a monolayers in flow cells 1, 2, 3, and 4 respectively. The same procedure was used to prepare asialo-GM1 surface including sensor, to obtain an order GM1, asialo-GM1, GT1b and GD1a in flow cell 1, 2, 3 and 4 respectively. All the measurements and surfaces regeneration were carried out in HEPES buffered saline which contained 10mM HEPES, pH 7.4 and 150 mM NaCl. Analyses were performed at 25 °C.

Peptide injections- Peptides (Table 1) were dissolved in HEPES buffer pH 7.4 to 400-3.65ug/mL and 15uL were injected individually at 5uL/min. Sensor surfaces were regenerated with HEPES buffer. For analysis of Ca^{2+} effect, peptides were dissolved in HEPES buffer pH 7.4 but all the measurements and surfaces regeneration were carried out in HEPES buffered saline which contained 10mM HEPES, pH 7.4 and 150 mM NaCl and 2.8mM $CaCl_2$.

Analysis of peptide-ganglioside interaction-Association and dissociation rate constants were calculated by nonlinear fitting of the primary sensorgram data using the BIA evaluation 2.0 software. The dissociation rate constant (K_{off}) is derived using the equation

$$R_t = R_{t0}e^{-K_{off}(t-t0)},$$

where R_t is the response at time t, R_{t0} is the amplitude of the initial response. The association rate constant (k_{on}) can then be derived using equation

$$R_t = [k_{on}CR_{max}(1 - e^{-(k_{on}C+K_{off})t})]/k_{on}C + K_{off}.$$

Where R_t is the response at time t, R_{max} is the maximum response, C is the concentration of

125

peptide in solution and K_{off} the dissociation rate constant. Affinities were calculated from rate constants.

Results

HPA chip preparation: The washing of flow cells surfaces with n-OG before liposome fusion gave better characteristics of the sensorgramas than with CHAPS and the stability of the base line is recovered immediately after the detergent injection. For that reasons, we used n-OG in all the next experiments. Monolayer surfaces containing glycolipids were obtained injecting NaOH on the bilayer surfaces (Fig. 1). Typically the liposome monolayers showed RU values around 1000 for polysialogangliosides GT1b 20%, GD1a 15%, and about 2000 RU for DMPC 20%, GM1 20% and asialo-GM1 20%. All the prepared surfaces provided a stable baseline for determination of peptide binding specificity and kinetics. Liposomes containing 20% of gangliosides were also tested, but with liposomes containing GT1b15% was obtained a higher monolayer yield respect to bilayer. Liposomes containing only DMPC were used as blank surfaces to determine non-specific binding.

Binding Specificity and Affinities of peptides:

The profiles of peptides binding to different gangliosides are shown in Fig. 2. All the peptides showed some interaction with gangliosides. ENK had the lowest binding and SUB the highest. The peptide specificity to GT1b and GD1a were higher in all the cases than to GM1, except for SUB and AMY42. Tacking in account only the peptides that showed RU values higher than 250 RU, the specificity decreased as follows:

for GM1, SUB>SOM>DYN>AMY as shows the Fig.2a);
for GD1a, SUB>SOM>DYN>BRA>AMY42 as shows the Fig.2b) and
for GT1b, SUB>SOM>DYN>AMY42>BRA as shows the Fig.2c).

The affinities of ganglioside-peptide interaction are shown in Table 2. All the studied peptides showed affinity from 10^{-5} to 10^{-7} M with the gangliosides, but following the scheme:

for GM1, DYN=AMY42=GAL=SUB>SOM=BRD>OXY=ENK;
for GD1a, DYN>AMY42=GAL=SUB=SOM=BRA=OXY=ENK and
for GT1b, DYN=AMY42=SUB >GAL=SOM=BRA=OXY>ENK

Peptides binding kinetics:

In all the cases, SUB showed the highest RU values when compared with the other peptides, and these interactions depended markedly on peptide concentration. The interaction of SUB with surfaces containing DMPC, GM1, GD1a and GT1b at 9.25 uM compared with the sensorgrams at 2.31 uM shows more rapid association for liposomes containing di- and trisialo gangliosides and slower dissociation rate in the intaraction with all

the liposomes. At 37 uM all the sensorgrams have the same linear pattern in the dissociation phase and the liposomes containing gangliosides have similar binding. At 148 uM the sensorgrams of the liposomes containing gangliosides recovered the curve shape in the association phase, the association-rates were faster and the binding strength were similar for all the gangliosides. The linearity in the association phase was also found for AMY42 at 5.5uM with GM1, GD1a and GT1b. For SUB, AMY42 and DYN higher association-rates were found at lower concentrations (Table 2).

Binding to asialo-GM1:

When the peptides were injected simultaneously on surfaces containing asialo-GM1 and GM1 respectively, and the obtained sensorgrams compared, in most of the cases a higher RU values were observed for binding to GM1. For ENK, OXY, SOM and GAL the differences were higher than 300 RU. Nevertheless for DYN and AMY42 not significant differences were observed (Fig. 3).

Effect of Ca^{2+} on peptide binding to liposomes. When the HEPES buffer containing 2.8mM of $CaCl_2$ was used in the assays, several changes occurred for peptide-glycolipid interactions (Table III). For BRD, in all the cases the presence of Ca^{2+} had a positive effect (increasing) and a negative effect (decreasing) for AMY42, mainly in the interaction with liposomes containing glycolipids. For ENK, also an increasing in affinity was observed, except in the interaction with GD1a. For SOM and DYN the Ca^{2+} did not exert effect on the interaction with surfaces containing gangliosides, nevertheless the affinity with Asialo-GM1 increased. OXY showed and irregular behavior: the binding increased for Asialo-GM1 and GM1, decreased for GD1a and did not change for GT1b. The highest change observed was the increase of GAL binding to GT1b (about 800RU) (Fig. 4).

Discussion

The use of HPA sensor chip in our experiments allowed to characterize the interaction of liposomes containing gangliosides with such small molecules like neuropeptides, which is difficult to do by other means. Moreover, the fact that using this sensor chip the surfaces containing gangliosides are presented in form of a flat bilayer and not like liposomes, provides more accessibility to the binding sites which is a fundamental feature when analyzing very small molecules.

Nowadays, the information about the structures, biodistribution and biosynthesis of neuropeptides is extensive, and the mechanisms by which many of these peptides act on peripheral tissues are now quite well understood. However for a full understanding of the functions of neuropeptides within the CNS, the knowledge of the interaction with gangliosides may have an important role. Although not all the peptides may function directly through the interaction with gangliosides, the fact that gangliosides are concentrated in the

membrane of neuron and have been proposed to be implicated in signal transduction enlarge the possibility of the interaction of peptide with gangliosides in some stage of its mechanisms [9,10]. To our knowledge, we report first time the use of SPR using HPA sensor chip for the study of small molecules such as neuropeptides. We also report we first time series of kinetics data about the interaction of opiod and no opioid peptides with gangliosides that we consider valuable for further experiments. The Ca^{2+} may exert its effect by changes the three dimensional sturcture of gangliosides[11] or by interfere the binding sites of ganglioside, or by combination of both. This way it is possible to explain the irregular effects of Ca^{2+} on peptide-ganglioside interactions.

References

1) Goettl V., Tejwani G., Hadjiconstantinou M., Neurorep. 10(1999)513-516.
2) MacLaurin J., Franklin T., Fraser P., Chakrabartty A., J. Biol. Chem, 273(1998)4506-4515.
3) Takahashi H., Hirokawa K; Ando, S.; Obata, K., Acta Neuropathol. 81(1991)626-631.
4) Choo-Smith L.P., Garzon-Rodriguez W., Glabe C., Surewicz, W.K., J. Biol, Chem. 272 (1997)22987-22990.
5) MacLaurin J., Chakrabatty A., J. Biol, Chem. 271 (1996) 26482-26489.
6) Kuziemko G.M., Stroh M., Stevens, R.C. Biochem. 35(1996)6375-6384.
7) Harrinson B., MacKenzie R., Hirama T., Lee K.K., Altman E. J. Immunol. Meth. 212(1998) 29-30.
8) MacKenzie R., Hirama T., Lee K., Altman E., Young N.M. J. Biol, Chem. 272(1997)5533-5538,.
9) Gonzalez M., Lezcano N., Celis M., Fidelio D., Pept. 17(1996)269-274,.
10) Mousli M., Bueb J.L., Bronner C., Rouot B., Landry Y., Trends. Pharmacol. Sci. 11(1990) 358-362.
11) Behr J.P., Lehn J.M. FEBS lett. 31(1973)297-299,.

Table 1. Characteristics of peptides used in this study.

Peptide	Fragment weight	Structure
ENK Enkephalin	555.6	Tyr-Gly-Gly-Phe-Leu
OXY Oxytocin	1007.2	Cys-Tyr-Ile-Gln-Asn-Cys-Pro-Leu-Gly-NH$_2$ (Cys3-Cys14 disulf)
BRD Bradykinin	1060.2	Arg-Pro-Pro-Gly-Phe-Ser-Pro-Phe-Arg
SOM Somatostatin	1637.9	Ala-Gly-Cys-Lys-Asn-Phe-Phe-Trp-Lys-Thr-Phe-Thr-Ser-Cys (Cys3-Cys14 disulf)
SUB Substance P	1347.6	Arg-Pro-Lys-Pro-Gln-Gln-Phe-Phe-Gly-Leu-Met-NH$_2$
DYN Dynorphin	2147.5	Tyr-Gly-Gly-Phe-Leu-Arg-Arg-Ile-Arg-Pro-Lys-Leu-Lys-Trp-Asp-Asn-Gln
GAL galanin	3164.6	Gly-Trp-Thr-Leu-Asn-Ser-Ala-Gly-Tyr-Leu-Leu-Gly-Pro-His-Ala-Val-Gly-Asn-His-Arg-Ser-Phe-Ser-Asp-Lys-Asn-Gly-Leu-Thr-Ser
AMY 42 Beta-Amyloid 42	4514.1	Asp-Ala-Glu-Phe-Arg-His-Asp-Ser-Gly-Tyr-Glu-Val-His-His-Gln-Lys-Leu-Val-Phe-Phe-Ala-Glu-Asp-Val-Gly-Ser-Asn-Lys-Gly-Ala-Ile-Ile-Gly-Leu-Met-Val-Gly-Gly-Val-Val-Ile-Ala

Table 2. Affinities and rate constants for peptide binding to liposomes.

Ganglioside	Peptide	$kass$ $(M^{-1}s^{-1})$	$kdiss$ (s^{-1})	$K_D{}^a$ (M)
GM1	ENK	8.61×10^2	1.26×10^{-2}	9.4×10^{-5}
	OXY	9.54×10^2	1.45×10^{-2}	1.5×10^{-5}
	BRD	1.42×10^3	2.17×10^{-3}	1.5×10^{-6}
	SOM	8.18×10^3	4.60×10^{-2}	5.6×10^{-6}
	SUB	1.92×10^4	1.00×10^{-2}	3.3×10^{-7}
	DYN	1.38×10^4	4.13×10^{-3}	3.0×10^{-7}
	GAL	6.6×10^3	2.72×10^{-3}	4.0×10^{-7}
	AMY 42	1.58×10^4	8.17×10^{-3}	5.2×10^{-7}
GD1a	ENK	8.79×10	4.1×10^{-4}	4.6×10^{-6}
	OXY	9.89×10^2	4.13×10^{-3}	4.2×10^{-6}
	BRA	1.72×10^3	7.71×10^{-1}	6.9×10^{-6}
	SOM	4.31×10^3	2.09×10^{-2}	4.9×10^{-6}
	SUB	1.04×10^4	1.07×10^{-2}	1.1×10^{-6}
	DYN	1.16×10^4	5.88×10^{-3}	5.1×10^{-7}
	GAL	3.97×10^3	7.30×10^{-3}	1.8×10^{-4}
	AMY 42	3.23×10^3	4.00×10^{-1}	1.2×10^{-4}
GT1b	ENK	7.96×10	1.13×10^{-3}	1.4×10^{-5}
	OXY	1.09×10^3	4.49×10^{-3}	4.1×10^{-6}
	BRD	1.04×10^3	2.58×10^{-3}	2.5×10^{-6}
	SOM	4.17×10^3	3.72×10^{-2}	8.91×10^{-6}
	SUB	1.88×10^4	8.31×10^{-3}	4.4×10^{-7}
	DYN	4.14×10^4	5.26×10^{-3}	1.3×10^{-7}
	GAL	4.98×10^3	9.95×10^{-3}	2.0×10^{-6}
	AMY42	5.68×10^3	4.41×10^{-3}	7.7×10^{-7}

^{a} $kdiss$ /$kass$

Table 3. Effect of 2.8mM $CaCl_2$ on peptide-ganglioside bindings.

Ganglioside / Peptide	Asialo GM1	GM1	GT1b	GD1a
ENK	+	+	+	—
OXY	+	++		- -
BRD	++	+	+	++
SOM	++			
DYN	+	—	—	—
GAL		-	+++	-
AMY 42	—	- -	- -	- -

+ Binding increased in (+) 50-100 RU, (++) 100-200 RU or (+++) 300-800 RU.
-Binding decreased in (-) 50-100 RU, (- -) 100-200 RU or (- - -) 300-800 RU.
— Binding changes were lower than 50 RU
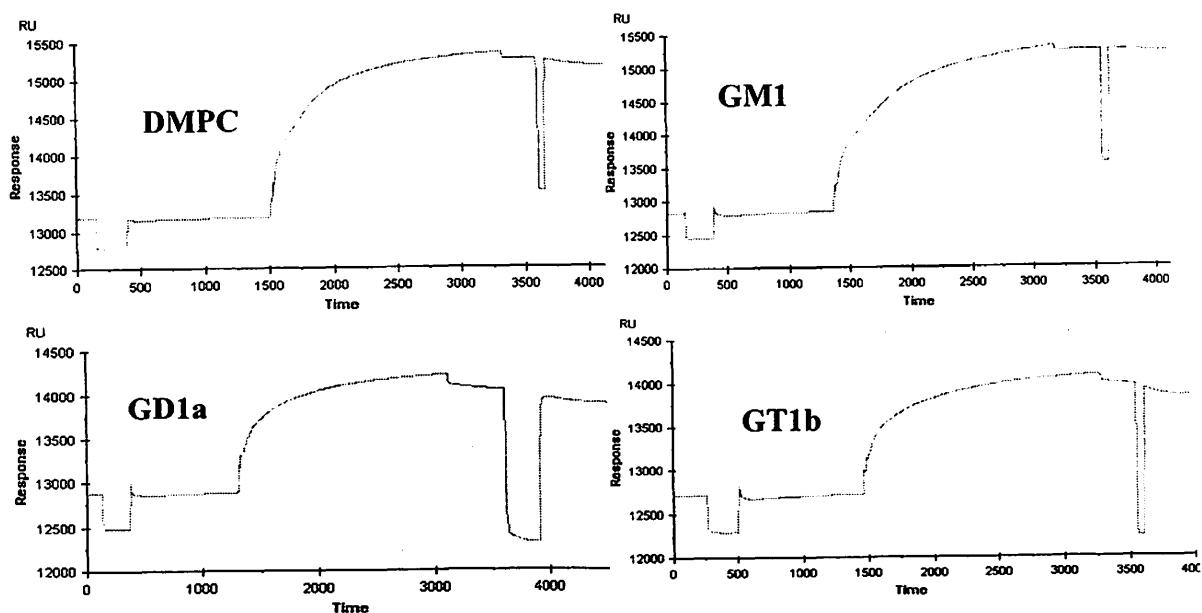
Fig. 1. Sensorgrams showing the fusion of ganglioside-containing liposomes on HPA sensorchips.
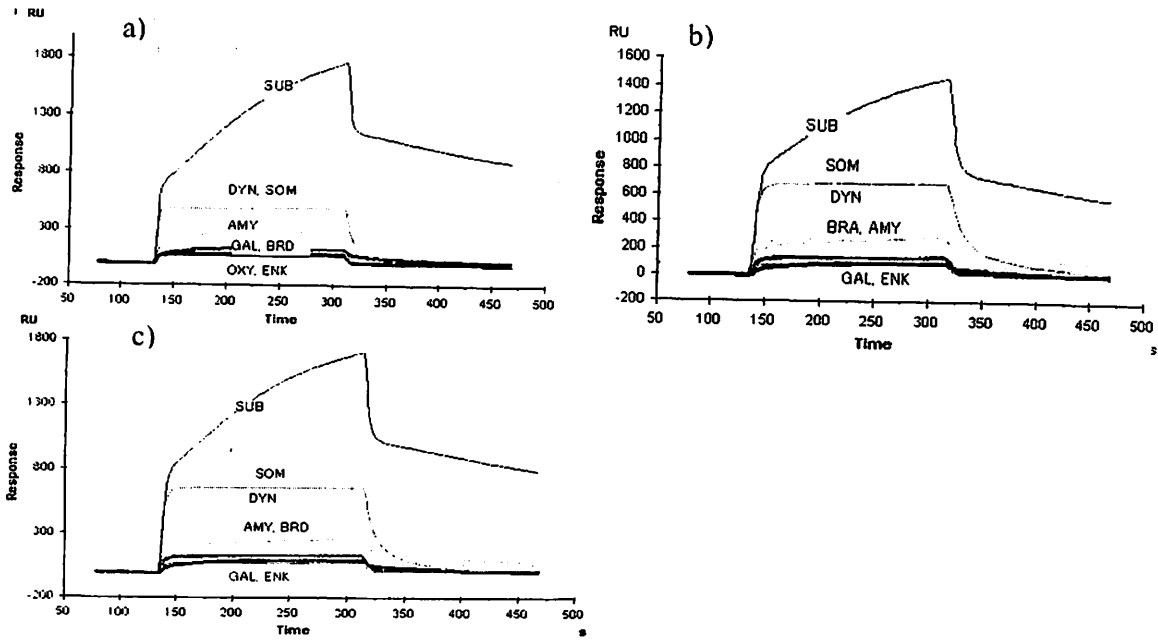
Fig. 2. Specificities of peptides for different gangliosides. Sensorgrams showing peptides 100ug/mL binding to a)GM1, b)GD1a and c)GT1b liposomes.
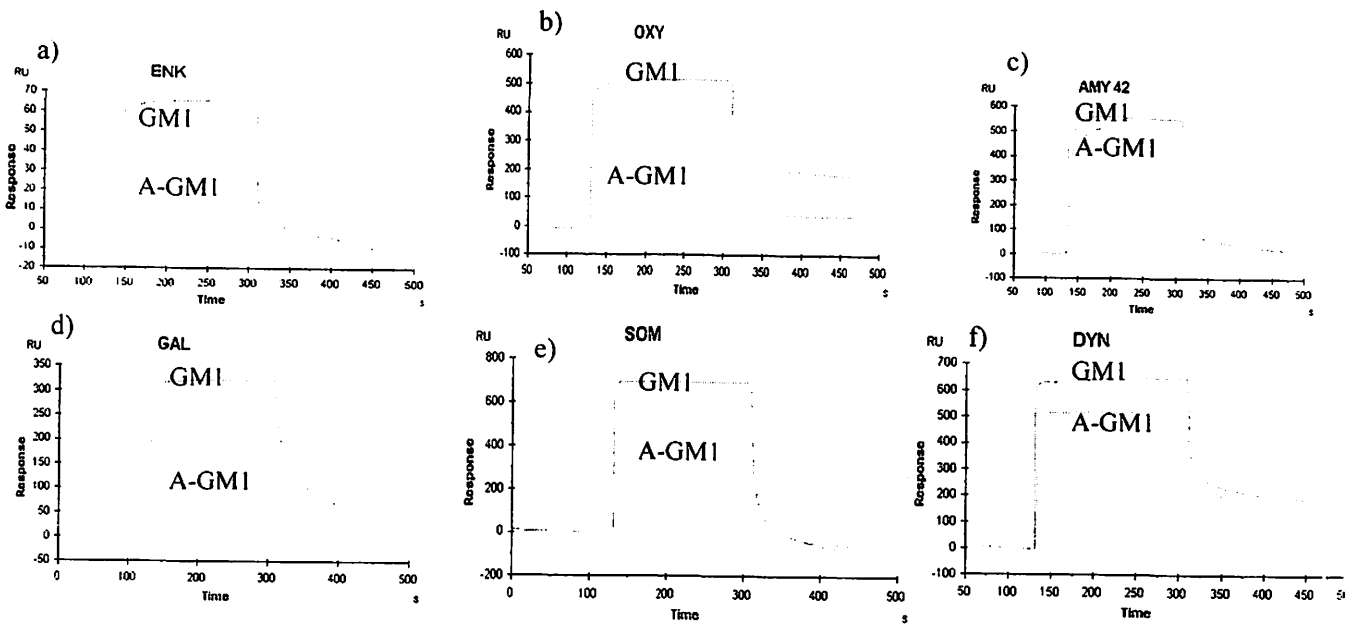
Fig. 3. Specificities of peptides for GM1 and asialo GM1. Overlay plots of 100ug/mL peptides a)ENK b)OXY, c)AMY42, d)GAL, e)SOM and f)DYN binding GM1 and asialo GM1 liposomes.
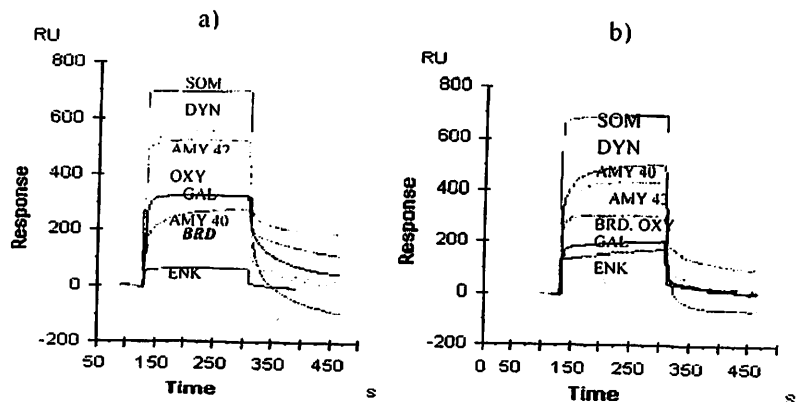
Fig. 4. Effect of Ca^{2+} on peptide binding to loposomes. Overlay plots of peptides binding GM1 a) in buffer with Ca^{2+} and b) in buffer containing 2.8mM $CaCl_2$.

III. 6. Biochemical changes in the brain of 1-methyl-4-phenyl-1,2,3,6-tetrahydropyridine (MPTP) -treated mouse

Mikami T., Araki T.*, Tanji H.**, Imai Y.*, Mizugaki M and Itoyama Y.**

Department of Pharmaceutical Science, Tohoku University Hospital
Department of Clinical Pharmacology and Therapeutics, Tohoku University Graduate School of Medicine and Pharmaceutical Sciences *
Department of Neurology, Tohoku University School of Medicine **

Introduction

Parkinson's disease is mainly characterized by the progressive loss of dopaminergic neurons in the substantia nigra that projects to the striatum.   So far, many studies have focused on neurochemical and neuropathological mechanisms in this disease.   The selective neurotoxicant 1-methyl-4-phenyl-1,2,3,6-tetrahydropyridine (MPTP) is well known to deplete striatal dopamine and cause neuronal degeneration of the nigrostriatal pathway when administered to humans, non-human primates and rodents.   The resulting neurochemical and histopathological deficits are similar to those observed in idiopathic Parkinson's disease[1-3].   Some of these studies have demonstrated that mice, especially the C57BL mouse strain, are highly susceptible to the neurotoxic effects of MPTP and are useful as animal models of Parkinson's disease[3,4].

The neurotoxic effects of MPTP are thought to be initiated by the 1-methyl-4-phenylpyridinium ion (MPP$^+$), which is metabolite formed by monoamine oxidase (MAO)-B mediated oxidation of MPTP.   MPP$^+$ is known to be actively accumulated by dopaminergic neurons, where it is further concentrated within mitochondria by an energy-dependent mechanism.   The inhibition of mitochondrial electron transport at Complex I (NADH-ubiquinone oxidoreductase) results in decreased oxygen consumption and ATP production and a disruption of ion homeostasis[5-7].   It is also suggested that the oxidative stress produced by MPP$^+$ may potentiate its toxicity to dopaminergic neurons[8,9].   Furthermore, recent studies suggest that the toxic effects of MPP$^+$ are mediated, in part, through an excessive production of nitric oxide (NO)[10,11].   Based on these observations, it is conceivable that MPTP-treated mouse model may be useful for evaluating brain functions in Parkinson's disease.   However, little is known about the acute changes of brain functions in mice after MPTP treatment.   In the present study, therefore, we conducted to examine the biochemical changes in the mouse brain after acute treatment with MPTP.

Materials and Methods

Male C57BL/6 mice (22-28 g) were used in this study. The mice received intraperitoneal four injections of MPTP (10 mg/kg) at 1h intervals, the total dose per mouse being 40 mg/kg. In the present study, there were no died animals after MPTP treatment. The mice were sacrificed by cervical dislocation at 3 and 7 days after the last injection for biochemical studies as described below.

Receptor autoradiography

The mice were sacrificed by cervical dislocation at 3 and 7 days after MPTP treatment, and the brains were quickly removed, frozen in powdered dry-ice and stored at-80 °C until receptor assay. Coronal sections, 12 μm in thickness, were cut at the level of the striatum and the substantia nigra of MPTP-treated and control mouse brains on a cryostat and thaw-mounted onto silane-coated cover glasses.

Autoradiographic localization of dopamine D_1 receptors was detected using [^{3}H]SCH23390 according to the method of Dawson et al[12] with minor modifications[13]. The sections were incubated with 1 nM [^{3}H]SCH23390 (specific activity 70.3 Ci/mmol, New England Nuclear) in 50 mM Tris-HCl buffer (pH 7.4) containing 120 mM NaCl, 5 mM KCl, 2 mM $CaCl_2$ and 1 mM $MgCl_2$ for 30 min at room temperature. After incubation, the sections were then dipped in fresh buffer at 4 °C, followed by 25-min rinses in fresh buffer at 4 °C. Non-specific binding was determined using 1 μM non-labeled SCH23390 (Research Biochemicals Int.).

Autoradiographic distribution of dopamine D_2 receptors was determined using [^{3}H]raclopride according to the method of Köhler and Radesäter[14] with minor modifications. The sections were incubated with 3 nM [^{3}H]raclopride (specific activity 79.3 Ci/mmol, New England Nuclear) in 170 mM Tris-HCl buffer (pH 7.4) containing 120 mM NaCl, 5 mM KCl, 2 mM $CaCl_2$ and 1 mM $MgCl_2$ for 30 min at room temperature. After incubation, the sections were washed four times in fresh buffer for 1 min at 4 °C and dipped in distilled water at 4 °C. Non-specific binding was determined using 10 μM haloperidol (Sigma).

Autoradiographic localization of dopamine uptake sites was detected using [^{3}H]mazindol according to the method of Przedborski et al[15] with minor modifications[16]. The sections were pre-incubated for 15 min at 4 °C in 50 mM Tris-HCl buffer (pH 7.9) containing 120 mM NaCl and 5 mM KCl. The sections were then incubated with 15 nM [^{3}H]mazindol (New England Nuclear, specific activity 24 Ci/mmol) in 50 mM Tris-HCl buffer (pH 7.9) containing 300 nM NaCl, 5 mM KCl and 0.3 μM desmethylimipramine (Sigma). Desmethylimipramine was added to block the binding of [^{3}H]mazindol to norepinephrine uptake sites, as described previously[17]. After incubation, the sections were washed twice in fresh buffer for 3 min at 4 °C and dipped in ice-cold distilled water. Non-specific binding was determined using 30 μM benztropine (Sigma).

Data analysis

The sections were quickly dried under a cold air stream and then exposed for 1-3 weeks with [^{3}H]-labeled graded standards (Amersham) to tritium-sensitive imaging plates (Fuji Photo Film, Japan) coated with minutes crystals of photostimulable phosphor. A computer-assisted image-processing system, BAS5000 (Fuji Photo Film, Japan), was used for the quantitative analysis of radioactivity. Regions of interest (ROIs) on the autoradiograms were placed at the dorsolateral and ventromedial parts of the striatum separately and in the whole substantia nigra according to an atlas of mouse brain. The radioactivity of each ROI was quantified using the calibration lines obtained from [^{3}H]-labeled graded standards, and the values for radioactivities were converted to fmol/mg tissue. Specific binding activities of each ligand in the striatum and substantia nigra were calculated by subtracting the non-specific binding from the total binding. All values were expressed as means±S.E. and statistical significance was evaluated using an analysis of variance (ANOVA) followed by Dunnett's multiple range test (two-side).

Measurement of dopamine and its metabolite

The mice were killed by cervical dislocation at 3 and 7 days after MPTP treatment. After decapitation, brains were quickly removed and the two striata were rapidly dissected out freehand on an ice-cold glass Petri dish. Samples were immediately weighted, then frozen and stored at −80 °C until assay. The dissection procedure was performed in less than 2 min. Striata were sonicated ice-cold 0.2 M per chloric acid containing 100 ng/ml isoproterenol as internal standard. Homogenates were centrifuged at 2,500 rpm for 15 min at 4 °C. The supernatant was filtered (pore size 0.45 μm, Millipore filter) and a 30 μl aliquot of the supernatant was used for determination the dopamine, 3,4-dihydroxyphenyl acetic acid (DOPAC) and isoproterenol by high-performance liquid chromatography (HPLC) with an electrochemical detector (ECD) (Eicom, Japan). The mobile phase consisted of 0.1 M sodium citrate-0.1 M sodium acetate solution (pH 3.5) including 1.064 M octane sulfonic acid 0.013 mM EDTA 2Na and 15% (v/v) methanol. The recoveries of dopamine, DOPAC and isoproterenol through the present procedures were > 93%. Levels of dopamine and its metabolite were calculated from the comparison of simple peak area with internal standard peak region and were expressed as μg/g tissue weight. Each group contained 5-9 mice. All values were expressed as means±S.E. and statistical significance was evaluated using an analysis of variance (ANOVA) followed by Dunnett's multiple range test (two-side).

Results

Receptor autoradiography

[^{3}H]SCH23390 binding showed no significant change in either the dorsolateral and ventromedial striatum or the substantia nigra of MPTP-treated mice compared with saline-

treated group for the 7 days after MPTP treatment (Table 1).

[^{3}H]Raclopride binding showed no significant change in both the striatum and substantia nigra 3 days after MPTP treatment, as compared with saline-treated group. Seven days after MPTP administration, a significant decrease in [^{3}H]raclopride binding was observed in the substantia nigra. However, the striatum showed no significant change in [^{3}H]raclopride binding (Table 1).

[^{3}H]Mazindol binding showed a marked reduction in the striatum 3 and 7 days after MPTP treatment, as compared with saline-treated group. In the substantia nigra, a significant decrease in [^{3}H]mazindol binding was also observed 3 and 7 days after MPTP administration (Table 1).

Dopamine and its metabolite

Striatal levels of dopamine and DOPAC are illustrated in Fig. 1. In mice subjected to MPTP, the dopamine concentrations were markedly decreased (82.2%) in the striatum 3 days after MPTP treatment as compared with saline-treated group. Also, the DOPAC concentrations were significantly reduced (59.7%) in the striatum 3 days after MPTP administration. Seven days after MPTP treatment, furthermore, the dopamine and DOPAC concentrations were significantly reduced (74.2 and 57.1%) in the striatum, respectively. In addition, the dopamine and DOPAC concentrations in the striatum of saline-treated mice were similar to the values of a previous report[3].

Discussion

The purpose of the present study was to determine the changes in dopamine D_1 and D_2 receptors and dopamine uptake sites in the striatum and substantia nigra of mouse brain at early stages after acute administration of MPTP. The results of the present study show that MPTP does not cause the changes in dopamine D_1 and D_2 receptors in the striatum up to 7 days after MPTP treatment. In contrast, dopamine uptake sites showed a marked reduction in the striatum 3 and 7 days after acute treatment with MPTP. In the substantia nigra, on the other hand, dopamine D_1 receptors exhibited no significant change up to 7 days of postlesion, whereas dopamine D_2 receptors showed a significant reduction 7 days after MPTP treatment. Dopamine uptake sites showed a marked decrease in the substantia nigra 3 and 7 days after MPTP treatment. These findings suggest that the change in dopamine uptake sites precede any change in dopamine D_1 and D_2 receptors in the striatum and substantia nigra after acute treatment with MPTP. Interestingly, many studies utilizing rat brains have reported that the localization of dopamine receptors in the substantia nigra is heterogeneous for the two subtypes. Dopamine D_1 receptors are distributed on the terminals of striatonigral projections, which are well-recognized to be far denser in the pars reticulata than in pars compacta of the substantia nigra[18,19]. In contrast, dopamine D_2 receptors in the substantia nigra are located

on the dopaminergic cell bodies or their dendrites in the pars compacta, and the density of dopamine D_2 receptors is shown to be minimal in the pars reticulata[20-22]. Therefore, it is conceivable that the difference between the effects of MPTP on dopamine D_1 and D_2 receptors observed in the present study may be due to their heterogeneous localization in the substantia nigra of mice.

In clinical studies, there have been several reports on striatal dopamine D_1 receptors in patients with Parkinson's disease utilizing PET (Positron Emission Tomography) or autopsied brains. Some reports have demonstrated no significant change in dopamine D_1 receptors[23,24], but others have described an up-regulation of dopamine D_1 receptors[25,26] at post-synaptic sites. Also, there have been a few reports on dopamine D_1 receptors in the substantia nigra of patients with Parkinson's disease. Cortés et al[24] demonstrated no significant alteration in nigral dopamine D_1 receptors, whereas Rinne et al[26] described a significant decline in the binding using autopsied brains. Thus, several evidence for changes in dopamine D_1 receptors is contradictory. On the other hand, there have also been many studies on dopamine D_2 receptors in the striatum of patients with Parkinson's disease using PET or autopsied brains. Most studies have suggested an up-regulation in untreated patients with early Parkinson's disease[27-29], but the down-regulation of dopamine D_2 receptors might underlie the fluctuating response to L-DOPA observed in chronically treated Parkinson's patients[27,28]. Interestingly, Cortés et al[24] demonstrated no significant change in dopamine D_2 receptors in the substantia nigra between Parkinson's disease and control using autopsied brains. In contrast, Murray et al[30] demonstrated marked reduction of dopamine D_2 receptors in the substantia nigra of Parkinson's disease using autopsied brains. From these observations, it is conceivable that receptor autoradiographic approach under the same experimental conditions may help to explain the dopamine receptor changes in Parkinson's disease.

[^{3}H]Mazindol is a specific ligand for dopamine uptake sites[15,17] and its binding is located on pre-synaptic terminals of dopaminergic axons originating in the substantia nigra, especially in the pars compacta[17]. Therefore, measurement of dopamine uptake sites is useful for detecting functional changes of dopaminergic neurons in Parkinson's disease or in animal models of Parkinson's disease. Many studies have reported marked reduction of dopamine uptake sites in the striatum and substantia nigra using [^{3}H]mazindol in MPTP-treated animals, such as monkeys[31], cats[32] and marmosets[33]. Furthermore, Alexander et al[31] reported that there was a good correlation between the reductions in [^{3}H]mazindol binding sites and in tissue dopamine levels in the striatum. The present study showed that marked reduction in [^{3}H]mazindol binding was evident in the striatum where severe reductions of dopamine and DOPAC contents were found 3 and 7 days after acute treatment with MPTP. Therefore, our findings also suggest that there is a good correlation between the decreases in [^{3}H]mazindol binding sites and in dopamine levels in the striatum.

In conclusion, the present study demonstrates that severe functional damage in dopamine uptake sites occurs in the striatum and substantia nigra 3 and 7 days after acute treatment with MPTP. In contrast, dopamine D_1 receptors are unaltered in the striatum and substantia nigra after the treatment. Dopamine D_2 receptors are significantly decreased in the substantia nigra 7 days after the MPTP treatment, whereas no significant change in the receptors is observed in the striatum. Our results also suggest that marked reduction in dopamine and its metabolite (DOPAC) contents is found in the striatum 3 and 7 days after acute treatment with MPTP. Our studies may provide valuable information for the pathogenesis of acute stage of Parkinson's disease.

References

1) Burns R.S., et al., Proc. Natl. Acad. Sci. USA. **80** (1983) 4546.
2) Langston J. W., Ballard P. A., Tetrud J.W., and Irwin I., Science. **219** (1983) 979.
3) Heikkila R. E., Hess A., and Duvoisin R. C., Science. **224** (1984) 1451.
4) Sundström E., Strömberg I., TsuTsumi T., Olson L., and Jonsson G., Brain. Res. **405** (1987) 26.
5) Vias I., Heikkila R. E., and Nicklas W. J., J. Neurochem. **46** (1986) 1501.
6) Scotcher K. P.,et. al., Neurochem. **54** (1990) 1295.
7) Gluck M. R., et al., J. Biol. Chem. **269** (1994) 3167.
8) Hasegawa E., et al., Biochem. Biophys. Res. Commun. **170** (1990) 1049.
9) Chiueh C. C., and Rauhara P., Adv. Pharmacol. **42** (1998) 796.
10) Shultz J. B., et al., J. Neurochem. **64** (1995) 936.
11) Przedborski S., et al., Proc. Natl. Acad. Sci. U.S.A. **93** (1996) 4565.
12) Dawson T. M., et al., Eur. J. Pharmacol. **108** (1985) 323.
13) Araki T., Kato H., Kogure K., and Kanai Y., Br. J. Pharmacol. **107** (1992) 437.
14) Köhler A. C., and Radesäter A. C., Neurosci. Lett. **66** (1986) 85.
15) Przedborski S.,et al., J. Neurochem. **57** (1991) 1951.
16) Araki T., Kato H., Shuto K., Fujiwara T., and Itoyama Y., J. Neurol. Sci. **148** (1997) 131.
17) Javitch J. A., Strittmatter S. M., and Snyder S. H., J. Neurosci. **5** (1985) 1513.
18) Filloux F. M., Wamsley J. K., and Dawson T. M., Brain. Res. **408** (1987) 205.
19) Filloux F. M., Dawson T. M., and Wamsley J. K., Brain. Res. Bull. **20** (1988) 447.
20) Boyson S. J., McGonigle P., and Molinoff P. B., J. Neurosci. **6** (1986) 3177.
21) Charuchinda C., Supavilai P., Karobath M., and Palacios J. M., J. Neurosci. **7** (1987) 1352.
22) Wamsley J. K., et al., J. Chem. Neuroanat. **2** (1989) 119.
23) Pierot L., et al., J. Neurol. Sci. **86** (1988) 291.
24) Cortès R., Camps M., Gueye B., Probst A., and Palacios J. M., Brain. Res. **483** (1989) 30.
25) Raisman R., Cash R., Ruberg M., Agid F. J., and Agid Y., Eur. J. Pharmacol. **113** (1985) 269.
26) Rinne J. O., Rinne J. K., Laakso K., Lönnberg P., and Rinne U. K., Brain. Res. **359** (1985) 306.
27) Guttman M., and Seeman P., Adv. Neurol. **45** (1986) 51.
28) Brooks D. J., et al., Ann. Neurol. **31** (1992) 184.
29) Sawle G. V., et al., Brain. **116** (1993) 853.
30) Murray A. M., et al., Ann. Neurol. **37** (1995) 300.
31) Alexander G. M., et al., Brain. Res. **588** (1992) 261.
32) Frohna P. A., Rothblat D. S., Joyce J. S., and Schneider J. S., Synapse. **19** (1995) 46.
33) Gnanalingham K. K., et al., Eur. J. Pharmacol. **277** (1995) 235.

Table 1. Time course of the changes in [^{3}H]SCH23390, [^{3}H]raclopride and [^{3}H]mazindol binding in the striatum and substantia nigra of mice after MPTP treatment

	Saline (n=12)	After MPTP treatment	
		3 days (n=6)	7 days (n=6)
[^{3}H]SCH23390 binding			
Striatum lateral	734±26	694±45	727±46
medial	686±30	655±39	686±48
Substantia nigra	310±8	291±8	327±7
[^{3}H]Raclopride binding			
Striatum lateral	68±1.8	66±2.6	65±2.8
medial	55±1.9	56±0.8	55±1.9
Substantia nigra	12±0.3	12±0.3	9±0.4**
[^{3}H]Mazindol binding			
Striatum lateral	141±4	42±6**	44±5**
medial	120±4	21±4**	22±4**
Substantia nigra	37±3	18±3**	13±3**

Values are mean±S.E. (fmol/mg tissue).
* $p < 0.05$, ** $p < 0.01$ vs. saline-treated group (Dunnet's multiple range test). n=6-12 mice.
Striatum (lateral): dorsolateral part.
Striatum (medial): ventromedial part.
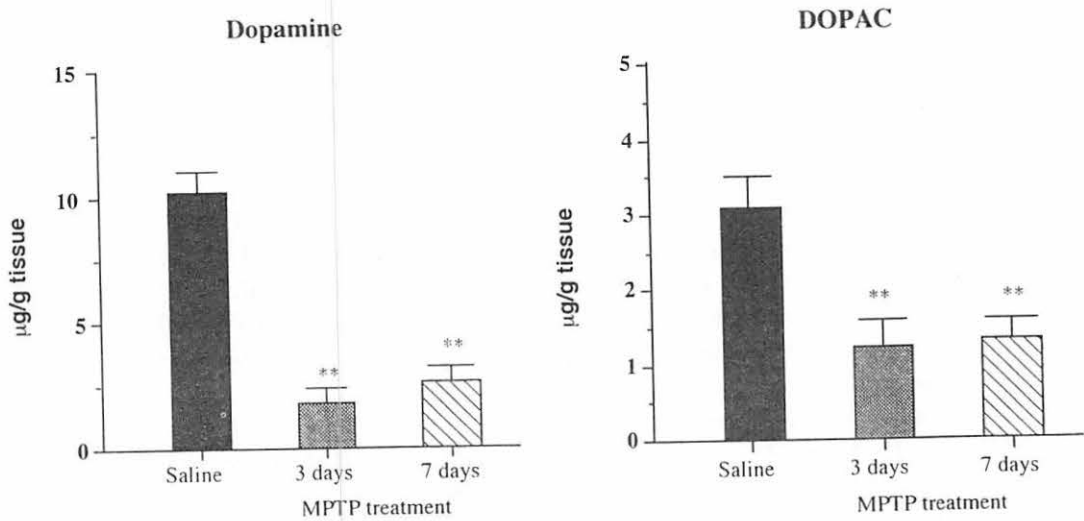
Fig. 1. Striatal concentration of dopamine and its metabolite (DOPAC) 3 and 7 days after acute treatment with MPTP in mice. n=6 mice. * $p < 0.05$, ** $p < 0.01$ vs. saline-treated group (Dunnett's multiple range test).

III. 7. Excitoxicity Induces Changes in Rat Brain Gangliosides.

Valdes-Gonzalez T., Morita Y., Suzuki K., and, Ido, T.

Cyclotron and Radioisotope Center, Tohoku University.

The behavior of major gangliosides in rat hippocampus and olfactory bulbs after microinjections of Ibotenic acid, an NMDA receptor agonist was examined in vivo. Four days after injection in the olfactory bulbs under free-movement conditions, the ratio of gangliosides in rats injected with the the excitatory amino acid increased significantly for GQ1b, GT1b and GD1b in hippocampus and a decreased for GQ1b, GT1b, GD1b, GD1a and GM1 in the olfactory bulbs. The alterations in gangliosides were minimal one day after injection. Five weeks after, the amount of GD1a and GM1 in the hippocampus remained at normal levels while GQ1b, GT1b and GD1b dramatically decreased. In the olfactory bulbs ganglioside recovery was observed. Experiments with Beta-N-oxalylamino-L-alanine (L-BOAA), an AMPA receptor agonist corroborated the suggestion that gangliosides play an active role during excitotoxicity. The changes of hippocampal gangliosides could be related with a compensatory mechanisms. Experiments with PBS confirmed that the changes observed were due to the action of the excitotoxicity. The results obtained explain in part, the data published in recent reports concerning the effectiveness of ganglioside in the treatment of degenerated brain cells due to excitoxicity.

Introduction

Hippocampal gangliosides have been the focus of interest in several reports because of the fundamental role that hippocampus plays in memory formation and its vulnerability to several neurological diseases[1,2,3]. Glutamate excitotoxicity seems to play an important role as a factor in many acute and chronic neurologic diseases[3,4], glutamatergic pathway predominates in the hippocampus[5] and exogenous gangliosides promote changes on glutamate receptors[1]. Taking in account these three facts, the authors utilized the signal transmission pathway between olfactory system and hippocampus[6,7,8] in order to clarify the effect of excitotoxity on endogenous gangliosides. First, Ibotenic acid and beta-N-oxalylamino-L-alanine (L-BOAA) which are glutamate-like excitatory aminoacids (NMDA and AMPA glutamate receptor agonists respectively)[9,10,11,12], were microinjected into the olfactory bulbs of rats under free movement conditions in order to observe the behavior of gangliosides in this organ. Second, the possible effect of induced excitatory signals from

the olfactory bulb on hippocampal gangliosides was investigated. Besides the effect of excitoxicity in the total neuraminic acid amount in hippocampus was determined.

Materials and Methods

Microinjections

Rats (male, 10 weeks) were anesthetized with pentobarbital (50mg/kg) and placed in a stereotaxic apparatus. A guide-cannula was permanently implanted to a depth of 2.5 mm in the left olfactory bulb (6.2 mm forward and 0.9 mm lateral from bregma)[13]. Two days after the implantation procedure, the animals were injected under free-movement conditions with 4 uL 0.01M Ibotenic acid in PBS (pH 7.4) at a flow rate of 1 uL/min using the micro-syringe pump and Hamilton syringes. The rats were decapitated 1, 4 or 35 days after the injection and the left and right hippocampus and olfactory bulbs were dissected. Non-injected rats were used as control. The same procedure was repeated with injections of 1 uL of 0.05M L-BOAA in PBS (pH 7.4) at a flow rate of 0.1 uL/min or 4 uL of PBS (pH 7.4) at a flow rate of 1uL/min flow rate. Four days after the injection, the rats were decapitated and the left and right hippocampi and olfactory bulbs were dissected.

Ganglioside extraction:

The left and right hippocampi and olfactory bulbs were processed and prepared separately. Approximately 25 mg of wet tissue was homogenized in 4 mL of chloroform/methanol/water (1.5:3:0.4), centrifuged at 2500 rpm for 10 min, and the supernatant was collected. The pellet was re-homogenized in chloroform/methanol (0.75:1.5) and centrifuged at 2500 rpm for 30 min. The supernatants were then combined and ran through a DEAE Sephadex column (0.5 idx3 cm). The neutral lipids were washed out with 5 mL of chloroform/methanol/water (30:60:8). The acidic lipids were eluted with 5 mL of chloroform/methanol/2M sodium acetate (30:60:8). The acidic fractions were then evaporated to remove the solvents and redissolved in 2 mL of 0.1N potassium hydroxide in methanol. After 2 hours of hydrolysis at 37°C, the reaction was stopped with 2 mL of 0.1N acetic acid, the solvent removed by evaporation, and the hydrolisate dialyzed against water for 1 day. The solution was then evaporated to remove the water, the sample redissolved in chloroform/methanol (9:1), and put through an IATROBEADS column (0.5 idx3 cm). The first fraction eluted with 5 mL of chloroform/methanol (85:15) was discarded. The second fraction eluted with 5 mL of chloroform/methanol (3:7) was collected, evaporated to remove the solvent, redissolved in 1.5 mL of chloroform/methanol (1:1), and dried under nitrogen stream. Finally, chloroform/methanol (3:7) was added to obtain concentrations of 1mg/uL that corresponded to the initial wet weight of the tissues, for the samples of Ibo after 35 days the prepared concentrations were of 2mg/uL.

TLC:

Ganglioside composition was determined by TLC-densitometry. Calibration curves were drawn using an authentic ganglioside mixture. This mixture was composed of known amounts of GM1, GD1a, GD1b, GT1b, and GQ1b. In addition, a bovine ganglioside mixture was used as standard. The correlation coefficients for linearity of calibration curves of standards were between 0.98 and 0.99 ($p<0.01$). Spots of 2 uL of samples were applied to the TLC plates, using a Hamilton syringe and developed for 20 min in chloroform/methanol/0.2% calcium chloride (55:45:10). Standards samples were developed in parallel with the test samples. Gangliosides were visualized by the resorcinol-HCL reagent and measured at 580 nm using the scanner.

Ganglioside change determination:

Ganglioside changes in olfactory bulbs were calculated as follow:

Ganglioside ratio (GgR)=amount of neuraminic acid in gangliosides of left olfactory bulb (injected side of olfactory bulb)/amount of neuraminic acid in gangliosides of right olfactory bulb (non-injected side of olfactory bulb).

GgR changes in hippocampi were calculated as follow:

Ganglioside ratio (GgR)=amount of neuraminic acid in gangliosides of left hippocampus (hippocampus corresponding to injected side of olfactory bulb)/amount of neuraminic acid in gangliosides of right hippocampus (hippocampus corresponding to non-injected side of olfactory bulb).

For the statistical analysis of the results were used first ANOVA and then a multiple comparison Dunett test ($p<0.05$).

Total neuraminic acid determination:

The rats were microinjected and the hippocampus dissected. The hippocampal tissues were homogenized in 300 uL of 0.1N H_2SO_4, hydrolyzed for 2 hours at 80°C, centrifuged at 3000 rpm for 20 min at 4°C, and the supernatants were collected. Next, 20 uL of 0.1N H_2SO_4 and 50 uL of 7mM DMB in solution containing 1.0 M 2-mercaptoethanol and 18mM Na_2SO_4 were added to 30 uL of supernatant. The samples were heated for 2.5 hours at 60°C, purified on a reverse phase chromatography column using chloroform/methanol/water (25:4:91) as an effluent at a rate of 1.2 mL/min, and the neuraminic acid was analyzed with the fluorometer. For the statistical analysis of the results ANOVA was used ($p<0.01$).

Results

The gangliosides from the hippocampus were purified separately and developed by TLC 1, 4 and 35 days after Ibotenic acid injection (Fig. 1).

Hippocampal GgR were calculated and compared with GgR of normal rat brain. The results showed that one and four days after injection the ganglioside ratio in the rats injected with the excitatory aminoacid increased, significantly for GQ1b, GT1b and four GD1b days after injection. Five weeks after, the ratio of GD1a and GM1 remained at normal levels, but the amount of GQ1b, GT1b and GD1b decreased significantly from the initial stage ($p<0.05$) (Fig. 2).

The analysis of the gangliosides purified from the olfactory bulbs was performed in the same manner as the hippocampal gangliosides (Fig. 3). The results showed that there was no significant changes one day after injection of Ibotenic acid. However, after four days, compared with the ganglioside ratio in the normal rat olfactory bulb, the ratio in rats injected with the excitatory amino acid decreased, particularly with respect to GQ1b, GT1b, GD1b, GD1a and GM1 levels. Five weeks after, the gangliosides recovered to normal rat brain levels ($p<0.05$) (Fig.4).

Four days after injection fundamental changes induced by Ibotenic acid were observed in both, hippocampus and olfactory bulbs, therefore the subsequent experiments, considered this interval of time to investigate the effect of L-BOAA injections on the GgR in olfactory bulbs and hippocampi. The gangliosides were purified separately and developed by TLC and the respective GgR calculated. The results obtained with L-BOAA were compared with the GgR of rats injected with PBS. The results obtained for Ibotenic acid four days after injections were also compared in order to determine whether the microsurgery and injection affect the results (Fig 5 and Fig. 6)

We found for rats injected with L-BOAA, significant increases in hippocampal GgR in terms of GT1b, GD1b and GM1 and significant decreases in GgR of olfactory bulbs, in particular for GT1b, GD1a and GM1. In rats injected with Ibotenic acid hippocampal GgR showed significant increases for GT1b and GD1b (GQ1b was not calculated and for olfactory bulbs there were observed significant decreases for GD1a and GM1 when compared with rats injected with PBS ($p<0.05$).

Moreover some significant differences were found when the results of rats injected with L-BOAA and rats injected Ibotenic acid were compared. Hippocampal GgR showed significant differences for GM1, due to the higher increment of GM1 in rats injected with L-BOAA. For GgR in olfactory bulbs significant differences were observed for GT1b and GD1a due to the greater decline in GgR of those gangliosides in rats injected with L-BOAA ($p<0.05$).

There were no observable changes in the total hippocampal neuraminic acid content of rats that had received L-BOAA and Ibotenic acid injections in the olfactory bulbs when compared with non-operated rats and rats injected with PBS ($P<0.01$) (Table 1).

Dicussion

The excitotoxicity is characterized by the increase of intracellular Ca^{2+} and excessive glutamate release that triggers a cascade of process, many of which remain activated long time

after the initial stimulus is removed, leading to neuronal cell injury, even death. Our results show that excitotoxicity induced by injections of Ibotenic acid in the rat olfactory bulbs promote transient changes of ganglioside amount in olfactory bulb and permanent changes in hippocampus. The decreases of GgR in olfactory bulbs are due to neuronal injury caused by the direct effect of excitotoxicity. The observed increase of hippocampal pathway B gangliosides suggests the action of a compensatory process to increase the number of glutamate receptor that decreased due to neuronal loss as a result of the induced excitoxicity from the olfactory bulb. The results obtained with L-BOAA strengthen the results observed in the experiments with Ibotenic acid. The recovery of GgR in the olfactory bulbs five weeks after the injection of Ibotenic acid could be related with the capacity of regeneration of olfactory neurons. The non-recovery of hippocampal polysialo-gangliosides GgR to normal levels indicates that these are the most involved gangliosides in the protective response to counteract the effect of excitotoxicity. The changes in the hippocampus were permanent due to the higher sensibility of hippocampus to the excitotoxicity. Our results demonstrate that gangliosides have an active role during excitotoxicity as modulation molecules and explain, in part, the published data concerning the effectiveness of ganglioside in the treatment of degenerated brain cells due to excitoxicity.

Acknowledgements

References

1) Hollmann, M. and Seifert, W., Neuros. Lett. 65(1986)133-138.
2) Obrenovitch, T. P., Urenjak J. and Zilkha E., J. Neurochem. 66(1996)6, 2446-2454.
3) Thomas, P. D. and Brewer G. J. Biochem. Bioph. Act 1031(1990)277-28.
4) Massieu, L., Morales-Villagran, A and Tapia R., J. Neurochem., 64(1995) 2262-2272.
5) Fishman, P. H. and Brady., R.O. Sci., 194(1976)906-915,.
6) Kandel, E.R., Schwartz, J. H., and Jessel, T. M. (Eds.), Principles of Neural Science, III Edition, 512-518, 1991.
7) Nolte J. (Eds). The human brain. An introduction to its functional anatomy. Second Edition, 366-389, 1988.
8) Staubli, U., Ivy, G., and Lynch G., Proc. Natl. Acad. Sc. USA, 81(1985)5885-5887.
9) Contestabile, A., Virgili, M., et al., J. Neurosc. Res. 26(1990)483-487.
10) Lipska, B. K., Jaskiw, G. E., Chrapusta, S et al., Br. Res. 585(1992)1-6.
11) Ross, S.M., Roy, D. N., and Spencer, P. S., J. Neurochem. 53(1989) 710-715.
12) Sabri, M. I., Lystrup, B., Roy, D. N. and Spencer, P. S., J. Neurochem. 65(1995)1842-1848.
13) Paxinos, G., and Watson, C. (Eds.), The rat brain in stereotaxic coordinates. 1982.

Table 1

Effect of injections of L-BOAA and Ibotenic acid into olfactory bulb on total neuroaminic acid in rat hippocampus.

Parameter measured	Control	PBS	L-BOAA	Control	PBS	Ibotenic acid
Total neuroaminic acid	3.8 ± 0.20	3.7 ± 0.3	3.63 ± 0.2	4.7 ± 0.3	4.8 ± 0.1	4.7 ± 0.1

Values are mean ± S.E.M (nmol/mg wet tissue: brain) from 3 animals in each group. *PBS* are the data of the rats injected with PBS, *L-BOAA* are the data of the rats injected with L-BOAA, *Ibotenic acid* are the data of the rats injected with Ibotenic acid and *Control* are the data of not operated rats. Values were compared by ANOVA (P<0.01).
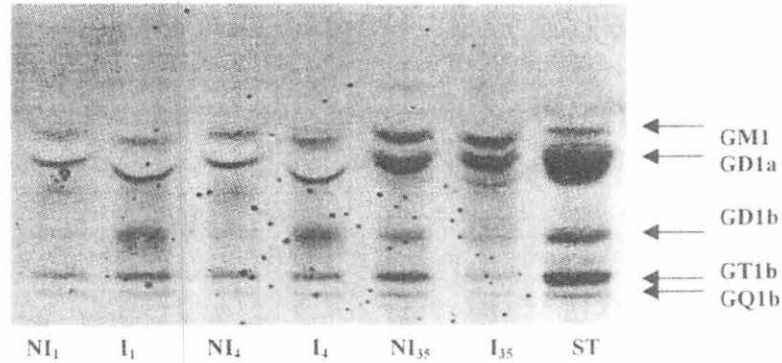
Fig. 1. Thin layer chromatogram of rat hippocampal gangliosides after injection with Ibotenic acid. NI, hippocampus corresponding to the side of olfactory bulb that was not injected. I, hippocampus corresponding to the injected side of olfactory bulb. Subscripts 1, 4 and 35 different days after injection. ST is the standard.
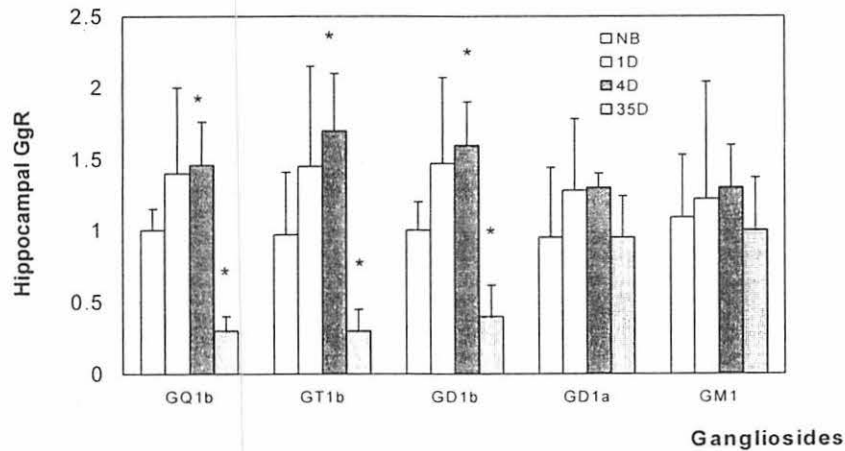
Fig. 2. Time-dependent changes of Hippocampal ganglioside ratio (GgR) after injections with Ibotenic acid. NB are non-injected rats. Rats were sacrificed 1, 4 or 35 days after injections. Values are mean ± S.E.M. from 3 animals. The data were evaluated by ANOVA and then by a multiple comparison Dunett test (p<0.05).

143
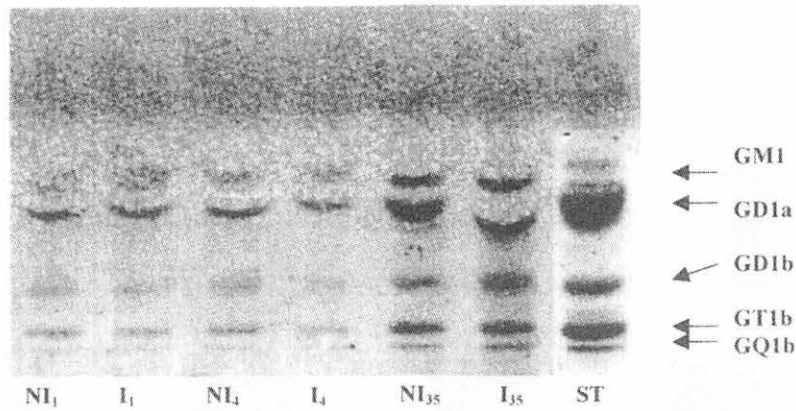
Fig. 3. Thin layer chromatogram of gangliosides of rat olfactory bulbs after injection with Ibotenic acid. NI, refers to the no injected olfactory bulb. I, refers to the injected olfactory bulb. Subscripts 1, 4 and 35 represent different days after injection and subscript ST represent the standard.
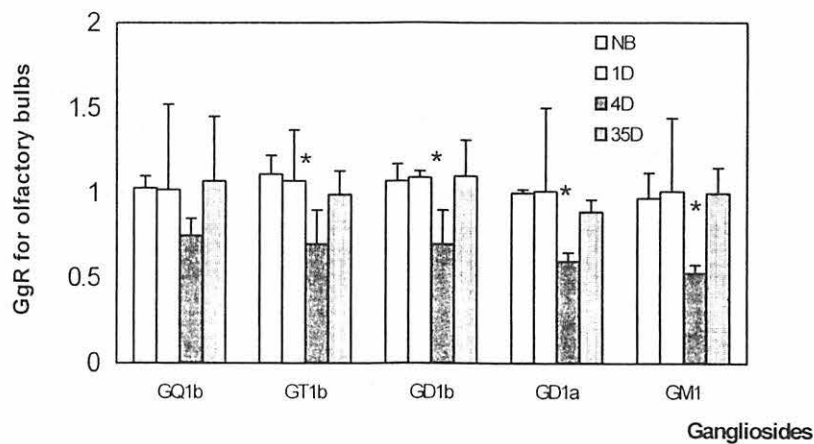
Fig. 4. Time-dependent changes of ganglioside ratio (GgR) in olfactory bulbs after injections with Ibotenic acid. NB are non-injected rats. Rats were sacrificed 1, 4 or 35 days after injections. Values are mean ± S.E.M. from 3 animals. The data were evaluated by ANOVA and then by a multiple comparison Dunett test (p<0.05).
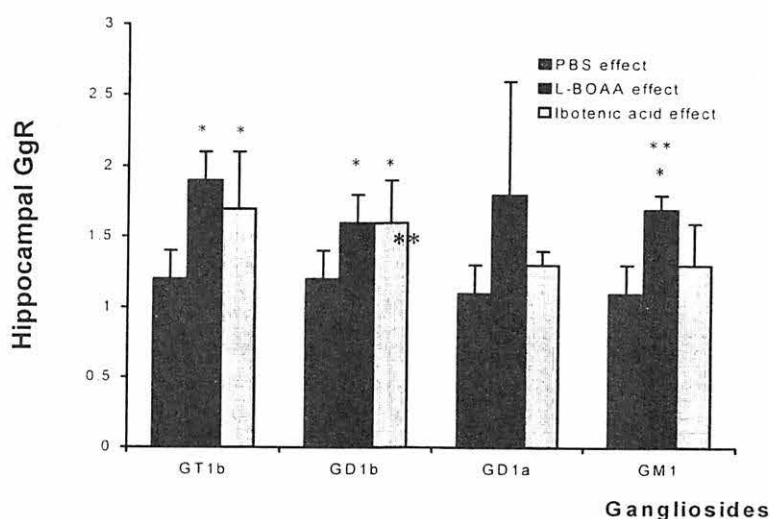
Fig. 5. Hippocampal ganglioside ratio (GgR) for rats injected with L-BOAA or Ibotenic acid. PBS are the data of rats injected with PBS. Rats were sacrificed 4 days after injections. Values are mean ± S.E.M. from 3 animals. The data were evaluated by ANOVA and then a multiple comparison Dunett test. *significance for comparison with PBS, **significance for comparison between L-BOAA and Ibotenic acid (p<0.05).

144
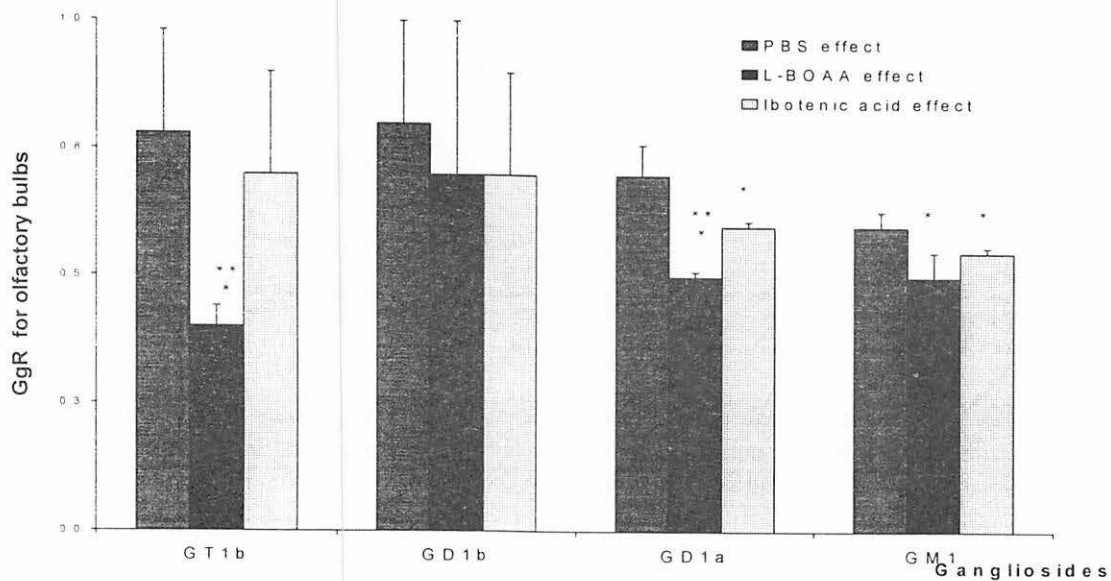
Fig. 6. Ganglioside ratio (GgR) in olfactory bulbs for rats injected with L-BOAA or Ibotenic acid. PBS are the rats injected with PBS. Rats were sacrificed 4 days after injections. Values are mean ± S.E.M. from 3 animals. The data were evaluated by ANOVA and then a multiple comparison Dunett test. *significance for comparison with PBS, **significance for comparison between L-BOAA and Ibotenic acid. (p<0.05).

IV. MEDICINE AND BIOLOGY (Clinical)

IV. 1.   Dynamic PET Imaging of Whole Body Glucose Distribution after Oral Administration of [^{18}F]-fluoro-deoxy-glucose

Yamaguchi K., Ozaki K., Itoh M., Masud M., Watanuki S., Miyake M., Rikimaru H., and Ido T.

Cyclotron and Radioisotope Center; Tohoku University

Introduction

[^{18}F]-labeled-2-deoxy-2-fluoro-D-glucose (FDG) is a positron-emitting analogue of glucose and has been used for investigating pathophysiology of the brain, heart and other organs in vivo in human.   So far, its usage has been confined to through the intravenous route only as it was thought that its structural complexity might pose some prohibition to intestinal absorption.   Uptake of sugar from intestinal lumen is an active process, which requires sodium dependent glucose transporter, SGLUT1.   However, the SGLUT1 has been known to be specific for the structure of pyranose ring with hydroxy group at the second position[1].   FDG is hardly to be a substrate for this enzyme because it has fluorine at this position.   Therefore intestinal uptake of FDG seemed quite unlikely.   However, Martinez et al first tried the oral FDG administration as an alternative method for brain imaging[2].   Their study suggested the possibility of FDG absorption from the small intestine.   The intestinal absorption is often matter of interest in clinical situations such as malabsorption syndromes and extensive intestinal surgery.   Practical PET tracer is necessary to quantitative glucose uptake from the intestine.   Recent advance in PET technology has promoted whole body imaging using sequential movement of PET coach.   We attempted to image dynamic change of whole body FDG distribution after its oral administration.   The process of alimentary uptake and transfer of glucose from blood to tissue has been successfully visualized.

Method and Materials

Six normal volunteers (mean age 28.6 years) were studied with a multi-ring tomography, SET-2400 (Shimadzu, Japan) in three-dimensional data acquisition mode. Dynamic whole-body imaging was performed every 2 minutes from pelvis to head after oral intake of ^{18}FDG (37 MBq).   The image acquisition continued up to 90 minutes and image analysis was performed.   The analysis was to calculate the tracer accumulation changes in each organ to the total FDG intake doses (fraction % of intake dose, %ID) and to try the mono exponential fittings to evaluate the mean passage time (T1/2) after setting the ROI in the

organs.

Result

Figure 1 shows the time-related changes in whole body ^{18}FDG distribution. ^{18}FDG passed through the stomach and disappeared from the alimentary tract. Following FDG accumulation was observed to the liver and the brain. Figure 2 shows the time-related %ID changes for the stomach, the small intestine, liver and the brain. The T1/2 for the stomach and for the small intestine were 18.3 (+/-4.0) and 59.3 (+/- 4.8) minutes respectively. The accumulation to the brain was observed after 30 min of oral intake and showed a gradual increase up to the end of measurement.

Discussion

Three subtypes of glucose transporter has been reported which contribute the sugar absorption from the small intestine i.e. SGLT1, GLUT2 and GLUT5[3]. The SGLUT1 and GLUT5 locate at the luminal side and the GLUT2 locates at the visceral side of intestinal epithelium. This specific location of glucose transport system is observed in both small intestine and kidney for glucose absorption or reabsorption. SGLT1 plays an active role for the glucose absorption from the small intestinal lumen to the epithelium. It is specific for the structure of pyranose ring with hydroxy radical at the second-position[4]. FDG dose not match the aforementioned structure as it has fluorine at the second position (deoxy-glucose). GLUT5 is specific for the lactate absorption and no significant affinity to the deoxyglucose[5,6]. GLUT2 has an affinity to FDG, however locates at the visceral side of the epithelium and transform from the epithelium to the portal vein[7,8].

So FDG cannot be assimilated from the lumen to the blood following the previous established mechanism. However, Our image has clearly shown the absorption of FDG and its distribution to the various organs, even to the brain. There are two possibilities to explain our images. The one possibility is the SGLUT1's structural requirement to glucose analogue is not so strict in human. The affinity of SGLUT1 to the 2-deoxy glucose has varied according to the animal spices[1], then that to the FDG might be varied. The other possibility is some alternative carrier of FDG absorption. Halaihel et al has reported the heterogeneity of glucose transport system in pig intestine[9]. We also assume that similar heterogeneity of glucose absorption system not only existing the pig but also human. Substantially, this recent heterogeneity mode of glucose transport not only clarifies our imaging finding but also advocate its usage through oral ingestion in various scanning protocol with PET. We did not analyze the plasma to identify the radioactive component is FDG. A possible explanation of FDG uptake from intestine is its metabolism by intestinal bacteria. Free 18F-fluorine, when released from FDG, may enter into circulation. However, fluorine ions are known to accumulate in the bones strongly and do not cross the blood-brain

barrier, which was not our case.

Even Though the FDG absorption mechanism is still not clear, most possible FDG absorption will be the same mechanism of glucose absorption. FDG has the steady Km value for the glucose transporter, and then the quantitative visualization of FDG using PET will be quite useful to evaluate the glucose absorption ability in case of the malabsorption syndrome and the extensive intestinal surgery. Our procedure also can be used to evaluate the natural glucose absorption related to the other organs.

References

1) Kleinzeller A., McAvoy E., Biochim. Biophys. Acta, **600** (1980) 513-29.
2) Martinez Z., Colgan M., Baxter R., et al., Am. J. Primatol. **42** (3) (1997) 215-24.
3) Thorens B., Am J Physiol **270** (4 Pt 1) (1996) G541-53.
4) Crane K., Am. Physiol. Soc., ed., 1989 p. 1323-1351.
5) Kane S., Seatter M., Gould G., Biochem. Biophys. Res. Commun. **238** (2) V503-5.
6) Rand E., Depaoli A., Davidson N., et al.,. Am. J. Physiol. **264** (6 Pt 1) (1993) G1169-76.
7) Thorens B., Cheng Z., Brown D., et al., Am. J. Physiol. **259** (6 Pt 1) (1990) C279-85.
8) Thorens B., Annu. Rev. Physiol. **55** (1993) 591-608.
9) Halaihel N., Gerband D., Vasseur M., et al., Am. J. Physiol. **277** (6 Pt 1) (1999) C1130-41.
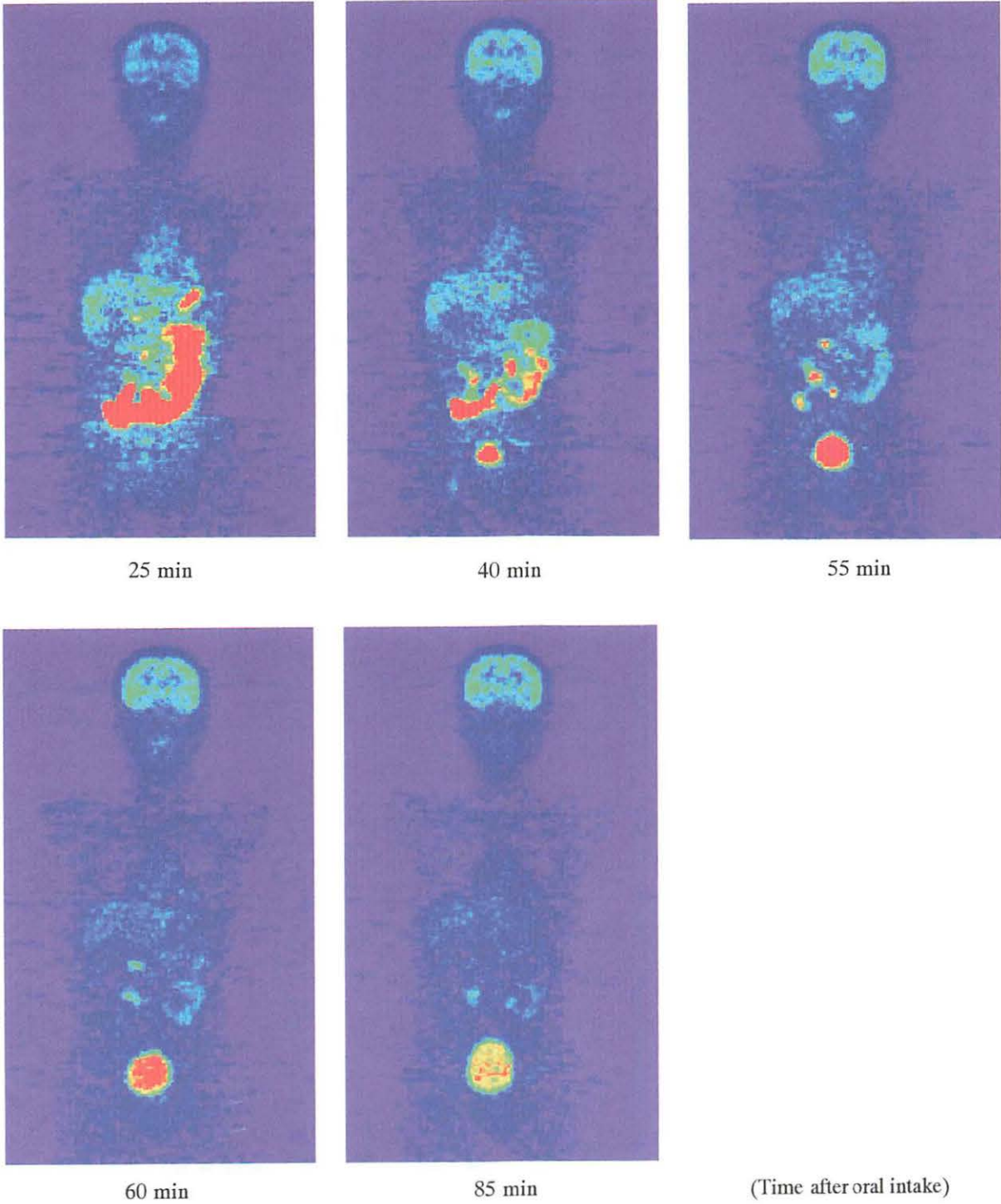
Figure 1. Time course whole body image of oral intake FDG. The whole body image was obtained every 15min. FDG elimination from the abdomen and gradual accumulation to the brain is clearly observed.

149
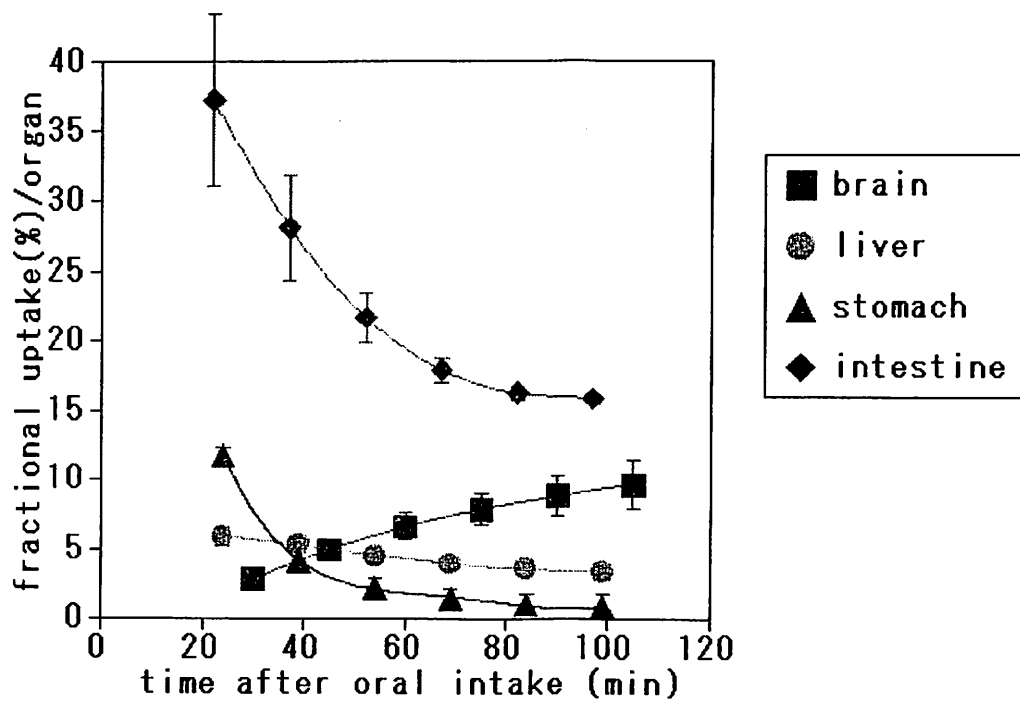
Figure 2. Time activity curve in every organ. The transverse axis shows time after oral intake and the vertical axis shows the fractional uptake. The stomach and intestinal activity decrease rapidly. The brain activity increases gradually.

IV. 2. Image Analysis of Intractable Epilepsy:[18]F-FDG PET Scan of the Cortical Dysplasia

Togashi N., Haginoya K., Munakata M., Kato R., Yokoyama H., and Iinuma K.

Department of pediatrics, Tohoku University School of Medicine

INTRODUCTION

Cortical dysplasia was studied by various imaging method, but only a few reports compared FDG-PET, SPECT, and EEG in the same case[1]. In this study, we assessed the FDG-PET findings in 9 patients with cortical dysplasia. The results were compared with those of MRI, interictal SPECT, and EEG in order to study the pathophysiology of cortical dysplasia.

MATERIALS AND METHODS

Patients

This study was performed, included nine patients (two males, seven females, age range one year to 26 years) with cortical dysplasia, diagnosed by MRI findings (Table 1) after informed consent for the patients or their guardians. Two was diagnosed band heterotopia, two was hemimegalencephaly, four cortical dysplasia, and one pachygyria. No cases were operated on.

SPECT procedure

^{99m}Tc-ethyl cysteinate dimer (ECD) was intravenously injected while the patients were awake. The SPECT images were acquired 30 minutes after injection using a Multispect 3 (Siemens, Gerfahldt, Germany) with a low-energy, high-resolution, fan-beam collimater. The patients were sedated with trichloryl hydrochloride or diazepam during scan. None of the patients showed clinical evidence of seizures during SPECT scan.

FDG-PET procedure

Out of the nine patients, six patients were studied with SET-2400W (Shimadzu Co., Japan), and three patients were studied with a model PT-931 scanner (CTI Inc., USA). Emission scan was performed 30 to 45 minutes after the 7.4-74 MBq FDG injection.

We analyzed MRI findings, EEG patterns, regional blood flow by SPECT, and regional glucose utilization by FDG-PET. SPECT and FDG-PET scans were assessed

visually by independent physicians on two separate occasions.

RESULTS

The following results were obtained (Table 2): (1) in all cases EEG showed spike focus in the dysplastic region, (2) the hyperperfusion was found in three patients, the isoperfusion in two, and the hypoperfusion in four patients in dysplasitic region, (3) the hypermetabolic pattern was found in five patients, the isometabolic pattern in three, and the hypometabolic pattern in one patient in dysplasitic region, (4) In one of bandheterotopia, area of inner heterotopia showed hypoperfusion by SPECT and isometabolism by PET. But other patients showed isoperfusion by SPECT and hypermetabolism by PET (Figure A,B,C). (5) FDG-PET and interictal SPECT was not concordant in 4 patients.

DISCUSSION

In the past literatures, SPECT show abnormal area as hyperperfusion in ictal state, hypoperfusion in interictal state, and FDG-PET show abnormal area as hypometabolism, reflecting neuronal activity in the epileptic foci of partial epilepsy[2,3]. In cortical dysplasia, however, both hyperperfusion and hypoperfusion by SPECT were reported, there is little agreement about that[4].

In our report, one case of hemimegalencephaly showed hyperperfusion by interictal SPECT and hypometabolism by FDG-PET (Figure D,E,F). We can not exclude the possibility that alteration with age of hemimegalencephalic hemisphere might cause this discrepancy, because FDG-PET was examined two years after SPECT. Although Tagawa et al.[5] reported serial IMP-SPECT of hemimegalencephaly, which was pathological hemispheric findings changed from hyperperfusion pattern to hypoperfusion pattern during 3 to 7 months. However, this may be unlikely to apply our case aged over 20 years. Dyscrepancy between perfusion and metabolism such as hyperperfusion of SPECT and hypometabolism of FDG-PET, was reported in subacute stage of ischemic brain disease[6]. It needs further consideration what discrepancy and metabolic characteristics of hemimegalencephaly.

Miura et al.[7] reported a case with isometabolism of band heterotopia. Although De Volder et al.[8] reported two cases with isometabolism or hypermetabolism by FDG-PET of band heterotopia. The comparative study of FDG-PET and SPECT were not published to the best of our knowledge. Pinard et al.[9] reported a case which showed an activation of both subcortical band heterotopia and the true cortex by functional MRI. Our two cases suggest the heterogeneity in band heterotopia.

CONCLUSION

FDG-PET does not necessarily showed the same pattern as SPECT in cortical

dysplasia. There can be characterisitic pathophysiolosy of cortical dysplasia, other than partial epilepsy.

References

1) Sasaki M., Kuwabara Y., Yoshida T., et al., J. Nucl. Med. **39** (1998) 974-7.
2) Maeda N., Wananabe K., Negoro T., et al., Jpn. J. Psychiatry Neurol. **46** (1992) 458-461.
3) Won H.J., Chang K.H., Cheon J.E. et al., Am. J. Neuroradiol. **20** (1999) 593-9.
4) Maehara T., Shimizu H., Yagishita A., et al., Brain Dev. **21** (1999) 407-412.
5) Tagawa T., Otani K., Futagi Y., et al. Brain Dev. **16** (1994) 475-9.
6) Moretti J.L., Defer G., Cinotti L., et al. Eur. J. Nucl. Med. **16** (1990) 17-22.
7) Miura K., Watanabe K., Maeda N., et al., Brain Dev. **15** (1993) 288-90.
8) De Volder A.G., Gadisseux J-FA., Michel C.J., et al., Pediatr. Neurol. **11** (1994) 290-294.
9) Pinard J.M., Feydy A., Carlier R., et al., Nerology **54** (2000) 1531-1533.

Table 1. Clinical data of the patients. Abbreviations: MRI, magnetic resonance imaging; MR, mental detardation; rt, right; lt, left; FCD, focal cortical dysplasia; ND, not done.

	MRI	Age	Sex	Symptoms
1	band heterotopia	25	F	mild MR, several seizure
2	band heterotopia	17	F	mild MR several seizure
3	rt. hemimegalencephaly	2	M	hemiplesia partial seizure
4	lt. hemimegalencephaly	26	F	hemiplesia, mild MR partial seizure
5	bilateral perisylvian syndrome	9	F	disarthria several seizure
6	rt. FCD	1	F	several seizure
7	rt. hemispheric FCD	9	M	hemiplesia, mild MR
8	rt. hemispheric FCD	7	F	hemiplesia, MR, seizure
9	pachygria	8	F	severe MR, frequent seizure

Table 2.　EEG, SPECT and PET Findings with Cortical Dysplasia.　Abbereviations: MRI, magnetic resonance imaging; SPECT, single photon emission computed tomography; PET positron emission tomography; bil., bilataral; rt, right; lt, left; FCD, focal cortical dysplasia; O, occipital; F, frontal; P, parietal; mT, midtemporal; ND, not done; [SPECT] hypo, hypoperfusion; iso, isoperfusion; hyper, hyperperfusion; [PET] hypo, hypometabolism; iso, isometabolism; hyper, hypermetabolism.

	MRI	Age	Sex	EEG Foci	SPECT	PET
1	band heterotopia	25	F	bil. O	hypo	iso
2	band heterotopia	17	F	bil. O	iso	hyper
3	rt. hemimegalencephaly	2	M	rt. F	hyper	iso
4	lt. hemimegalencephaly	26	F	lt. F	hyper	hypo
5	bilateral perisylvian synedome	9	F	lt. P rt. mT	hyper	iso
6	rt. FCD	1	F	rt. O	hypo	iso
7	rt. hemispheric FCD	9	M	rt. F-C	hypo	hyper
8	rt. hemispheric FCD	7	F	rt. C	hypo	hypo
9	pachygria	8	F	bil. F	iso	hypo
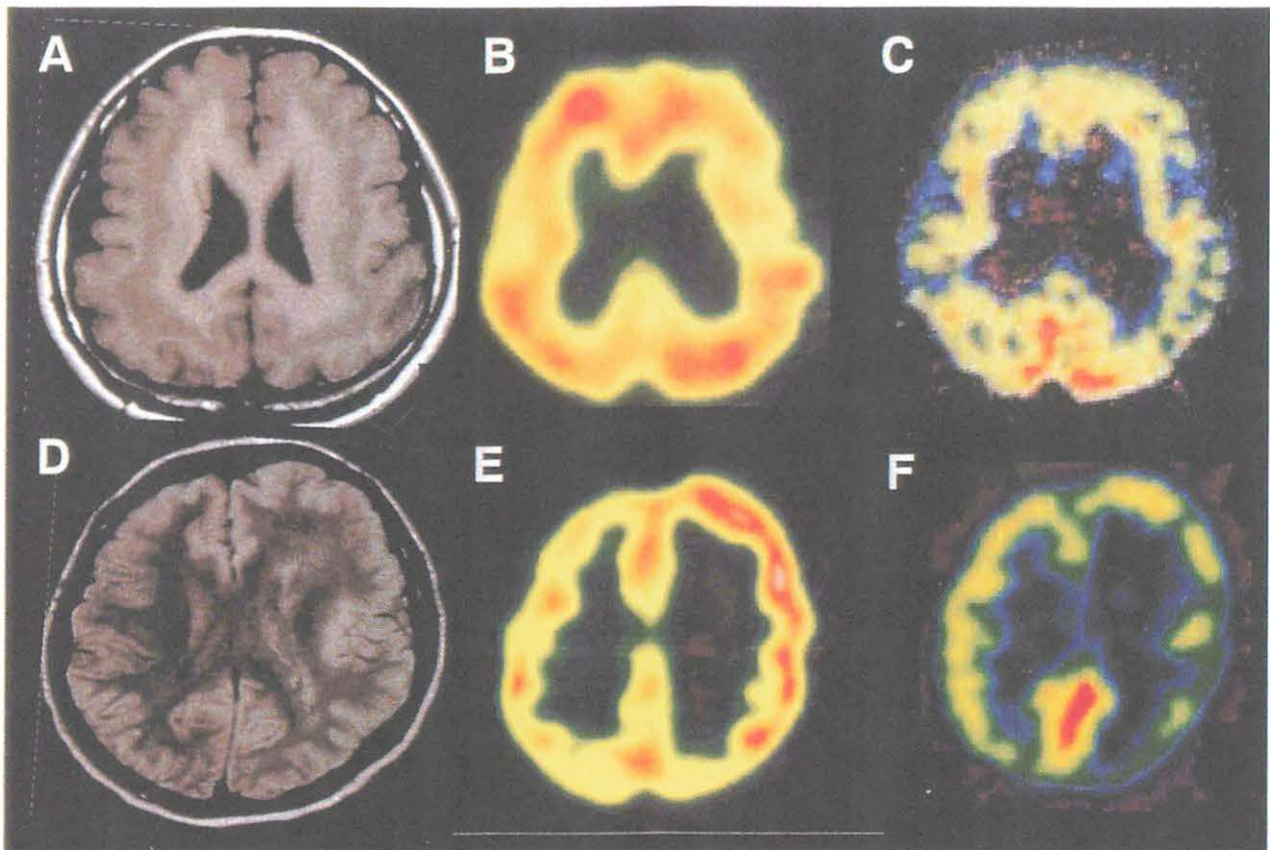
Figure 1.
Case 2: MRI(A), interictal SPECT (B), and FDG-PET (C) of bandheterotopia
FDG-PET showed hypermetabolism in subcortical heterotopic zone.
Case 4: MRI (D) , interictal SPECT (E), and FDG-PET (F) of left hemimegalencephaly.　SPECT showed hyperperfusion in left hemisphere, but FDG accumulation was low.

IV. 3. A Comparative Study of Brain Activity between two Different Resting Conditions using 3D-PET

Masud M., Itoh M., Yamaguchi K., Rikimaru H., Tashiro M., Ozaki K., Jeong M., Ido T., Watanuki S., and Miyake M.

Cyclotron and Radioisotope Center, Tohoku University

Introduction

Positron Emission Tomography (PET) can evaluate brain function using energy metabolism[1] or cerebral blood flow changes[2] as markers. The FDG-PET method, has been widely used to explore regional cerebral glucose metabolism to assess neuronal function. By applying appropriate statistical analysis (SPM in particular) over the brain image data, the activation of brain regions induced by tasks was detected (Friston et al.)[3]. From the time being, FDG was administered to the body through intravenous route for human studies. We attempted to apply FDG introduction through oral route for the evaluation of glucose absorption by the alimentary system. This method has also advantages to record regional metabolic rate of glucose (rCMRGlu) in organs other than digestive tracts.

In this brief article we investigated possible differences in regional brain functions in similar resting conditions measured two different imaging protocols, i.e. i.v. or oral FDG administration.

Subjects and Methods

Two groups of healthy male volunteers engaged as the i.v. and the oral groups. The i.v. group (mean age, 26.9±9.3y,± S.D) were studied during resting condition with intravenous FDG administration, while the oral group (mean age, 27.9±11.3y, ±S.D) received FDG orally. Each group comprised of 10 male subjects. They served as resting control subjects for the other studies. The resting condition was termed as remaining on the sitting posture after injection of FDG in a lit quiet room with eyes open without ear-plug. They were refrained from eating and drinking at least 3 hours before the experiment. Written informed consents were obtained from all the subjects after detailed explanations of the protocol. The study protocol was approved by the Clinical Committee for Radio-isotope Use of Tohoku University School of Medicine. An intravenous blood sample was obtained from all the subjects to measure blood glucose level before the FDG injection.

Study Protocol

I.V. group: The i.v. group subjects rested for around 5 min in a comfortable chair before FDG injection through the antecubital vein. The radio-isotope dose was in average 55.5±31.4 MBq. They remained at the same sitting posture for 30 minutes before PET measurement in the same room. After voiding they lay on a PET examination coach and emission scan was started about 45 min later following the FDG injection. A set of 3D whole body emission scan was performed by using a PET Scanner [SET-2400W, Shimadzu Co. Japan] with the intrinsic in-plane spatial resolution of 3.9 mm of full width at half maximum (FWHM) and 200 mm axial field of view. Ten incremental scans were obtained from leg to the head to cover the whole body. Emission scan continued for 30-33 min (depending on subjects' body size) using 180 sec per scan for each bed position. Transmission scan lasted for 30-33 min (180 sec/scan) by using a 68Ge/68Ga external rotating line source (370 MBqs).

Oral group: FDG (40.40±3.9 MBq) was administered orally to the subjects about 15 min before the emission scan. Dynamic whole body emission scan (3 min/scan) was performed in every 3 min from pelvis to the vertex. The brain images scanned around one hour following the oral intake of FDG were used for the analysis. Transmission scan was performed about 18 min (3 min/scan) to correct the attenuation of photons.

PET image data were reconstructed into a 128×128×63 matrix for a set of 3D volume images by applying filtered 3D back projection algorithm using a Tohoku University supercomputer (SX-4/128H4)(Fujiwara et al.)[4].

STATISTICAL ANALYSIS

The statistical parametric mapping (SPM-96) package was used for the analysis. The brain images were spatially normalized to minimize anatomical variations between the subjects. Smoothing was performed by using 14-14-14 mm isotropic Gaussian filter. Voxel based statistical analysis was performed on these smoothed images by choosing 'compare-groups: 1 scan per subject' analysis. The locations of relative hypermetabolic brain regions for each group were listed using the x, y and z co-ordinates (Talairach and Tournoux, 1988)[5] with a statistically significant threshold level of $p<0.001$ without correction for multiple comparisons.

Results

Figure 1. and Figure 2. depict the relative hypermetabolic regions in i.v. and oral group respectively. Applying the statistical analysis, the i.v. group showed hyperactive brain regions in the right superior frontal gyrus, left superior parietal lobule, right inferior parietal lobule, left lingual gyrus and right superior occipital gyrus (Brodmann's area (BA),

BA6, BA7, BA40, BA17 and BA19 respectively) (Table-1). The oral-group showed regional relative hypermetabolism in the right gyrus rectus, left superior parietal lobule, left superior temporal gyrus, bilateral middle and inferior temporal gyrus and left parahippocampal gyrus (BA11, BA7, BA22, BA21 and 20, BA28 respectively). Bilateral cerebellar hemisphere, right ventral lateral nucleus of thalamus (VLN) and right amygdaloid nucleus also showed higher metabolism (Table-2).

Discussions

Intravenous administration of FDG is the most common use in clinical PET practices. We attempted to compare resting brains obtained either via FDG-oral intake or intravenous administration in normal resting subjects. Since glucose is the principal energy source for brain tissue, regional cerebral FDG uptake is a close indicator of functional level of the brain in physiological or pathological conditions. The most remarkable difference in FDG uptake between i.v. and oral FDG administration in this study were found in the limbic structure (parahippocampal gyrus, thalamic (VLN) and amygdaloid nucleus) in the oral group and visual association cortex (lingual gyrus and superior occipital gyrus) in the i.v. group. A previous report which compared between i.v. and oral-FDG administration as a case report, suggested no difference in regional glucose metabolism in the brain[6]. However, that study used a simple subtraction technique in stead of the statistical comparisons. We searched brain regions with statistical difference applying the SPM between two groups of resting subjects (i.v. vs. oral). The relative hypermetabolism found in our study between via i.v. and oral-FDG administration, might emerge from inter-subject variations because different subjects comprised each group. Although we tried to keep similar resting condition during PET scans. However, the scanning set ups were not completely matched between the two groups due to differences in each study purpose. The build up phase of radioactivity in the brain continued significantly longer in the oral group because of slow FDG transfer from intestine to the plasma compared to a bolus FDG injection.

Figure 3. shows as example the average input functions of FDG-tracer in normal volunteer for oral and i.v. routes respectively. It is presumably assumed that time related arterial-kinetics of FDG is rather slow in oral intake than i.v. administration. This slow input function of FDG apparently induced brain activations in resting subjects of oral group. The prolonged scanning time and longer buid-up phase in the oral study may be the most possible explanation for this difference. The contamination of behavioral distress is suggested by the regional distribution of significant hypermetabolic area in the oral group which includes the limbic structure such as parahippocampal gyrus and amygdaloid nucleus. The visual association cortex (lingual gyrus; B.A17 and superior occipital gyrus; B.A19) was activated in the i.v. group only. Although the both group subjects kept their eyes open until PET measurement, many subjects closed their eyes later during PET scan. This time was

still within the build-up phase only in the oral group. The difference in the timing of the FDG build-up phase is a possible explanation in the difference of regional glucose metabolism between the two conditions. Significantly different brain areas were detected by the statistical analysis especially in the limbic structures and occipital brain regions. The most possible explanation for this difference is longer-up time in the oral administration. This study suggests the need of substantial caution when a pooled control population were used for activation studies.

References

1) Fahey F.H., Wood F.B., Flowers D.L., et al., J. Comput. Assist. Tomogr., 22 (6)(1998) 953-961.
2) Itoh M., Miyazaki H., Tashiro M., et al., J. Intl. Soc. Life. Info. Sci. 15 (2)(1997) 282-287.
3) Friston K., J Holmes A., P Worsley K., J, et al., Hum. Brain Mapping 2 (1995) 189-210.
4) Fujiwara T., Watanuki S., Yamamoto s., et al., Ann. Nucl. Medicine 11 (1997) 307-313.
5) Talairach J., Tournoux; Rayport M. (translator), Theim, Stuttgart, 1988.
6) Martinez Z.A., Colgan M., Baxter L.R. Jr., et al., Am. J. Primatol., 42 (3) (1997) 215-24.

Table 1. Activated brain areas in I. V. group.

Structures	Brodmann's area (B.A)	Hemisphere	Talairach Co-ordinates of statistical peak			Z score of statistical peak.
			x	y	z	
Superior frontal gyrus	6	Right	6	4	80	4.00
Superior parietal lobule	7	Left	-40	-46	64	3.58
Inferior parietal lobule	40	Right	50	-8	52	3.44
Lingual gyrus	17	Left	-4	-84	0	3.27
Superior occipital gyrus	19	Right	36	-84	44	3.38

Z score =>3.00 (corresponded to p=<0.001) suggested the significant metabolic activation of brain regions.

Table 2. Activated brain areas in oral group.

Structures	Brodmann's area (B.A)	Hemisphere	Talairach Co-ordinates of statistical peak			Z score of statistical peak.
			x	y	z	
Gyrus rectus	11	Right	4	44	-28	3.62
Superior parietal lobule	7	Left	-14	-66	-52	3.67
Superior temporal gyrus	22	Left	-62	4	-4	3.69
Middle temporal gyrus	21	Right	52	-12	-16	4.38
		Left	-52	-16	-12	3.77
Inferior temporal gyrus	20	Right	46	-6	-24	4.54
		Left	-46	-22	-8	3.70
Parahippocampal gyrus	28	Left	-22	-22	-16	3.24
Amygdaloid body		Right	18	-10	16	3.81
Thalamus (VLNucl)		Right	12	-26	-24	3.67
Cerebellum		Right	20	-56	-40	3.34
		Left	-22	-50	-32	3.55

Z score =>3.00 (corresponded to p=<0.001) suggested the significant metabolic activation of brain regions.
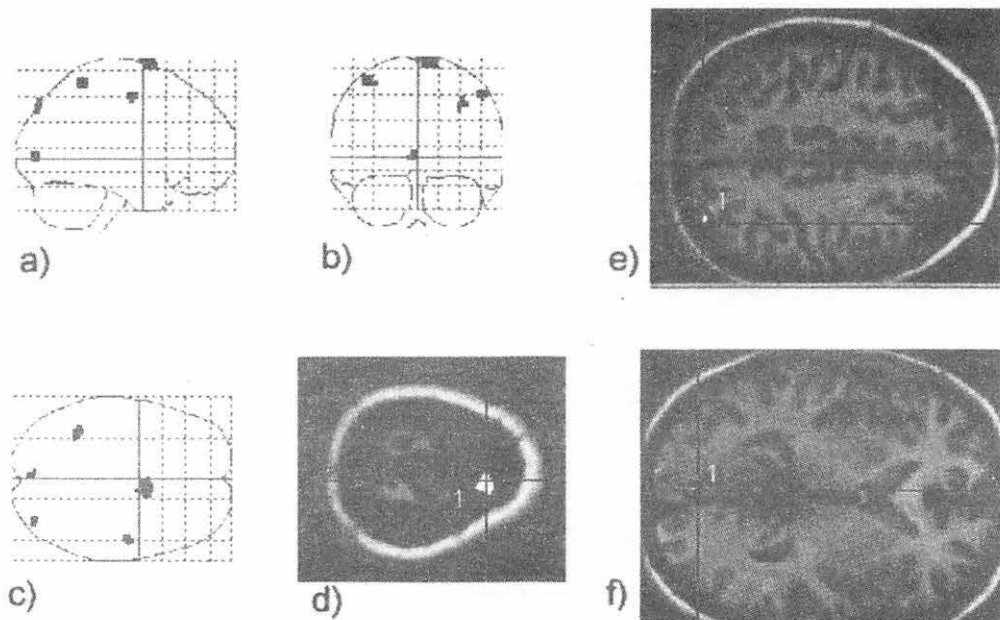
(Contrast: i.v-oral)

Fig. 1. Hypermetabolic brain areas with statistical significance (Z score >3.0, corresponding to p<0.001) are shown in black colors in i.v. group (contrast: i.v.-oral). The projection images a, b and c illustrates the views from right superolateral, posterior side and top view of brain respectively. Right superior frontal gyrus, right occipital gyrus and left lingual gyrus are visualized in d (1), e (1) and f (1) respectively, those explore hypermetabolism of corresponding brain areas.
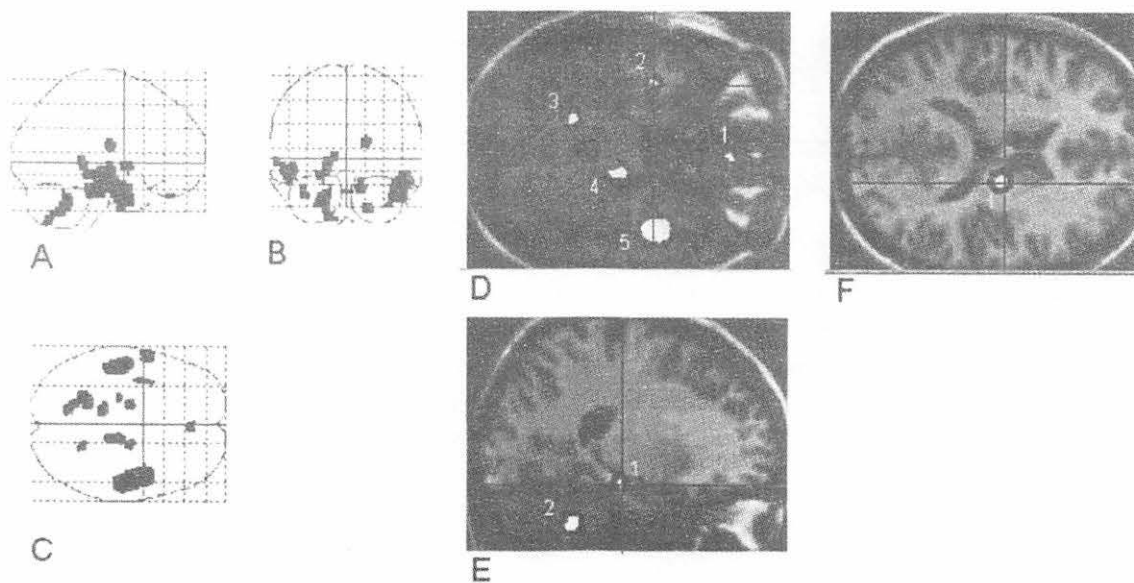
(Contrast: oral-i.v)

Fig. 2. Hypermetabolic brain structures are illustrated in resting subjects of oralgroup (contrast: oral-i.v.) as A = right superolateral surface, B = posterior view and C = top view. According to SPM-96, metabolic activated areas are significant when Z score =>3.00, corresponding to p =< 0.001. Right gyrus rectus (1), left inferior temporal gyrus (2), left cerebellar hemisphere (3), right ventral lateral nucleus of thalamus (VLN) (4), right middle and inferior temporal gyrus (5) are visualized in D as activated regions. E and F suggested the activated areas as left parahippocampal gyrus (1), left cerebellar hemisphere (2) and right amygdaloid body (1) respectively.

159
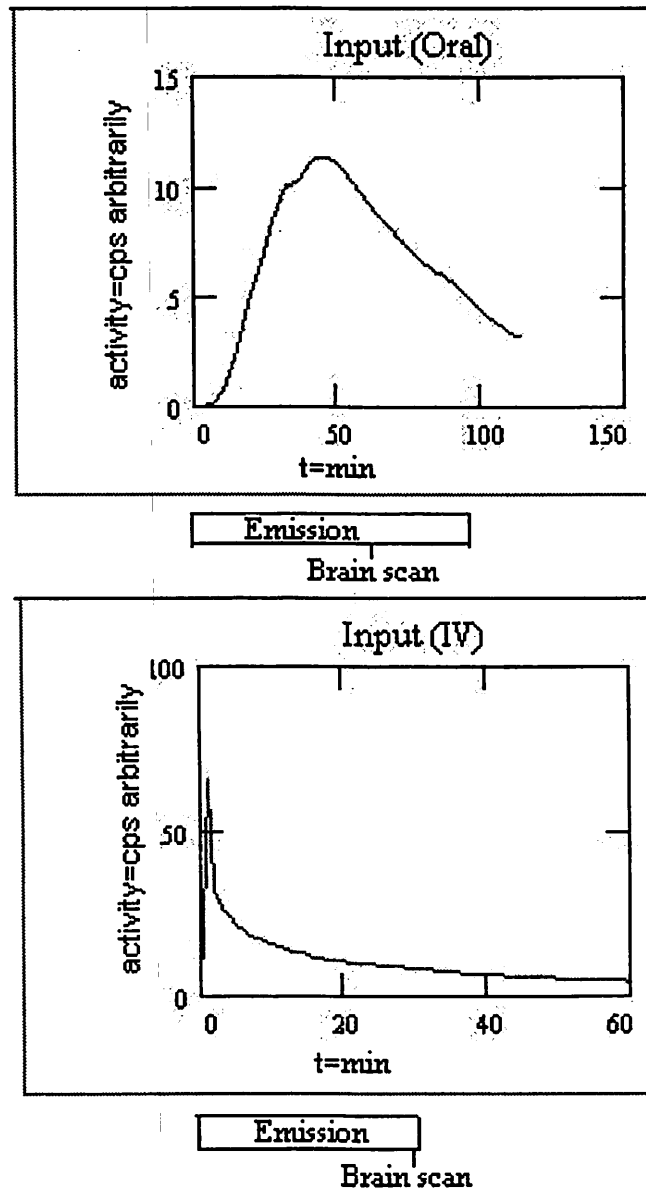
Fig. 3. This figure illustrates the average arterial input functions for oral (upper) and i.v. (lower) resting subjects. The x-axis suggests the time duration and y-axis depicts the tracer (FDG) distribution kinetics according to time. Emission scan schedule of i.v. and oral group are also shown. According to time schedule brain was scanned around 60 minutes later following FDG administration for i.v. and oral groups. The FDG-input function cuurves clearly depict that the oral PET images reflect brain activity at latter phase because of slow arterial input kinetics.

IV. 4. Relationship between Cerebral Glucose Metabolism and CSF Markers in Neurodegenerative Dementia

Okamura N., Arai H., Higuchi M., Tashiro M, Matsui T., Hu X.S., Itoh M.*,
and Sasaki H.

Department of Geriatric Medicine, Tohoku University School of Medicine
Division of Nuclear Medicine, Cyclotron and Radioisotope Center, Tohoku University*

Introduction

Amyloid-β peptide (Aβ) and microtubule-associated protein tau are two principal molecules that constitute the pathological hallmarks of AD, i.e. senile plaques and neurofibrillary tangles[1,2]. Cerebrospinal fluid (CSF) assays showing elevation in levels of tau (CSF-tau) and reduction in levels of Aβ ending at amino acid position 42 (CSF-Aβ1-42) have suggested them to be the most reliable biochemical markers in the diagnosis of AD at the present time[3,4] (For more details, see Consensus report[5]). Moreover, recent reports have demonstrated that a combinatorial analysis of CSF-tau and CSF-Aβ1-42 may provide a more accurate diagnostic strategy for the diagnosis of AD[6,7]. Although these biological markers are potentially useful to aid in the diagnosis of AD, it is not clearly understood if these molecules in CSF reflect fundamental features of neuron dysfunction or synapse loss in the AD brain. Furthermore, elevation of the CSF-tau levels and reduction of the CSF-Aβ1-42 levels are frequently observed in patients with non-AD neurodegenerative dementias including dementia with Lewy bodies (DLB), fronto-temporal dementia (FTD), corticobasal degeneration (CBD) and Creutzfeldt-Jakob disease (CJD)[3,7,8]. On the other hand, functional imaging techniques, including positron emission tomography (PET), have been used and accepted as methods to assess functional abnormalities in central nervous system disorders. In particular, cerebral glucose metabolism measured by PET and 2-[^{18}F] fluoro-2-deoxy-D-glucose (FDG) provides unique and quantitative functional data that might explain a regional distribution of neuron death and synaptic dysfunction in AD brain[9-11]. In order to get more insights into the clinical usefulness of the analysis of CSF-tau and CSF-Aβ1-42 as measures to monitor neurodegenerative processes of the brain, we quantified the CSF levels of these molecules in AD and non-AD patients, and these data were compared with cerebral glucose metabolic ratios measured by FDG-PET.

Patients and Methods

Fifteen patients with "probable AD" (69±7 years, M/F=6/9) and nine patients with

other neurodegenerative diseases (62±7 years, M/F=5/4) including DLB (n=4), FTD (n=3), CBD (n=1) and CJD (n=1) were examined. The diagnosis of probable AD was made according to the NINCDS-ADRDA criteria[12]. The diagnosis of other neurodegenerative diseases was performed according to the consensus guidelines proposed by McKeith et al. for DLB[13], the criteria by the Lund and Manchester groups for FTD[14] and the original description by Gibb et al. for CBD[15]. All patients underwent extensive neurological and neuroimaging studies as well as laboratory examinations to exclude other possible causes of dementia. Dementia severity was assessed by Mini-Mental State Examination (MMSE) within 3 month intervals of PET/CSF examination. The MMSE scores in AD patients were 19.1±5.4 points (range 5-26 points), and duration of the disease was 3.7±3.4 years (range 1.5-13 years). In the non-AD patients, the MMSE scores were 16.8±7.0 points (range 6-27 points) and duration of the disease was 2.2±1.0 years (range 0.5-4 years).

CSF was taken into sterile polypropyrene tubes by lumbar puncture. CSF-Aβ ending at amino acid position 42 was quantified by a sandwich enzyme-linked immunosorbent assay (ELISA) using two end-specific antibodies (21F12 and 3D6)[16]. Total tau in CSF was quantified by another sandwich ELISA (INNOTEST hTauAg, Innogenetics, Belgium) as previously described[3,17].

Cerebral glucose metabolism with FDG was measured using an ECAT PT931 (CTI Inc, Knoxville, TN, USA) tomograph. Following a ^{68}Ge/Ga transmission scan of 7 min duration, an emission scan was performed for about 60 min after intravenous injection of FDG. Arterial blood sampling was performed from the radial artery during the scan, and the cerebral metabolic rate of glucose (CMRglu) was calculated by an autoradiographic method using an input function obtained by the measurement of plasma radioactivity. The global glucose metabolism was defined as an average CMRglu value over both gray and white matter structures of 5 slices. ROIs were placed on individual PET images in the cerebellar hemisphere, superior and inferior frontal cortices, superior and inferior temporal cortices, parietal, occipital, medial temporal, striatum and thalamus, referring to the individual magnetic resonance images. The global and regional to cerebellar ratio (global and regional metabolic ratio) was determined to eliminate individual variance of activity. Correlations of the glucose metabolic ratio with the CSF-Aβ1-42 and CSF-tau levels were assessed by Pearson's simple correlation methods. Multiple regression analysis was performed to eliminate the effect of age on global and regional glucose metabolism.

Results

The mean levels of CSF-Aβ1-42 and CSF-tau were 322.0±118.2 pg/ml and 82.2±49.8 pg/ml in the AD group, and 356.0±239.0 pg/ml and 53.2±33.7 pg/ml in the non-AD group. The MMSE scores in the AD patients showed a trend toward decreasing with decreasing CSF-Aβ1-42 levels. A simple correlation analysis demonstrated that the CSF-

162

Aβ1-42 levels in the AD patients had a significant and positive correlation with the global metabolic ratio (r=0.647, p=0.008). Notably, in the analysis of non-AD patients, the CSF-Aβ1-42 levels also significantly correlated with the global glucose metabolic ratio (r=0.896, p =0.0004) (Figure). However, there was no consistent correlation between the CSF-tau levels and the global metabolic ratios in either AD or the non-AD group. Results obtained by multiple regression analysis adjusted by age further demonstrated that the CSF-Aβ1-42 levels independently correlated with the global metabolic ratios in both the AD group (p=0.010) and the non-AD group (p=0.001). In particular, the CSF-Aβ1-42 levels in the AD patients significantly correlated with regional metabolic ratio in the ROI of the inferior temporal cortex (r=0.479, p=0.048). In other areas, no significant correlation was observed between the regional metabolic ratio and the CSF-Aβ1-42 levels in the ROI analysis (Table) (For further details, see Ref 18).

Discussion

Despite a small sample size, this study is the first to describe a positive and strong correlation between CSF-Aβ1-42 levels and PET measures of cerebral glucose metabolism in AD. At the beginning of the present study, we hypothesized that we might see a negative correlation between CSF-tau levels and the PET measures of cerebral glucose metabolism since numerous studies have demonstrated that the CSF-tau levels are elevated in AD probably due to a progressive and massive death of neurons[3-7]. Instead, we found that the CSF-Aβ1-42 levels, but not the CSF-tau levels, had a positive correlation with brain metabolism, and this correlation was most significant in the temporal region. Our finding that the positive correlation between the CSF-Aβ1-42 and the global cerebral glucose metabolism in AD naturally leads us to assume that the CSF-Aβ1-42 levels might be high in the early stages of AD followed by a decline as the disease progresses. Indeed, there was a trend between MMSE scores and CSF-Aβ1-42 levels in our limited number of patients, and an another recent study also demonstrated the relationship between CSF-Aβ1-42 and MMSE scores in a larger sample size of AD patients[19]. Further, a longitudinal study demonstrated that the CSF-Aβ1-42(43) levels continuously declined during a follow-up in AD patients[7]. Taken these results together, it is likely that CSF-Aβ1-42 levels may decline as AD becomes more severe. To further clarify the relationship between the CSF-Aβ1-42 levels and the disease severity, it is necessary to examine temporal changes in the CSF-Aβ1-42 levels and in the PET measures of brain metabolism by a longitudinal analysis.

References

1) Goedert M., Trojanowski J.Q. and Lee V.M-Y., The neurofibrillary pathology of Alzheimer's disease. In: Prusiner S.B.et al., eds. The Molecular and Genetic Basis of Neurological Disease. Boston: Butterworth Heineman Press, 1997:613-627.

2) Selkoe D.J., Cellular and molecular biology of the beta-amyloid precursor protein and Alzheimer's disease. In: Prusiner S.B. et al., eds. The Molecular and Genetic Basis of Neurological Disease. Boston: Butterworth Heineman Press, 1997:601-612.

3) Arai H, Terajima M., Miura M. et al., Ann. Neurol. 38, 649-652 (1995).

4) Motter R., Vigo-Pelfrey C., Kholodenko D. et al., Ann. Neurol. 38, 643-648 (1995).

5) The Ronald and Nancy Reagan Institute of the Alzheimer's Association and the National Institute on Aging working Group. Neurobiol. Aging 19, 109-116 (1998).

6) Galasko D., Chang L., Motter R. et al., Arch. Neurol. 55, 937-945 (1998).

7) Kanai M., Matsubara E., Isoe K. et al., Ann. Neurol. 44, 17-26 (1998).

8) Urakami K., Mori M., Wada K. et al., Neurosci. Lett. 259, 127-129 (1999).

9) Rapoport S.I., Cerebrovascular Brain Metabol. Rev. 3, 297-335 (1991).

10) Guze B.H., Hoffman J.M., Baxter L.R. Jr. et al., Alzheimer Dis. Assoc. Disord. 5, 215-230 (1991).

11) Salmon E., Gregiore M.C., Delfiore G. et al., J. Cereb. Blood Flow Metabol. 16, 399-408 (1996).

12) McKhaan G., Drachman D., Folstein M. et al., Neurology 34, 939-944 (1984).

13) McKeith I.G., Galasko D., Kosaka K. et al., Neurology 47, 1113-1124 (1996).

14) The Lund and Manchester Groups., J. Neurol. Neurosurg. Psychiatry 57, 416-418 (1994).

15) Gibb W.R.G., Luthert P.J., Marsden C.D. et al., Brain 112, 1171-1192 (1989).

16) Vanderstichele H., Blennow K., D'Heuvaert N. et al., Development of a specific diagnostic test for measurement of s-amyloid 1-42 in CSF. In: Fisher A. Et al., eds. Progress in Alzheimer's and Parkinson's Diseases. New York: Plenum Press, 1998:773-778.

17) Vandermeeren M., Mercken M., Vanmechelen E. et al., J. Neurochem. 61, 1828-1834 (1993).

18) Okamura N., Arai H., Higuchi M. et al., Neurosci. Lett. 273, 203-207 (1999).

19) Samuels S.C., Silverman J.M., Marin D.B. et al., Neurology 52, 547-551 (1999).

Table 1. Regression parameters and detemination coefficients for regional metabolic ratio.

	CSF-Aβ_{1-42}	Age	R^2
inferior frontal	0.267	-0.507	0.335
superior frontal	0.337	-0.594	0.476[*]
inferior temporal	0.479[*]	-0.440	0.433[*]
superior temporal	0.223	0.026	0.050
parietal	0.123	0.166	0.042
occipital	-0.221	0.231	0.105
medial temporal	0.319	0.082	0.108
striatum	0.196	-0.241	0.019
thalamus	0.364	-0.304	0.230

[*]: $p < 0.05$
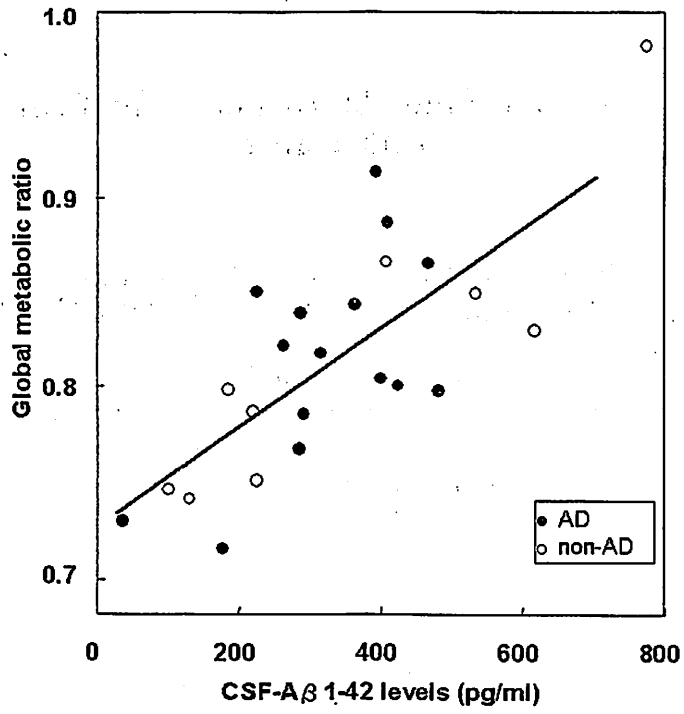
Figure 1. Correlation between CSF levels of Aβ1-42 and the global glucose metabolic ratio in fifteen AD and nine non-AD patients.

IV. 5. Regional Metabolic Abnormality in Brains of Patients with Cancer

Tashiro M.[1,7], Kubota K.[2], Itoh M.[1], Yamaguchi K.[1],
Yoshioka T.[3], Yoshida M.[4], Nakagawa Y.[5], Kumano H.[6], Sasaki H.[7]

Division of Nuclear Medicine, Cyclotron and Radioisotope Center (CYRIC);[1]
Divisions of [2]Nuclear Medicine and Radiology and [3]Clinical Oncology, Institute of Development,
Aging and Cancer; Tohoku University;
Departments of [4]Radiology, [5]Ophthalmology, [6]Human Behavioral Science,
[7]Gerontology and Respiratory Medicine, Tohoku University School of Medicine

Introduction

Imaging technique using positron emission tomography and ^{18}F-fluoro-deoxyglucose (FDG PET) has been utilized for a few decades as a useful tool to detect malignant tumors at early stages, as well as for differentiation from benign diseases[1,2]. FDG PET has been also useful for evaluation of a variety of neuropsychiatric disorders such as depression[3,4] and obsessive compulsive disorder[5] by examining regional cerebral metabolic rate of glucose (rCMRglu). So far, it does not seem that this technique has been applied for evaluation of neuropsychiatric abnormalities of cancer patients before. Functional brain imaging techniques might be helpful in evaluating neuropsychiatric problems in cancer patients, too.

We previously reported the results of preliminary examination on the regional cerebral abnormalities of glucose metabolism in patients with cancer[6,7,8]. In the previous reports, we reported that cancer patients manifest regional hypometabolism in the prefrontal cortex and limbic system[7,8]. The metabolic decline seemed to be associated with pain and types of disclosure to patients[7]. The present report is trying to supplement detailed description of this tendency.

Materials and Methods

Subjects were 19 cancer patients who were studied with FDG PET at the Cyclotron and Radioisotope Center (CYRIC), Tohoku University during the period of 1995 to 1997[2]. The 19 cancer patients over 40 years old, who fulfilled the two following criteria, were selected from the data base: (1) absence of focal signs of brain metastasis and cerebrovascular diseases in MRI or CT and PET, and (2) absence of invasive treatments such as surgery, chemotherapy and radiotherapy before PET examination. The 19 patients were diagnosed with malignant diseases of various organs as follows: twelve patients as lung cancer (including one small cell lung cancer), three as malignant mediastinal tumor, two as

esophageal cancer, one as malignant lymphoma and the other as gastric cancer (mean age +/- S.D., 65 +/- 10, range 44 to 84, two women and 17 men). Patients were scanned approximately 30 min after injection of FDG taking about 30 min. Seventeen patients in the control group had ophthalmopathy such as optic neuritis and macula hole (mean age +/- S.D., 64 +/- 9, range 48 to 78, seven women and 10 men)[7].

The study protocol was approved by the Ethics Committee for clinical Research of Tohoku University and informed consent for the all examinations for the study was obtained in advance from each patient.

Clinical data and subgroups:

Clinical information of each cancer patient was retrospectively collected from medical charts. Pain, sleep disturbance, appetite loss, and types of disclosure were graded according to the following criteria.

Pain: (-) no pain (n=13), (+) mild pain controlled by non-steroidal anti-inflammatory drugs (NSAIDs)(n=3), and (++) severe pain which required narcotics (morphine and opiates)(n=3).

Sleep disturbance: (-) no sleep disturbances (n=15), (+) mild sleep disturbances successfully controlled by a hypnotic (n=2), and (++) moderate to severe sleep disturbances which required more than two hypnotics for control (n=2). Four patients manifested sleep disturbances.

Amount of hospital meals taken by each patient was reviewed for 5 days prior to PET examination: (-) when a patient ate more than 90 percent of meals served for the 5 days (n=15), (+) more than 50 percent (n=3), and (++) less than 50 percent (n=1).

Types of disclosure of malignant nature of the disease: 1) complete disclosure (CD) group (n=3), already informed of the malignant nature before PET examination, 2) possible malignancy (PM) group (n=9), being informed of malignant findings possibly detected by PET examination, 3) non-disclosure (ND) group (n=3), intentionally given a false benign diagnosis by doctors at the request of patients' families, and 4) no information group, in case no information was found in the medical charts (n=4), omitted from the comparison.

We attempted preliminary statistical evaluation for the regional metabolic rate ratios among subgroups graded for clinical information using Mann-Whitney's U-test due to small sample size. Plasma glucose concentrations of subjects were within normal ranges (99.8 +/- 6.0mg/dL).

Results

Statistical analysis using SPM96 identified several regions with decreased regional metabolic rate ratios in cancer patients compared to the control. The metabolic reduction was found in the prefrontal cortex and limbic and paralimbic structures[7,8].

The severe pain group showed a trend for decreased regional metabolism in the anterior cingulate gyrus compared to other sub-groups. Similar trend was observed in the striatum, too, but both were insignificant by Mann-Whitney's test (Figure 1). As to the types of disclosure, CD group manifested relatively increased metabolic rate ratios (figure 2).

The regional metabolic rate ratio in the anterior cingulate gyrus of the appetite loss group showed a trend for higher metabolism but the difference was not significant. No significant difference was detected between the groups with and without metastasis.

Discussion

In an attempt to normalize the influence of stress due to hospitalization, the authors selected benign disease in-patients as the control group. This comparison was expected to highlight the neuropsychiatric problems of cancer. In the present study, no patients had anti-cancer therapies before the PET study. Derogatis et al. reported that 47 percent of cancer patients met the DSM-III criteria[9]. Minagawa et al. reported that 53.7 percent of terminally-ill cancer patients met DSM-III-R criteria[10]. According to previous studies, neuropsychiatric problems of cancer patients could be induced by both psychological factors and invasive treatments[11]. Etiological factors which possibly cause resultant psychiatric abnormalities could be classified grossly as follows: 1) psychological response, 2) biological effects due to existence of cancer, 3) biological effect due to treatments, and 4) pain.

The authors preliminarily examined the correlation between the metabolic rate ratios and the degrees of sleep disturbances and appetite loss, both of which constitute chief physical symptoms of depression. The results suggest that these physical symptoms are not appropriate for this study because they could be caused by malignant disease itself. Concerning the grade of pain, the severe pain group showed a trend for lower metabolism in the anterior cingulate gyri compared to the other sub-groups. Our result could be interpreted in association with alteration in the threshold of pain sensation due to the use of narcotics[12,13] (Figure 2).

As to types of disclosure, in Japan, some doctors still hesitate to tell truth to their patients. The rate of complete disclosure might be lower in Japan than in Western countries as demonstrated in the present study (3/19), too, as well as in previous reports[14,15]. The author examined whether any regional metabolic differences could be detected among groups with different disclosure types.

Conclusion

In conclusion, the brain of cancer patients showed a clearly different metabolic pattern compared to controls, showing declined metabolism in the limbic system. This abnormality seems to be difficult to explain by physical factors. Since the brain metabolic pattern resembles that of major depression, more association with psychiatric or psychological factors should be examined. Due to the small size of patient groups, intra-group comparisons did

not clarify the causes and effects. More studies are necessary to clarify the relationship. In future, evaluation of cerebral glucose metabolism with PET may offer an objective method to assess psychological and neurological problems of cancer patients.

References

1) Di Chiro G., De La Paz R.L., Brooks R.A., *et al., Neurology* **32** (*1982*) 1323-1329.
2) Kubota K., Matsuzawa T., Fujiwara T., *et al., J. Nucl. Med.* **31** (1990) 1927-1932.
3) Wu J.C., Buchsbaum M.S., Johnson J.C., *et al., J. Affect Disord.* **28** (1993) 15-25.
4) Drevets W.C., Price J.L., Simpson J.R. , *et al., Nature* **386** (1997) 824-827.
5) Reiman E.M., *Psychiatr. Dev.* **5**(1987) 63-78.
6) Tashiro M., Kubota K., Itoh M., *et al., Psycho-Oncology* **7** (1998) suppl. 41.
7) Tashiro M., Kubota K., Itoh M., *et al., Psycho-oncology* **8** (1999) 283-286.
8) Tashiro M., Juengling F.D., Reinhardt J.M., *et al.,* Psycho-oncology **9** (2000)157-163.
9) Derogatis R.L., Morrow G.R., Fetting J., *et al., JAMA* **249** (1983) 751-757.
10) Minagawa H., Uchitomi Y., Yamawaki S., *et al., Cancer* **78** (1996)1137.
11) Meyers C.A., Byrne K.S., Komaki R., *Lung Cancer* **12** (1995) 231-235.
12) Lyons D., Friedman D.P., Nader M.A., Porrino L.J., *J. Neuroscience* **16** (1996) 1230-1238.
13) Lenz F. A., Rios M., Zirh A., *et al., J. Neurophysiol* **79** (1998) 2231-2234.
14) Mijagi N. T., *N. Engl. J. Med.* **331** (1994) 810.
15) Tanida N., *Lancet* **352** (1998) 1787.
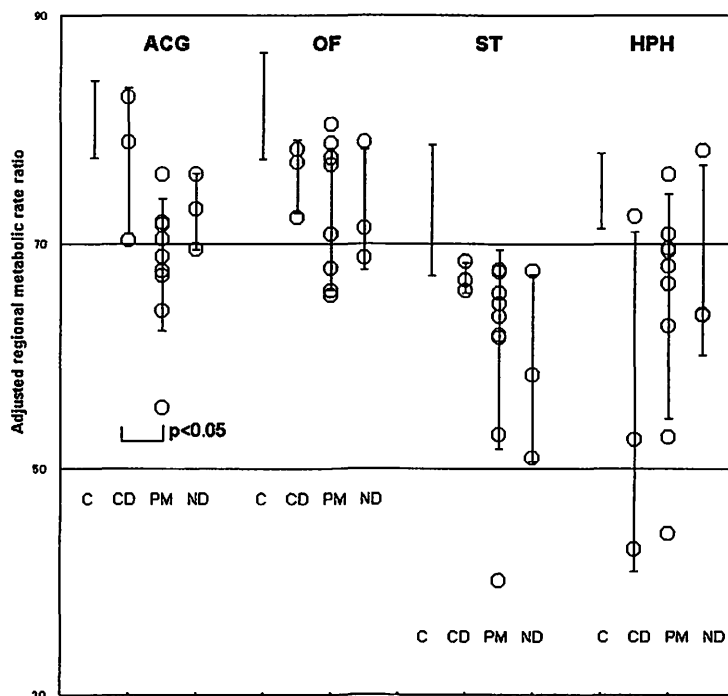
Figure 1. Type of Disclosure and Regional Metabolic Rate Ratios in Brain of Cancer Patients.
Result of intra-group comparison based on types of disclosure. Abbreviations: ACG= anterior cingulate gyrus, OF= orbitofrontal cortex, ST= striatum, HPH= hippocampus and parahippocampal gyrus, C= control group, CD= complete disclosure group, PM= possible malignancy group, ND= non-disclosure group. Symbols: p<0.05: compared between CD and PM groups by Mann-Whitney's test.
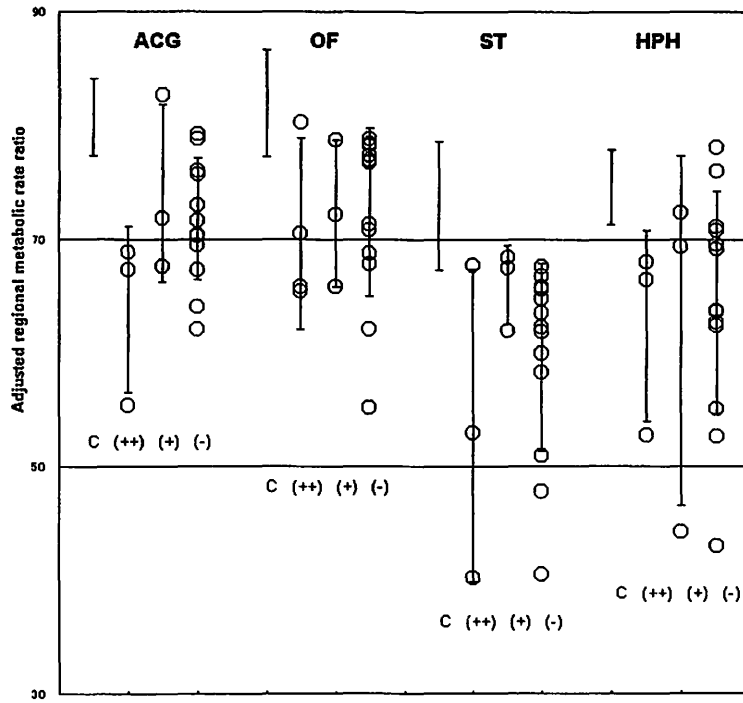
Figure 2. Degree of Pain and Regional Metabolic Rate Ratios in Brain of Cancer Patients.

Result of intra-group comparison based on degree of pain. Abbreviations: ACG= anterior cingulate gyrus, OF= orbitofrontal cortex, ST= striatum, HPH= hippocampus and parahippocampal gyrus, C= control group, (++) moderate to severe pain, (+) mild pain, and (-) no pain. Symbols: p<0.05: compared between CD and PM groups by Mann-Whitney's test.

IV. 6. Imaging of Psycho-neuro-immune Interaction in Human

Tashiro M.[1,4], Kubota K.[2], Itoh M.[1], Kumano H.[3] and Sasaki H.[4]

Division of Nuclear Medicine, Cyclotron and Radioisotope Center[1],
Department of Nuclear Medicine and Radiology, IDAC[2],
Department of Human Behavioral Science, Tohoku University[3],
Department of Geriatric and Respiratory Medicine, Sendai, Japan[4]

Introduction

Interaction between psychological factors and bodily functions has been discussed for a long time. There may be positive and negative aspects in this interaction. Some mention immune enhancing effects of relaxation and imagery techniques[1,2] and exercise[3]. Others deal with high incidence of cancer and poor prognosis associated with certain psychological factors in cancer patients and so on[4,5,6]. Existence of psycho-neuro-immune interaction seems to be doubtless, but the mechanism would be complex. It has tended to be explained by involvement of the hypothalamic-pituitary-adrenal (HPA) axis. But this model seems to be lacking important components. Since psychosocial events must be "recognized" and "judged" in order that our consciousness feels them stressful, it seems that the model should include the cerebral cortex and limbic system. There might be a missing link between psychosocial events and body abnormal function of the HPA axis[7].

Previous animal studies demonstrated alteration of immune functions following selective destruction of brain structures such as the hypothalamus, cerebral cortex, and limbic system[8,9-12]. Recently, Wik and coworkers' honorable study demonstrated state-dependent correlation between cellular immune functions and the regional cerebral blood flow in normal human subjects by using $^{15}O\text{-}H_2O\text{-}PET$[13]. Since the brain of cancer patients might be already affected by various causes, such as psychological, therapeutic and paraneoplastic factors, manifesting decreased regional glucose metabolism in the limbic system and the prefrontal cortex as demonstrated in our previous study, the result similar to that of Wik and coworkers' study could not be guaranteed[14]. It would be worthwhile examining comparable relationship in patients with cancer. Since psychological factors have been said to influence on prognosis of patients, research in this direction might give a useful information in explaining how the psychological factors determine physical conditions. The authors investigated the relationship between NKA, regional glucose metabolism and psychological scores in the brain of cancer patients.

Materials and Methods

Subjects were 8 cancer patients (mean age +/- s.d., 65 +/- 13, ranging 40 to 80, one woman and seven men) at various stages. They were admitted to the Hospital of Institute of Development, Aging and Cancer, Tohoku University. Their brain images were free from focal signs in MRI or CT. The study protocol was approved by the Ethics Committee for Clinical Research of Tohoku University and informed consent was obtained from each patient.

FDG was prepared using an automated synthesis system, and quality assurance tests were performed. Patients refrained from eating and drinking for at least 5 hours before the PET examination. The blood glucose level was measured before the injection of FDG. After injection of FDG, patients were requested to wait for 30 min, sitting quietly on a comfortable chair. PET examinations were performed using a SET2400W scanner (Shimadzu Inc., Kyoto, Japan) with the transaxial spatial resolution of 4 millimeter. The axial field of view of the scanner is 200-millimeter-long which was long enough to cover the whole brain in one scan. The brain was scanned about 60 min after injection (for 4 min) as a part of whole-body scan. Transmission scans were performed using a $^{68}Ge/^{68}Ga$ external rotating line source for tissue attenuation correction after emission scan[15].

PET images were reconstructed using a filtered-back projection (FBP) algorithm and were dead time- and decay- corrected. There was no significant patient movement or mis-positioning between transmission scan and emission scan. After reconstruction, brain images of the patients were extracted from the whole body images. The extracted brain images were spatially normalized by linear and non-linear transformations to minimize anatomical variation among patients, while preserving the regional metabolic activity using Statistical Parametric Mapping software package (SPM96)[16,17]. Statistics was applied on these image data at pixel-by-pixel basis. In the following analysis, all the pixel data were normalized to the group mean of the whole brain count of each patient (ANCOVA). Location of specific regions in the cancer patient group was represented in x, y, z coordinates and were identified in the stereotaxic coordinate human brain atlas[18].

Psychological status of each patient was evaluated using Zung's SDS[19-21] and Taylor's MAS[22,23] in Japanese translation[21,23].

NKA was measured as follows. The whole blood sample of 5 ml was taken from each patient just prior to injection of FDG. These samples were measured at Sumitomo Metal Bio-Science Inc. Laboratory (^{51}Cr Free Floating Method K-562 cell line kit was used with $Na_2^{51}CrO_4$ presented by Amersham Japan).

Results

Half of patients (4 out of 8) manifested decreased NKA compared with normal ranges (13-51: laboratory specific data). Mean score of MAS in cancer patients was 19.4+/-3.1, and SDS 35.6+/-6.9. Mean MAS was moderately elevated compared with normal

distribution measured with the Japanese version $(14.3+/-7.8)^{23)}$. Two patients were categorized as highly anxious (grade I), three patients as moderately anxious (grade II) and three patients (one female and two males) as mildly anxious (within normal range). For SDS, general distribution was identical to that of normal group $(35+/-12)^{21)}$. Only three patients belonged to the neurotic range (49+/-10), suggesting that they were possibly in mild mood disturbances.

Positive correlation was detected between NKA and MAS scores (r= 0.96, p< 0.001 by Pearson correlation test). No correlation was observed between patient age and psychological scores and between patient age and NKA.

According to SPM results, NKA correlated positively with rCMRglu in the left visual association cortex, left primary motor and premotor cortices, and right anterior cingulate gyrus. The NKA also correlated with the left primary sensorimotor cortex and left posterior parietal cortex but they did not survive Bonferroni correction (extent threshold:p<0.4), because of their small pixel cluster sizes. NKA correlated negatively in the right basolateral prefrontal cortex, right prefrontal cortex, orbitofrontal cortex, and inferoanterior temporal cortex (Figure 1 and Table 1).

Discussion

Links between psychosocial events and immune response have been studied well[24,25)]. However, roles of cortical and limbic systems in psycho-immune responses have not been studied well yet. This response could be understood based on the fundamental framework as follows:

1) psychosocial behavior,
2) regional change in the brain, and
3) physiological changes (autonomic, endocrine and immune).

While there are enormous number of studies dealing with one or two dimensions introduced here, few study has been done taking all of the three dimensions into account because of its complexity. A functional brain imaging study might enable it.

Previous animal studies demonstrated altered immune functions following destruction of brain structures such as cerebral cortex, limbic system and brain stem[8-12)]. Previous lesioning studies on the anterior hypothalamic area induced immune dysfunction in mice. Lesioning of the posterior hypothalamus gave rise to various results. Some studies suggested that destruction of the limbic structure induced enhancement of immune functions[8-12)] and that lesioning of the cerebral cortex induced decreased immune function[10-12)]. The purpose of these lesioning studies were to clarify the role of specific brain regions in the immune modulating interaction. Similar purpose could be accomplished in human non-invasively by using PET technique.

A recent work done by Wik and coworkers[13] demonstrated correlation between the regional cerebral blood flow (rCBF) and NKA and Concanavalin-A (Con A) response of lymphocytes in normal human subjects. This may be only one study available on this topic. They, after carefully excluding subjects with moderate to high anxiety, demonstrated that NKA correlated negatively with rCBF in the secondary somatosensory cortex whereas Con-A response correlated positively with rCBF bilaterally in the visual association, motor, sensory cortices, thalamus, putamen, and left hippocampus. Purpose of the present study was to see if a comparable trend can be detected in cancer patients. Naturally, patients built up moderate degree of anxiety or depression. To see a certain effect of emotional load on the immune consequences, anxious patients were not necessarily to be excluded. Curiously, our results looked opposing to that of NKA in Wik's study but seemed to be in accordance with that of Con-A study. Interpretation of this discrepancy is still unclear.

In the present study, at least it seemed that anxiety, NKA and metabolism in the cingulate and primary cortices correlated to each other. It seems to be relatively easy to explain the effects of imagery and exercise by possible close contact between immune cells and the visual and sensorimotor cortices, as demonstrated in the present study (Figure 1 and Table 1). However, anatomical connection between the two is unclear, and further interpretation is still difficult.

Combined with the results of lesioning studies on animals, the present result seems to demonstrate an antagonistic relationship between the cortical (including anterior cingulate gyrus) and limbic (including prefrontal cortex) systems concerning immunological consequences. In future, it could be expected that this approach will elucidate functional neuroanatomy of immune enhancing effects accompanied by relaxation, imagery and biofeedback techniques[1,2] and exercise[3] as well as psycho-biological mechanism of poor prognosis in cancer patients associated with certain psychological factors[4-6].

Conclusion

In spite of the small sample size, this observation might provide further support for the presence of interactions between the brain and immune system. The cerebral cortex and limbic system may take some important roles in psycho-neuro-immune-modulation. Functional brain mapping technique could produce reasonable results in investigating this interaction.

References

1) Gruber B.L. Hall N.R., Hersh S.P., Dubois P., *Scand. J. Behav. Ther.* **17** (1988) 25.

2) Gruber B.L., Hersh S.P., Hall N.R., *et al.*, *Biofeedback Self Regul.* **18** (1993) 1.

3) LaPerriere A., Ironson G., Antoni M.H., *et al.*, Med. Sci. Sports Exerc. **26**(1994) 182-190.

4) Derogatis R.L., Abeloff M.D., Melisaratos N., *JAMA* **242** (1979) 1504-1508.

5) Greer S., Morris T., Pettingale K.W., *et al. Lancet* **1** (1990) 49-50.

6) Watson M., Haviland J.S., Greer S., *et al. Lancet* **354** (1999) 1331-6

7) Tashiro M., Juengling F., Reinhardt M., *et al. Lancet* (2000) (in press).

8) Brooks W.H., Cross R.J., Roszman T.L., *et al. Ann. Neurol.* **12** (1982) 56-61.

9) Cross, R.J., Brooks W.H., Roszman T.L., *et al. J. Neurol. Sci.* **53** (1982) 557-566.

10) Renoux G., Biziere K., Renoux M., *et al. J. Neuroimmunol.* **5** (1983) 227-238.

11) Renoux G., Biziere K., Renoux M., *et al. Immunopharmacology* **7** (1984) 89-100.

12) Renoux G., Biziere K., Renoux M., *et al. Ann. N Y Acad. Sci.* **496** (1987) 346-353.

13) Wik G., Lekander M., Fredrikson M., *Brain Behav. Immun.* **12** (1998) 242-246.

14) Tashiro M., Kubota K., Itoh M., *et al. Psycho-oncology* **8**(1999) 283-286.

15) Fujiwara T., Watanuki S., Yamamoto S., *et al. Ann. Nucl. Med.* **11** (1997) 307-313.

16) Friston K.J., Frith C.D., Liddle P.F., *et al. J. Cereb. Blood Flow Metab.* **11** (1991) 690-699.

17) Friston K.J., Holmes A.P., Worsley K.J., *et al. Human Brain Mapping* **2** (1995) 189-210.

18) Talairach J., Tournoux P., *Co-Planar Stereotaxic Atlas of the Human Brain.* Stuttgart: George Thieme Verlag; 1988.

19) Zung W.W.K., Richards C.B., Short M.J., *Arch. Gen. Psychiatry* **12** (1965) 63-70.

20) Zung W.W.K., Richards C.B., Short M.J., *Arch. Gen. Psychiatry* **13** (1965) 508-515.

21) Zung W.W.K.,FukudaK., Kobayashi S., *Manual for Self-rating Depression Scale.* Kyoto; Sankyobo Ltd.: 1983. (in Japanese)

22) Taylor J.A., *J. Abnorm. Soc. Psychol.* **48** (1953) 285-290.

23) Taylor J.A., Abe M., Takaishi N., *Manual for MMPI Manifest Anxiety Scale (MAS).* Kyoto; Sankyobo Ltd.: 1968. (in Japanese)

24) Ader R., Felton D.L., Cohen N., *Psychoneuroimmunology.* 2nd Ed. New York: Academic Press; 1991.

25) Levy J.K., Bell K.E., Lachar BL, *et al.*, *Psychoneuroimmunology.* In: Eds by Rolak L.A. and Tarati Y., (Ed), Neuroimmunology for the Clinician, USA MA: Butterworth-Heinemann; 1997. p. 35-56.

Table 1. Regions of Linear Correlation to NKA.

Structure	Brodmann's Area	Hemi-Sphere	Talairach Coordinates Of statistical peak			Z score of Statistical peak
			X	Y	Z	
(positive correlation)						
Visual association cortex	18	L	-32	-80	0	4.12
Anterior cingulate gyrus	32	R	12	26	40	3.60
Motor area	4/6	L	-45	-14	60	3.69
(negative correlation)						
Basolateral prefrontal cortex	47	R	36	46	-10	4.72
Prefrontal cortex	10	R	22	64	-2	4.41
Orbitofrontal cortex	11	L	-16	40	-16	3.86
Anterior temporal cortex	20	L	-26	12	-44	3.59
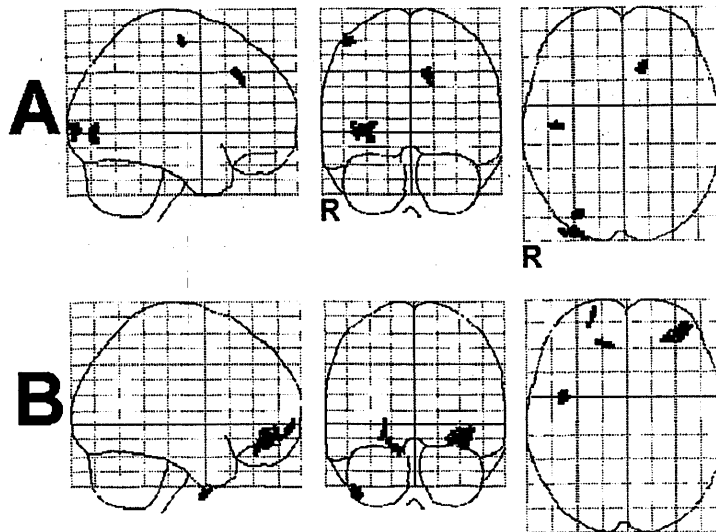
Figure 1.   Regions Correlating with Natural Killer Cell Activity (NKA).A: positive correlation and B: negative correlation.Regions of significant correlation, denoted by black, are superimposed on MRI templates. (pixel height threshold $p<0.005$, extent threshold $p<0.4$ (43 voxel minimum).

IV. 7.   Three Dimensions in the State of Memory and Emotion Concerned with a Person: Factor Analysis Using Subject's Self Evaluation and PET.

Sugiura, M.*, Kawashima, R.*[t], Gotoh, R.*, Okada, K.*, Watanabe, J.*, Satoh, K.*, Yamaguchi, K.[t], Itoh, M.[t], Schormann T.[s], and Fukuda, H.*[t]

Department of Nuclear Medicine and Radiology, Institute of Development, Aging and Cancer,
Tohoku University*
Aoba Brain Imaging Research Center, Telecommunications Advancement Organization[t]
Cyclotron and Radioisotope Center, Tohoku University[t]
Institute for Neuroanatomy, Heinrich-Heine-University, P.O.Box 101007, D-40001 Duesseldorf, Germany[s]

Introduction

Although memory and emotion are closely related and intertwined in our daily life, they are usually separately studied on simple models based on the animal models in previous studies.   Human brain imaging is expected to reveal the neurobiological correlates of human memory and emotion.   However, so far, there seems to be no established model of human memory and emotion which can be compared with brain activity.   Normal adults can verbally describe their states of memory and emotion with various terms.   Many terms are used to discribe similar states of memory and emotion, but each term expresses specific nuance.   We need to choose appropriate terms to construct a model of memory and emotion without a priori hypothsis.   Here we propose new a approach to extract essential factors from these terms using factor analysis on phisyological data.   In this study, rCBF image was obtained during the normal subject was retrieving memory concerening a specific person (target person), using positron emission tomography (PET).   The subject evaluated his states of memory and emotion concerning the target person using the questionnaire with 23 items with five grade rating, after the PET scan.   We made correlation map for each item, and principal component analysis (PCA) was performed for 23 items using correlateion coefficients of all voxels in the whole brain.

Methods

Subjects

Nine right handed normal male volunteers (age 18-21) participated in this study. Handedness was assessed by the Edinburgh Handedness Inventory[1].   None had any sign or history of psyconeurological disease.   Written informed consent was obtained from each subject in accordance with the guidelines approved by Tohoku University and the Helsinki

Declaration of Human Rights, 1975. The protocol was approved by the local ethics committee of the Institute of Development, Aging and Cancer, Tohoku University.

Personal memory retrieval tasks

Each subject performed six tasks in each of which retrieval of memory about a specific person (target person) was required. The target person was specified before each task among the people with variety of relationships with the subjects (a comic character, a social figure, his recent friend, his old friend, one of his siblings, and his father). A single word or a sentence which describes a person, such as "honest", "tall", or "runs fast", was visually presented, in each trial. The subjects were required to determine whether the description of each presented word or sentence suites the target person. The subjects performed 40 trials during 120 sec in each task.

rCBF measurement

The PET scans were performed with a SET-2400W PET scanner (Shimadzu, Kyoto, Japan) in three-dimensional mode. The physical characteristics of this scanner have been described previously[2]. During each personal memory retrieval task, bolus injection of 200MBq $H_2^{15}O$ was followed by 60sec data aquisition.

Evaluation of memory/emotion states

Immediately after each task finished, the subject was asked to complete a questionnaire with five grade rating which consists of following 23 items which evaluate his state of memory and emotion concerned with the person.

1) I have memory for this person.
2) I have knowledge of this person.
3) I can visually imagine this person.
4) I like this person.
5) I hate this person.
6) I was influenced by this person.
7) I influenced this person.
8) I feel familiarity (intimacy) with this person.
9) I have loving memory for this person.
10) I have joyful memory for this person.
11) I have sad memory for this person.
12) I have fearful memory for this person.
13) I have experating memory for this person.
14) I feel love when I think of this person.
15) I feel joy when I think of this person.

16) I feel sad when I think of this person.

17) I feel fear when I think of this person.

18) I feel anger when I think of this person.

19) I feel love when I am with this person.

20) I feel joy when I am with this person.

21) I feel sad when I am with this person.

22) I feel fear when I am with this person.

23) I feel anger when I am with this person.

Data analysis

The PET images were anatomically normalized to the standard brain of the Human Brain Atlas[3] using the Automated Image Registration[4] and Elastic transformation[5]. All PET images were proportionally scaled into the global mean cerebral blood flow of 50ml/dl/min. Using all 54 normalized images, correlation coefficient was calculated for each voxel for each item, to make correlation map. Among some items, their correlation maps resemble each other, and these items may share some common memory/emotion factor(s). Correlation coeficients were Z transformed ($Z=\log((1+r)/(1-r))/2$), and resulting Zr maps (vectors with approximately 2×10^5 values (the number of voxels)) were used to calculate covariance matrix (23×23). Eigenvalues and eigenvectors were calculated using the covariance matrix. Calculation of correlation map and PCA were performed on MATLAB 4.2 (Mathworks Inc., Sherborn, Mass., USA). Cumulative proportion reached 80% by the third principal component, and first three principal components were considered as effective. Pricipal component score (PCS) map was calculated from Zr map and the eigenvector for each effective principal component (inverse Z transformation was performed to obtain correlation coefficient like characters).

Results and discussion

For three principal components, items are listed from those with larger absolute factor loading until sum of square of the loadings exceeds 0.8 (Table 1), and PCS map is shown (Figure).

In the first principal component, large positive loadings were seen for the items evaluating a positive impression and memory for the target person. We refer this principal component as "Positive Emotion" factor. This factor was associated with high activity in the bilateral anterolateral prefrontal cortex and the right occipitotemporal region, and low activity in the bilateral anterolateral temporal cortex, superior part of amygdala, lateral orbitofrontal cortex, and sensorimotor cortex.

In the second principal component, large negative loadings were seen for the items evaluating a negative impression and memory for the target person. We refer this principal component as "Negative emotion" factor. This factor was associated with high activity in

179

the bilateral anteromedial temporal cortex, inferior part of amygdala and the left occipitotemporal region.

In the third principal component, large positive loadings were seen for the items evaluating a knowledge and visual imagenability of the target person, and large negative loadings were seen for the items evaluating memories bearing negative emotion. We refer this principal component as "Nonemotional Memory" factor. This factor was associated with high activity in the left inferior temporal cortex, which is in cotrast to the high activity in the right inferior temporal cortex associated with "Positive Emotion" and "Negative Emotion".

Application of the factor analysis to PET data and psychological measurements seems to be a powerful approach for the study of human memory and emotion.

References

1) Oldfield, R., Neuropsychologia 9 (1971) 97-113.
2) Fujiwara, T., Watanuki, S., Yamamoto, S., Miyake, M., Seo, S., Itoh, M., Ishii, K., Orihara, H., Fukuda, H., Satoh, T., Kitamura, K., Tanaka, K., and Takahashi, S., Ann. Nucl. Med. 11 (1997) 307-313.
3) Roland, P. E., Graufelds, C. J., Wahlin, J., Ingelman, L., Andersson, M., Ledberg, A., Pederson, J., Akerman, S., Dabringhaus, A., and Zilles, K., Hum. Brain Mapp. 1 (1994)173- 184.
4) Woods, R. P., Grafton S. T., Watson, J. D. G., Sicotte, N. L., & Mazziotta, J. C., J. Comput. Assist. Tomogr. 22 (1998) 153-165.
5) Schormann, T., Henn, S. & Zilles, K., Lecture Notes in Computer Science 1131 (1996) 337-342.

Table 1. Items with large absolute value of factor loadings for three principal component.

item	loading
first principal component	
I feel love when I am with this person	0.36
I have loving memory for this person	0.33
I feel love when I think of this person	0.31
I have knowledge of this person	0.29
I feel joy when I am with this person	0.25
I have memory for this person	0.25
I can visually imagine this person	0.24
I like this person	0.23
I have joyful memory for this person	0.22
I have sad memory for this person	0.21
I feel joy when I think of this person	0.20
I was influenced by this person	0.19
second principal component	
I feel fear when I am with this person	0.38
I feel sad when I am with this person	0.36
I feel anger when I think of this person	0.33
I feel anger when I am with this person	0.33
I feel sad when I think of this person	0.33
I have experating memory for this person	0.29
I hate this person	0.23
I like this person	-0.19
third principal component	
I have knowledge of this person	0.48
I have experating memory for this person	-0.44
I can visually imagine this person	0.38
I have sad memory for this person	-0.35
I have fearful memory for this person	-0.27
I feel familiarity with this person	-0.25

Figure PCS maps

first principal component
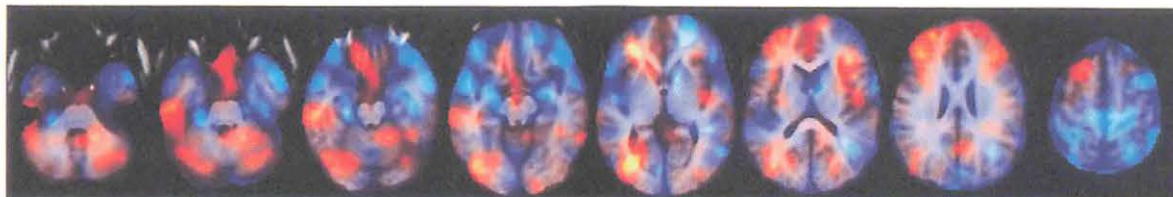
second principal component
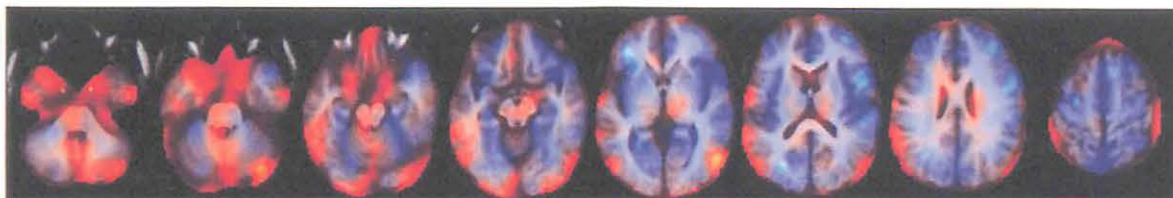
third principal component
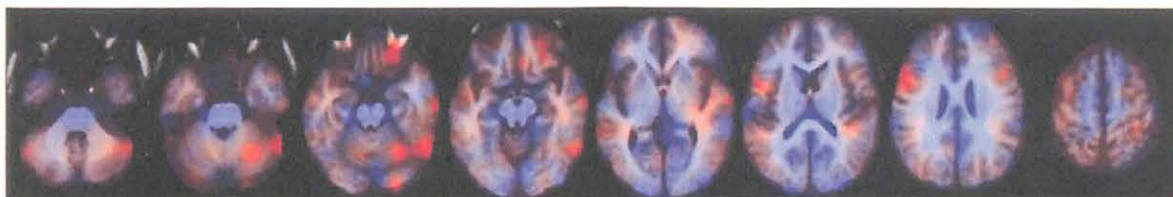
Figure 1. PCS maps are superimposed onto the mean normalized MRIs of all subjects. Positive correlation is shown in red and negative correlation is shown in blue. The left side of the brain is shown in the right side of the figure.
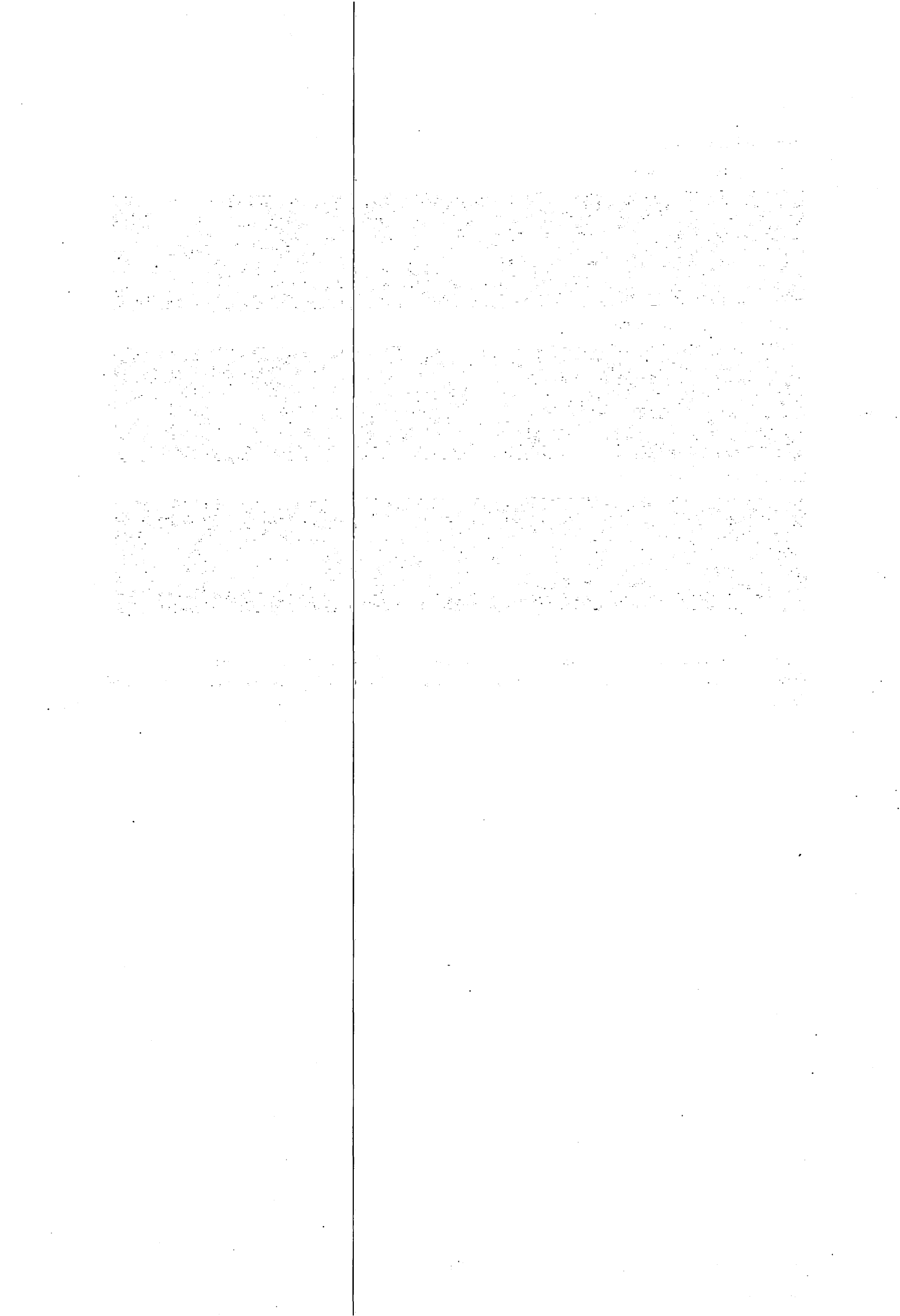
IV. 8. Clinical Application of SPM and PET to Localize Epileptogenic Foci in Temporal Lobe Epilepsy

Nakajima T., Shamoto H.*, Shirane R., Itoh M.**, and Yoshimoto T.

Department of Neurosurgery, Tohoku University School of Medicine
Department of Neurosurgery, Kohnan Hospital*
Cyclotron and Radioisotope Center, Tohoku University**

Introduction

Positron emission tomography using ^{18}F-fluoro-deoxyglucose (FDG) has been widely applied to epileptic patients to localize epileptogenic foci for presurgical evaluation, and to investigate the pathophysiology around the lesion. Numerous studies have confirmed a 60 to 90 % incidence of interictal hypometabolism in patients of temporal lobe epilepsy[1]. Because PET images have been analyzed usually by visual inspection or semi-quantitative method applying regions of interest (ROIs) on the suspected areas, these methods are likely to be affected by the operator bias.

The Statistical Parametric Mapping (The Wellcome Department of Cognitive Neurology, London, SPM 99) has recently established as a tool for detection of regional brain activations or physiological abnormalities in the analysis of brain images obtained by PET, SPECT or fMRI[2,3]. In this article we report the reliability of SPM and PET to localize functional brain abnormalities in epileptic patients.

Method

Subjects and method

Nine patients with temporal lobe epilepsy and 24 healthy normal volunteers participated in this study. PET scan was carried out using Shimadzu HEADTOME-V scanner in 3-D data acquisition mode at 45 minutes after intravenous injection of 37 MBq in average of FDG. The subjects lay comfortably in the scanner bed and all studies were performed with their eyes close in a dim room and minimal auditory stimulation. The studies of epileptic patients were undergone in interictal condition. PET images were analyzed with SPM 99 implemented on Matlab (Mathworks, Natick, Mass., USA)[2,3]. At first PET images obtained from subjects were anatomically normalized to the standard template brain in the standard stereotaxic space defined by Talairach and Tournoux[4]. This process was undergone using linear and non-linear transformation algorithm. The transformed PET images were smoothed with a Gaussian filter kernel of 15 * 15 * 13 mm

FWHM. PET images were compared between from one patient and from 24 healthy volunteers using the 'compare group' statistics with the threshold at p<0.001, uncorrected for the multiple comparisons and p<0.05, with voxel-based correction. Subsequently, the regions with decreased relative glucose consumption were displayed as the MIP images (glass brain) and over the T1-weighted MR template images included in SPM99. The precision and reliability of this method was assessed both by visual inspection of the original PET images and SPM analysis.

Results

In eight of nine patients, decreased glucose metabolism was detected by visual inspection only in the temporal lobe. Statistical analysis using SPM99 with a threshold at p<0.001, uncorrected for the multiple comparisons, localized the lesions also, which matched the region detected by visual inspection. On the other hand, the lesion was much smaller than visual inspected area with a threshold set at P<0.05, with voxel-based correction.

All the normalized images of 8 patients were checked visually. Normalization using linear and nonlinear algorithm could transform all the PET images to a standard image adequately in spite of focal abnormalities. In one patient SPM analysis successfully revealed focal lesion in lateral portion of the temporal lobe, which was not detected by visual inspection.

Case presentation

In case 1 magnetic resonance (MR) imaging showed the left hippocampal atrophy. Electrocorticography (ECoG) indicated the epileptogenic spikes in the left temporal and frontal lobes. FDG PET image demonstrated evident glucose hypometabolism spreading over the whole left temporal and parietal lobes (fig. 1A). The normalization process transformed the raw PET image to almost adequate brain image (fig. 1B). SPM analysis also revealed the glucose hypometabolism in the left temporal and parietal lobes (fig. 1C).

In case 2 the scalp EEG suggested that epileptic focus is located in the mesial temporal lobe. However, FDG PET image scanned at interictal condition did not reveal apparent focal lesion (fig. 2A). The normalization was successful (fig. 2B) and SPM analysis could localize a focal lesion in the lateral portion of the temporal lobe (fig. 2C).

Discussion

Functional neuroimaging to measure cerebral blood flow and metabolism is reported to be most effective non-invasive technique for localization of epileptogenic foci. Previous studies have shown a 60 - 90 % incidence of glucose hypometabolism by FDG PET in the epileptogenic area suspected by EEG study[1]. These metabolic disturbances are often larger than areas proved pathologically by surgical procedures or than the lesions detected by [11]C-

flumazenil (FMZ) PET, uptake of which was though to be correlated with regional neuronal loss. These findings implied functional disturbances around the focus, which was the source of epileptic discharge[5]. Visual inspection and ROI method have been often applied to detect hypometabolic regions on PET images. However, these methods are subjective and not sufficient to be used for small or subtle lesions. In this study we applied a statistical imaging analysis and compared its validity with the conventional methods.

The results revealed that In 8 of 9 temporal lobe epilepsy cases, the SPM analyses clearly delineated hypometabolic regions of glucose which was comparable with the visual inspection. However, In 1 case, SPM disclosed a significant hypometabolic region in the lateral portion of the temporal lobe, which was not picked up by visual inspection.

Although the number of cases in this study is still small, the SPM analysis proved to be potentially useful for detection of abnormal regions, which might be missed or not conclusive by visual inspection due to its subtlety. We stress the robust and objectiveness of this SPM analysis which is essential for presurgical examinations of epilepsy treatment.

It is reported that some temporal lobe epilepsy patients with suspected foci in mesial portion of the temporal lobe showed marked hypometabolism in the lateral portion of the temporal lobe[6]. This phenomenon was explained by either trans-synaptic effects by disturbed efferent pathways due to reduced viable cells in the focus in mesial temporal lobe or due to a reduced number of efferent fibers to the temporal neocortex from the hippocampal formation[6]. In case 2 SPM analysis demonstrated this pathophysiological abnormality as a spotty hypometabolic area in the lateral temporal lobe.

The anatomical normalization in SPM basically employs linear (affine) transformation which assumes regional similarity between the target and the template images. Substantial caution is required to apply this technique to the images where regional abnormality is expected. Previous studies indicated that only linear transformation without nonlinear algorithm should be applied to this situation. Some authors suggested that the anatomical transformation should be first applied to MR images (patient's to the template) and the obtained transformation matrices could be used for PET images afterward, with MRI and PET images co-registered beforehand. However, normalization of PET images only was found almost adequate in this study with relatively mild functional abnormalities. Technical simplicity is important for clinical evaluation.

References

1) Duncan J.S., Brain 120 (1997) 339-77.
2) Friston K.J., Worsley K.J., Frackowiack R.S.J., Mazziotta J.C., Evans A.C., Hum. Brain Mapp. 1 (1994) 214-220.
3) Friston K.J., Holmes K.J., Worsley K.J. et al., Hum. Brain Mapp. 2 (1995) 189-210.
4) Talairach J., Tournoux P., Stuttgart Thieme (1998).
5) Savic I., Ingvar M., Stone-Elander S., J. Neurol. Neurosurg. Psychiatry 56 (1993) 615-621.

6) Lares J.C., Siegel G.J., Abou-Khalil B.W., Hood T.W., Gilman S., McKeever P.E., Hichwa R.D., Hutchins G.D.,Neurology **40** (1990) 1420-1426.

Fig. 1A.

Fig. 1B.

Fig. 1C.

SPM{T_{23}}
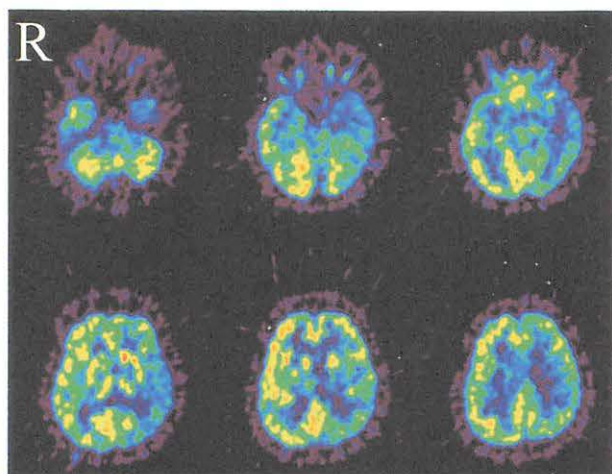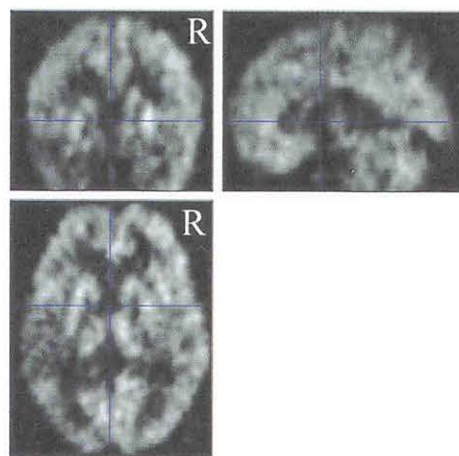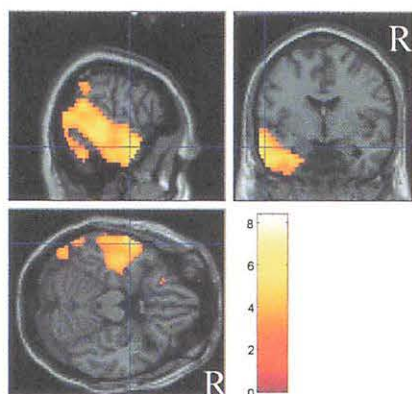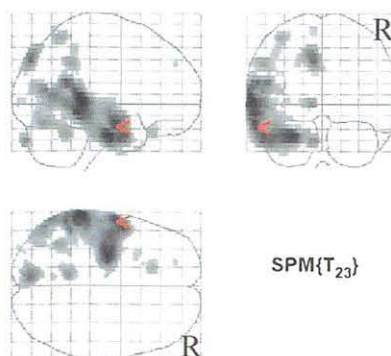
Fig. 1.   Case 1.   (A) FDG PET images delineated apparent hypometabolism spreading over the temporal and parietal lobes.   (B) The normalized image generated by SPM reveals almost adequate brain shape.   (C) The regions with decreased relative glucose consumption detected by SPM analysis are displayed over the T1-weighted MR template images (left) and as the MIP images (glass brain) included in SPM99 (right).   The regions almost correspond to the area identified by visual inspection of the original PET image.

Fig. 2A.

Fig. 2B.

Fig. 2C.

SPM{T₂₃}
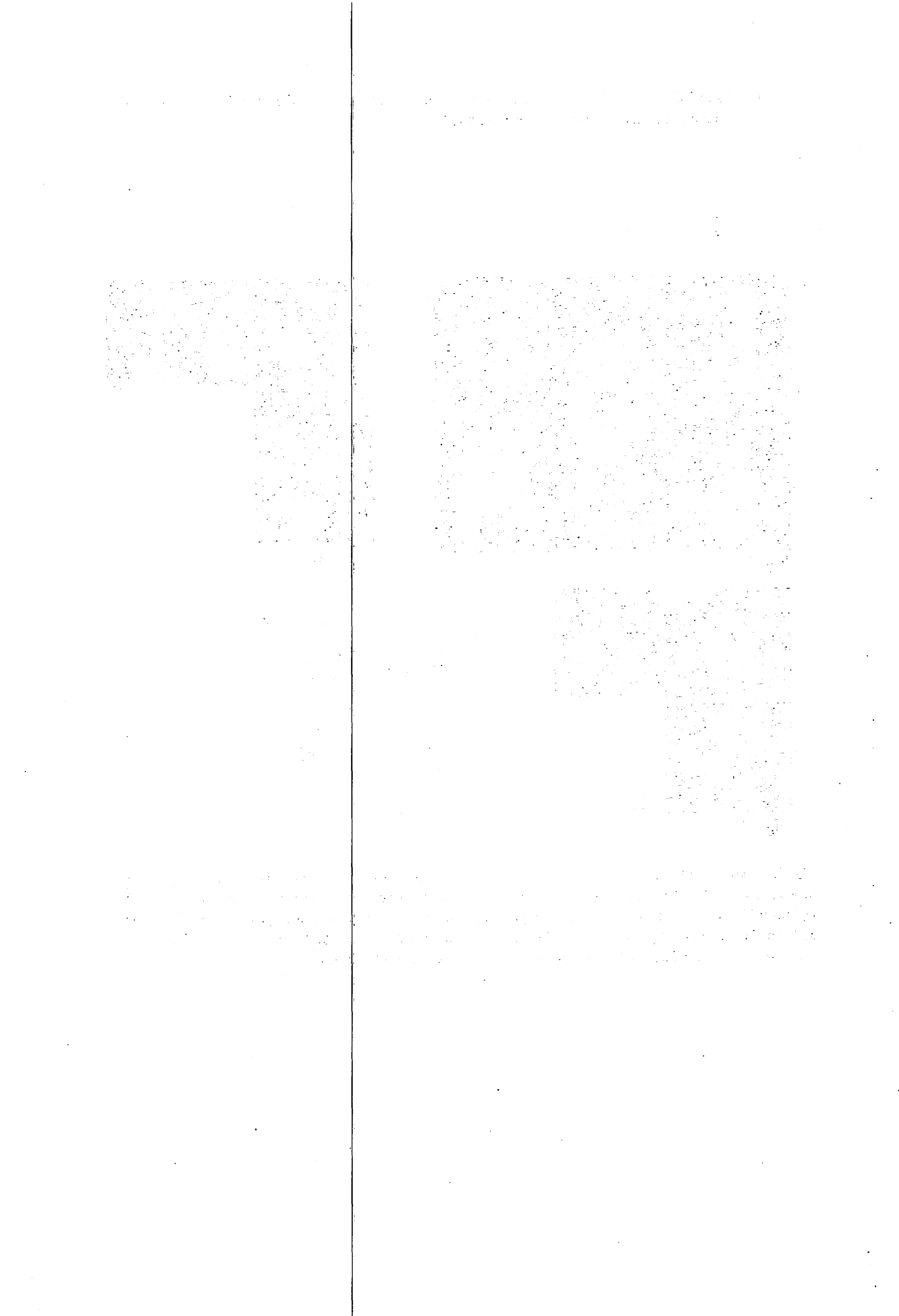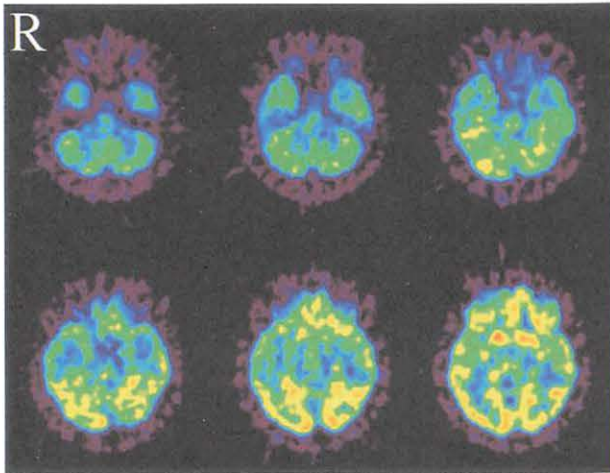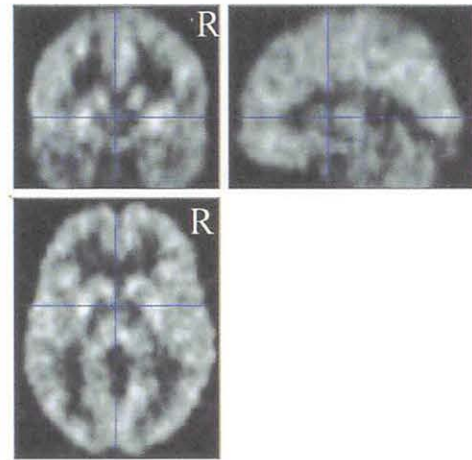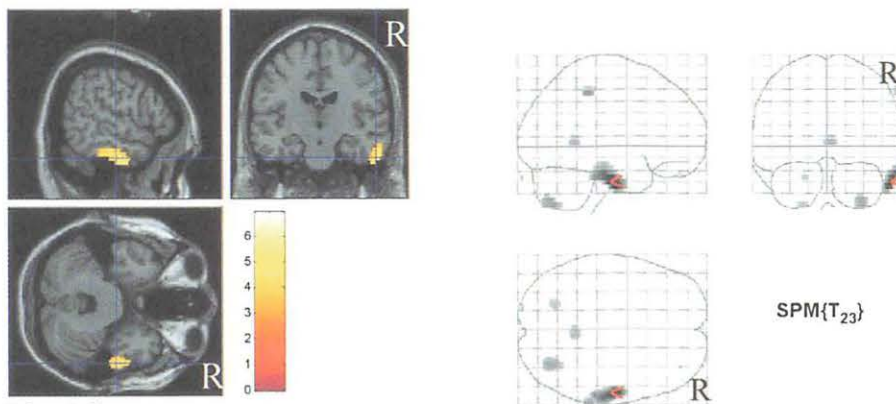
Fig. 2. Case 2. (A) FDG PET images scanned at interictal condition does not reveal apparent hypometabolic region. (B) The normalized image generated by SPM shows adequate brain shape. (C) The focal hypometabolic lesion in the lateral portion of the right temporal lobe detected by SPM is displayed over the T1-weighted MR template images (left) and as the MIP images (right).

IV. 9. Effects of Stereotactic Pallidal Surgery on Regional Cerebral Glucose Metabolism in Advanced Parkinson's Disease

Nakajima T., Nimura T.*, Ando T.*, Shirane R, Yamaguchi K.**, Itoh M.**,
and Yoshimoto T.

Department of Neurosurgery, Tohoku University School of Medicine
Department of Neurosurgery, Miyagi National Hospital*
Cyclotron and Radioisotope Center, Tohoku University**

Introduction

Stereotactic pallidotomy has been established as an alternative treatment for advanced Parkinson's disease (PD)[1-4]. Although it is effective for relieving akinesia, tremor and rigidity, has also some risks of adverse effect such as dysfunction of higher brain functions, and bulbar palsy.   In this study we evaluated changes in regional cerebral glucose metabolic rate (rCMRGlu) in PD patients using positron emission tomography (PET) before and after stereotactic pallidotomy.   Correlations between rCMRGlu and clinical outcomes following the pallidotomy were also investigated.

Subjects and methods

Subjects

Three PD patients and 24 healthy volunteers participated in the study.   The clinical characteristics of the patients are shown in Table 1.   By Magnetic resonance (MR) imaging evident cortical or subcortical atrophy was not found both in patients and volunteers.   All patients had quantitative PET 1 to 2 weeks prior to the pallidotomy and post-operative study was undergone after the operation.   The protocol was approved by Clinical Committee of Radioisotope Use of this institution and all subjects gave their written informed consent for the study.

Positron emission tomography

The ^{18}F-fluorodeoxyglucose (FDG) PET was performed using Shimadzu HEADTOME-V scanner in 2-D data acquisition mode.   A transmission scan was performed for attenuation correction of annihilation photons using a rotating 68Ge/68Ga line source. The subjects lay comfortably in the scanner bed and all studies were performed with their eyes close in a dim room and minimal auditory stimulation.   185 MBq in average of FDG was injected intravenously and 16 arterial blood samples were obtained for 50 minutes after the

tracer injection. Radioactivity of the plasma was counted with a well-type gamma counter to obtain a FDG input function. Cerebral glucose metabolic rate was calculated using the autoradiographical method scaned for 10 minutes beginning 40 minutes after injection. The lumped constant was 0.42 and the rate constants were as follows: $k1=0.102$, $k2=0.130$, $k3=0.062$, $k4=0.0068$.

Image analysis

To analyze focal metabolic changes between pre- and post- operative conditions, we applied a voxel-based statistical analysis using the Statistical Parametric Mapping (SPM99, Wellcome department of Cognitive Neurology, London) implemented on Matlab (Mathworks, Natick, Mass., USA)[5,6]. We defined the hypometabolic regions by comparing PET images of each patient over the Student's t-distribution obtained from 24 healthy normal volunteers adopting the statistical significance threshold at $p<0.001$ without correction for multiple comparisons.

Results

Case 1

Pre-operative PET study disclosed hypometabolic region mainly spreading over the prefrontal cortex corresponding to Brodmann area 9 and 10 (Fig. 1A). This patient underwent implantation of stimulator electrodes in the bilateral globus pallidus interna. Clinical performance assessed with Unified Parkinson Disease Rating Scale (UPDRS) revealed substantial improvement; from 51/100 at pre-operative state to 34/76 in stimulator-on condition. Two weeks after the operation, FDG PET in stimulating condition was performed. SPM analysis demonstrated a more intense and larger hypometabolic region in the prefrontal area (Fig. 1B). This patient's higher brain function assessed with WAIS-R and WMS-R revealed not-negligible deterioration after the operation.

Case 2

Pre-operative PET study of this case disclosed significant hypometabolic region over Brodmann area 39 and 40 which were considered to be strongly linked with association functions (Fig. 2A). This patient underwent left posteroventral pallidotomy (PVP). After the operation drug induced dyskinesia mainly in left side remarkably improved. But WAIS-R and WMS-R disclosed some impairment of intelligence as well as the bulbar palsy. SPM analysis demonstrated a newly developed hypometabolic region in bilateral prefrontal cortex; Brodmann area 9 (Fig. 2B).

Case 3

In case 3, PET study prior to the right PVP revealed no significant hypometabolic

region (Fig. 3A). The PVP could release the patient from severe wearing-off, akinesia and gait disturbance. However, impairment of general intelligence on WAIS-R and WMS-R appeared. Post-operative PET study demonstrated glucose hypometabolism in the right prefrontal cortex (Fig. 3B).

Discussion

PET has been established as the most useful method to evaluate the pathophysiological mechanism and quantitative evaluation of Parkinson's disease[7]. ^{18}F-fluorodeoxyglucose was applied to measurement of glucose metabolism in cerebral cortex and other deeply located structures such as globus pallidum, putamen and thalamus.

Previous PET study described that PD is associated with increased glucose metabolism in the thalamus and lentiform nucleus and decreases in the lateral frontal, paracentral, inferior parietal and parietooccipital areas. This metabolic profile has been showed to correlate with the disease progression as measured by the Hoehn and Yahr score[8]. Post-operative evaluation using FDG PET demonstrated that metabolic decreases in the thalamus ipsilateral to surgery site with increases in motor, premotor and supplement motor cortex (SMA) were correlated with the improvement of post-operative motor performance of the limb contralateral to pallidotomy. Furthermore post-operative hypometabolism in ipsilateral lentiform nucleus and the thalamus has been reported to have covaried with increases of glucose metabolism in bilateral SMA[9]. These findings are consistent with the basic concept involvement of the basal ganglia-thalamo-cortical circuitry and the theory that the pallidotomy effects result from artificial disruption of uncontrolled pallidal inhibitory output to the ventrolateral thalamus which consequently causes a reduced thalamocortical input and depressed cortical activity[7].

Previous report described that there was a greater risk of adverse effects such as cognitive and bulbar dysfunction after the pallidotomy, especially when employed to the bilateral targets[10]. From our cases, unilateral pallidotomy seems to have an enough potential to deteriorate higher brain function. FDG PET studies after the operation revealed the appearance of hypometabolic region in the prefrontal cortex bilaterally in case 1 and 2, and ipsilaterally in case 3. These metabolic reductions are a pathophysiological proof of the clinical adverse effects and presumably resulted from a functional disconnection of basal ganglia-thalamo-cortical circuitry as mentioned above.

We stress that the unilateral as well as the bilateral pallidotomy have a potential danger of deterioration of higher brain functions and this adverse effect can be functionally assessed by FDG PET.

References

1) Dogali M., Fazzini E., Kolodny E., Eidelberg D., Sterio D., Devinsky O., Beric A., Neurology 45

(1995) 753-61.

2) Baron M.S., Vitek J.L., Bakay R.A., Green J., Kaneoke Y., Hashimoto T., Turner R.S., Woodard J.L., Cole S.A., McDonald W.M., DeLong M.R., Ann. Neurol. **40** (1996) 355-66.

3) Kishore A., Turnbull I.M., Snow B.J., de la Fuente-Fernandez R., Schulzer M., Mak E., Yardley S., Calne D.B., Brain **120** (1997) 729-37.

4) Svennilson E., Torvik A., Lowe R., Leksell L., Acta Psychiatr. Scand. **35** (1960) 358-77.

5) Friston K.J., Worsley K.J., Frackowiack R.S.J., Mazziotta J.C., Evans A.C., Hum Brain Mapp **1** (1994) 214-220.

6) Friston K.J., Holmes K.J., Worsley K.J. et al., Hum Brain Mapp **2** (1995) 189-210.

7) Iacoboni M., Baron J.C., Frackowiak R.S., Mazziotta J.C., Lenzi G.L., Clin. Neurophysiol. **110** (1999) 2-23.

8) Eidelberg D., Moeller J.R., Dhawan V., Spetsieris P., Takikawa S., Ishikawa T., Chaly T., Robeson W., Margouleff D., Przedborski S., et al., J. Cereb. Blood Flow Metab. **14** (1994) 783-801.

9) Eidelberg D., Moeller J.R., Ishikawa T., Dhawan V., Spetsieris P., Silbersweig D., Stern E., Woods R.P., Fazzini E., Dogali M., Beric A., Ann. Neurol. **39** (1996) 450-9.

10) Lang A.E., Lozano A.M., J. Med. **339** (1998) 1130-43.

Table 1. Parkinson's disease patients undergoing stereotactic pallidotomy.

patient	age (yr)	sex	duration (yr)	surgery	Hoehn and Yahr stage		UPDRS	
					pre ope	post ope	pre ope	post ope
1	38	F	15	Blt. GPi stimulation	3/5	3/4	51/100	34/76
2	50	M	35	Lt. PVP	3/3	3/3	32/55	19/32
3	68	M	18	Rt. PVP	3/4	4/4	46/96	43/63
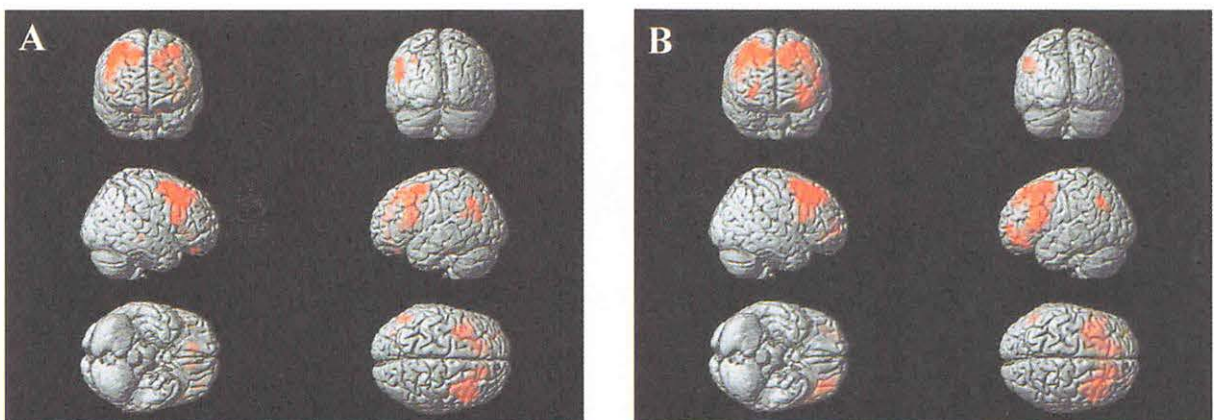
Fig. 1. Case 1. The glucose hypometabolic regions detected by SPM analysis are projected together onto a surface-rendered representative brain in standard stereotactic space (p<0.001, uncorrected for the multiple comparisons). (A) Pre-operative study revealed hypometabolism widely spreading over the lateral frontal lobe. (B) Post-operative study disclosed appearance of more intense and larger hypometabolism in the prefrontal area.

Fig. 2. Case 2. (A) Pre-operative study reveals hypometabolic region over Brodmann area 39 and 40. (B) After the operation SPM analysis of the FDG PET images discloses a newly developed hypometabolic region in bilateral prefrontal cortex; Brodmann area 9.
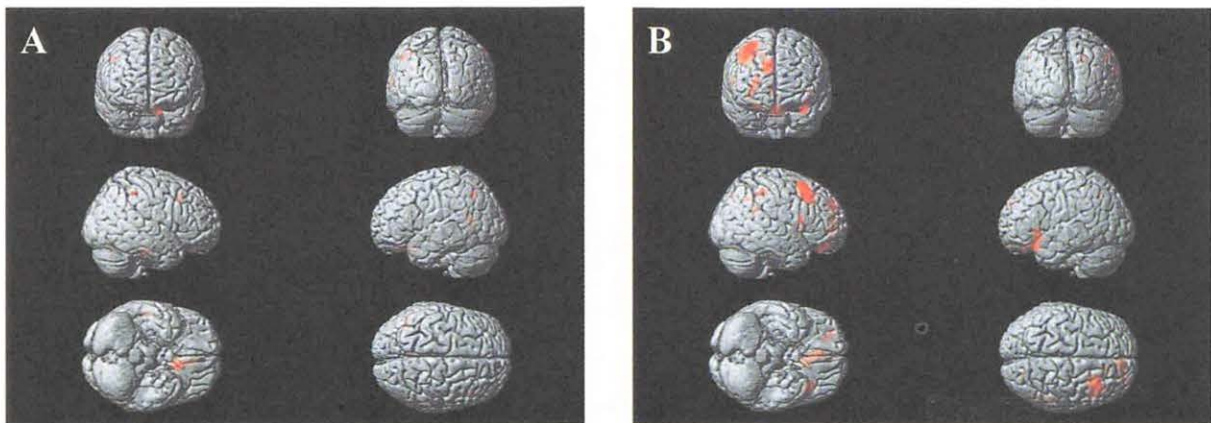
Fig. 3. Case 3. (A) SPM analysis does not detect significant hypometabolism before the operation. (B) Post-operative study reveals appearance of glucose hypometabolism in the right prefrontal cortex.

IV. 10. A case of Autoimmune-related Pancreatitis- Usefulness of Fluorodeoxyglucose Positron Emission Tomography for the Evaluation of the Effect of Steroid Therapy -

*Takasu A., Satoh K., Satoh A., Asakura T., Nagasaki Y., Shimosegawa T., and Itoh M.**

Department of Gastroenterology, Tohoku University School of Medicine
*Cyclotron Radioisotope Center , Tohoku University**

A 73-year-old male patient was hospitalized because of repeating abdominal pain. Imaging studies showed diffusely enlarged pancreas, stricture at the distal portion of the common bile duct and diffuse narrowing of the main pancreatic duct. Laboratory data showed an increase in serum pancreatic enzymes, gammaglobuline, and some positive autoantibodies.   Autoimmune pancreatitis was highly suspected.   Before steroid therapy, ^{18}F-fluorodeoxyglucose positron emission tomography (FDG PET) showed a diffuse and intense accumulation of the radioactivity in the pancreas.   After starting steroid therapy, an enlargement of the pancreas was improved remarkably on CT, accompanied by an improvement of laboratory data and no accumulation of FDG was recognized on PET.   It was considered that FDG PET showed an enhanced glucose metabolism in the inflammatory cells infiltrating to the pancreas before therapy and its improvement after steroid therapy. We concluded that FDG PET may be useful for evaluating the effect of steroid therapy in this disease.

Introduction

Autoimmune pancreatitis is a relatively new entity and is characterized for its remarkable improvement by steroid therapy.   We report a patient with this disease in whom the effect of steroid therapy was evaluated by FDG PET.

Case report

A 73-year-old male patient developed repeating abdominal pain in early January 1999, and was admitted to another hospital.   Pancreatic cancer was suspected on the basis of the radiographic findings, that is diffusely swelling of the pancreas and stricture of common bile duct.   He was admitted to our hospital for further examinations on April 1st.   The patient had a history of diabetes since he was 66 years old and he has been left without treatment for more than two years because control was good.   He had no history of alcohol

consumption and no family history of pancreatic diseases.

On physical examination, no tumor was palpable in the abdomen, and no superficial lymphonodes were palpable.

The laboratory data on the admission showed evidence of cholestatic liver dysfunction, and elevation of pancreatic enzyme, fasting blood sugar and CA19-9. Furthermore, gammaglobuline was remarkably increased (2.65 g/dl) and immunoglobulin G was also elevated (2936 mg/dl). Antinuclear antibody (ANA) was positive and the pattern was diffuse. Anti carbonic anhydrase-II(CA-II) antibody was also positive. Antimitochondorial antibody (AMA) was negative. Pancreatic exocrine function test such as PFD test and fecal chymotrypsin test was shown to be almost normal. (Table).

Ultrasonography showed diffuse enlargement of the pancreas with a slight hypoechoic pattern. Particularly, the head of the pancreas seemed like a mass (Fig. 1 a,b). CT scans revealed diffuse enlargement of the pancreas without cyst or calcification (Fig.2 a.b). Endoscopic retrograde cholangiography (ERC) showed stricture of the distal common bile duct (Fig. 3a) and MR cholangiopancreatography (MRCP) showed irregularly narrowing of the main pancreatic duct (Fig. 3b). Autoimmune pancreatitis was highly suspected from these findings. FDG PET demonstrated a remarkably high and diffuse accumulation in the pancreas which could not deny pancreatic cancer (Fig. 4 a,b). Although operation was recommended, the patient and his family were unwilling and against it. Furthermore, he showed no symptoms after admission and laboratory data including the enzymes of the pancreas and the bile duct system and CA19-9 returned to normal during the course, and diabetes control was improved by diet therapy, so we decided to get him discharged. While being followed as an outpatient, the pancreas remained diffusely enlarged on ultrasonography and pancreatic enzymes such as serum amylase and lipase repeated elevation while he had no symptoms. On the other hand, diabetes control got worse gradually. Thus the patient was admitted to our hospital again on October 8th in 1999 for the control of diabetes and for receiving diagnostic therapy of autoimmune pancreatitis by corticosteroid. Predonisolone at an initial dose of 30 mg/day was administrered orally for one week, and the dose was gradually reduced. The pancreas swelling resolved by 6 weeks after starting steroid therapy on ultrasonography (Fig. 1c) and on CT (Fig. 2 c,d), and the stricture of the common bile duct was also improved on ERCP (Fig. 3c). Along with it, the laboratory data such as elevated gammaglobuline and immunoglobuline G returned to normal and the elevation of pancreatic enzymes and cholestatic liver dysfunction was also improved. Antinuclear antibody showed negative (Table). FDG accumulation was not recognized on PET performed 8 weeks after starting steroid therapy (Fig. 4c). However, ERCP showed that the main pancreatic duct remained diffusely narrowed (Fig. 3d).

193

Discussion

Since Yoshida et al[1]. proposed the concept of autoimmune pancreatitis, numbers of authors have reported about this disease so the concept has been increasingly permeating recently. It is characterized by no symptoms or mild symptoms, diffuse swelling of the pancreas, diffuse and irregular narrowing of the pancreatitic duct, cholestatic liver dysfunction caused by constriction of the common bile duct in the pancreas, hyperimmunoglobulinemia, eosinophilia, positive anti-nuclear antibody (ANA) and CA-II antibody, histologically fibrotic change with lymphocyte infiltraion in the pancreas, and effective steroid therapy[1,2]. In our case, though histological diagnosis had not been made, it fulfilled all the other criteria of this disease. So we postulate an autoimmune mechanism as the etiology of this patient's pancreatitis.

Some experiments have suggested that this pancreatitis is mediated by a cellular autoimmune mechanism[3,4]. It has been reported that HLA-DR antigens were expressed on the epithelial cells of the pancreatic duct, and the pancreas was infiltrated by activated CD-4 or CD-8 positive T lymphocytes, which caused the segmental narrowing of the pancreatic duct[3]. Carbonic anhydrase-II (CA-II) and lactofferin existing on the exocrine cells have been considered to be possible target antigens[5].

FDG PET has been thought as useful modality for distinguishing malignant tumors from benign disease[6,7]. However FDG sometimes accumulates in inflammatory sites which causes false positive[8,9]. Recently, Nakamoto et al. has reported that FDG uptake in the pancreas with this disease was as high as pancreatic cancer lesion, therefore the differentiation from cancer is difficult and care must be paid[10]. It may be the results of enhanced glucose metabolism in massive lymphocytes or fibroblast infiltrating to the pancreas. FDG PET performed after starting steroid therapy revealed no accumulation. It may be because the lymphocyte infiltration was improved or activation of these inflammatory cells was released by steroid therapy.

In our case, the main pancreatic duct remained diffusely narrowed on ERP, even after the swelling of the pancreas improved on CT and hypergammaglobulinemia improved by steroid therapy. Moreover, diabetes was worsened even after steroid therapy, although many authors have reported that diabetes in this disease improved by steroid therapy[2,3]. Recently, Tanaka et al. investigated the mechanism of developing diabetes in autoimmune pancreatitis. They have found that the number of the islet is decreased by replacement with massive fibrotic tissue and lymphocyte infiltration in the pancreas in diabetes associated with this disease, and some mechanisms of islet regeneration by steroid therapy may participate in the improvement of diabetes[11]. But details are still unknown. Concerning our case, the reason why diabetes has not been improved by steroid may be because more than five years have passed since he developed diabetes, so the fibrotic change in the pancreas involving islets may have been advanced and irreversible. Or, diabetes in this case may not have been associated with autoimmune pancreatitis.

194

In conclusion, although FDG PET may reveal high accumulation in the entire pancreas or focal intense uptake in patients with autoimmune pancreatitis which makes it difficult to differentiate from cancer, it may be useful for evaluating the effect of steroid therapy.

References

1) Yoshida K., Toki F., Takeuchi T., et al., Dig. Dis. Sci. **40** (1995) 1561-1568.
2) Ito T., Nakano I., Koyanagi S., et al., Dig. Dis. Sci. **42** (1997) 1458-1468.
3) Ohana M., Okazaki K., et al. , Am. J. Gastroenterol **93** (1998) 99-102.
4) Kanno H., Nose M., Itoh J., et al., Clin. Exp. Immunol. **89** (1992) 68-73.
5) Kino-Osaki J., Nishimori I., Okazaki K,et al. , Gastroenterology **110** (1996) 1579-1586.
6) Zimmy M., Bares R., Jurgen Fa β. et al. , Eur. J. Nucl. Med. **24** (1997) 678-682.
7) Keogan M.T., Tyler D., Clark L., et al., Am J. Roentgenol. **171** (6)(1998) 1565-70.
8) Paul D., Eur. J. Nucl. Med. **25** (1998) 259-264.
9) Strauss L.G., Eur. J. Nucl. Med. **23** (1996) 1409-1415.
10) Nakamoto Y., Sakahara H., Higashi T. et al., J. Clin Nucl Med **24** (1999) 778-80, 1999.
11) Tanaka S., Kobayashi T., Nakanishi K., et al., Lancet (in press).

Table 1.   Laboratory data before and after steroid therapy.

	before	after	
WBC	7700	8100	$\times 10^3$ /ml
eosinophil	693	81	$\times 10^3$ /ml
T-bil	0.8	0.8	mg/dl
ALP	515	146	IU/l
γ-GTP	285	51	IU/l
GOT	35	21	IU/l
GPT	64	32	IU/l
serum-amylase	249	112	IU/l
serum-lipase	51	3	IU/l
T.P	8.7	5.9	g/dl
γ-globuline	2.65	1.08	g/dl
IgG	2936	1197	mg/dl
AMA	(-)	-	
ANA	(+) speckled homogeneous	(-)	
CA-II antibody	(+)	(+)	
CA19-9	62.8	27.1	U/ml
Dupan 2	140	-	U/ml
FBS	366	146	mg/dl
PFD-test	69.3	67.1	%
fecal chymotrypsin test	normal	normal	
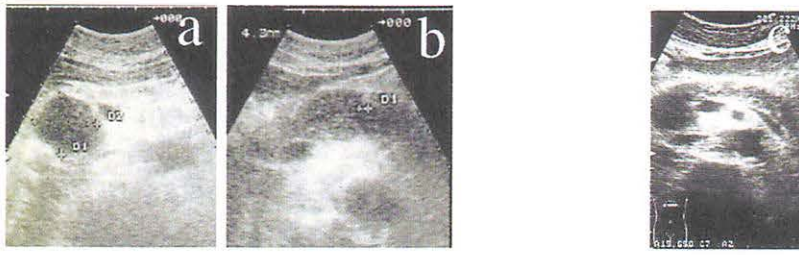
Fig. 1. **a,b**: Ultrasonography images on the first admission, showing sausage-like enlargement of the pancreas. Particularly, the head of the pancreas seemed like a mass. **c**: Ultrasonography image after starting steroid therapy revealing improvement of enlargement of the pancreas.
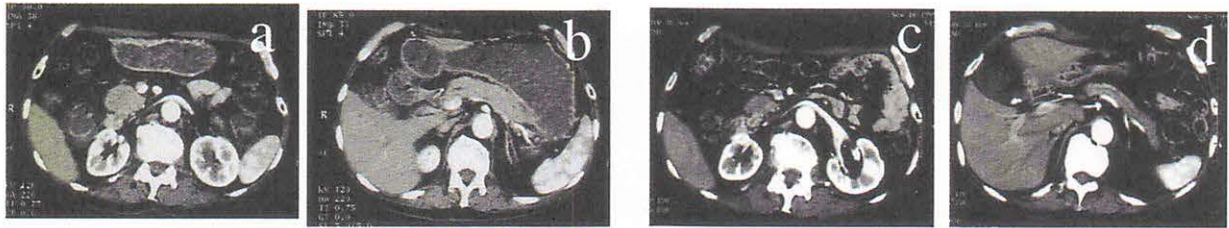
Fig. 2. **a,b**: Pretreatment CT scans, showing diffuse enlargement of the pancreas. **c,d**: CT scans after starting steroid therapy, demonstrating remarkable improvement of enlargement of the pancreas.
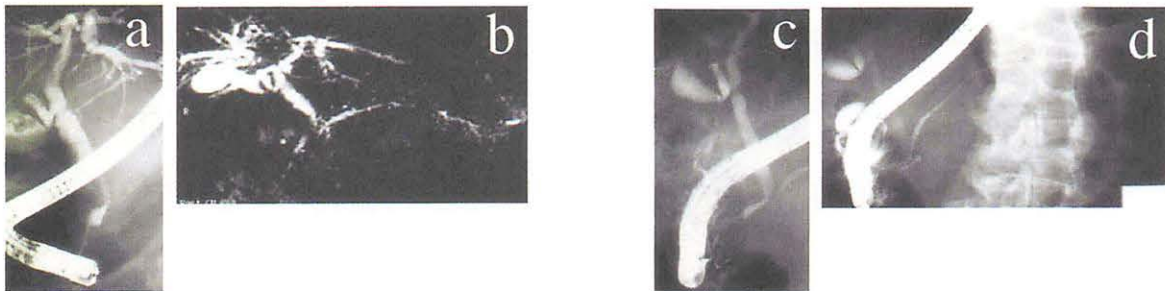
Fig. 3. **a,b**: Pretreatment ERC and MRCP images, showing stricture of the of the common bile duct in the pancreas and diffuse irregular narrowing of the main pancreatic duct. **c,d**: ERCP images obtained after starting steroid therapy, demonstraing improvement of the common bile duct stricture and remains of narrowing of the main pancreatic duct.
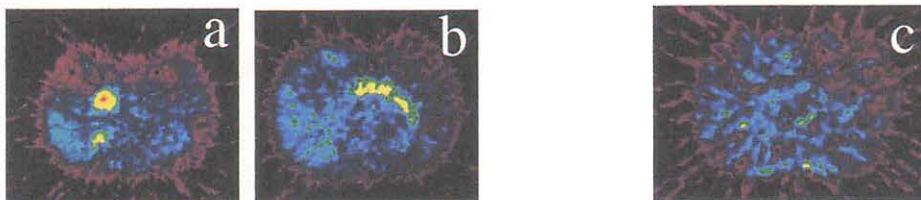
Fig. 4. **a,b**: Pretreatment FDG PET images, demonstrating diffuse and high accumulation in the pancreas, which could not deny malignancy. **c**: FDG PET image after starting steroid therapy, showing no FDG accumulation in the pancreas.

196

V. RADIATION PROTECTION AND TRAINING OF SAFE HANDLING

V. 1. Development of Gamma Ray Monitor Using CdZnTe Semiconductor Detector

Rasolonjatovo A. H. D., Shiomi T., Nakamura T.
Tsudaka Y., *Fujiwara H.*, *Araki H.*, *Matsuo K.*, *and Nishizawa H.**

Cyclotron and Radioisotope Center, Tohoku University,
Mitsubishi Electric Corporation, Japan

INTRODUCTION

These days the CdZnTe (CZT) semiconductor detector is preferably used for X-ray and gamma-ray detection, because of its high efficiency, low bias voltage and good energy resolution in use at room and higher temperatures.   In this study, we aimed to develop a new gamma-ray monitor using a $Cd_{0.5}Zn_{0.5}Te$ semiconductor detector.   We tried to get the gamma-ray monitor with higher sensitivity than the commercially available Si semiconductor gamma-ray monitor and at the same time to have a flat energy response to dose-equivalent over the photon energy region from 10 keV to 7 MeV.

EXPERIMENTS

A $Cd_{0.5}Zn_{0.5}Te$ detector having 10mm×10mm size by 2mm thickness was used as a sensor.   The preamplifier is a low noise preamplifier (Model 850) fabricated by Clear-Pulse Co. Ltd.   The bias voltage of +24 V was supplied to the detector.   The amplifier is a linear amplifier ORTEC 571 with a 2μs shaping time.

In order to get the energy response of the CZT detector, the measurements were done using the mono-energetic X-ray beam sources from 10 to 40 keV and the radioactive photon sources of [241]Am (368 kBq), [57]Co (96 kBq), [137]Cs (418 kBq), [60]Co (372 kBq) and [88]Y (439 kBq) having photon energies of 59.54 keV to 1836 keV.

The experiments using X-ray beam sources were performed at a beam line of the Photon Factory of High Energy Accelerator Research Organization (KEK), Tsukuba.   The X-ray energy spectra and the absolute values of the X-ray fluence were measured with the HP Ge detector and the free-air ionization chamber respectively.   In order to investigate the variation of the detection efficiency with the filters, the pulse height distributions of the CZT detector covered with the Al, Cu, Cd and Pb filters of various thicknesses were also measured.

The measurements using point sources were carried out at the Hot Laboratory of the

Cyclotron and Radioisotope Center (CYRIC), Tohoku University. By setting a lead shadow bar of 80 mm long and 40mm diameter between the source and the detector, the contribution of the room-scattered photons was subtracted from the measured results. The measurements using point sources were performed only for the non-filtered CZT, but in the directions of 0 to 90° by rotating the CZT detector in order to get its angular dependence. The ^{137}Cs source was covered with a 1.5 mm thick Al foil to absorb the 661.7 keV conversion electrons from the electron capture reaction. The ^{60}Co source was covered with a 1 mm thick Al foil to absorb the β ray at 318 keV.

CALCULATIONS

The calculations of the pulse height spectra of the detector were performed with the electron-photon cascade Monte Carlo code EGS4[1] with taking into account the carrier trapping effect[2]. For the case of our detector the product of the mobility μ and lifetime τ for electron is 3×10-3 cm^2.V^{-1}, and for hole 2×10^{-5} cm^2.V^{-1}. The energy needed to create an electron-hole pair is 4.43 eV[3].

RESULTS AND DISCUSSIONS

Pulse height spectra

The output pulse height spectra were measured with the multi-channel analyzer. The noise level of the system was about 6 keV. Figure 2 shows the comparison of measured and calculated pulse height spectra of 20, 40 keV X-ray beams, ^{57}Co (14.4, 122.1 and 136.5 keV) and ^{60}Co (1173 and 1333 keV). For 20 and 40 keV X-ray sources, there can be seen a single sharp photopeak. For ^{57}Co, the pulse height spectra for the above three photon energies were calculated and summed up considering their branching ratios. For 1173 and 1333 keV photons of ^{60}Co, no photopeaks can be seen. This is because the charge collection efficiency degrades and the energy loss in the detector is dominated by the Compton scattering with the increase of photon energy.

The agreement between the measured and calculated pulse height spectra is very good in general.

Energy response

The efficiency of the 10×10×2mm^3 CZT detector for photon energy range from 10 keV to 1836.01 keV is shown in Fig. 3. In Fig. 3, the conversion factor of fluence to dose equivalent given by ICRP Publ.74[4] is used. The measured and calculated efficiencies were obtained by summing the measured and calculated pulse height spectra by fixing the cut-off energy at 6 keV. But for ^{241}Am the subsidiary peaks from X-ray and the 26.35 keV gamma ray were not considered and the peaks of 14 and 136 keV gamma rays of ^{57}Co and 30 keV X-ray of ^{137}Cs were also excluded from the measured results in the efficiency estimation. The

agreement between experiment and calculation is generally good, but the slight difference at high energy results from the fact that the counts in the experiment are very high at low energy around the cut-off energy fixed to 6 keV. The efficiency is high for 10 keV and rather flat from 20 keV to 120 keV, and rapidly decreases with energy.

Angular dependence of the 10×10×2 mm³ CZT detector

Figure 4 shows the angular dependence of the efficiency of the CZT detector using radioactive photon sources for 6 keV cut-off energy. The angular distribution of the efficiency is almost constant for ^{137}Cs, ^{60}Co and ^{88}Y in the directions of 0 to 90°, but for lower energy photons of ^{241}Am and ^{57}Co, the efficiency decreases beyond 60. It means that this CZT detector has an almost isotropic efficiency in the forward hemisphere.

Effect of various filters

Figure 5 shows the variation of the efficiencies for 10, 20 and 40 keV X-rays with various thickness' (in mm) of the filters of Al and Cd. Solid lines are the measured results and the dotted lines the calculated results. The cut-off energy was also fixed at 6 keV. The variation of the pulse height is significant at 10 keV but is scarce at 40 keV when using an Al filter. The agreement between measurement and calculation is good except for 10 keV in the case of Cd.

Cut-off energy dependence and flat energy response to effective dose

In order to realize the flat energy response of CZT to effective dose, we varied the cut-off energy of the pulse height spectra from 6 to 1500 keV and used different filters. For low energy below 100 keV, a flat energy response can be obtained with a cut-off energy around 6 keV but for higher energies, a cut-off energy higher than hundreds of keV is necessary. The flat energy response to effective dose within ±30% (Fig.6) and within ±10% (Fig.7) of 10 keV to 7 MeV photon energies were obtained with using two and three detectors having different dimensions, respectively.

CONCLUSION

In this study, the pulse height spectra and the efficiencies of the CZT detector are given by experiment and calculation. The agreement between the experiment and the calculation is rather good. The variation of the detector response with the cut-of energy and with various filters was also obtained. The flat energy response to effective dose within ±30% and ±10% of 10 keV to 7 MeV photon energies were obtained. Field measurements will be carried out and the efficiency of the detector will be compared to other semiconductor detector.

REFERENCES

1) Hirayama H., EGS4, KEK Internal 97-5- 97-10 (1997).
2) Nishizawa H., Ikegami K., Takashima K., Usami T., Hayakawa T., Yamamoto T., Development of Multi-layered CdTe Semiconductor Detectors, Radiation Journal Vol.22, (1996).
3) Dardenne Y.X., Wang T.F., Lavietes A.D., Mauger G.J., Ruhter W.D., Kreek S.A., Cadmium Zinc Telluride Spectral modeling. NIMPH A 422, 159-163 (1999).
4) Conversion Coefficients for use in Radiological Protection against External Radiation, ICRP PUBLICATION 74, (1995).
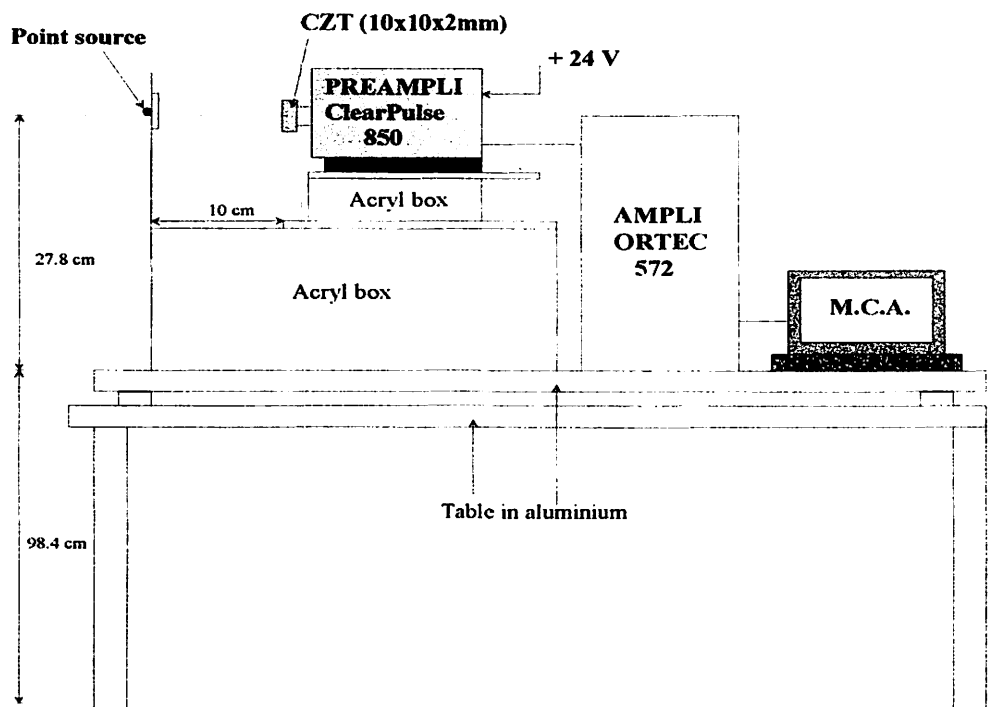
Fig. 1. Experimental set-up at the hot laboratory of CYRIC.
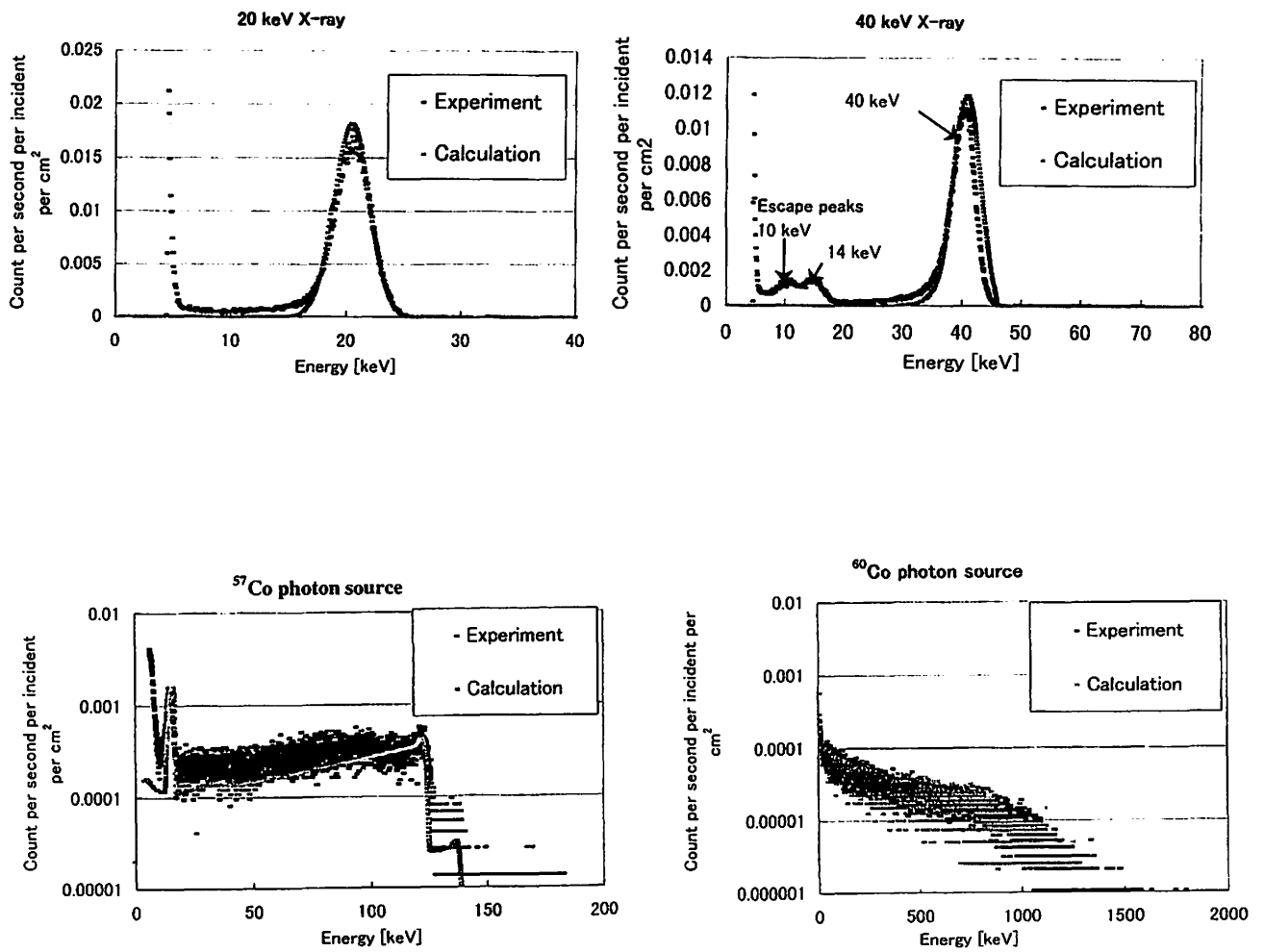
Fig. 2. Comparison of measured and calculated pulse height spectra.
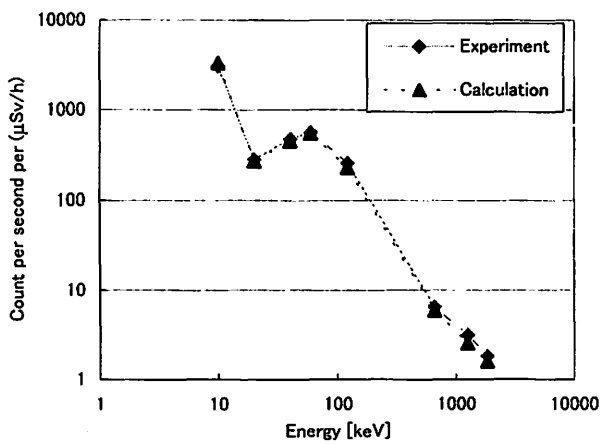
Fig. 3. Efficiency of the CZT detector for a cut-off energy of 6 keV.
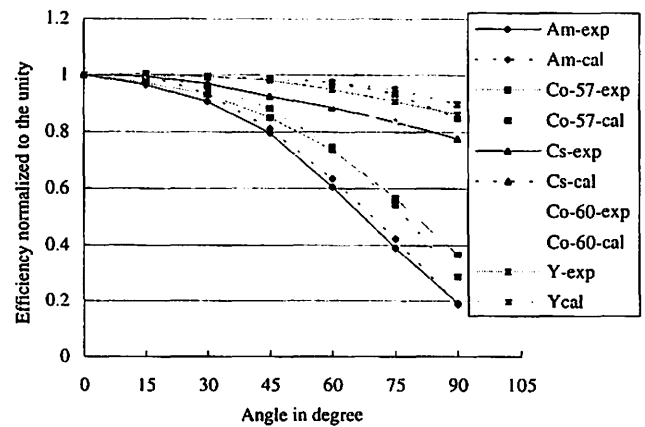
Fig. 4. Angular distribution of the 10×10×2mm³ CZT detector efficiency from experiments and calculations.
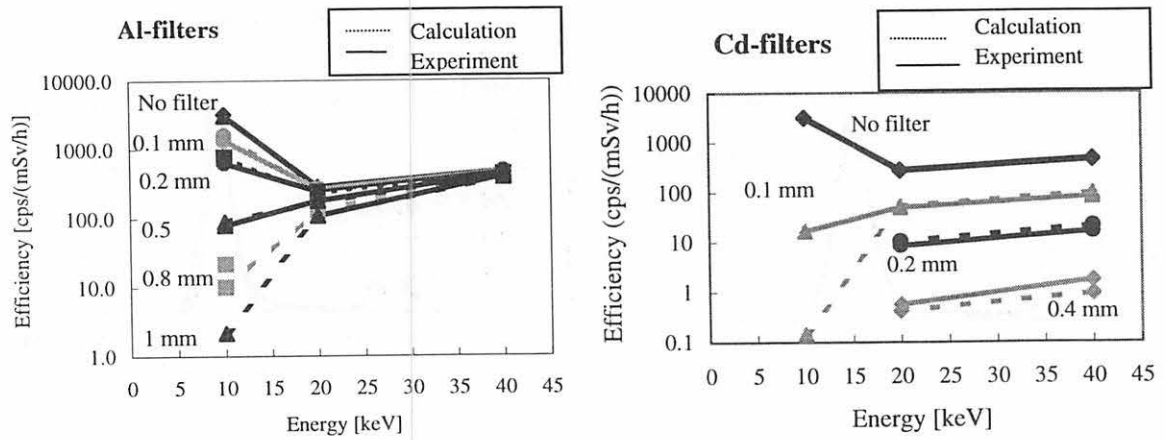
Fig. 5. Variation of the efficiency with Al and Cd filters for 10 keV, 20 keV and 40 keV X rays by calculation and measurement.
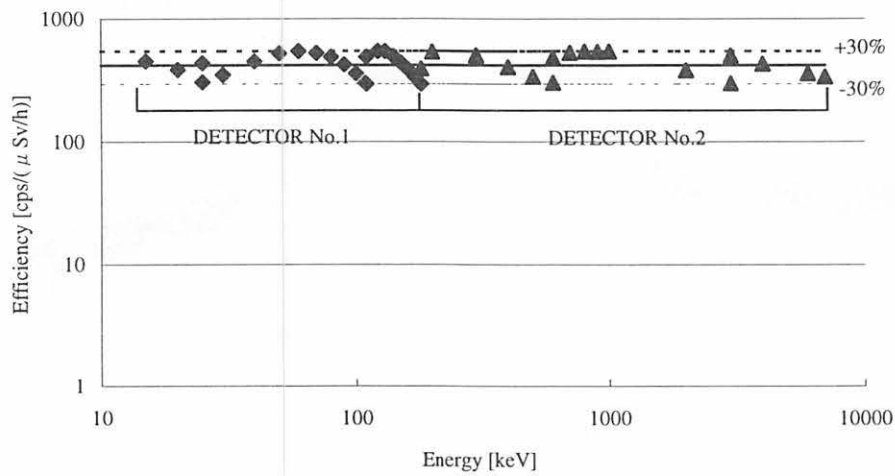
Fig. 6. Energy response to effective dose within 30% difference by using the combination of two detectors.
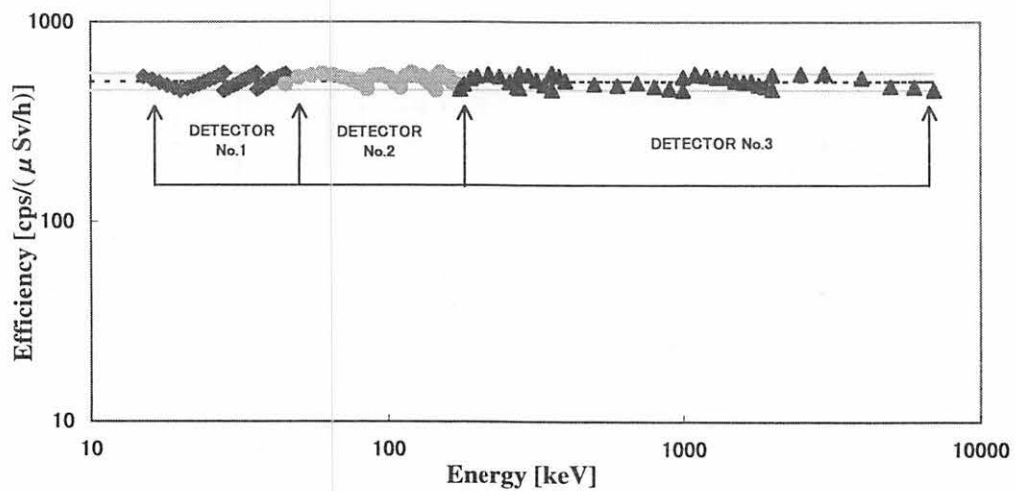
Fig. 7. Energy response to effective dose within 10% difference by using the combination of three detectors and Pb filter

202

V. 2. Fast Neutron Profiling with Imaging Plate (4) -Neutron Scattering Effects in Fast Neutron Imaging-

Miura T[1]., Hiroishi T[1]., Aoki T[1]., Sanami T[2]., Nakamura T., Baba M*., and Yamadera A*

Quantum Science and Energy Engineering, Tohoku University
Cyclotron and Radioisotope Center, Tohoku University*

INTRODUCTION

Measurement of fast neutron spatial distribution (neutron profiling) is required in various fields, *i.e.*, neutron fields characterization and neutron radiography. Fast neutron radiography will be effective to the nondestructive inspection of deep parts of bulk objects.

We continued a study on the neutron profile measurement using a combination of an imaging plate (IP) and a polyethylene or polypropylene (CH_2) film as a converter of fast neutrons[1,2], and applied the device to the neutron field characterization[2] and fast neutron radiography for an accelerator-based neutron source[3]. In our study, the performance of the technique was evaluated by radiography method by using mono-energetic neutrons with various energy from 1 MeV to 15 MeV, and test samples with multiple steps. By optimizing experimental conditions[2,3], we obtained fairly clean images. Nevertheless, there still remained problems of 1) deformation and 2) insufficient contrast of images which should be eliminated for further improvement of the technique. This year we have traced the problem.

Method and Problems

The profiling measurements were carried out at the Tohoku University 4.5 MV Dynamitron facility. Fast neutrons of 1-15 MeV from the neutron production target were first collimated by a 15 cm-long copper collimator and entered into CH_2-IP through a step type sample. The step type samples were used for the convenience to inspect the quality of the profile and made of stainless steel (SUS) and acrylic resign with 1 cm wide steps. The sample was placed in close contact with CH_2-IP.

In our experiments for fast neutrons of 1-15 MeV, the best results were obtained for 5 MeV neutrons which are produced by the D(d,n) reaction at the D_2 gas cell with a platinum beam-stop (1 cm-diam and 3 cm-long, 1.2 atom D_2 gas) due to low γ-ray contamination. Therefore most experiments were carried out for 5 MeV neutrons. The distance between the target and the CH_2-IP was ~80 cm, and the neutron flux was ~3.5×10^4 $cm^{-2}s^{-1}$ at the place of the CH_2-IP.

Employed IP was of X-ray type BAS-SR manufactured by FUJI Photo Film Co., LTD. The polypropylene film as a proton converter should be thicker than the recoil proton range to avoid sample-protons entering IP-CH_2. We employed 0.5 mm-thick one for 5 MeV neutrons whose recoil proton range is ~0.35 mm.

The neutron profile image was obtained by irradiation of CH_2-IP for 1-2 hrs. Typical projected result in this setup is shown in Fig. 1. The image reproduces the shape of step samples qualitatively. However there remained problems that 1) there was rounding in images even for the flat parts in the steps, and 2) the contrast was not so good as expected from the neutron transmission ratio. We looked for the reasons of the deformation and the way for improvement.

Reduction of Rounding

In the present imaging, we expect detection of neutrons transmitted the sample without any collision. Neutrons detected on CH_2-IP after collision in the sample makes distortion. In the present case, the rounding was traced to be due to neutrons scattered in the sample which act as backgrounds overlapping on the transmitted neutrons. The shape of rounding is explained by the pass-length of scattered neutrons within the sample as shown in Fig. 2 which illustrates an example for a simple sample with only 2-step. By this scheme, smaller deformation around the lateral surface in the experimental result is interpreted because no scattered neutrons come in from outside.

The effects of neutron scattering inside a sample in the fast neutron radiography was discussed by Yoshii and Kobayashi[4] for a simpler right cylinder sample. The present interpretation is consistent with their one. In the fast neutron cases, the effect of neutron scattering is more serious than in thermal neutron cases because of much larger ratios of scattering to capture cross sections.

As the way to reduce the effects of scattered neutrons, a honeycomb-shaped collimator is useful for the case of thermal neutrons[5]. In the present case, however, a collimator in front of the CH_2-IP will result in worse contrast because it will increase scattered neutrons and γ-rays in IP.

Instead, separation of CH_2-IP from the sample will be effective for reduction of the effect. We made simulation of the phenomena using the MCNP code to confirm the above argument. Calculations were made for parallel incident neutron flux to the 3-step acrylic sample as a function of distance between the sample and CH_2-IP. The calculation results are shown in Fig. 3. In the case of direct contact (0-cm), the result is similar with the observation in above experimental results. As the distance increases, the rounding structures become smaller. Separation of ~3cm is enough to reduce the rounding structures to a negligibly small level.

204

Improvement of Contrast (n/γ)

In the present CH_2-IP configuration, the intensity of PSL (Photo Stimulated Luminescence) for the area without CH_2 is provided by γ-rays alone while those at the area with a CH_2 film are due to both neutrons and γ-rays. Therefore, PSL values for CH_2-IP and bare IP correspond approximately to n + γ and γ yields, respectively. For the reason, the contrast of profile becomes worse with increasing contribution of γ-rays. Hence reduction of γ-to-neutron ratio is important to obtain clear profiles.

We performed two attempts to improve the contrast.

1) Shielding by lead-blocks around CH_2-IP was performed in order to decrease environmental γ-rays. However, the result was even worse than the case without shielding, probably because lead produced a larger number of γ-rays by inelastic reactions with 5 MeV neutrons. Therefore, γ-rays reduction should be done around neutron production target employing collimators with low γ-rays emission but good shielding ability for fast neutrons.

2) Then, appropriate collimator was looked for. A combination of copper (10 cm long) + paraffin (30 cm long) has heavier shielding effect for 5 MeV neutrons than the paraffin alone. Then, we measured neutron to γ-rays ratio on the IP. However, the experimental result of (n+γ) /γ was 4.8 for the former and 7.4 for the latter, respectively. The collimator using copper resulted in higher γray ratio than paraffin despite of higher shielding effect for both neutrons and γ-rays. From the results, the inferior contrast in previous experiment is supposed to be caused by a copper collimator with higher γ-ray production cross sections.

Improved experimental results

According to the results in the above described experiments, the experimental geometry was modified as follows to reduce deformation and improve contrast in image;

1) the sample-CH_2-IP distance was extended to ~20 cm,

2) the neutron collimator material was changed to paraffin,

3) source neutrons were collimated more tightly not to illuminate the floor and stage of the sample to avoid floor-scattered neutrons from the images.

Typical result is shown in Fig. 4.

The step type sample was a combination of SUS step 3 cm (1cm-wide step) and acrylic resign (1cm step). Irradiation time was ~2 hrs, and the neutron fluence at the place of CH_2-IP was ~1.35×10^8 n/cm^2. The image became much more uniform and the rounding structure became much smaller than in the previous setup. Furthermore, the background level is also improved markedly owing to tighter neutron collimation. In the case of this background level, this method enables to analyze the sample up to 19~20 cm in thickness.

Therefore, this technique will be useful for nondestructive inspection of bulk materials

Summary

We have improved the experimental conditions for the fast neutron profile technique using CH_2-IP.

1) Rounding structure in profiles proved to be caused by neutrons scattered in the sample, and can be reduced by separating the sample from the CH_2-IP.

2) To improve the contrast, reduction of γ-rays fraction is essential. For improved contrast, it is important to adopt shielding and collimator materials with low γ-ray emission for fast neutrons.

By improving the experimental conditions according to the above findings, we obtained good profiles for fast neutrons of 5-15 MeV. This method will be applied to neutron filed characterization and radiography.

However, CH_2-IP profile-detector has essential problems of a) very low sensitivity to lower energy neutrons[2], $E_n < 1$MeV, and b) no information on energy deposits which is important for particle selection. We are designing another active type profile-detector to complement the CH_2-IP detector.

References

1) Yoshii K., Miya K., Niimura N., and Karasawa Y., *Proc. 1996 Annual Meeting of the Atomic Energy Society of Japan*, (1996) G12.
2) Sanami T. et al., *Proc. 11th Workshop on Radiation Detectors & Their Application* (1997) p.74.
3) Sanami T., Baba M., Saito K., and Hirakawa N., *Nucl. Instrum. Methods* A440 (2000) 403.
4) Yoshii K. and Kobayashi H., *Nucl. Instrum. Methods* A377 (1996) 102.
5) Oda M., Tamaki M., Takahashi K., and Tasaka., *Nucl. Instrum. Methods* A377 (1996) 323.
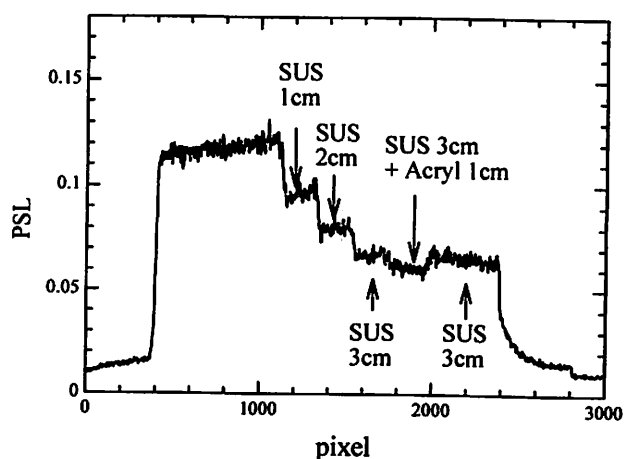
Fig. 1. Result in previous experimental geometry.
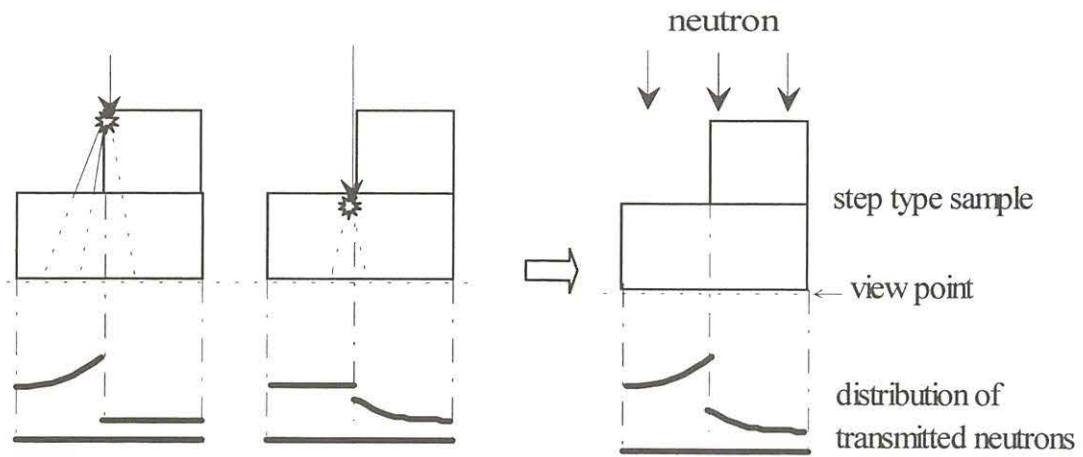
Fig. 2. Deformation due to neutrons scattered in the sample.
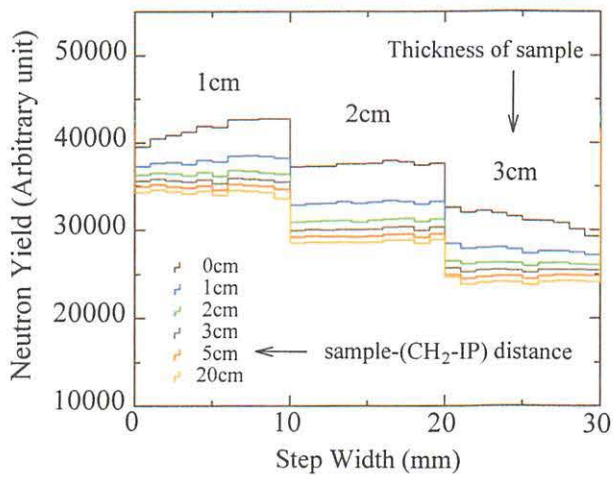
Fig. 3. Simulation result as a function of sample-IP distance.
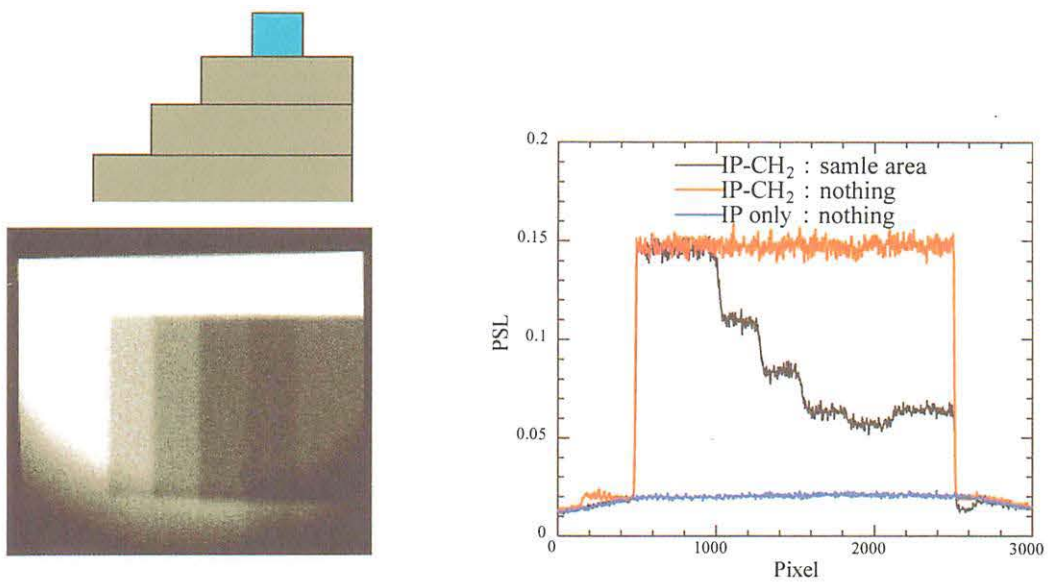
Fig. 4. Result of profile (SUS-3step & Acryl 1-step) and its projection.

V. 3. Functional Equation for the Fading Correction of Imaging Plates II

Ohuchi H., Yamadera A. * *and Nakamura T.* * *

Graduate School of Pharmaceutical Sciences, Tohoku University,
Cyclotron and Radioisotope Center, Tohoku University *
Graduate School of Engineering, Tohoku University * *

Introduction

In a previous report[1], we investigated the effects of temperature on the fading of the commercially available imaging plates (IPs) BAS-UR after irradiation with ^{238}U alpha-ray and ^{60}Co gamma-ray sources. The results led us to the conclusion that the fading curves could be divided into three components and the fading effect could be expressed in the following equation, which is the sum of three exponentially-decaying components, called the first, the second, and the third in order of half-life:

$$(PSL)_t / (PSL)_0 = A_1 \cdot \exp(-\ln2 \cdot t/T_1) + A_2 \cdot \exp(-\ln2 \cdot t/T_2)$$
$$+ A_3 \cdot \exp(-\ln2 \cdot t/T_3) \tag{1}$$

where $(PSL)_t$ and $(PSL)_0$ mean the photo-stimulated luminescence (PSL) of elapsed time t and 0 after irradiation, respectively, A_1 to A_3 are the component amplitudes, and T_1 to T_3 are the half-lives of each component.

We allowed some cooling period after irradiation to avoid the effect of the first component and determined a two exponentially-decaying components formula for each source that includes two variables: elapsed time(t) and absolute temperature(K).

The PSL calculated by each equation showed good agreement with the results of experimental ones between 0-40°C, however, the calculated PSL were below the experimental values over 40°C. This results indicates the existence of another component behind the third one, called the forth component. Because of the inadequate radioactivity of the ^{238}U and ^{60}Co sources, significant PSL to be analyzed the forth component could not be obtained over 40°C at long elapsed time.

In this study, our objective is to clarify this point and determine a formula which can show a good agreement with the results of experimental ones between 0-60°C by irradiating the IP with ^{244}Cm alpha-ray source, which has more than 100 times higher specific radioactivity than a ^{238}U source. Determination a formula of the fading effect of a different

kind of IP(BAS-MS) after irradiation with ^{238}U alpha-ray source is also attempted.

Theoretical analysis

The following results were found in a previous study[1];

1) The component amplitudes are independent of temperature. So that a formula can be determined by the half-lives of each component of fading curves.

2) The fading curve at 40°C is chosen as the reference curve because it typically shows the second and third components. The values of the half-lives at each temperature can be obtained by multiplying the half-lives at 40°C by the value of r, which is the ratio of the elapsed time at 40°C to that at each temperature having the same PSL as at 40°C.

To get the values of r accurately, we improved a method as shown in Fig.1. and explained below.

1. Several values at the elapsed time, e_1, ... , e_n , on the fading curve at 40°C are selected as the reference point.

2. Each elapsed time, d_1, ... , d_n , at which the same PSL is given on the different fading curve as on the reference curve is determined (in Fig.1, the fading curve at 50°C is shown as an example).

3. The ratios of e to d, $r_1 = e_1/d_1$, ... , $r_n = e_n/d_n$, are obtained.

4. The value of r is finally determined by taking the average of the values of r_n.

Experimental

The IPs used were the commercially available IP (Fuji Film Co.) BAS-UR and BAS-MS. A ^{244}Cm and a ^{238}U planchet sources (specific radioactivity of 1,638.5Bq/cm^2 and 10.8Bq/cm^2 each) were used. During irradiation and the time elapsed prior to reading, the IP was kept in an aluminium IP cassette inside an incubator having a temperature controlled to ±1°C. The fading characteristics were measured at temperatures varied by 10°C between 0-60°C. The IP was irradiated with the ^{244}Cm source for 15minutes and with the ^{238}U source for 60minutes by putting the source directly on the IP.

Results

Functional analysis

Several fading curves after irradiation with the ^{244}Cm source were obtained in the temperature range of 0 - 60°C. The fading curve at 60°C at long elapsed time clearly shows the existence of the forth component. The correlation between the values of r and the temperature (°C) for exciation with the ^{244}Cm source is shown in Fig. 2, comparing with that for the ^{238}U and ^{60}Co sources. The r values for each excitation with these three sources are almost the same. The logarithmic values of r show a single linear relationship to the temperature in all cases.

Using the half-lives obtained by the method mentioned in theoretical analysis, we develop a following formula consists of four terms for correcting four components of fading effect.

$$(PSL)_{t,k}/(PSL)_{0,k} = 0.582\exp \{-6.93 \times 10^{11} \cdot t \cdot \exp(-8.11 \times 10^{3}/K)\}$$

$$+0.378\exp \{-5.59 \times 10^{10} \cdot t \cdot \exp(-8.93 \times 10^{3}/K)\}$$

$$+0.038\exp \{-1.59 \times 10^{11} \cdot t \cdot \exp(-9.85 \times 10^{3}/K)\}$$

$$+0.002\exp \{-6.75 \times 10^{9} \cdot t \cdot \exp(-9.97 \times 10^{3}/K)\} \tag{2}$$

The PSL calculated from Eq.(2) is compared with the experimental results in Fig. 3. They are in quite good agreement in the temperature range of 0-60°C. There is no disagreement over 40°C which was shown in the comparison of the PSL for the ^{238}U and ^{60}Co sources calculated from equations and the experimental results.

Correspondence to the temperature change

To ascertain whether our formula can give the proper calculated PSL which corresponds to the temperature change between the time elapsed, a following experiment was done. After irradiation with the ^{244}Cm source, the IP was left inside the incubator kept at 30°C during a certain period, then it was moved into another incubator kept at 50°C.

Fig. 4 shows the comparison of the calculated PSL from Eq.(2) and the experimental results when the temperature has changed approximately 100 hours after irradiation. In contrast to this, the fading curves at 30°C and 50°C without the temperature change are also shown in Fig. 4. The calculated PSL shows a good correspondence to the temperature change and is consistent with the experimental results well.

Formula for a different kind of IP

Although it is well known that the fading effect depends on the type of IP, our investigation suggests that a different kind of IP such as BAS-MS, which is a highly sensitive and waterproof IP, shows the same temperature dependence as BAS-UR. Then, determination a formula of the fading effect after irradiation with the ^{238}U source using BAS-MS was attempted and a following formula was obtained.

$$(PSL)_{t,k}/(PSL)_{0,k} = 0.355\exp \{-7.74 \times 10^{12} \cdot t \cdot \exp(-9.21 \times 10^{3}/K)\}$$

$$+0.210\exp \{-6.08 \times 10^{13} \cdot t \cdot \exp(-1.12 \times 10^{4}/K) \}$$

$$+0.435\exp \{-4.00 \times 10^{14} \cdot t \cdot \exp(-1.24 \times 10^{4}/K) \} \tag{3}$$

The comparison of the PSL calculated from Eq.(3) and the experimental results shows good agreement in the temperature range of 0-50°C, however, the former values are

below the latter at 60°C. This disagreement is considered to come from the lack of the forth term in Eq.(3) to correct the forth component.

Discussion

The activation energies of the first, second, third, and forth component,Ea, Eb, Ec, and Ed are obtained from Arrhenius' equation. The values for ^{238}U , ^{244}Cm, and ^{60}Co sources are listed in Table 1. It seems that there is no quite a difference of the values among these three sources. However, it is clearly shown that the activation energy becomes higher as the component proceeds.

While several attempts to explain the mechanism of fading have been done, it still remains unclear. The fading of the PSL density (PSL/mm^2) of the IP might be induced by the dispersion of the stored energy through recombination of electron centers with trapped hole center[2]. It also might be due to the F(Br) centers shallowly trapped at impurities or dislocations in the BaFBr:Eu^{2+} crystal[3]. Our results imply that thermal excitation of electrons from F centers must be substantially concerned in the mechanism of fading.

References

1) Ohuchi H., Yamadera A. and Nakamura T., Nucl. Instrum. & Methods, in press.
2) Kimura T. and Inabe K., Jpn. J. Appl. Phys. 37 (1998) 2670.
3) Kondo Y., Tezuka T. and Iwabuchi Y., The proceedings of ICDIM(2000).

Table 1. Activation energies of the first, second, third, and forth component; Ea, Eb, Ec, and Ed obtained by using Arrhenius' equation.

	^{238}U	^{60}Co	^{244}Cm	^{238}U
Kind of IP	BAS-UR	BAS-UR	BAS-UR	BAS-MS
E_a(eV)			0.70	0.79
E_b(eV)	0.96	0.93	0.77	0.96
E_c(eV)	0.96	0.93	0.85	1.07
E_d(eV)			0.86	
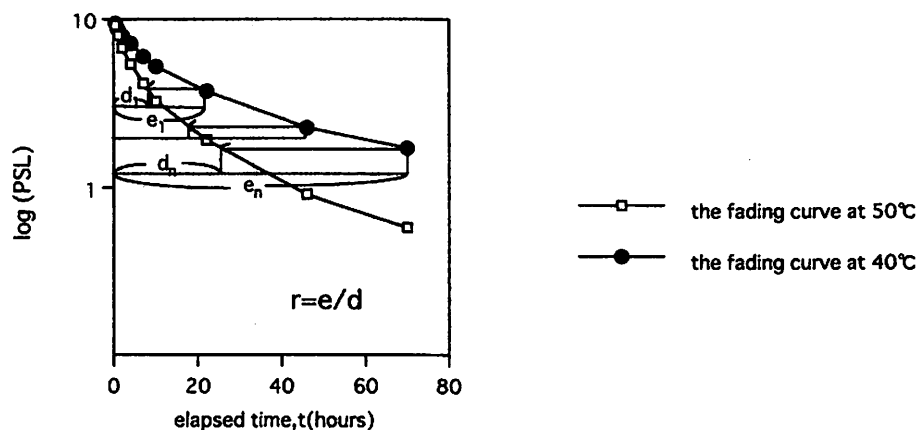
Fig. 1. Method of data analysis to get the values of half-lives for each fading curve.
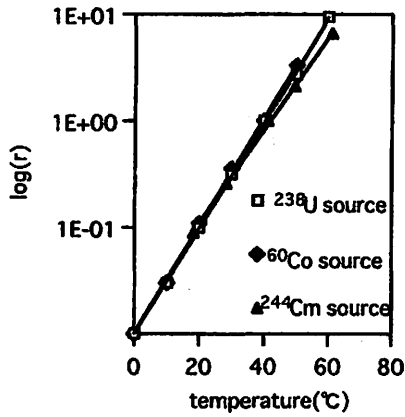
Fig. 2. Correlation between the values of r and the temperature (°C) for each excitation with the ^{238}U, ^{60}Co, and ^{244}Cm sources.
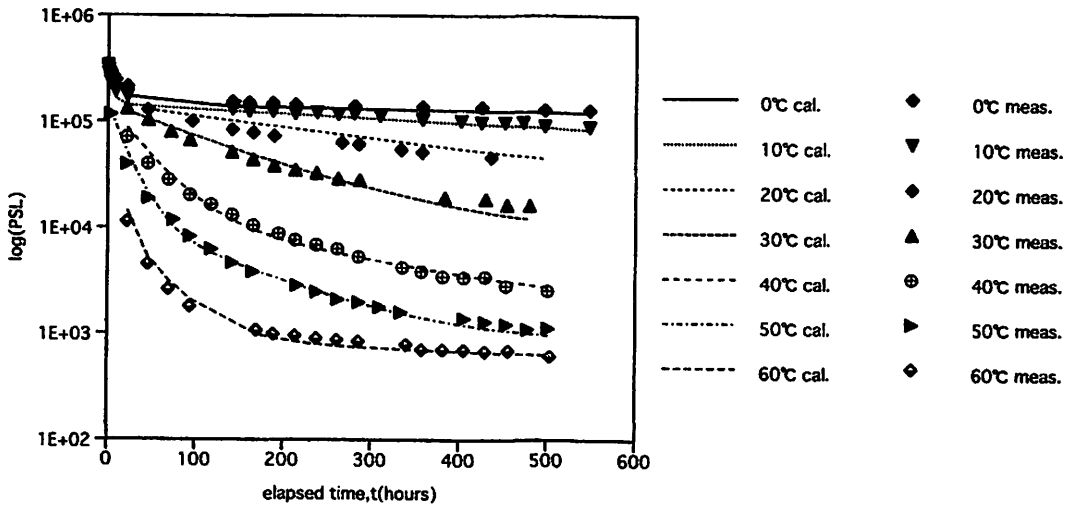
Fig. 3. Comparison of the PSL of fading curves for ^{244}Cm alpha rays calculated from Eq.(2) and the experimental results.
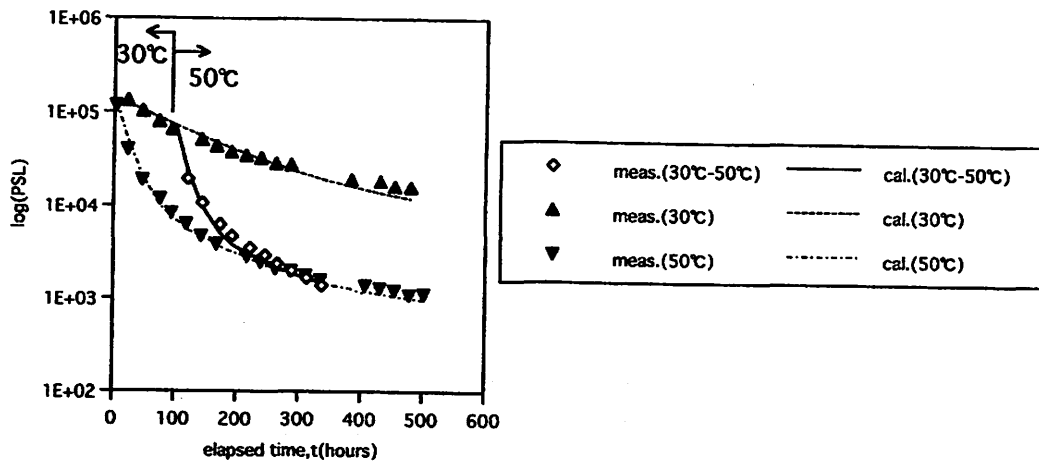
Fig. 4. Comparison of the PSL for ^{244}Cm alpha rays calculated from Eq.(2) and the experimental results when the temperature has changed from 30°C to 50°C for approximately 100 hrs after irradiation.

V. 4. Training for Safehandling of Radiation and Radioisotopes and X-Ray Machines for Beginners in Tohoku University

Nakamura T.,Baba Y., Yamadera A., and Miyata T.

Cyclotron and Radioisotope Center, Tohoku University

Training for safehandling of radiation and radioisotopes for beginners has been conducted twice a year from 1977 in Tohoku University. The contents of lectures and practices are shown in Table 1. In 1999 the training was performed for 495 persons. The departments to which they belong are given in Table 2.

Training for safehandling of X-ray machines and electron microscopes began from the end of 1983. The training is scheduled to be held twice a year at the same time as the safehandling of radiation and radioisotopes. Only lectures are given and not practices. The contents of the lectures and the distributions of trainees are shown in Tables 3 and 4, respectively.

Training for safehandling of synchrotron radiation began from the end of 1995. The contents of the lectures are the same as safehandling of radiation and radioisotopes for beginners and not practices. In 1999 the training was performed for 48 persons.

Table 1. Contents of lectures and practices for safehandling of radiation and radioisotopes in 1999.

Lectures (one day)	
Radiation physics and measurements	1.5 (h)
Chemistry of radioisotopes	1.0
Radiological protection ordinance	1.5
Effects of radiation on man	1.0
Safehandling of radioisotopes	1.5

Practices (one day)	
Treatment of unsealed radioactive solution	4.0 (h)
Measurements of surface contamination and decontamination	1.0
Measurements of gamma rays and beta rays	2.0

Table 2. Distribution of trainees for safehandling of radiation and radioisotopes in 1999.

Department	Staff	Student	Total
Medicine	17	116	133
Dentistry	8	14	22
Pharmacy	0	47	47
Science	0	73	73
Engineering	1	68	69
Agriculture	1	86	87
Research Institutes	4	50	54
The others	2	8	10
Total	33	462	495

Table 3. Contents of lectures for safehandling of X-ray machines and electron microscopes in 1999.

Safehandling of X-ray machines	1.5 (h)
Radiological protection ordinance	1.0
VTR for safehandling of radiation and radioisotopes	1.0

Table 4. Distribution of trainees for safehandling of X-ray machines and electron microscopes in 1999.

Department	Staff	Student	Total
Medicine	2	0	2
Science	2	30	32
Engineering	0	91	91
Research Institutes	14	95	109
The others	0	1	1
Total	18	217	235

Table 5. Distribution of trainees for synchrotron radiation in 1999.

Department	Staff	Student	Total
Dentistry	1	0	1
Science	0	11	11
Engineering	0	9	9
Agriculture	0	1	1
Research Institutes	3	23	26
Total	4	44	48

V. 5. Radiation Protection and Management

Miyata T., Yamadera A., Nakamura T. and Watanabe N. *

Cyclotron and Radioisotope Center, Tohoku University
Japan Radiation Protection Co., Ltd.*

(1) Unsealed radionuclides used in the center

The kinds and activities of unsealed radionuclides handled in the center in 1999 are shown in Table 1.   The table includes the isotopes produced by the cyclotron, purchased from the Japan Isotope Association and took over from another RI institutes.

(2) Individual monitoring

The exposure doses of the workers in the center in 1999 is given in Table 2.   They were less than the permissible doses.

(3) Monitoring of the workplace

Radiation dose rates inside and outside of the controlled areas were monitored periodically and as needed.   They were below the legal permissible levels.   Surface contamination levels of the floors inside the controlled areas were measured by smear method and with survey meters periodically and as needed.   They also cleared under the legal regulation levels.

(4) Wastes management

The radioactive wastes delivered to the Japan Radioisotope Association in 1999 are shown in Table 3.   The concentration of radioisotopes in the air released after filtration from the stack was monitored with stack gas monitors.   The levels were less than the legal regulation levels.   The radioactive water was storaged at the tanks at least for 3 days and then released to the sewerage after confirming that the concentration was less than permissible levels.

The treated volume of radioactive waste of organic scintillator was 624 l by the incinerator made by Fujikogyo Co., Ltd.

Table 1. Unsealed radionuclides used in the center in 1999.

(a)Cyclotron Building(kBq)

group 1,2	group 3		group4	
	^{11}C	900,905,200.000	^{18}F	1,038,560,400.000
	^{111}In	1,429,030.000		
total 0.000	total	902,334,230.000	total	1,038,560,400.000

(b)RI Building(kBq)

group 1,2		group 3		group 4	
^{90}Sr	192.000	^{32}P	1,012,535.040	^{3}H	84,811.348
^{22}Na	27,555.200	^{35}S	55,586.120	^{14}C	13,092.600
^{60}Co	3,029.050	^{86}Rb	57,540.820	^{18}F	465,117,400.000
^{68}Ge	92,434.000				
^{125}I	427,018.400				
^{137}Cs	30,397.910				
total	580,626.560	total	1,125,661.980	total	465,215,303.948

(c)Research Building(kBq)

group 1,2	group 3		group4	
	^{11}C	740,000.000	^{18}F	1,776,000.000
	^{15}O	45,066,000.000		
total 0.000	total	45,806,000.000	total	1,776,000.000

Table 2. Occupational radiation exposures at the center in 1999.

Dose range (mSv)	Number of individuals
No measurable exposure	48
Measurable exposure less than 1.0	6
1.0 to 3.1	4
Total persons monitored	58

Table 3. Radioactive wastes delivered to the Japan Radioisotope Association in 1999.

Wastes Number	Container	
solids		
Combustible Type I	50 ldrum	16
Combustible Type I	50 ldrum	12
Incombustibles 5	50	ldrum
Annimal carcasses 10	50 l drum	
Filters 0	1 l /unit	
liquids		
inorganic liquids	25 l PE bottle	8

Type I: Cloth and Paper made of natural cellulose.

Type II: Combustible Plastics such as Polyethylene and Polypropylene.

VI.   PUBLICATIONS

VI. PUBLICATIONS
(January 1999 ~ December 1999)

A

1. Lifetime measurement of the first excited state of ^{64}Ga
   M. Tanigaki, K. Sekiguchi, M. Fujita, T. Hoshino, T. Baba, N. Kawamura,
   T. Shinozuka, M. Fujioka
   THE EUROPEAN PHYSICAL JOURNAL **A 6** (1999)119-120.

2. Measurements of Activation Cross Sections on Spallation Reactions for ^{59}Co and natCu
   at Incident Neutron Energies of 40 to 120MeV
   Eun Joo KIM, Takashi NAKAMURA, Yoshitomo UWAMINO,
   Noriyoshi NAKANISHI, Mineo IMAMURA, Noriaki NAKAO, Tokushi SHIBATA,
   Susumu TANAKA
   Journal of Nuclear Science and Technology **36**, 29-40 (1999).

3. Measurements of Secondary Neutrons Produced from Thick Targets Bombarded by
   High Energy Neon Ions
   Tadahiro KUROSAWA, Noriaki NAKAO, Takashi NAKAMURA,
   Yoshitomo UWAMINO, Tokushi SHIBATA, Akifumi FUKUMURA,
   Ken MURAKAMI
   Journal of Nuclear Science and Technology **36**, 41-53 (1999).

4. Spectral measurements of neutrons, Protons, deuterons and tritons produced by
   100MeV/nucleon He bombardment
   T. Kurosawa, T. Nakamura, N. Nakao, T. Shibata, Y. Uwamino, A. Fukumura
   NUCLEAR INSTRUMENTS & METHODS IN PHYSICS RESEARCH **A430** (1999)
   400-422.

5. Measurements of Secondary Neutrons Produced from Thick Targets Bombarded by
   High-Energy Helium and Carbon Ions
   T. Kuroosawa, N. Nakao, T. Nakamura, Y. Uwamino, T. Shibata, N. Nakanishi,
   A. Fukumura, K. Murakami
   NUCLEAR SCIENCE AND ENGINEERING: **132**. 30-57 (1999).

6. CHARACTERISATION OF A REAL-TIME PERSONAL NEUTRON DOSEMETER
   WITH TWO SILICON DETECTORS
   T. Nakamura, M. Sasaaki, O. Ueda, T. Suzuki
   Radiation Rrotection Dosimetry **85**, 45-48(1999).

7. DEVELOPMENT OF A NEW PERSONAL DOSEMETER FOR LOW ENERGY X
   RAYS USING AN IMAGING PLATE
   S. Tniguchi, A Yamadera, T. Nakamura, K. Fukuda
   Radiation Rrotection Dosimetry **85**, 7-10 (1999).

8. ^{18}F-FDG PET Imaging of Muscle Activity in Runners
   Manabu Tashiro, Toshihiko Fujimoto, Masatoshi Itoh, Kazuo Kubota,
   Takehiko Fujiwara, Masayasu Miyake, Shoichi Watanuki, Etsuo Horikawa ,
   Hidetada Sasaki, Tatsuo Ido
   The journal of Nuclear Medicine **40**, 70-76 (1999).

9. Internal absorbed dose estimation by a TLD method for ^{18}F-FDG and comparison with the dose estimates from whole body PET
Hossain M Deloar, Takehiko Fujiwara, Miho Shidahara, Takashi Nakamura, Akira Yamadera, Masatoshi Itoh
Phys. Med Biol **44** (1999)595-606.

10. Easy detection of tumor in oncologic whole-body PET by projection reconstruction images with maximum intensity Projection algorithm
Takehiko FUJIWARA, Masayasu MIYAKE, Shoichi WATANUKI, Marco A MEJIA, Masatoshi ITOH Hiroshi FUKUDA
Reprint from Annals of Nuclear Medicine **13**, 199-203 (1999).

B

11. Isomeric yield ratios of fission products in proton-induced fission of 232Th
S. Goto, D. Kaji, H. Kudo, M. Fujita, T. Shinozuka, M. Fujioka
Journal of Radioanalytical and Nuclear Chemistry **239**, (1999) 109-112.

12. Differential vnlnerability of dopamine receptors in the mouse brain treated with MPTP
Hiroaki Tanji, Tsutomu Araki, Haruo Nagasawa, Yasuto Itoyama
Brain Research **824** (1999)224-231.

13. Sclerosing Mediastinitis Findings on Fluorine-18 Fluorodeoxyglucose Positron Emission Tomography
MUHAMMAD BABAR IMRAN, KAZUO KUBOTA, SEIROU YOSHIOKA, SUSUMU YAMADA, TACHIO SATO, HIROSHI FUKUDA, TAKASHI YOSHIOKA, RYUNOSUKE KANAMARU, TAKEHIKO FUJIWARA, MASATOSHI ITOH
CLINICAL NUCLEAR MEDICINE **24**, 5 (1999).

14. Comparison of the distriibution of fiuoine-18 fluoromisonidazole deoxyglucose and methionine in tumour tissue
Kazuo Kubota, Masao Tada, Susumu Yamada, Kastuyoshi Hori Sachiko Saito, Ren Iwata, Kazunori Sato, Hiroshi Fukuda, Tasuo Ido
European Journal of Nuclear Medicine **26** (1999) 751-757.

15. Alteration of neurotensin receptors in MPTP-treated mice
Hiroaki Tanji, Tsutomu Araki, Kazuo Fujihara, Haruo Nagasawa, Yasuto Itoyama
Peptides **20** (1999) 803-807.

16. Increases in [^{3}H]FK-506 and [^{3}H]L-NG-Nitro-Arginine Binding in the Rat Brain After Nigrostriatal Dopaminergic Denervation
T. Araki, H. Tanji, K. Fujihara, H. Kato, Y. Itoyama
Metabolic Brain Disease **14**, 21-31(1999).

17. Alterations of second messenger systems in the rat brain after 6-hydroxydopamin lesions of the medial forebrain bundle
Tsutomu Araki, Hiroaki Tanji, Hiroyuki Kato, Michinao Mizugaki, Yasuto Itoyama
European Journal of Pharmaceutical Sciences **8** (1999) 261-267.

VII. MEMBERS OF COMMITTEES

VII. Members of Committees (as of Jan. 1, 2000)

General

(Chairman)	Hikonojo	Orihara	(CYRIC)
	Osamu	Hashimoto	(Graduate School of Science)
	Hiroshi	Kudo	(Graduate School of Science)
	Akira	Takahashi	(Graduate School, Division of Medicine)
	Tadashi	Yamada	(Graduate School, Division of Dentistry)
	Yasushi	Ohizumi	(Faculty of Pharmaceutical Sciences)
	Katsunori	Abe	(Graduate School of Engineering)
	Teruo	Miyazawa	(Draduate School of Agricultural Science)
	Reimon	Hanada	(Institute for Materials Research)
	Minoru	Issiki	(Institute for Advanced Materials Processing)
	Hiroshi	Fukuda	(Institute for Development, Aging and Cancer)
	Jirohta	Kasagi	(Laboratory of Nuclear Science)
	Syogo	Yamada	(University Hospital)
	Manabu	Fujioka	(CYRIC)
	Tatsuo	Ido	(CYRIC)
	Takashi	Nakamura	(Graduate School of Engineering)
	Masatoshi	Itoh	(CYRIC)
	Ren	Iwata	(Graduate School of Engineering)
	Akira	Yamadera	(CYRIC)
	Keizo	Ishii	(Graduate School of Engineering)
	Tadao	Saitou	(Draduate School of Agricultural Science)
	Makoto	Watanabe	(Research Institute of Scientific Measurements)
	Michiharu	Katoh	(Institute for Chemical Reaction Science)

Research Program

(Chairman)	Takashi	Nakamura	(Graduate School of Engineering)
	Takemi	Nakagawa	(Graduate School of Science)
	Tsutomu	Sekine	(Graduate School of Science)
	Akira	Takahashi	(Graduate School, Division of Medicine)
	Kazuhiko	Yanai	(Graduate School, Division of Medicine)
	Hidetada	Sasaki	(Graduate School, Division of Medicine)
	Katsunori	Abe	(Graduate School of Engineering)

Reimon	Hanada	(Institute for Materials Research)
Hiroshi	Fukuda	(Institute for Development, Aging and Cancer)
Manabu	Fujioka	(CYRIC)
Tatsuo	Ido	(CYRIC)
Keizo	Ishii	(Graduate School of Engineering)
Masatoshi	Itoh	(CYRIC)
Ren	Iwata	(Graduate School of Engineering)

Cyclotron

(Chairman)	Manabu	Fujioka	(CYRIC)
	Osamu	Hashimoto	(Graduate School of Science)
	Takemi	Nakagawa	(Graduate School of Science)
	Toshio	Kobayashi	(Graduate School of Science)
	Satoru	Kunii	(Graduate School of Science)
	Tsutomu	Sekine	(Graduate School of Science)
	Kazushige	Maeda	(Graduate School of Science)
	Keizo	Ishii	(Graduate School of Engineering)
	Akira	Hasegawa	(Graduate School of Engineering)
	Reimon	Hanada	(Institute for Materials Research)
	Minoru	Issiki	(Institute for Advanced Materials Processing)
	Tatsuo	Ido	(CYRIC)
	Takashi	Nakamura	(Graduate School of Engineering)
	Masatoshi	Itoh	(CYRIC)
	Ren	Iwata	(Graduate School of Engineering)
	Tsutomu	Shinozuka	(CYRIC)
	Astuki	Terakawa	(CYRIC)

Radiation Protection and Training of Safe Handling

(Chairman)	Tadashi	Yamada	(Graduate School, Division of Dentistry)
	Yoshiaki	Fujii	(Graduate School of Science)
	Hiroshi	Kudo	(Graduate School of Science)
	Yoshihiko	Uehara	(School of Medicine)
	Yoshihiro	Takai	(University Hospital)
	Yasushi	Yamazoe	(Graduate School, Division of Pharmaceutical Sciences)
	Keizo	Ishii	(Graduate School of Engineering)
	Toshiyasu	Yamaguchi	(Graduate School of Agricultural Science)
	Masayuki	Hasegawa	(Institute for Materials Research)
	Hiroshi	Fukuda	(Institute for Development, Aging and Cancer)

221

	Manabu	Fujioka	(CYRIC)
	Takashi	Nakamura	(Graduate School of Engineering)
	Akira	Yamadera	(CYRIC)
	Tanetoshi	Koyama	(Institute for Chemical Reaction Science)

Life Science

(Chairman)	Tatsuo	Ido	(CYRIC)
	Kazuo	Yamamoto	(Graduate School of Science)
	Yasuhito	Itoyama	(Graduate School, Division of Medicine)
	Kazuie	Iinuma	(Graduate School, Division of Medicine)
	Syogo	Yamada	(Graduate School, Division of Medicine)
	Reizo	Shirane	(Graduate School, Division of Medicine)
	Masahiko	Yamamoto	(Graduate School, Division of Medicine)
	Michinao	Mizugaki	(University Hospital)
	Makoto	Watanabe	(Graduate School, Division of Dentistry)
	Yasushi	Yamazoe	(Graduate School, Division of Pharmaceutical Sciences)
	Keizo	Ishii	(Graduate School of Engineering)
	Satoshi	Yokota	(Graduate School of Agricultural Science)
	Hiroshi	Fukuda	(Institute for Development, Aging and Cancer)
	Kazuo	Kubota	(Institute for Development, Aging and Cancer)
	Shin	Maruoka	(College of Medical Sciences)
	Manabu	Fujioka	(CYRIC)
	Takashi	Nakamura	(Graduate School of Engineering)
	Masatoshi	Itoh	(CYRIC)
	Kei-ichiro	Yamaguchi	(CYRIC)
	Yoshihito	Funaki	(CYRIC)

Prevention of Radiation Hazards

(Chairman)	Takashi	Nakamura	(Graduate School of Engineering)
	Takemi	Nakagawa	(Graduate School of Science)
	Tsutomu	Sekine	(Graduate School of Science)
	Ken	Abe	(Graduate School of Engineering)
	Manabu	Fujioka	(CYRIC)
	Tatsuo	Ido	(CYRIC)
	Akira	Yamadera	(CYRIC)
	Iwao	Suzuki	(CYRIC)
	Takamoto	Miyata	(CYRIC)

VIII.   PERSONNEL

VIII. Personnel (as of Jan. 1, 2000)

Director Hikonojo   Orihara

Division of Accelerator

Manabu	Fujioka
Osamu	Hashimoto[1]
Tsutomu	Shinozuka
Akiyoshi	Yamazaki
Masahiro	Fujita
Shizuo	Kan[6]
Shizuo	Chiba[6]
Yasushi	Ohmiya[6]
Naoto	Takahashi[6]

Division of Instrumentations

Hikonojo	Orihara
Keizo	Ishii[2]
Astuki	Terakawa
Toshiyuki	Misu
Sho-ichi	Watanuki
Tsutomu	Ichikawa

Division of Radiopharmaceutical Chemistry

Tatsuo	Ido
Ren	Iwata[2]
Yoshihito	Funaki
Masahiro	Yu-ki
Akari	Kagaya
Hideo	Takahashi
Yo-ichi	Ishikawa[7]

Division of Cyclotron Nuclear Medicine

Masatoshi	Itoh
Kei-ichiro	Ymaguchi
Kazuhiko	Yanai[4]
Kaoru	Ozaki

223

Takashi   Rikimaru

Masayasu   Miyake

Division of Radiation Protection and Safety Control

Mamoru   Baba

Takashi   Nakamura[2]

Akira   Yamadera

Takamoto   Miyata

Noboru   Watanabe[7]

Graduate Student and Researcher

Yasumori	Kanai	(Graduate School of Science)
Tsuyoshi	Hoshino	(Graduate School of Science)
Takero	Baba	(Graduate School of Science)
Tetsu	Sonoda	(Graduate School of Science)
Takehiko	Suzuki	(Graduate School of Science)
Hiroshi	Suzuki	(Graduate School of Science)
Kazuaki	Kumagai	(Graduate School of Science)
Yasuo	Saito	(Graduate School of Science)
Yu-ji	Kikuchi	(Graduate School of Science)
Takeo	Uekusa	(Graduate School of Science)
Shinji	Nagata	(Graduate School, Division of Pharmaceutical Sciences)
Syozou	Furumoto	(Graduate School, Division of Pharmaceutical Sciences)
Ryo	Kosaka	(Graduate School, Division of Pharmaceutical Sciences)
Kentaro	Wakayama	(Graduate School, Division of Pharmaceutical Sciences)
Kumagai	Toshihiko	(Graduate School, Division of Pharmaceutical Sciences)
Sachiko	Tanaka	(Graduate School, Division of Pharmaceutical Sciences)
Manabu	Tashiro	(Graduate School, Division of Medicine)
Md. MEHEDI MASUD		(Graduate School, Division of Medicine)
Laxmi	Singh	(Graduate School, Division of Medicine)
Tadahiro	Kurosawa	(Graduate School of Engineering)
Yoshihiro	Nakane	(Graduate School of Engineering)
Michiya	Sasaki	(Graduate School of Engineering)
Miho	Shidahara	(Graduate School of Engineering)
Rasolonjatovo Daniel		(Graduate School of Engineering)
Hiroshi	Sugita	(Graduate School of Engineering)
Masaharu	Kinno	(Graduate School of Engineering)
Sayaka	Satoh	(Graduate School of Engineering)
Tomoya	Munomiya	(Graduate School of Engineering)

Hiroshi	Iwase	(Graduate School of Engineering)
Tomoyuki	Shiomi	(Graduate School of Engineering)
Hiroshi	Yashima	(Graduate School of Engineering)
Hisaki	Satoh	(Graduate School of Engineering)
Syunji	Takagi	(Researcher)
Yo	Makita	(Researcher)

Office Staff

Iwao	Suzuki
Yukinori	Mitobe
Kyoko	Fujisawa
Junko	Matsuno
Fumiko	Mayama
Mitsuko	Endo
Yu-ko	Yamashita
Keietsu	Aizawa
Kietu	Takahashi
Yuri	Okumura
Noriko	Suzuki
Kimiko	Abe
Toshiyuki	Watanabe[7]

1) Graduate School of Science
2) Graduate School of Engineering
3) Institute for Materials Research
4) Graduate School, Division of Medicine
5) Institute for Development, Aging and Cancer
6) SUMI-JU Accelerator Service Ltd.
7) Japan Radiation Protection Co., Ltd.

225